

**Microwave Kinetic Inductance Detector Camera  
Development for Millimeter-Wave Astrophysics**

by

**James A. Schlaerth**

B.S., Vanderbilt University, 2004

M.S., University of Colorado, 2010

A thesis submitted to the  
Faculty of the Graduate School of the  
University of Colorado in partial fulfillment  
of the requirements for the degree of  
Doctor of Philosophy  
Department of Physics  
2010

This thesis entitled:  
Microwave Kinetic Inductance Detector Camera Development for Millimeter-Wave Astrophysics  
written by James A. Schlaerth  
has been approved for the Department of Physics

---

Prof. Jason Glenn

---

Prof. Nils Halverson

Date \_\_\_\_\_

The final copy of this thesis has been examined by the signatories, and we find that both the content and the form meet acceptable presentation standards of scholarly work in the above mentioned discipline.

Schlaerth, James A. (Ph.D., Physics)

Microwave Kinetic Inductance Detector Camera Development for Millimeter-Wave Astrophysics

Thesis directed by Prof. Prof. Jason Glenn

This thesis describes my contribution to the design, assembly and testing required for a camera using antenna-coupled Microwave Kinetic Inductance Detectors (MKIDs). MKIDs are superconducting resonators in which the resonance frequency and quality factor are sensitive measures of Cooper pairs broken by incident radiation. The MKID camera, called the Multicolor Submillimeter Inductance Camera (MUSIC), is built to detect and characterize the physics of dusty submillimeter galaxies, the primary component of the far-infrared background discovered by the *COBE* satellite. The camera will have 576 pixels sensitive to 4 colors simultaneously in the range of 150-360 GHz. With these bands, combined with shorter wavelength data from instruments on the *Spitzer* and *Herschel* far-infrared satellites, we can find the integrated flux from high-redshift dusty galaxies and identify galaxies likely to be at extremely high redshift. We have achieved first light using a demonstration instrument (“DemoCam”), testing two colors, centered at 240 GHz and 350 GHz, in 2007, and demonstrated three-color operation in 2010.

In the thesis is discussed the design, testing and optimization of DemoCam, in particular its function in testing several iterations of arrays of antenna-coupled MKID resonators. The arrays tested are  $4 \times 4$  arrays of two-color antenna pixels, and newer  $6 \times 6$  arrays of three-color antenna pixels, the latter with a “dark” or uncoupled resonator for each antenna. This testing has been used to explore the physics of the detectors, test which properties maximize the detector signal-to-noise ratio, and to inform the MKID camera’s optical design. The goal of this testing is to find how to improve sensitivity to minimize Noise Equivalent Power in the presence of large background loads, as in ground-based sub/millimeter astronomy. The DemoCam is shown to reach interesting levels of sensitivity on the sky in three colors (230, 290 and 350 GHz), and to have effective calibration mechanisms, with the readout system used for the final camera.

## **Dedication**

To the Army and the Navy and the battles they have won. To America's colors, the colors  
that never run. May the wings of liberty never lose a feather.

## Acknowledgements

I would like to first acknowledge my advisor, Jason Glenn, for giving me the chance to work on such an amazing project, and for all the help and advice along the way.

My thesis work often took me to Caltech for great lengths of time. During these travels, I appreciated the support of Sunil Golwala and Jonas Zmuidzinas, my advisors away from home in my months spent in Pasadena. In lab work to understand MKIDs and develop DemoCam, I particularly thank Tasos Vayonakis, Nicole Czakon and Jiansong Gao. Without their discussions or lab work, the development of MKIDs would not be anywhere near what it is today. Although I spent less time at JPL, I would like to mention in particular Peter Day, my technical advisor at JPL, and Rick LeDuc, who made excellent devices for us throughout – the true basis of this thesis.

The development of a sub/millimeter MKID camera is a huge project, and takes the best efforts of many very talented and motivated individuals. Tom Downes, Ran Duan, Matt Hollister, Shwetank Kumar, Phil Maloney, Ben Mazin, Omid Noroozian, and Jack Sayers all contributed an enormous amount to this project, and showed their commitment with the high quality of their work.

In addition to long periods of time at Caltech, I also spent much time at the CSO on Mauna Kea. I must thank Ed Bufil, Steve Baca, Allen Guyer and Pat Nelson, the day crew at the CSO, for their tremendous support and patience during two engineering runs.

Throughout the years I've been able to interact and have helpful discussions with many very good scientists; in particular, I'd like to mention James Aguirre, Randol Aikin, Amy Bender, Clint Bockstiegel, Lieko Earle, Megan Eckhart, Dave Moore, Hien Nguyen, Mike Skrutskie, and John

Vaillancourt. All of them helped with this in their own way, as did many others that I do not have room to mention.

My family was very supportive through this entire process, particularly during my long stays in Pasadena. Indeed, their questions about the actual size of submillimeter galaxies (much larger than 1 millimeter) and their assertion that “time stops at absolute zero” made it fun to be the physicist in a family of physicians.

Finally, I could not have worked on such a project without the support of the NSF and the Moore Foundation, who funded our camera, and NASA, who funded me. I still marvel at the fact that I was paid to complete a Ph.D., and I hope never to take this for granted.

## Contents

### Chapter

<b>1</b>	<b>Introduction</b>	<b>1</b>
1.1	Submillimeter and Millimeter Astrophysics and Cosmology . . . . .	1
1.1.1	The Cosmic Far-Infrared Background . . . . .	1
1.1.2	Resolving the background – submillimeter galaxies . . . . .	2
1.1.3	Other sub/millimeter astrophysics . . . . .	9
1.2	MKIDs in context . . . . .	10
1.2.1	Sub/millimeter detectors and why we need arrays . . . . .	11
1.2.2	Competing detector technologies . . . . .	13
1.2.3	MKID advantages . . . . .	16
1.2.4	Coupling to sub/millimeter radiation . . . . .	17
1.2.5	Future developments of low temperature detectors . . . . .	17
1.3	Description of thesis . . . . .	18
1.3.1	Description of collaboration . . . . .	19
1.3.2	Conventions . . . . .	19
<b>2</b>	<b>Introduction to MKIDs</b>	<b>21</b>
2.1	The Physics of MKIDs . . . . .	21
2.1.1	Microwave resonant circuits as detectors . . . . .	21
2.1.2	Principle of detection in MKIDs . . . . .	25

2.1.3	Resonator noise . . . . .	33
2.2	Use of MKIDs for sub/millimeter detection . . . . .	35
2.2.1	Sub/millimeter MKID designs . . . . .	36
2.2.2	Antenna coupling . . . . .	41
2.2.3	On-chip filtering and band definition . . . . .	43
2.2.4	MKID readout . . . . .	44
2.3	Parameters and measurements necessary to understand MKID Camera performance	47
2.3.1	Optical efficiency . . . . .	48
2.3.2	Excess load . . . . .	48
2.3.3	Beam maps and point source response . . . . .	50
2.3.4	Spectral bandpass measurements . . . . .	50
2.3.5	Resonator internal and external noise . . . . .	51
2.3.6	Systematic effects . . . . .	52
2.3.7	MKID performance as a function of readout power . . . . .	52
<b>3</b>	<b>MKID NEP and mapping speed optimization</b>	<b>53</b>
3.1	Responsivity . . . . .	53
3.2	Noise-limiting cases . . . . .	56
3.2.1	NEP in the substrate TLS noise limit . . . . .	56
3.2.2	NEP in the amplifier noise limit . . . . .	57
3.2.3	NEP in the photon noise limit . . . . .	59
3.2.4	Combined NEP . . . . .	59
3.3	Mapping speed optimization . . . . .	61
3.4	Scatter in resonance frequency spacing . . . . .	62
3.5	Other effects on sensitivity . . . . .	65
3.5.1	Critical coupling . . . . .	65
3.5.2	Non-uniform power absorption . . . . .	68

3.5.3	Excess power driving: “distortion” and “saturation” of MKIDs . . . . .	69
<b>4</b>	<b>DemoCam design and laboratory testing</b>	<b>72</b>
4.1	Dewar Assembly . . . . .	72
4.1.1	Device Layout . . . . .	72
4.1.2	Cryostat Assembly . . . . .	75
4.2	MKID device testing . . . . .	78
4.2.1	Resonator fitting routine . . . . .	78
4.2.2	Measurement of fundamental MKID parameters - Dark Testing . . . . .	81
4.2.3	Optical measurements . . . . .	100
4.2.4	Resonance frequency scatter . . . . .	117
4.3	Summary . . . . .	117
<b>5</b>	<b>MKID DemoCam Telescope Data - First Light with KIDs</b>	<b>120</b>
5.1	Optical Design/Telescope Interface . . . . .	120
5.2	Description of observing mode . . . . .	122
5.3	Integration with Bolocam pipeline . . . . .	124
5.4	Telescope data . . . . .	125
5.4.1	Data cleaning - sky subtraction and magnetic field cleaning . . . . .	125
5.4.2	Beam sizes . . . . .	126
5.4.3	Responsivity . . . . .	127
5.4.4	Total sensitivity - noise equivalent flux density . . . . .	130
5.4.5	Magnetic response . . . . .	133
5.5	Discussion - contributing factors to the sensitivity found . . . . .	134
<b>6</b>	<b>The MKID DemoCam rebuilt</b>	<b>136</b>
6.1	Magnetic shield implementation and hardware changes . . . . .	136
6.2	New devices . . . . .	142

6.2.1	General device design . . . . .	142
6.2.2	Devices made and tested . . . . .	143
6.2.3	Testing methods . . . . .	145
6.3	Device 4 - testing and parameters . . . . .	145
6.3.1	Device Parameters . . . . .	146
6.3.2	Inter-resonator coupling . . . . .	148
6.3.3	Response, excess load and out-of-band pickup . . . . .	153
6.4	Device 5 - A second iteration . . . . .	156
6.4.1	Device design . . . . .	156
6.4.2	Device testing . . . . .	158
6.4.3	Conclusions . . . . .	160
6.5	Device 7 - the third iteration . . . . .	162
6.5.1	Changes in design . . . . .	162
6.5.2	Device 7c testing . . . . .	162
6.5.3	Conclusions . . . . .	169
6.6	Device 8 - a final iteration . . . . .	169
6.6.1	Changes in design . . . . .	169
6.6.2	Device 8b testing . . . . .	170
6.7	IDC devices - a final analysis . . . . .	175
<b>7</b>	<b>Optimal Operation of MKIDs</b>	<b>177</b>
7.1	Noise and multi-channel noise removal . . . . .	177
7.1.1	Amplifier noise . . . . .	177
7.1.2	Noise removal . . . . .	179
7.2	Signal-to-noise ratio optimization in detectors exposed to background loads . . . . .	184
7.2.1	Responsivity to sky loading . . . . .	185
7.2.2	Noise in open-window observations . . . . .	189

7.3	Conclusions . . . . .	192
<b>8</b>	Astronomical Observations the MKID DemoCam	<b>194</b>
8.1	Miscellaneous testing . . . . .	194
8.1.1	Skydips . . . . .	195
8.1.2	Magnetic response . . . . .	199
8.2	Readout system . . . . .	201
8.3	Calibration . . . . .	203
8.3.1	A proxy for atmospheric opacity . . . . .	204
8.3.2	Dark pickup and calibration systematic effects . . . . .	206
8.3.3	Coaddition of multiple detectors . . . . .	208
8.4	Sensitivity and future prospects . . . . .	210
8.5	Conclusions reached on MKID design from the entirety of lab and telescope testing .	213
8.5.1	Accomplishments . . . . .	213
8.5.2	Lessons for the future of MKIDs . . . . .	216
8.5.3	Future work on the understanding of MKID behavior . . . . .	217
<b>9</b>	MKID Camera and future work	<b>219</b>
9.1	Cryostat design . . . . .	219
9.2	Array mounting . . . . .	220
9.2.1	Tiles . . . . .	220
9.2.2	Magnetic shield and coaxes . . . . .	220
9.3	Optics . . . . .	224
9.4	Readout electronics . . . . .	224
9.5	Deployment and observation . . . . .	225

<b>Bibliography</b>	227
---------------------	-----

## Appendix

<b>A</b> Cooper pair effect on kinetic inductance	238
A.1 What is kinetic inductance? . . . . .	238
A.2 Change in inductance with quasiparticles . . . . .	239
<b>B</b> Resonance conditions for quarter-wave detectors	245
B.1 Derivation of the resonance condition . . . . .	245
B.2 Expected signal in amplitude and phase . . . . .	250
B.2.1 Phase response . . . . .	250
B.2.2 Amplitude response . . . . .	251
B.3 Complexity in $S_{21}$ profiles . . . . .	251
<b>C</b> Telescope Calibration	253
C.1 Laboratory responsivity . . . . .	253
C.2 Lab-to-telescope calibration . . . . .	255
C.3 Linearity in response . . . . .	256
<b>D</b> Resonance finding, I/Q projection and telescope data	260
D.1 Resonance frequencies “on-the-fly” . . . . .	260
D.2 Proper projection of I and Q . . . . .	261
D.3 Telescope data acquisition . . . . .	262
<b>E</b> Optical testbed setup	265
E.1 Description of testbed . . . . .	265
E.2 FTS measurements . . . . .	266
E.3 Beam maps . . . . .	266

<b>F</b> Variable reference	270
-----------------------------	-----

## Tables

### **Table**

3.1	Band 1 (240 GHz) optimal $Q_s$ , allowing up to 1% overlap. . . . .	66
3.2	Band 1 (240 GHz) optimal $Q_s$ , allowing up to 10% overlap. . . . .	67
4.1	Devices tested, and dates of testing, in the original DemoCam configuration. . . . .	73
4.2	Average parameters $\alpha$ and $\Delta_0$ across several resonators. . . . .	90
4.3	. . . . .	114
5.1	The parameters involved in quick fits to resonator IQ sweeps. . . . .	123
5.2	The response in several resonators to observations of Jupiter. . . . .	129
6.1	Devices of the new design tested in the new DemoCam. . . . .	144
6.2	Results of the different versions of $\alpha$ testing. . . . .	150
6.3	Calculated efficiency from measurements in the DemoCam. . . . .	168
6.4	Calculated efficiency from optical elements in the rebuilt DemoCam. . . . .	169
6.5	Number of usable resonators given empirical 5.3 MHz scatter. . . . .	175
7.1	The ratios of low- and high-power responses in frequency, dissipation and $S_{21}$ . . . . .	186
8.1	The shift in resonance frequency due to change in azimuth. . . . .	199
8.2	The predicted relative responsivity among bands. . . . .	210
F.1	Greek variables used in this thesis. . . . .	271

F.2 Latin variables used in this thesis. . . . .	272
F.3 Abbreviations and Acronyms. . . . .	273

## Figures

### **Figure**

1.1	Integrated brightness in the three backgrounds. . . . .	3
1.2	Effect of negative K-correction on submillimeter galaxy sensitivity. . . . .	5
1.3	NEP level following Moore's law. . . . .	12
1.4	Number of detectors following Moore's law. . . . .	13
2.1	The concept of a resonator capacitively coupled to the feedline. . . . .	23
2.2	The transmission, $S_{21}$ , of an ideal resonator. . . . .	24
2.3	Ratio of the change in the real and imaginary conductivity vs. temperature. . . . .	30
2.4	Cross-section of a CPW resonator. . . . .	34
2.5	A CPW quarter-wave resonator coupled to a feedline. . . . .	37
2.6	An LEKID resonator coupled to a feedline. . . . .	38
2.7	Diagram of an IDC resonator coupled to a feedline. . . . .	39
2.8	The antenna layout and microstrip feedline to the MKID resonator. . . . .	42
2.9	An antenna feed junction, dividing into two different colored filters. . . . .	43
2.10	The approach of analog readout [76]. . . . .	44
2.11	A schematic of the approach of digital multiplexed readout . . . . .	46
2.12	A diagram of internal and external noise sources. . . . .	51
3.1	NEP as a function of $Q$ . . . . .	60
3.2	The number of usable detectors as a function of $Q$ . . . . .	63

3.3	The mapping speed for different detector spacings as a function of $Q$ . . . . .	64
3.4	The change in complex conductivity as a function of temperature. . . . .	70
4.1	DemoCam focal plane antenna layout. . . . .	74
4.2	The DemoCam cryostat in its first iteration. . . . .	75
4.3	DemoCam cryostat with coax inputs and magnetic shielding. . . . .	76
4.4	DemoCam with the 4K shield, including snout and magnetic shielding. . . . .	76
4.5	The DemoCam optical train in the configuration taken to the telescope. . . . .	79
4.6	The DemoCam optical train in the wider window configuration. . . . .	80
4.7	The fit of a resonator to the resonance curve. . . . .	82
4.8	The residual of the resonance fit. . . . .	82
4.9	Best-fit values as a function of minimum temperature considered. . . . .	85
4.10	A fit to all temperature sweep data above 280 mK. . . . .	85
4.11	The residual of the fit in Figure 4.10, divided by the error at each point. . . . .	86
4.12	A temperature sweep fit for a sapphire device resonator. . . . .	86
4.13	The residual of the fit in Figure 4.12, divided by the error at each point. . . . .	87
4.14	Temperature sweep fit to all data in silicon device resonator. . . . .	87
4.15	The residual of the fit to all data of the silicon device resonator . . . . .	88
4.16	Confidence regions for $\alpha$ and $\Delta$ in silicon device resonators . . . . .	89
4.17	$\alpha/\Delta_0$ confidence regions for the sapphire device (Device 2). . . . .	90
4.18	Lifetime as a function of quasiparticle density . . . . .	93
4.19	Measured ratio of response between frequency and dissipation . . . . .	94
4.20	Total resonator response for several powers, 300-285 mK. . . . .	96
4.21	Total resonator response for several powers, 345-330 mK. . . . .	96
4.22	Total resonator response for several powers, 375-360 mK. . . . .	97
4.23	Response as a function of power for several resonators. . . . .	98
4.24	The I and Q response as a function of temperature. . . . .	99

4.25	Sapphire device responsivity in frequency shift. . . . .	101
4.26	Silicon device responsivity in frequency shift, in telescope configuration. . . . .	101
4.27	Beam maps of 240 GHz and 350 GHz pixels from the silicon device. . . . .	102
4.28	FTS spectra of bandpass measurements of bands on the silicon device . . . . .	103
4.29	$Q_i$ 's inverse plotted against quasiparticle density . . . . .	105
4.30	Excess loading for a Band 1 resonator as a function of temperature. . . . .	107
4.31	Excess loading in both bands of silicon DemoCam device. . . . .	108
4.32	Excess loading for all resonators in two different configurations. . . . .	109
4.33	Optical efficiency as a function of resonator thickness. . . . .	111
4.34	Optical efficiency as a function of thickness etched away. . . . .	111
4.35	Absorption efficiency from a microstrip as a function of sheet resistance. . . . .	114
4.36	Scatter of intended versus actual resonance frequency spacing . . . . .	118
5.1	The Bolocam optics box. . . . .	121
5.2	The DemoCam mounted to the Bolocam optics box at the CSO. . . . .	121
5.3	The beamsize found from observations of planets. . . . .	127
5.4	The I (projected) responsivity at the telescope. . . . .	128
5.5	The Q (projected) responsivity at the telescope. . . . .	129
5.6	An image of G34.3 observed with two pixels in two colors. . . . .	131
5.7	Jupiter in 2 bands from the same observation. . . . .	132
6.1	View of lens and coaxial cable mounts inside magnetic shield. . . . .	138
6.2	Sapphire device mounted in new DemoCam hardware. . . . .	139
6.3	A new $6 \times 6$ device mounted on the new ultracold stage. . . . .	140
6.4	The magnetic shield mounted in the DemoCam Dewar. . . . .	140
6.5	New optical design, with Teflon lens. . . . .	141
6.6	IDC resonator plot of best $\alpha/\Delta_0$ fit . . . . .	148
6.7	IDC resonator residual to best Mattis-Bardeen $\alpha/\Delta_0$ fit. . . . .	149

6.8	IDC resonator $\alpha/\Delta_0$ contour plot.	149
6.9	An assortment of IDC resonator $\alpha/\Delta_0$ contour plots	150
6.10	Histogram of $Q_c$ for IDC resonators	151
6.11	Results of “pumping” on a resonance.	152
6.12	Typical response in Device 4 FTS measurement.	154
6.13	Responsivity of Device 4 with different 4K filter materials.	154
6.14	Excess load of Device 4 with different 4K filter materials.	155
6.15	Design of IDC resonator with stepped-impedance filter.	157
6.16	Hot/cold response for IDC resonators on Device 5.	159
6.17	Hot/cold response for several IDC resonators on Device 5.	161
6.18	A resonator as it progresses to power saturation.	161
6.19	Device 7c detector hot/cold response.	163
6.20	Excess load for Device 7c detectors.	164
6.21	Frequency-to-dissipation ratio for Device 7c detectors.	166
6.22	Optical efficiency inferred for light resonators.	168
6.23	Ratio of frequency to dissipation response for several devices.	171
6.24	Response of Device 8b compared to 7c.	172
6.25	Histogram of $Q_c$ for device 8b.	173
6.26	Deviation of the frequencies from the designed spacing for Device 8b.	174
7.1	PSD weighted amplifier gain noise removal from off-resonance tones.	181
7.2	PSD weighted amplifier phase noise removal from off-resonance tones. The subtracted signal is of the form given in Equation 7.6.	181
7.3	A simulated resonance loop with noise directions.	183
7.4	Total frequency response as a function of readout power.	187
7.5	The average ratio of response at a given readout power to low power.	187
7.6	The expected decrease in NEP as a function of readout power.	188

7.7	NEP for frequency readout as a function of power, under 77 K load.	190
7.8	NEP for dissipation readout as a function of power, under 77 K load.	191
8.1	Skydip response scaled to 300-77 K values.	196
8.2	Skydip response scaled to 300-77 K values, no dark response	196
8.3	Skydip response in fractional frequency.	197
8.4	Skydip excess load.	198
8.5	Typical resonator's response to change in azimuth.	200
8.6	A schematic of the software defined MKID readout.	202
8.7	Average resonance frequency shift as a function of $\tau_{225}$ .	205
8.8	The response to the calibration source G34.3 for a typical Band 1 resonator.	206
8.9	Mars viewed in a single resonator of three colors and dark.	207
8.10	A typical detector's relative response vs. $\tau_{225}$ .	209
8.11	Calibration curves for all three bands.	209
8.12	Sensitivity reached with the observed resonances during a typical observation.	212
9.1	The four designed bands of the final MKID camera.	221
9.2	The camera's interior with radiation shields removed.	222
9.3	A cross-section of the camera's 4-Kelvin volume.	223
A.1	Complex conductivities vs. temperature.	240
A.2	Complex impedance vs. temperature.	242
A.3	Complex impedance vs. temperature, near $T_c$ .	243
B.1	Diagram of a feedline-coupled resonant circuit.	246
B.2	Diagram of a three-port representation of a feedline-coupled resonator.	247
C.1	The response to a point source with a flux density up to 20 Jy.	257
C.2	The derivative of a resonator's response curve out to 20 Jy.	257
C.3	The response to a point source with a flux density up to 200 Jy.	258

C.4	The derivative of a resonator's response out to 200 Jy.	258
C.5	The response to a point source with a flux density up to 2000 Jy.	259
D.1	Flow chart of the planned telescope data acquisition pipeline.	263
E.1	FTS spectra taken from the optical testbed.	267
E.2	Beam maps taken in the DemoCam, 4.3 inches beyond the window.	268
E.3	Beam maps taken from the optical testbed.	269

## **Chapter 1**

### **Introduction**

The fields of extragalactic astrophysics and cosmology have a common goal of understanding the formation and evolution of galaxies and structure in the universe. This has led to observation and analysis of galaxies at every wavelength, including recent advances in the study of galaxies at submillimeter and millimeter wavelengths. Here we discuss what can be learned by observations at these wavelengths. In particular, we look at the study of the cosmic far-infrared background, including its causes and implications for cosmology and the formation and evolution of galaxies. Once the goal of study is established, we consider the best way to achieve it, particularly what detector technologies are available. This thesis is devoted to the development of one such technology, Microwave Kinetic Inductance Detectors (MKIDs), for cameras designed to detect light at millimeter and submillimeter wavelengths.

#### **1.1 Submillimeter and Millimeter Astrophysics and Cosmology**

In this introduction, we explore the types of measurement to be made by MKID cameras, in particular the primary science goal of understanding submillimeter galaxies. We also review the current understanding of the sources of this millimeter-wave radiation.

##### **1.1.1 The Cosmic Far-Infrared Background**

In the twentieth century, astrophysicists began studying two types of cosmic radiation – the diffuse optical light emitted by stars in distant galaxies, and the Cosmic Microwave Background

(CMB) radiation discovered by Penzias and Wilson [84]. These have long been the primary tools for understanding the evolution of the universe from the earliest moments to the present day. An additional, far-infrared background was predicted long before its discovery, as it was postulated by Partridge and Peebles that young galaxies at high redshifts should emit largely in the infrared [90]. However, the level of this expected signal remained unknown until observational data could constrain it.

This far-infrared background radiation was first measured by the Cosmic Background Explorer's (*COBE*'s) FIRAS and DIRBE instruments [34, 89]. *COBE* data and later infrared observations showed that this excess at wavelengths longer than  $5 \mu\text{m}$  has integrated power comparable to all optical and ultraviolet light [60], seen in Figure 1.1. The dust causing this background must be heated by significant power sources to reach this level of emission, leaving Partridge and Peebles' initial explanation – that dust in galaxies reprocesses ultraviolet light from bright stars, thermally emitting the light at lower temperatures – as the most plausible. This explanation leaves two primary candidates for the power sources heating the dust: extreme starbursts, with many large, young stars emitting heavily in the ultraviolet, and Active Galactic Nuclei (AGN) [12]. Thus, it should be possible to resolve the background into constituent galaxies that are bright at submillimeter wavelengths.

### 1.1.2 Resolving the background – submillimeter galaxies

The primary astrophysical motivation for a multicolor sub/millimeter camera is the study of the spectral energy distributions (SEDs) of dusty, high-redshift galaxies, the likeliest to comprise the long wavelength end of the cosmic infrared background. Although this includes low redshift, heavily infrared emitting galaxies, the least understood and cosmologically most interesting galaxies are those at high redshifts (typically  $z > 1.5$ ), which are brightest in submillimeter and millimeter wavelengths. The first instrument to detect these galaxies was the Submillimeter Common-Use Bolometer Array (SCUBA) on Mauna Kea's James Clerk Maxwell Telescope (JCMT), observing at  $850 \mu\text{m}$  wavelength. Surveys first detected these galaxies by observing suspected lensing galaxy

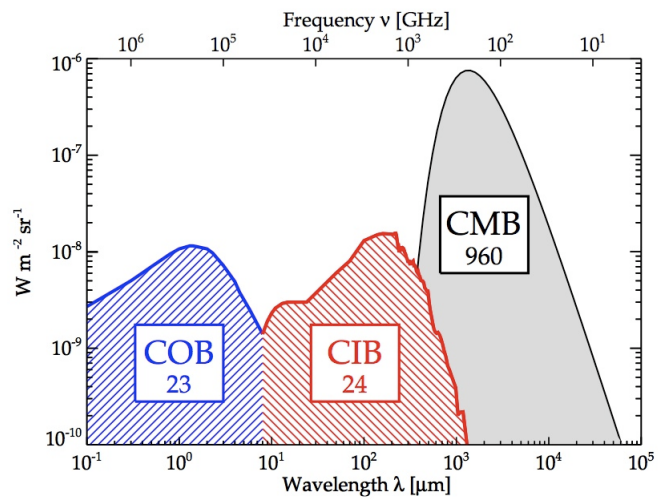


Figure 1.1: Integrated brightness in the three backgrounds – the cosmic optical, infrared and microwave background radiation – on a logarithmic scale. From Ref. [27].

clusters [5, 107] and areas with multi-wavelength coverage, such as the Hubble Deep Field [51].

Submillimeter-bright galaxies have high dust temperatures, likely powered by bright stars in dusty regions with large amounts of star formation. High energy light from bright stars is reprocessed by dust in the galaxy and emitted thermally in the far infrared. To power the observed galaxies, the bursts of star formation must be extreme, at  $\sim$ 100-1000  $M_\odot$  per year. The dust obscures and reprocesses the high energy radiation from the starburst, causing the galaxies to be bright in the infrared and submillimeter, but largely dark in the optical and ultraviolet. The properties of these galaxies are reviewed in Blain *et al.* [12] and Lagache *et al.* [60].

These galaxies are useful tools for probing the high redshift universe due to the relative independence of their flux density with redshift at millimeter wavelengths. A source at high redshift ( $1 < z < 10$ ) would be detected at nearly the same flux density at a wavelength of 1 mm as a  $z = 1$  galaxy, because the dust peak becomes redshifted into the longer wavelength bands (see Figure 1.2). This effect is known as a negative K-correction.

A major outstanding question relates to the nature of submillimeter galaxies – whether they are intrinsically interesting objects, or relatively mundane objects in an interesting evolutionary phase. In particular, we wish to understand if the brightest of these objects form as massive bursts of star formation, caused possibly by a major galaxy-galaxy merger, or are the hierarchical results of mergers of less-massive galaxies. This will help us understand if these are typical galaxies undergoing brief epochs of star formation, or very massive galaxies undergoing continuous high star formation. We must learn if they are simply high- $z$  analogues of local ( $z < 1$ ) ultraluminous infrared galaxies (ULIRGs), and if they are uniform populations or represent several types which are bright in the submillimeter.

Observational studies can constrain the modeling of high-redshift star-forming galaxies. Theoretical modeling focuses on how much star formation is occurring to fuel the submillimeter radiation. This theoretical dustsceawung<sup>1</sup> must be aided by further observations, particularly at high resolution, to constrain the predicted dust temperatures as a function of redshift. Recent numerical

---

<sup>1</sup> Old English, meaning contemplation of dust

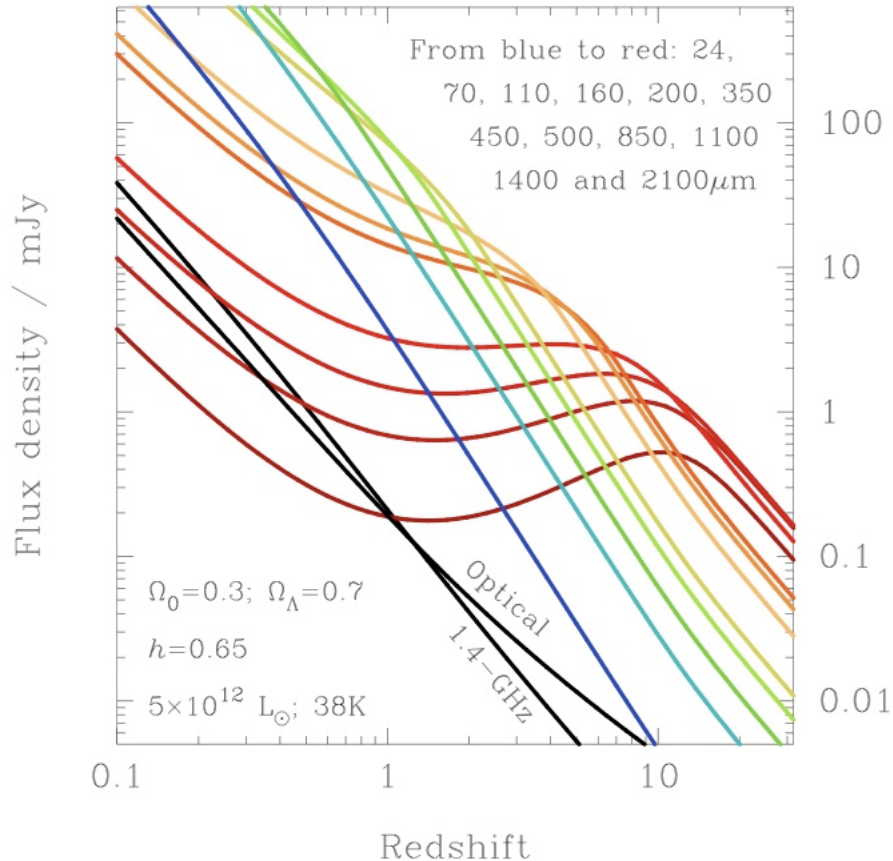


Figure 1.2: Effect of negative K-correction on submillimeter galaxy sensitivity, seen in this plot of flux density for a given wavelength vs. redshift. At short wavelengths, galaxies become dimmer at high  $z$ . Near 1 mm, however, the dusty galaxies become brighter, as the dust peaks are redshifted into those wavelengths. From Ref. [12].

studies have used observational constraints for semi-analytic galaxy evolution modeling, typically by assuming similarities to ULIRGs [7, 109]. Cosmological models have challenged this hierarchical model, showing submillimeter galaxies emerge directly from cosmological simulations without mergers [21]. Additional deep surveys from the next generation of sub/millimeter instruments are necessary to pin down spectral energy distributions to test the differences between these models. When combined with follow-up redshift surveys, the full SED measurement will provide a discriminatory test between the models, showing whether they are likely the product of mergers or of simple primordial potential wells.

Progress has been made toward constraining galaxy formation models, but complete understanding of the role of submillimeter galaxies remains elusive. For significant progress to be made, redshifts and SEDs must be obtained for a large, unbiased sample of galaxies. Redshift measurements are difficult to obtain for large numbers at very high redshift due to cosmological dimming. Photometric redshifts are confronted with a degeneracy between the dust temperature and redshift; emission peaking at long wavelengths can mean the source is either very cold or highly redshifted. With enough multicolor photometric data in the sub/millimeter, galaxies with long wavelength SED peaks can be selected out, as these are the most likely to be useful in differentiating between competing models. Finding counterparts at radio, infrared and optical wavelengths give the total intrinsic brightness, from which one can infer star formation rates [67]. Combined, this purely photometric data allows progress in finding the connection, or discrepancy, between high- $z$  and local infrared objects by comparison of spectral energy distributions. Multicolor submillimeter and millimeter data alone can distinguish AGN synchrotron-dominated sources from starbursts, and together with infrared data can find if the dust is primarily heated by star formation or AGN. These sources may otherwise contaminate survey samples designed to understand the starburst population of submillimeter galaxies.

The main constraints on observing are the practicality of multi-wavelength analyses and finding redshifts, which are necessary to properly model and constrain star formation histories. The intrinsic difficulty is that many of the surveys have point-spread functions on the order of

tens of arcseconds. Combined with low signal-to-noise detections, it can be difficult to determine source locations to better than a few arcseconds, a radius which can contain many radio and optical sources. This remains one of the main hurdles facing submillimeter astrophysics. High-resolution millimeter-wave imaging, combined with submillimeter counterpart identification, can pinpoint the sources, tell us the morphology, and allow discrimination between starbursts induced by large, short timescale mergers and those from other causes. Wide-scale, deep, multicolor sub/millimeter surveys are necessary for targeting and discriminating these sources.

#### **1.1.2.1 Surveys and multicolor analyses to date**

Many recent surveys from ground-based instruments have uncovered information about the properties of these high-redshift galaxies. These include observations of the Hubble Deep Field (HDF) and Great Observatories Origins Deep Survey-North (GOODS-N) [14, 85, 87], Lockman Hole [64, 44, 20], and the COSMOS field [10, 106, 2] by SCUBA (850  $\mu\text{m}$ ), Bolocam (1.1 mm), AzTEC (formerly Bolocam-2, 1.1 mm) and MAMBO (1.2 mm, wideband). These surveys typically consist of a fraction of a square degree to several square degrees, to varying depths in sensitivity. Several follow-up analyses have been performed at short wavelengths near the emission peak, and have found high luminosities, typically  $10^{11} - 10^{13} L_\odot$  [57, 65]. From the surveys so far, there have been various estimates of the number counts as a function of flux density, all in rough agreement. Model-dependent fluctuation analyses have been performed on several datasets showing the likely population at low flux densities [70, 83]. Redshifts have been obtained for those with identifiable radio counterparts, and the 850  $\mu\text{m}$ -selected population has been shown to have a median redshift of 2.4 [17].

Comparison of sources in the same field from surveys at different wavelengths has not typically yielded good agreement on multiwavelength detections of sources (e.g. [64]). Typically, surveys are performed at long wavelengths, and follow-up is done on known targets at the more difficult high-frequency bands. Therefore, to some degree the different wavelengths represent different populations [43]. Recent multicolor surveys have begun addressing this phenomenon. Balloon-borne

BLAST (250, 350 and 500  $\mu\text{m}$  [82]) surveyed the GOODS-South field at submillimeter wavelengths, and used its images in multiple colors to discern that the majority of sources in these bands lie at  $z > 1.2$  [25]. In addition, a two-color analysis of long wavelength (1.4 and 2.0 mm) point sources by the South Pole Telescope (SPT) discovered strong evidence for a clear divide between AGN-dominated synchotron-like sources, and dusty galaxies [112]. However, this survey was very large ( $\sim$ 100 degrees) and comparatively shallow ( $\text{RMS}_{1.4 \text{ mm}} \sim 3.4 \text{ mJy}$ ) and would benefit from deeper surveys including more colors. Ideally, long-wavelength coverage would be combined with BLAST-like bands to good depth to create complete SEDs. This would give some idea as to the total star formation in these galaxies, and could further differentiate populations.

There are two large problems in the observation of submillimeter galaxies: finding counterparts at other wavelengths, and measuring redshifts. Systematic millimeter-wave redshifts will have to wait for the next generation of multi-object spectrographs. However, some progress is already being made on multiwavelength counterpart identification. This is difficult because the detections in the submillimeter are generally not significant enough to allow precise positions, and typically several radio sources can lie near the most likely position. These radio counterparts are the key to identify possible optical or infrared counterparts. For radio-selected sources, a comparison of *Spitzer* infrared fluxes has been performed [47]. Multicolor analysis of these galaxies has shown that a large majority of the high-redshift sample are not AGN-dominated. Another recent approach used Mauna Kea’s Submillimeter Array (SMA) to identify precise locations of 890  $\mu\text{m}$  emission in the COSMOS field from the AzTEC survey [120]. Although this limits the number of galaxies detected, it eliminates a source of bias in the sample: radio-selected galaxies are more likely to lie at low redshift. This analysis found that 10 of the 15 sources had multi-wavelength properties indicating higher redshift than radio-selected samples, typically  $z > 3$  [119]. This provides a challenge to the hierarchical theories of submillimeter galaxy formation, which struggle to produce these sources at high redshifts under radical stellar initial mass function assumptions. More data are required to differentiate between these traditional merger models and cosmological simulations showing massive submillimeter galaxies to naturally emerge in deep gravitational potential wells.

It is clear that multicolor (both in the sub/millimeter and in other regimes) analysis is necessary for understanding the properties, including star formation rates, dust temperature, and redshift, of a large number of objects. The NASA/ESA *Herschel Space Telescope* is instrumental in this regard, providing short-wavelength submillimeter and far-infrared imaging with the PACS and SPIRE instruments. However, Herschel and BLAST are limited by relatively small apertures, which can limit the sensitivity due to source confusion, and in turn limit the knowledge of the luminosity function of these galaxies. A future goal will be to do photometry of galaxies in the wavelength range from 200-2100  $\mu\text{m}$  from the ground, using a 10-to-25 meter diameter dish. With the increased resolution will come the need for cameras with larger numbers of detectors to take full advantage of a larger telescope. This will complement the development of new projects such as sub/millimeter multi-object spectrographs, and the observations of the Atacama Large Millimeter Array (ALMA) for high-resolution images of submillimeter point sources. With future surveys involving complete spectral coverage over the submillimeter and millimeter wavelengths, combined with unbiased spectroscopic redshifts, it will be possible to determine how these massive star forming galaxies formed.

### **1.1.3 Other sub/millimeter astrophysics**

#### **1.1.3.1 Galactic star formation**

Star formation within the Galaxy is not completely constrained because of the amount of dust obscuring the visible light emitted during star formation. It is best studied in the sub/millimeter because at these wavelengths the dust becomes optically thin. In addition, the only sources powering many pre-stellar cores are gravitational infall or cosmic rays, rather than stellar nuclear reactions. These cores would peak in emission in the submillimeter. Higher energy surveys, such as in the near-infrared, would miss pre-stellar cores completely. The full submillimeter SED can help constrain the state of a core in its evolution into a star or stellar system. Surveys of large areas (e.g. [33]) with large sample sizes, typically thousands of cores, are required for the statistical study of the

early stages of star formation. These surveys observe cores and clumps of gas within molecular clouds, sometimes heated by stars or protostars and sometimes not.

### 1.1.3.2 Galaxy Cluster Physics and the Sunyaev-Zel'dovich Effect

The Cosmic Microwave Background (CMB) is a useful tool for studying the formation and evolution of structure in the universe. At small angles, typically arcminute scales, one finds the effect of secondary anisotropy, caused by the inverse Compton-scattering of CMB photons off hot electrons in galaxy clusters' intracluster medium by CMB photons [15]. This effect, called the Sunyaev-Zel'dovich (SZ) effect, pushes the photons higher in energy, leaving a decrement at long wavelengths ( $\lambda > 1.38$  mm) and an increment at short wavelengths. Due to the nature of this backscatter, the sensitivity to the SZ is independent of redshift, allowing the earliest clusters to be detected. The overall amplitude of this effect has been constrained at 150 GHz [100, 91], along with a recent significant detection of secondary CMB anisotropy [66].

If redshifts can be obtained independently, the phenomenon of redshift insensitivity permits the study of the evolution of the number of clusters with redshift, as well as cluster mass, and the physics of the clusters. Thus large scale cluster studies are important insights into the growth of structure, and can place constraints on cosmological parameters  $\Omega_M$ , the matter density of the universe, and  $w$ , the dark energy equation of state. Much observation continues to investigate the relationship between the integrated SZ and cluster mass (e.g. [13]).

## 1.2 MKIDs in context

Now, we consider other technologies used in the submillimeter in comparison to MKIDs, to see how MKIDs may be a competitive technology in astronomical cameras. Here we briefly look at the potential advantages of using MKIDs compared other detectors and summarize the mode of operation compared to other technologies. We also make note of example instruments operating with competing technologies which have similar science goals: submillimeter galaxies, SZ clusters, and galactic star formation.

### 1.2.1 Sub/millimeter detectors and why we need arrays

In the field of submillimeter and millimeter astrophysics, there are two methods of improving the mapping speed – the time it takes to map a solid angle of sky to a given noise level on a telescope. The first method is to reduce the noise equivalent power (NEP) of the detector used, defined as the power giving a signal-to-noise of unity in a 1 Hz bandwidth [94]. This is particularly helpful because mapping speed is inversely proportional to  $(\text{NEP})^2$ . The second method is to increase the number of detectors,  $N_{det}$ , as the mapping speed scales proportionally with  $N_{det}$ .

The sensitivity of millimeter-wave detectors has increased exponentially as a function of time. The initial advance was to operate at low temperatures, generally at or below 4 Kelvin, to reduce noise (e.g. Johnson noise) and improve responsivity to the point that today all millimeter detectors operate at low temperature. The decrease in NEP from new detector development is seen by Figure 1.3, as detectors become sensitive enough to reach photon background-limited performance (BLIP) in settings with lower background loads. One caveat in this description is that the context is important in discussing sensitivity – a detector built for use in a high-background environment like ground-based photometry will have higher NEP than one developed for low-background space-based spectroscopy, regardless of technological advances. Thus one must put the detector NEP in the context of the application.

Once a detector is significantly below background-limited noise levels, such as photon noise from sky loading, there is simply no advantage to making the detector more sensitive. The only way forward is to add more detectors, and to find the simplest and cheapest ways to do this. The world of single-pixel cameras has paved the way for two-dimensional arrays of pixels, but the two goals are not always readily compatible. A detector with high sensitivity may be unsuitable for large arrays, and an easily multiplexed detector may not easily reach interesting sensitivities. NEP has historically been the measure of success in detector research, rather than multiplexibility, as would be expected for generations of single-pixel or few-pixel instruments. However, significant strides have been made in the numbers of detectors in multiplexed cameras; indeed, it seems to

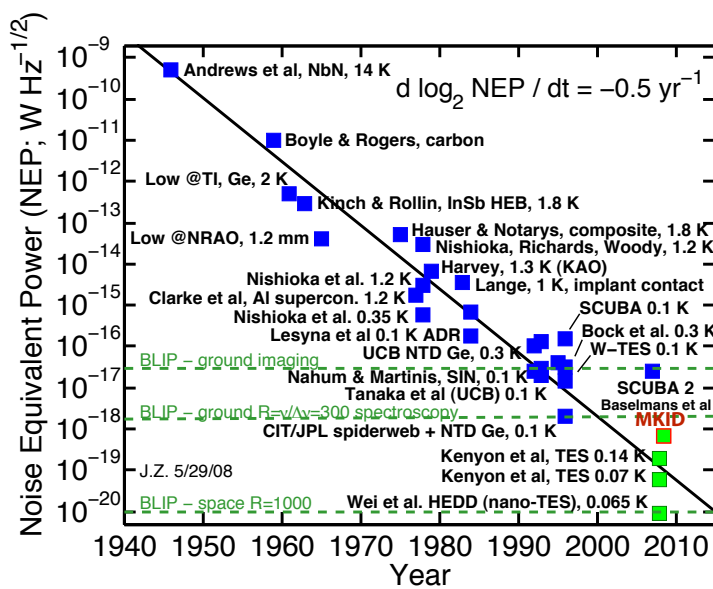


Figure 1.3: NEP level for continuum detectors following an exponential decrease with time. Plot courtesy of Jonas Zmuidzinas.

follow an exponential course of its own, as seen in Figure 1.4.

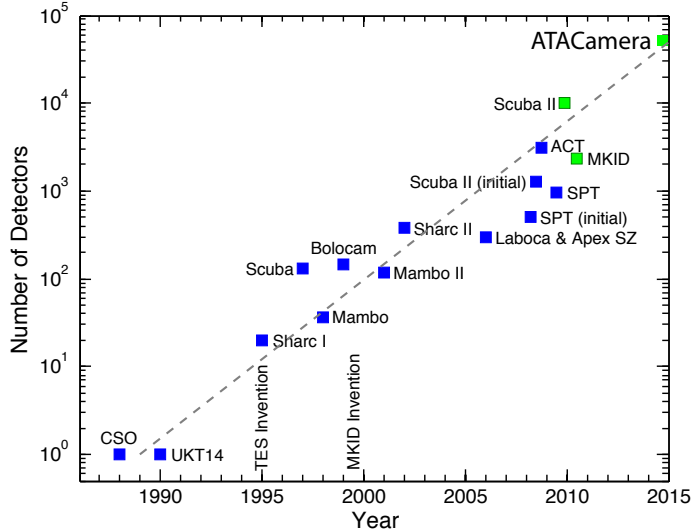


Figure 1.4: Number of detectors following an exponential increase with time. Plot courtesy of Jonas Zmuidzinas.

### 1.2.2 Competing detector technologies

MKIDs are competitive with other detector technologies for use in sub/millimeter cameras.

It is helpful to look at other detector types to show how MKIDs compare, and where they might be advantageous. The primary criteria in comparing detectors are sensitivity, simplicity in multiplexing, and cost. A review of the superconducting technologies used in the field of sub/millimeter astronomy is given in Ref. [123], and a summary of detectors is given below.

#### 1.2.2.1 Heterodyne receivers

Heterodyne instruments are examples of non-direct detection receivers, in that the amplitude and phase of a signal are recorded rather than the power on the detector. The detector is simply a mixer, mixing a local oscillator (LO) signal, typically a few GHz, with an astronomical signal of several hundred GHz. The mixer is typically an SIS mixer [93] or a hot electron bolometer (HEB) [18]. The result is a sideband signal at low frequency which is read out using a spectrometer.

These are among the oldest types used successfully in the submillimeter, and are generally used in single-pixel chopped observations. Their primary advantage is to provide spectral information. This information is typically very high resolution, optimal for spectral line studies. However, the spectral bandwidth has historically been limited, and they are not easy to multiplex. As an example, SuperCam at the Heinrich Hertz Submillimeter Telescope [45] deploys 64 receivers in an array, but requires an individual low noise amplifier for each receiver. Thus, while ideal for small-scale spectroscopic imaging and resolution of spectral lines, they are not ideal for either wide-band spectroscopy or large-format imaging.

### 1.2.2.2 NTD Bolometers

Neutron-transmutation-doped (NTD) semiconducting bolometers use direct detection, measuring power deposited on the detector, rather than amplitude and phase of a signal. The astronomical radiation is coupled to the bolometer, which is a semiconductor thermistor. The bolometers are current-biased, with any change in resistance being measured as a change in voltage. Submillimeter light heats the bolometer, which is weakly thermally coupled to a bath by conductivity  $G$ , and the high resistance change is measured by current biasing the detectors and reading out the voltage. The detector sensitivity is given by

$$(NEP)^2 = \frac{4k_B T^2 G}{\eta^2} + \frac{4k_B T R}{S^2} \quad (1.1)$$

where  $S$  is the responsivity in voltage per unit power,  $R$  is the bolometer resistance and  $\eta$  is the optical efficiency [92]. NTD bolometers can achieve high sensitivity by operating at low physical temperatures, as is done with the Z-Spec grating spectrometer [78]. The main limitation to these detectors is the difficulty with multiplexing. In effect, these require a four-wire measurement for each detector, severely limiting the multiplexibility. Several cameras, such as Bolocam [39] and AzTEC [118] with 144 and SHARC-II [28] with 384 detectors, do enjoy significant use. However, these numbers are close to the practical limit for the detectors, due simply to the number of wires required for readout.

### 1.2.2.3 Transition Edge Sensor Bolometers

Transition edge sensing bolometers (TES) take advantage of the superconducting transition, a point where the resistance of a superconductor goes from effectively zero to normal metal resistance over a very small temperature range. TES bolometers are thin superconducting films with transition temperature,  $T_c$ , weakly thermally coupled to a bath at much lower temperature. The bolometers are voltage-biased, as opposed to the traditional bolometer current biasing, eliminating the problem of bolometer heating [53]. This readout method allows the detector to stay in the transition despite changes in loading, maintaining its maximum sensitivity. The exact transition temperature can be tuned by the thickness of the superconducting layer, allowing for very sensitive detectors operating at relatively high temperatures, typically in the 100s of mK.<sup>2</sup> As in the case of NTD bolometers, lower temperature increases sensitivity, so operating at very low temperatures can still be beneficial.

TES bolometers are simpler to multiplex than semiconducting bolometers. A single line can read out many detectors through time-domain multiplexing [24], frequency-domain multiplexing [62], or code domain multiplexing [55]. In addition, coupling to microwave resonators, in order to mimic MKID readout, shows promising results for large-scale multiplexing [54, 71].

Several cameras using TES bolometers have been deployed over the past several years, or are in the process of deployment, including APEX-SZ [26], GISMO [108] and SCUBA-2 [49] (among others). The latter camera has over 5,000 detectors in each of two colors ( $450\text{ }\mu\text{m}$  and  $850\text{ }\mu\text{m}$ ), far larger than any previous array.

### 1.2.2.4 Other detectors

Thus far we have reviewed detectors making up the majority of major millimeter-wave instruments. Other low temperature detectors are developed for various applications (e.g. Magnetic Microcalorimeters), but are generally not as well suited for large arrays of sub/millimeter detectors. Superconducting Tunnel Junctions (STJs) can be used as direct detectors in the sub/millimeter

---

<sup>2</sup> Typically, TESs are optimally sensitive in operation with a refrigerator base temperature significantly lower than the transition temperature, so it is still best to have a very cold system such as a dilution refrigerator or adiabatic demagnetization refrigerator.

regime, as a source excites quasiparticles to tunnel across a superconductor-insulator-superconductor (SIS) junction. These detectors, while limited by leakage current, are being developed into large-format arrays with time-domain multiplex readout systems [72].

### 1.2.3 MKID advantages

Microwave Kinetic Inductance Detectors (MKIDs) are superconducting resonators with frequencies in the microwave regime (typically a few GHz), the physics of which is discussed thoroughly in the ensuing sections and chapters. Below is a brief description of their qualities for the purpose of comparison to other technologies. As discussed above, the principal reason for the development of MKIDs is to create a detector which is easily multiplexed and has background-limited NEP. By their nature, MKIDs should be competitive in this regard.

MKIDs are essentially superconducting RLC resonant circuits in which the inductance and resistance at the resonance frequency are determined by the density of paired or unpaired electrons. The resonators respond to light by becoming more lossy (lower resonant quality factor,  $Q$ ) and by changing the inductance, and therefore resonance frequency, as Cooper pairs are broken in the resonator. Thus, the resonator acts as both a millimeter-wave absorber, by having Cooper pairs broken, and as a microwave resonator, which allows the absorption to be measured by a probe signal at the resonance frequency. In principle, the sensitivity is limited only by the generation and recombination of these Cooper pairs, which sets a low baseline for NEP. In addition, the detectors can be tuned by altering their physical structure to have slightly different resonant frequencies from each other; thus, they are naturally frequency-multiplexed. Probe signals coupled to each of these resonators through a feedline can measure the change in frequency and dissipation as a change in phase and amplitude, respectively. This can be measured for a superposition of many probe signals sent on one feedline. The ultimate limit to the number of detectors is given by the bandwidth available for probe signal generation and in how closely spaced in frequency detectors can be and still avoid crosstalk with resonators nearby in frequency space. In principle, one can read out thousands of detectors with one input and one output coaxial cable. These detectors

therefore show great promise for high mapping speeds in sub/millimeter cameras. MKIDs will first be deployed in the cameras MUSIC [69], described in Chapter 9, and in NIKA, the Novel IRAM KIDs Array [95, 75].

#### **1.2.4 Coupling to sub/millimeter radiation**

To couple properly to sources on submillimeter telescopes, detectors must have a well-defined time-reverse beam pattern. This beam defines what angles of light couple well to the detector. Numerous methods have been developed to couple the detectors to submillimeter radiation in a way that maximizes efficiency and minimizes beam sidelobes, or coupling outside the main beam. The three typical approaches are feedhorn arrays, an optical-like free-space absorber approach, and an antenna-coupled detector approach, described in Ref. [42]. The feedhorn approach yields well-defined and easily coupled beams, but involves large metallic horns which are costly for large numbers of detectors and can lead to smaller filling factors. These are more common in CMB experiments, which require extremely low background loading, and are used in Bolocam and AzTEC. The optical-like approach involves arrays of bare absorbers, which have no stray-light control, but allow for optimal focal plane usage. This approach is used, for example, in SHARC-II. Finally, on-chip antennas can define the beam to have a specific profile and feed the sub/millimeter light into a detector, thus acting like a feedhorn while lithographed onto the detector array. This method is used in the MKID instruments discussed in this thesis.

#### **1.2.5 Future developments of low temperature detectors**

As seen in Figure 1.3, detectors have reached the necessary sensitivity for ground-based imaging, ground-based spectroscopy, and space-based imaging. While space-based spectroscopy is still a goal for missions such as SPICA (Space Infrared Telescope for Cosmology and Astrophysics), a major thrust is now going towards increased mapping speed with very large arrays. Designs are focusing on either very multiplexible feedhorn designs or lithographed antennas, away from older machined feedhorns, and toward easily multiplexed detectors from the multiple wires per detector

approach.

The goal in multiplexing is to achieve a continuing increase in detector numbers deployed. Given the significant strides in MKID multiplexing (4 in 2007 to 55 in 2010 to over 1,000 by 2011) it seems likely they will play a significant role in the future of long-wavelength detectors.

### 1.3 Description of thesis

In the following chapters, we will discuss the development of MKID detectors to be used primarily for the observation of submillimeter galaxies, but which may be used toward the other astrophysical applications discussed. Chapter 2 gives an introduction to MKID physics, and to how the detectors are used in the submillimeter. Chapter 3 discusses the parameters related to optimization of single-pixel sensitivity and full array mapping speed, and the tradeoffs associated in order to maximize performance. After this introductory calculation of how to optimize the detectors, we discuss the assembly of DemoCam, our demonstration instrument, and my laboratory testing and characterization of the device used for MKID first light in Chapter 4. Chapter 5 describes the performance of this device and instrument at the telescope, including overall efficiencies and optical properties. Chapter 6 discusses the subsequent device design iterations, and improvements to DemoCam, including the resulting lab tests. Chapter 7 explores the MKIDs in operation, in particular the optimal mode of operation in ground-based instruments. This chapter provides a summary of the primary lessons learned from lab testing numerous devices, including design parameters. Chapter 8 discusses the improved performance in our second DemoCam observing run with the upgraded device, including instrument calibration and sensitivity performance.

Chapter 9 describes the multicolor MKID Camera instrument, MUSIC, which is planned to achieve first light in the spring of 2011, and its expected performance as an astronomical instrument based on DemoCam results. This discusses its use in surveys for submillimeter and millimeter-wave sources, and how techniques developed for DemoCam will be carried forward into the MKID Camera.

### 1.3.1 Description of collaboration

Much of the work in this thesis is done in collaboration with members of the MKID team. Given the nature of the work, it is impossible to disentangle contributions from collaborators, and to say what is entirely the author's. The analysis of all data presented in this thesis, and all calculations beyond the introduction, are done solely by the author, unless explicitly stated. In addition, the design of all cryogenic components discussed, including the optics, and much of the assembly is done by the author.

Although input was given by the author, device design and fabrication was done solely by collaborators. The specific resonator designs are the work of Dr. Shwetank Kumar (formerly a Caltech graduate student), Dr. Jiansong Gao (formerly a Caltech graduate student) and Omid Noroozian (a current Caltech graduate student), and antennas are designed and simulated by Dr. Peter Day of JPL. Bandpass filters in various iterations have been designed by Dr. Kumar and Ran Duan, a graduate student at Caltech. The readout electronics are largely designed and tested by Ran Duan, Dr. Thomas Downes of Caltech and Prof. Benjamin Mazin of UC Santa Barbara (formerly a JPL staff scientist). All devices have been fabricated by Dr. Henry LeDuc in the NASA/JPL Microdevices Laboratory (MDL). The full MKID camera optics and cold hardware in Chapter 9 were designed by Dr. Jack Sayers and Dr. Matthew Hollister, respectively, of Caltech and JPL. Appendices cite the primary contributor where appropriate. Laboratory data is taken in collaboration with Anastasios (Tasos) Vayonakis and Nicole Czakon, graduate students at Caltech, and telescope data in collaboration with the entire submillimeter MKID team.

### 1.3.2 Conventions

Throughout this thesis, the conventions  $i = \sqrt{-1}$  and  $\hbar = 2\pi\hbar$  are used. Unless otherwise noted,  $\omega$  denotes frequencies in rad/s, while  $\nu$  or  $f$  denotes the same in Hz. To avoid confusion,  $Q$  represents the quadrature output of an IQ mixer, while the italicized  $Q$  denotes quality factor. Wherever applicable, MKS units are used in the spirit of J.D. Jackson's 3rd edition of *Classical*

*Electrodynamics.* The first person singular is eschewed in favor of the “royal we.”

For convenience to the reader, Appendix F lists all variables used in the thesis, as well as abbreviations and acronyms.

## Chapter 2

### Introduction to MKIDs

#### 2.1 The Physics of MKIDs

MKIDs have great potential advantages over other detectors, particularly in multiplexing. Here we establish the physics of how they actually work to detect light. This includes discussion of what is actually measured in response to loading changes, and what noise sources limit their performance.

##### 2.1.1 Microwave resonant circuits as detectors

MKIDs are simply superconducting resonant circuits with resonance frequencies in the microwave, typically <1 to 10 GHz. They are typically used by measuring the change in resonance frequency and resistive loss, or dissipation. These quantities depend on the impedance of the resonant circuit. Although MKIDs are superconducting and therefore have zero DC resistance, the impedance of a superconducting circuit is nonzero at finite frequencies. This total impedance is expressed as

$$Z = R + i\omega L + \frac{1}{i\omega C}. \quad (2.1)$$

This includes the impedance due to the geometry of the circuit, and the surface impedance from the conductor,  $Z_s = R_s + i\omega L_s$ . If all the electrons in the superconductor are in Cooper pairs [19], as is the case at very low temperature with no outside power source, then the resistive portion of the impedance is zero, and the impedance is purely imaginary. The inductance in the circuit is a combination of the magnetic inductance, from the geometry of the circuit, and the kinetic

inductance, from the kinetic energy associated with the Cooper pairs. The capacitance is due solely to geometrical factors.

Cooper pairs are broken either through temperature increasing towards the critical superconducting transition,  $T_c$ , or by coupling to photons with sufficient energy. This causes an increase in the resistance and kinetic inductance of the superconductor while leaving the magnetic inductance of the circuit unchanged, pushing the resonator to lower quality factor,  $Q$ , and to *lower* resonance frequency. The frequency decreases because, in the case of small real conductivity, the inductance increases when a Cooper pair is eliminated. This effect is explained in more detail in Appendix A.

Microwave circuits of this type are useful as detectors because the resonance frequency and  $Q$  are good measures of the density of quasiparticles, or unpaired free electrons. The density of quasiparticles changes the complex conductivity of the superconductor, which determines  $R_s$  and  $L_s$ . This allows us to infer the quasiparticle density using the frequency and  $Q$  of a superconducting resonant circuit. Light at frequencies greater than  $2\Delta/\hbar$ , where  $\Delta$  is the superconducting gap parameter, is able to create quasiparticles. This allows us to use MKIDs as detectors, with the frequency of detectable light determined by the gap energy of the material.

The measurement of MKID resonant frequency and dissipation is done by coupling the resonator to a feedline. A probe sine wave at the resonance frequency can be sent through the feedline to measure the changes in the resonance. This signal will effectively scatter off the resonator, because the impedance of the circuit near the resonance frequency is different from the impedance of the feedline alone (which is typically  $50 \Omega$ ). Thus, some fraction of the signal will be attenuated, and some will be reflected. The amplitude and phase of the wave transmitted past the resonator change depending on the resonator's  $Q$  and resonant frequency, respectively. These values change the impedance of the resonator, which cause shifts in amplitude and phase. This effect is discussed in detail in Appendix B.

The resonators in this thesis can be thought of as a shorted  $\lambda/4$  transmission line resonators,<sup>1</sup>

---

<sup>1</sup> Although this is the only type explored here, other types of MKIDs are possible, such as  $\lambda/2$  resonators discussed elsewhere (e.g. [76]).

capacitively coupled to the feedline, as seen in Figure 2.1. The resonance condition, or the frequency

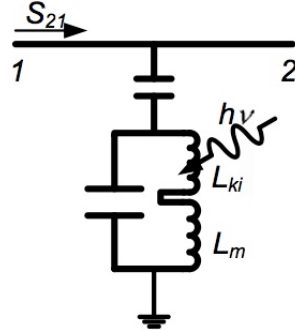


Figure 2.1: The concept of a resonator (here, a quarter-wave resonator) capacitively coupled to the feedline. Here a transmission line carries a sine wave from port 1 to port 2, with transmission  $S_{21}$ . The resonator is an LC circuit capacitively coupled to the feedline on one end, and shorted to ground on the other. Loading (for example, from measured photons) changes the inductance of the circuit, which due to the capacitive coupling changes  $S_{21}$ . Figure from Ref. [36].

and profile of the resonance as observed from the feedline, is found by considering the MKID as a lossy, grounded transmission line. This is shown in detail in Appendix B. In this model, the  $Q$  is seen to be a combination of internal  $Q$ , describing the loss of the resonator by itself, and coupling  $Q$ , which describes the loss to the feedline. The total  $Q$  is defined by

$$\frac{1}{Q} = \frac{1}{Q_i} + \frac{1}{Q_c}. \quad (2.2)$$

Our primary task is to measure the change in impedance seen by the input signal, which we observe as a change in the transmission of the probe signal. We consider this in terms of a two-by-two scattering matrix,  $S$ , in which the diagonal elements are reflected components and the off-diagonals are transmitted from either port. Considering the impedances seen by a wave at frequencies near the resonance, we find the transmission, normalized to unity transmission off-resonance, to be

$$S_{21}(f) = 1 - \frac{Q/Q_c}{1 + 2iQ\frac{f-f_0}{f_0}}. \quad (2.3)$$

This can be shown to be equivalent to Equation B.15. Here  $f_0$  is the resonance frequency, and  $f$  is the frequency at which the measurement is made. In this representation, one can see that the resonance is simply a Lorentzian dip from unity, with the depth determined by  $Q/Q_c$ . In the

complex plane, it simply maps out a circle, where far from the resonance frequency the value is 1, and on resonance the value is  $1 - Q/Q_c$ . At all other points around the resonance, the transmission is complex and falls on a resonance circle, or loop. This transmission is seen in Figure 2.2.

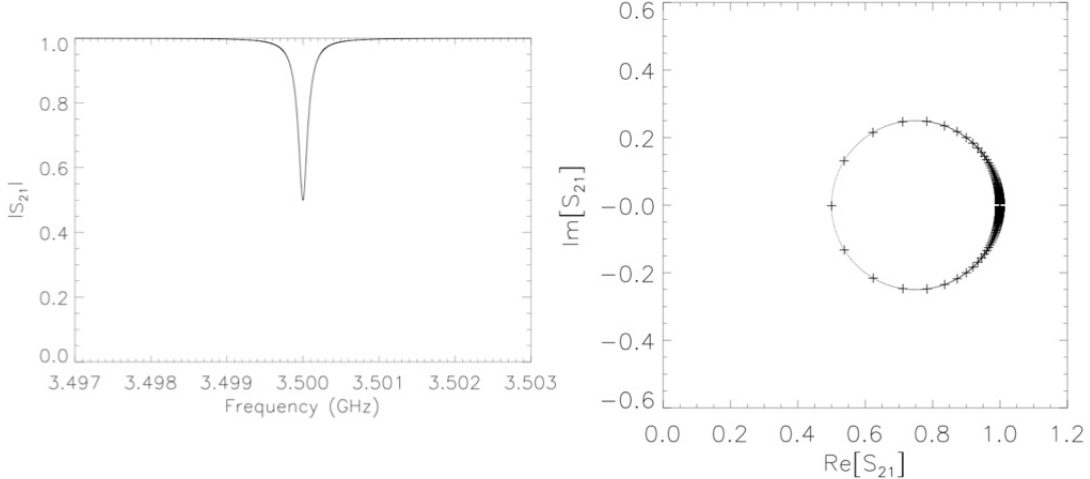


Figure 2.2: The transmission,  $S_{21}$ , of an ideal resonator at 3.5 GHz with  $Q=20,000$ . Here the resonator is optimally coupled, such that  $Q = Q_c/2$ . The left panel shows the magnitude of the transmission, while the right side shows the complex values plotted against each other in a loop. Different frequency points are given by each +, spaced by 25 kHz. Near the resonance, the distance between adjacent points in  $S_{21}$  space is maximized. In the ideal case, this also corresponds to the minimum transmission.

Now let us consider what happens if there is a change in resonance frequency. It is shown in Appendix B that a small frequency change relates purely to an imaginary change in  $S_{21}$  for a probe signal exactly on resonance, while a small change in  $Q$  changes only the real portion. The combined change given by<sup>2</sup>

$$\delta S_{21} = \frac{Q^2}{Q_c} \left( \delta \frac{1}{Q_i} - 2i \frac{\delta f_0}{f_0} \right). \quad (2.4)$$

The strength of the coupling to the feedline is therefore immensely important to the sensitivity. The probe signal is maximally responsive to changes in  $Q_i$  or  $f_0$  when  $Q=Q_c/2$ , or  $Q_i=Q_c$ .

Measurement of the imaginary component in Equation 2.4 is the “phase” readout, corresponding to a change in the phase of the probe signal, while the real component is the “amplitude”

<sup>2</sup> Here, the frequency change is given with a negative sign. This is different from Equation B.20, but it is effectively arbitrary. Adding a negative sign here ensures that both dissipation and frequency will respond to increased load by becoming more positive. This is the typical convention for MKIDs.

readout. This approximation of the equivalence between amplitude and dissipation (measured by  $Q_i$ ) as well as phase with frequency is invalid off-resonance, where the amplitude and phase signals are nonlinear combinations of the two, as discussed in Appendix B. At small enough signal of phase and amplitude response, it is always possible to project out a frequency and dissipation signal, but this is generally a mix of a phase and amplitude change. In addition, there are several real-world effects, for example relating to cable delay and “background transmission,” discussed in more detail in Appendix B and Chapter 4. These effects can also be taken into account to make the phase correspond to the frequency shift and the amplitude change correspond to the dissipation.

### **2.1.2 Principle of detection in MKIDs**

Above, it is established that the measurable quantities are the resonator’s frequency change and the change in the loss tangent, or the measure of resistive dissipation. Now we must consider how this change actually comes about in a superconductor, or how the impedance changes to give rise to this effect. The difference between the resonator’s total impedance and the surface impedance arises solely due to the thin superconducting material. In Equation 2.1, the surface impedance only accounts for some of the total impedance. The resistance arises completely from the surface impedance, as resistance is an effect specific to conductors, not to the geometry of circuits. Conversely, the capacitance is a wholly geometrical effect, which does not arise from the superconductor at all. The inductance, however, is mixed, with contributions from the kinetic inductance and from the generally larger geometric, or magnetic, inductance. We generally define  $\alpha$  as the fraction of the resonator’s total inductance attributed to kinetic inductance at low temperature,  $\alpha = L_k/(L_k + L_m)$ . The breaking of a Cooper pair will only change the surface impedance, as it does not affect the geometry, so this fraction is necessary for determining the magnitude of the frequency response.

### 2.1.2.1 Surface impedance and conductivity

The surface impedance can be expressed by its relationship to the complex conductivity, which is determined by the properties of the material (i.e. the normal state conductivity and the superconducting gap parameter, discussed below) [52]. This is useful because changes in the conductivities are measurable from resonator parameters, as is seen in the following section. Let us consider the dirty, or local, limit, applicable for thin film devices. This is the limit in which the electron mean free path is much less than the London penetration depth. In this limit, any deviation due to the geometry of thick films is small. In this case, the impedance in terms of complex conductivity  $\sigma = \sigma_1 - i\sigma_2$  is given by [36]

$$Z_s = R_s + i\omega L_s = \frac{1}{(\sigma_1 - i\sigma_2)t}. \quad (2.5)$$

This has the correct behavior in two limits: if the inductance is zero, then  $R_s = 1/\sigma_1 t$ , and if resistance is zero, then  $\omega L_s = 1/\sigma_2 t$ , as expected. Consider a change in impedance, as would be seen from response to light in MKIDs. It is simple to show that

$$\frac{\delta Z_s}{Z_s} = \frac{\delta R_s + i\delta(\omega L_s)}{R_s + i\omega L_s} = -\frac{\delta\sigma_1 - i\delta\sigma_2}{\sigma_1 - i\sigma_2}. \quad (2.6)$$

If we consider the starting point, from which we are measuring the change, at  $T = 0$ , then  $\sigma_1(0) = 0$ , and we are left with the change in inductance corresponding to

$$\frac{\delta(\omega L_s)}{\omega L_s(0)} = \frac{\delta L_s}{L_s(0)} = -\frac{\delta\sigma_2}{\sigma_2(0)} \quad (2.7)$$

and a change in resistance of

$$\frac{\delta(R_s)}{\omega L_s(0)} = \frac{\delta\sigma_1}{\sigma_2(0)}. \quad (2.8)$$

Thus, the change in reactance (and inductance) is the opposite direction from the change in  $\sigma_2$ .

### 2.1.2.2 Measurable quantities - frequency and loss

Now we have seen how resistance and inductance change in a resonator. We now consider how these effect the change in measurable quantities in Equation 2.4 – specifically, the loss tangent

due to resistive losses,  $1/Q_i$ ,<sup>3</sup> and the fractional frequency shift. The change in resonance frequency depends on inductance as expected for an  $LC$  circuit,

$$\delta f = -f_0 \frac{\sqrt{L} - \sqrt{L_0}}{\sqrt{L_0}} \simeq -\frac{f_0}{2} \frac{L - L_0}{L_0}, \quad (2.9)$$

where the change in inductance is assumed to be small. Given the fact that only the kinetic inductance is changing, we are left with an expression for a fractional frequency shift of

$$\frac{\delta f}{f_0} = -\frac{1}{2} \frac{\delta L_k}{L_k} \frac{L_k}{L_k + L_m} = -\frac{\alpha}{2} \frac{\delta L_k}{L_k}. \quad (2.10)$$

Combined with Equation 2.7, the imaginary part of the conductance responds to an effective temperature change<sup>4</sup> in the superconductor

$$\frac{\delta f}{f_0(T=0)} = \frac{\alpha}{2} \frac{\sigma_2(T_{eff}) - \sigma_2(0)}{\sigma_2(0)} \quad (2.11)$$

where we assume a small change in inductance. This formula arises simply because the shift in frequency is proportional to the change of the square root of the inductance.

The internal  $Q$  in a resonator is given by

$$Q_i = \frac{\omega L}{R}, \quad (2.12)$$

but is generally more useful in terms of its inverse,  $Q_i^{-1}$ . In the case involving both kinetic and geometric inductance, the change in loss tangent with changing resistance and inductance is given by

$$\delta \left( \frac{1}{Q_i} \right) = \frac{L_k}{(L_k + L_m)} \frac{\delta R}{\omega L_k} - \frac{R \delta(\omega L_k)}{\omega^2 (L_m + L_k)^2} \simeq \alpha \frac{\delta R}{\omega L_k}. \quad (2.13)$$

The term involving the change in inductance can be thrown away because it is much smaller than the resistance change term, given that  $R/\omega L$  is small for a superconductor well below  $T_c$ . Rewriting this in terms of conductivity using Equation 2.8, the change in loss tangent is given by

$$\delta \left( \frac{1}{Q_i} \right) = \alpha \frac{\delta \sigma_1}{\sigma_2(0)}. \quad (2.14)$$

---

<sup>3</sup> Here we are considering the case where  $Q_i$  is determined solely by resistive losses in the superconductor. This is not generally true, but is a good approximation in the limit of large quasiparticle densities associated with ground-based submillimeter astronomy. In this case, the loss tangent is given by  $1/Q_i$ .

<sup>4</sup> Effective temperature is a catch-all term used to mean either a real change in temperature, or a change in the quasiparticle density equivalent to that change in temperature. It is somewhat misleading because many parameters rely on the physical temperature of the superconductor, which is different from the temperature one would surmise from assuming all the quasiparticles were due to a real temperature change.

### 2.1.2.3 Mattis-Bardeen Theory

Knowing the effective change in complex conductivity, we can directly relate to the measurable change in a resonator. But the exact method of how the change in  $\sigma$  comes about in the first place requires a theoretical approach to quantify the effect. This theory was developed by Mattis and Bardeen in 1958 for describing the effects of quasiparticles on the complex conductivity of superconductors at a given frequency [73]. For a chemical potential,  $\mu$ , gap parameter  $\Delta$ , and temperature  $T$  the real part of the conductivity is

$$\sigma_1 = \frac{2\sigma_n}{\hbar\omega} \int_{\Delta}^{\infty} \frac{[f(E) - f(E + \hbar\omega - \mu)](E^2 + \Delta^2 + \hbar\omega E)}{\sqrt{(E^2 - \Delta^2)([E + \hbar\omega]^2 - \Delta^2)}} dE \quad (2.15)$$

while the imaginary part is given by

$$\sigma_2 = \frac{\sigma_n}{\hbar\omega} \int_{\Delta-\hbar\omega}^{\Delta} \frac{[1 - 2f(E + \hbar\omega - \mu)](E^2 + \Delta^2 + \hbar\omega E)}{\sqrt{(\Delta^2 - E^2)([E + \hbar\omega]^2 - \Delta^2)}} dE. \quad (2.16)$$

Here  $f(E)$  is the “Fermi function,”

$$f(E) = \frac{1}{1 + \exp(\frac{E - \mu}{k_B T})}, \quad (2.17)$$

which can be summed over all states to give the total number of fermions. The superconducting conductivities depend on the normal state conductivity, which is not always known. As discussed above, the quantities measured are given by ratios of conductivities, so the normal state conductivity will cancel. They are important because, if one knows the gap parameter and the resonance frequency, one can calculate the effect of a change in temperature on the measurable quantities of a resonator. Conversely, one can use the measured change in frequency and  $Q$  due to temperature changes to infer the gap parameter by relating the frequency shift to this known change in  $\sigma$ . In general, these integrals can be solved numerically, but approximate solutions can be found in specific cases, as seen in the following section.

These equations are particularly useful for understanding the response of MKIDs to changes in temperature, as when they are sealed off from radiation (i.e. “dark” MKID testing). We generally consider the effect of radiation, or of any general source of non-thermal quasiparticle

creation, to be the equivalent of adding an effective chemical potential to the system. If the system has a fixed density of quasiparticles in equilibrium, this is an effective approximation. However, there are cases in which the population is not in equilibrium, as in the case of MKIDs driven by large microwave readout powers. In these cases, the Fermi distribution must be replaced by something more accurate. Due to the complex nature of these systems, finding a replacement for the Fermi distribution is difficult. In general, this approximation is still useful for low-power MKID measurements.

The complex conductivity depends only on the gap parameter, the frequency and the temperature or effective chemical potential. The real and imaginary parts should have some relationship in how they respond to changes in the effective load. It is useful to define the relationship between the resistive and inductive response. Using Equations 2.14 and 2.11, we see this relationship is given by

$$\delta \left( \frac{1}{Q_i} \right) = \alpha \frac{\delta \sigma_1}{\delta \sigma_2} \frac{\delta \sigma_2}{\sigma_2(0)} = 2(\tan \psi) \frac{\delta f}{f_0}. \quad (2.18)$$

The parameter  $\tan \psi = \frac{\delta \sigma_1}{\delta \sigma_2}$  describes the relationship between the signal in each direction (i.e. dissipation and frequency directions) at a given resonant frequency, base temperature, and gap parameter. It is defined by the angle,  $\psi$ , between the imaginary and real response in the  $S_{21}$  plane. Its dependence on the temperature and frequency, from Mattis-Bardeen theory, is seen in Figure 3.4. In most regimes using MKIDs, the frequency response, or the imaginary response in conductivity, tends to dominate. At higher frequencies and lower temperatures, the ratio of frequency-to-dissipation response decreases.

#### 2.1.2.4 Quasiparticle density

We have shown how measurable quantities relate to changes in conductivity, but to understand MKIDs we need to consider these effects on a more fundamental level. Given that MKIDs are pair-breaking detectors, with frequency and loss determined by the number of Cooper pairs broken, it is necessary to consider these effects in terms of quasiparticles created either by temperature increases or by an external power source, such as light. In particular, the relationship between

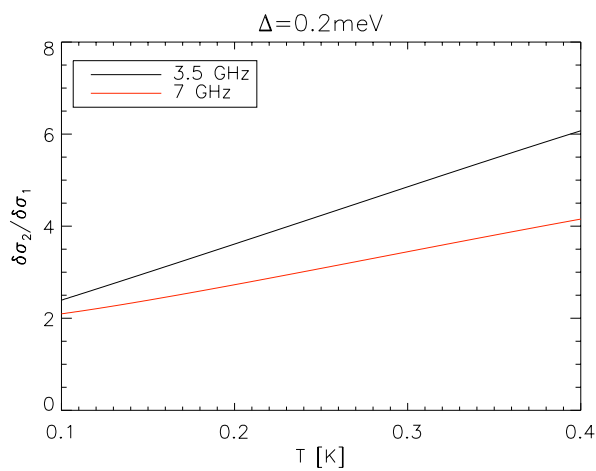


Figure 2.3: The ratio of the change in the real and imaginary conductivity as a function of temperature. Here the ratio for the change in conductivity in a superconductor at two different frequencies are shown. These frequencies and temperatures are typical for MKID resonators.

a power source and the effective chemical potential of the superconductor is non-trivial. It is much simpler to relate all these quantities to an inferred quasiparticle density. This is difficult given the complex relationships of Equations 2.15 and 2.16.

As fermions, the quasiparticles have a density given by

$$n_{qp} = 2N_0 \int_0^{\infty} \frac{1}{1 + \exp(\frac{\sqrt{\epsilon^2 + \Delta^2} - \mu}{k_B T})} d\epsilon \quad (2.19)$$

where  $N_0$  is the single-spin electron density of states at the Fermi energy level [81]. This equation arises simply from integrating the partition function for quasiparticles, given their density of states, over the all energies. For  $T \ll T_c$ , this expression can be approximated by

$$n_{qp} = 2N_0 \sqrt{2\pi k_B T \Delta} e^{-\frac{\Delta - \mu}{k_B T}}. \quad (2.20)$$

Using Equation 2.20 in the low-temperature limit of Equation 2.16 yields an expression for determining the frequency shift as a function of quasiparticle density. We can express the frequency shift, or change in  $Q$ , as a function of quasiparticle density through the equations

$$\sigma_2 = \frac{\pi \sigma_n \Delta_0}{\hbar \omega} \left[ 1 - \frac{n_{qp}}{2N_0 \Delta_0} \left( 1 + \sqrt{\frac{2\Delta_0}{\pi k_B T}} I_0 \left[ \frac{\hbar \omega}{2k_B T} \right] e^{-\frac{\hbar \omega}{2k_B T}} \right) \right] \quad (2.21)$$

and

$$\sigma_1 = \frac{2\sigma_n \Delta_0}{\hbar \omega} \frac{n_{qp}}{N_0 \sqrt{2\pi k_B T \Delta_0}} \sinh \left( \frac{\hbar \omega}{2k_B T} \right) K_0 \left( \frac{\hbar \omega}{2k_B T} \right), \quad (2.22)$$

respectively [36]. Here  $I_0$  and  $K_0$  are modified Bessel functions of 0<sup>th</sup> order, and  $\Delta_0$  is the gap energy at zero temperature. These simplifications make the process of relating measurable quantities,  $Q$  and  $f_0$ , to quasiparticle density much more tractable – we have above shown how they relate to  $\sigma$  in Equations 2.11 and 2.14, and in Equations 2.21 and 2.22 we now see how  $\sigma$  relates to  $n_{qp}$ . This is all we need to fully describe MKID behavior in response to changes in quasiparticle density.

One important feature of MKIDs is the difference between total quasiparticles and quasiparticle density. An external (non-thermal) power source generally creates quasiparticles, but the density of quasiparticles created depends on the volume of the detector. Both  $Q$  and  $f_0$  are purely sensitive to the density, not the total number of quasiparticles. Without knowing the precise volume, these detectors are inherently difficult to calibrate from first principles. A dark measurement

of parameters will not be sufficient to infer how much optical power is dissipated in the detector. While this can be largely overcome on a practical level, it is a core obstacle in understanding MKID physics.

#### **2.1.2.5 Discussion of important parameters that affect responsivity**

In calculating responsivity, the two most important parameters are the kinetic inductance fraction,  $\alpha$ , and the gap parameter at  $T = 0$ ,  $\Delta_0$ . The gap controls the number of quasiparticles created due to either thermal or nonthermal causes, as seen in Equation 2.20 while the kinetic inductance fraction controls the frequency shift per quasiparticle. Both these parameters vary with thickness and purity (or resistivity) in ways which are nontrivial to calculate, and are relatively unpredictable from device to device. The gap value typically varies by  $\sim 10\%$ , most likely due to variations in superconductor thickness. This modest variation has a large effect on quasiparticle density changes due to physical temperature changes. However, it has only a modest effect on the responsivity to nonthermal power sources. In both cases, the kinetic inductance fraction determines the proportionality between frequency shift and quasiparticle density. It can vary by factors of two for identical geometries, and thus its measurement is necessary to determine responsivity. While there is no easy way to measure these effects independently, it is possible to disentangle the effects of the two parameters in dark temperature sweeps, or measuring the resonance profile as a function of temperature. This is discussed further in Chapter 4.

In addition to these parameters, the lifetime of quasiparticles in a material is a parameter in determining the responsivity. Thus far, the discussion has focused on a fixed density of quasiparticles in a steady state, and its effect on resonator parameters. However, the density of quasiparticles created by an external power source relies on the effective recombination time of the quasiparticles. Qualitatively, if quasiparticles are created and quickly recombine, the density will be lower, and the detectors will be less responsive to power. In the absence of thermal quasiparticles, a source

creates quasiparticles by the generation-recombination equation

$$\frac{n_{qp}}{\tau} = \frac{P_{source}}{V\Delta} \quad (2.23)$$

where  $V$  is the detector volume and  $\tau$  is the quasiparticle lifetime, or the timescale for recombination. In Equation 2.23, the number of quasiparticles created depends on the power doing the pair breaking (here we assume the power is 100% efficient at breaking pairs) divided by the gap energy, to determine the number of quasiparticles that can be created. From a pure sensitivity perspective, Equation 2.23 shows that it is desirable to have the longest lifetime possible. The lifetime varies with quasiparticle density, as greater numbers of quasiparticles yield a higher probability of recombination. The lifetime is given by

$$\frac{1}{\tau} = \frac{1}{\tau_0} + Rn_{qp} \quad (2.24)$$

where  $\tau_0$  is here defined as the unloaded lifetime at  $T=0$ .  $R$  is the recombination constant, usually measured in  $\mu\text{m}^3/\text{s}$ , given by

$$R = \left( \frac{2\Delta}{k_B T_c} \right) \frac{1}{4\Delta N_0 \tau_{e\omega}}. \quad (2.25)$$

In Equation 2.25,  $\tau_{e\omega}$  is the timescale for electron-phonon interactions, elsewhere denoted as  $\tau_0$  [117, 56]. For applications with large quasiparticle densities, such as ground-based submillimeter astronomy and its associated large sky loading, this constant effectively determines the lifetime, and is thus a crucial value in determining the responsivity. Recent experiments have shown the possibility of very long unloaded lifetime, which are very useful for applications with low quasiparticle densities [3, 6].

### 2.1.3 Resonator noise

The responsivity is calculated from dissipation and frequency changes due to broken Cooper pairs in the detector. To find the precise NEP to evaluate their usefulness as detectors, we must consider the noise properties, including where the noise comes from and how it is best mitigated. There are two types of noise in MKIDs – noise intrinsic to the detector, and extrinsic noise added

to the probe signal (e.g., amplifier noise). This is discussed further in Section 2.3.5. Here we are concerned with noise sources intrinsic to the resonator. The ultimate limit to MKID sensitivity is given by the generation-recombination noise of quasiparticles. However, this noise level, which affects both frequency and dissipation, is typically far below the noise limit of the best cryogenic amplifiers. A more practical limit on sensitivity comes from excess frequency noise.

MKID resonators have repeatedly shown noise in excess of amplifier noise as an effective jitter in the resonance frequency [23, 76]. This jitter has been shown to be absent in the dissipation, or  $Q$ , where no noise is detected in excess of amplifier noise [38]. This has been extensively studied in thin-film coplanar waveguide (CPW) resonators, the cross-section of which can be seen in Figure 2.4. These are effectively two-dimensional analogues of coaxial cables. In such a setup, the noise can physically originate in the superconductor, on the substrate surface on which the superconductor is deposited, or in the bulk substrate. It is believed that this noise comes primarily from two level systems (TLSs) in the substrate, and not from the superconductor. In such a scenario, electrons switching between ground and excited states will effectively change the dielectric constant of the substrate, yielding excess noise solely in the resonance frequency. By contrast, the loss of the signal is not affected, which implies a stable  $Q$  with no excess noise.

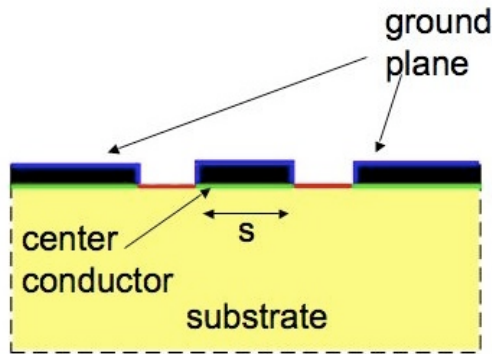


Figure 2.4: Cross-section of a CPW resonator.  $s$  gives the center strip width. Adapted from Ref. [36].

Investigations into the temperature and power dependence of this noise has yielded an effective model for the noise in the resonators. Evidence of the TLS origin of the noise comes from

the observed shifts in resonance frequency at low temperature [58]. As the device temperature is increased well above  $\hbar\omega/k_B$ , the noise significantly decreases. In addition, the noise power spectrum goes down as  $P_{int}^{-1/2}$ , where  $P_{int} = 2Q^2P_{\mu w}/\pi Q_c$  and  $P_{\mu w}$  is the microwave readout power [38, 37, 4]. These two cases also point to TLS effects, as increased power and high temperature saturate the two level systems, reducing the noise. The noise typically has a  $1/\sqrt{f}$  spectrum, which causes great difficulty for low-frequency applications such as submillimeter astrophysics.

Recent experimental evidence has indicated that the TLS effect is largely a surface substrate effect, because larger capacitors reduce the noise [37]. Let us consider what happens by increasing the width of a thin film CPW. In this case, there are electric field lines going from the center conductor to the outer ground plane due to the geometry. As the width  $s$  increases, the electric field lines become spread out throughout the volume of the substrate as they travel from one conductive surface to the other. If the TLSs are distributed evenly throughout the substrate, the effect of widening one conductor would be negligible, as there would still be as many TLSs per effective electric field line. However, if the TLSs are a surface distribution, the effective number of TLSs per electric field line will decrease with conductor width. Thus, a wider CPW resonator would see less effective noise than a narrower one. Evidence for a surface distribution is seen experimentally [37].

These revelations show that the size of the capacitive section determines the noise level; the smaller the capacitor, the larger the noise. Thus, more recent fabrications of MKID devices use interdigitated capacitors [80], discussed in the following Section 2.2, which have much larger surface area and significantly decreased noise, while retaining the original dimensions for the detector (mostly inductive) section.

## 2.2 Use of MKIDs for sub/millimeter detection

As discussed in Section 2.1, MKIDs are useful as detectors of light. Now we consider MKIDs specifically for submillimeter and millimeter-wave light. Detecting light at these wavelengths requires an efficient method of coupling the light to the detectors and reading out the physical changes

in the resonators. These methods, as well as specific designs used in the detectors, are discussed in the following sections.

### **2.2.1 Sub/millimeter MKID designs**

In practice, MKIDs can be divided into three types of resonators: quarter-wave coplanar waveguide (CPW) resonators, lumped-element resonators (LEKIDs), and resonators with an interdigitated capacitor (IDCs). These designs all have the same basic implementation, common to all submillimeter MKID detectors. They consist of a thin film of superconducting ground plane on a substrate, typically silicon or sapphire, which has a (usually coplanar waveguide) feedline running across it. This feedline is coupled to a coaxial cable at each end, through which the probe signal is sent in for measuring the resonator. The resonator is a pattern etched out of the groundplane, so that the resonator structure is weakly coupled to the feedline (i.e. generally with high coupling  $Q$ ). On a single such chip, tens or hundreds of resonators, tuned by their geometrical design to resonate at various frequencies, can be coupled to the same feedline and read out simultaneously.

Various other designs exist for MKIDs in the submillimeter, for example using microstrip resonators. But these designs are either not as well tested as those mentioned here, or have implementation or noise issues which have not yet been overcome. The examples given here are the most promising for use in sub/millimeter astrophysical applications.

#### **2.2.1.1 CPW MKIDs**

Coplanar waveguide resonators are the simplest design, being the effective two dimensional analog of a length of coaxial cable. Quarter-wave CPW resonators are open-circuited at the coupling end (creating a Dirichlet boundary condition in the resonator, where current is zero), and short-circuited to the ground plane at the far end (creating a von Neumann boundary condition, where current is constant) which ensure coupling to only odd harmonics of the resonant frequency. The current distribution is therefore just one quarter of a sine wave over the length of the resonator. The current is highest at the shorted end, and therefore the sensitivity is greatest there, whereas the

sensitivity is small at the coupling end.<sup>5</sup> The frequency is then set by the length of the resonator, the dielectric constant of the substrate, and the kinetic inductance fraction. CPWs have the advantage of being very easy to couple to an antenna, as a microstrip antenna feed overlapping the grounded end will necessarily transfer power into the lossy CPW resonator. In addition, coupling to the readout feedline is trivial with the use of an elbow coupler, in which the length of the coupling portion and the distance from the feedline determine the coupling strength. This type of resonator is seen in Figure 2.5.

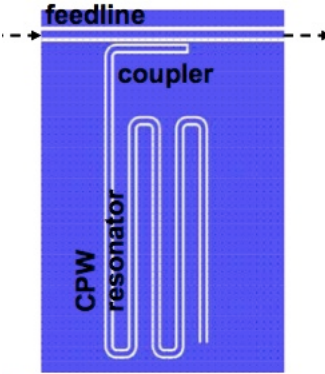


Figure 2.5: Diagram of a CPW quarter-wave resonator coupled via an elbow coupler to a feedline [36]. Blue represents the superconducting groundplane, and white where it is etched away exposing the bare substrate. The resonator is shorted to the groundplane at one end and open at the other, creating a quarter-wave condition.

This type of MKID is attractive because of its simplicity. There are no large structures, and the coupling is determined by the length of the resonator coupling to the feedline. The main drawback is its high frequency noise, given the small geometric size of the capacitive portion. In addition, it can be challenging to design for use at low frequencies, as this makes the resonator extremely long.

---

<sup>5</sup> For example, the  $Q_i$  is generally given by  $\omega \int LI^2(z)dz / \int RI^2(z)dz$ , where  $z$  is the position along the length of the resonator; Equation 2.12 is an approximation assuming  $R$  and  $L$  are constant over the length of the resonator. Change in  $Q_i$  is maximized if the quasiparticles are created in the area with the highest current, changing the resistance and inductance per unit length at that point.

### 2.2.1.2 LEKIDs

The second kind of detector, lumped-element resonators, involve an inductive meander coupled with an interdigitated capacitor. One can create a sensitive detector by using the inductive portion as a direct absorber. This design is more difficult to geometrically couple to submillimeter antennas, limiting the usefulness in multicolor arrays. However, these are being developed for single-color use in the millimeter-wave regime [29]. A diagram of a LEKID resonator is seen in Figure 2.6. A similar design is also the focus of research at shorter wavelengths [79].

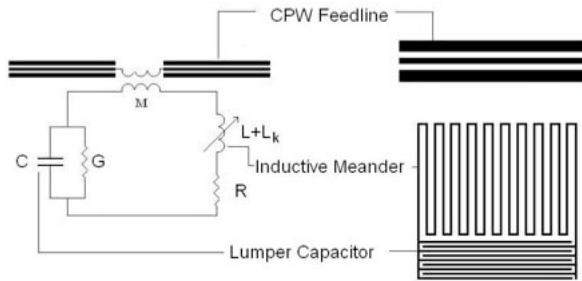


Figure 2.6: Diagram of a LEKID resonator coupled inductively to a feedline, from Ref. [29].

In addition to the lack of multicolor operation, LEKIDs also have a propensity for inter-resonator coupling. This is due to the very large structures giving the resonator its capacitance and inductance. Nearby detectors are likely to couple among themselves as well as to the feedline. This problem is not insurmountable, but must be accounted for.

### 2.2.1.3 IDC MKIDs

The Inter-Digitated Capacitor (IDC) resonators are effectively hybrids of lumped element and quarter-wave resonators [80]. The inductive portion is a CPW shorted at one end, rather than an inductive meander, but the capacitor is a large inter-digitated capacitor as seen in the lumped-element detectors. Thus, instead of relying on the CPW section for its capacitance, the bulk of capacitance comes from the large fingered structure, greatly reducing capacitive TLS noise. IDCs combine the effect of reduced noise in the capacitive section and straightforward coupling

to the antenna as in quarter-wave CPW resonators. The length does not determine the resonant frequency, as it does in CPWs, and therefore the harmonics and current distribution are not as simple. Coupling is effectively determined by the distance of the large capacitor to the feedline, rather than by a separate coupler. This type of resonator is seen in Figure 2.7.

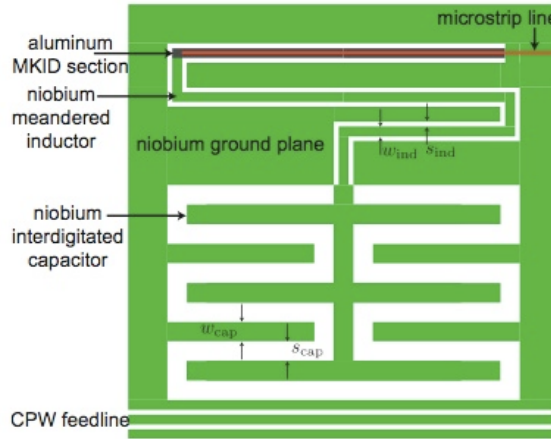


Figure 2.7: Diagram of an IDC resonator coupled to a feedline, courtesy of Omid Noroozian [80]. Green represents the superconducting groundplane, and white where it is etched away exposing the bare substrate.

The primary benefit of this type of detector is the reduction of noise compared to a CPW resonator. This improvement makes the measurement of frequency response competitive with the dissipation response in sensitivity. There are also significant drawbacks to this design. The capacitor is physically large, which gives the possibility of inter-resonator coupling in close-packed arrays as seen in LEKIDs. The second concern is that the capacitor will act as an antenna, coupling wideband and wide-angle radiation into the absorptive section. As in LEKIDs, these problems are not insurmountable, but pose significant challenges not seen in the simple CPW design. The quarter-wave CPW and IDC resonators are used in submillimeter applications described in this thesis. The exact types and geometries are discussed below.

#### 2.2.1.4 Designs tested

The first design iteration of submillimeter MKIDs used pure aluminum CPW resonators. This type is shown coupled to an antenna in Figure 2.8. The resonance frequencies were tuned by changing the length of the resonator, allowing for trivial multiplexing. The initial testing of these resonators is described in Ref. [59]. The direct pickup of radiation onto the long aluminum CPW (rather than through the antenna) ultimately limited their effectiveness, and they were replaced after initial device tests.

To mitigate direct pickup by the aluminum, a hybrid niobium/aluminum CPW resonator was introduced in the second iteration. This was effectively identical to the previous design, but the entire ground plane was replaced by niobium, which has a much higher gap frequency ( $\sim 700$  GHz). In addition, most of the CPW resonator was replaced by niobium, leaving only the 1 mm length closest to the grounded end of the resonator, where it is overlapped by the antenna feedline. This area had been calculated to be sufficient for the absorption of submillimeter photons, and the design degrades the sensitivity negligibly. These designs generally called for  $\sim 7$  GHz resonators, approximately 3 mm of niobium length in addition to the 1 mm of aluminum. The performance of these devices is discussed in Chapter 4.

The third design of MKIDs for sub/millimeter detection involved a hybrid design, but with an interdigitated capacitor made of niobium. This design was similar in effect to the previous designs, but has improved frequency noise performance. The IDC portion is connected to a length of CPW, which in turn is coupled to the antenna's microstrip feed. The last 1 mm section of the CPW portion was aluminum, as in the hybrid CPW resonators. Figure 2.7 shows this arrangement. The frequency multiplexing was obtained by either varying the length of the CPW section, or by altering some of the finger lengths in the capacitive section. The testing of these devices is discussed in Chapter 6.

### 2.2.2 Antenna coupling

Measuring incident photons with MKIDs requires a strategy for coupling the light into the detector. Direct pickup of photons is not necessarily preferable, as that would require large detector area and would not allow for multiple frequencies. Thus, the method used to couple to sub/millimeter radiation in this thesis involves a lithographed on-chip antenna which co-adds signals from across a  $> \lambda^2$  absorbing area and delivers them into a small MKID absorber area.

Phased-array slot antennas, which serve this purpose, have been developed at Caltech and JPL [40, 41]. These antennas consist of an array of slotlines with capacitive shorts to a microstrip feedline. Figure 2.8 shows the basics of the antenna and feed structure. The slotlines are simply etched in the niobium groundplane which disrupt the flow of current in the direction orthogonal to their length. The RF shorts allow for good coupling for this mode of incident radiation into the microstrip by matching the impedance of the microstrip to that of free space. The microstrip signal is propagated and deposited into the shorted end of the MKID, where it will break Cooper pairs in the center strip. The antenna itself is back-illuminated through the high-index silicon or sapphire substrate, making the antenna much more efficient in that direction than in the free-space direction [59].

Antennas used in this thesis are one of two designs – either 3 mm square antennas, with 16 slotlines, each with 16 taps, or 4.2 mm squares with 32 slotlines and 32 taps each. Each tap contains a capacitor used to short light in free space into the microstrip feedline by impedance matching. The former design, used on earlier devices, do not work as well at high frequency due to the lower density of taps. The larger antennas couple better at high frequency, and with larger size can be coupled to higher f/# optics and take up a greater portion of the focal plane. In either case, for optical purposes, the slotlines are close enough together to allow them to be considered, to good approximation, as uniformly illuminated square apertures. Thus, the time-reverse power pattern is defined as the square of a two-dimensional sinc function, with width determined by the wavelength of light it is sensitive to. With low sidelobes and a well-defined main beam, this pattern

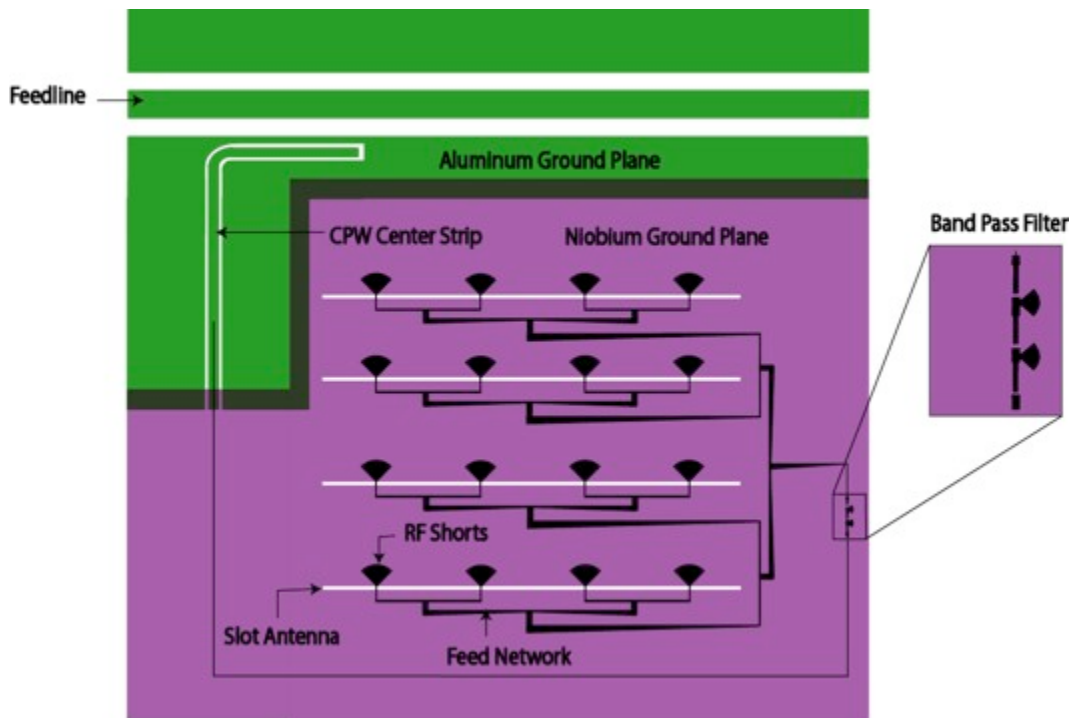


Figure 2.8: A representation of the antenna layout and microstrip feedline to the MKID resonator.

works well for submillimeter cameras.

### 2.2.3 On-chip filtering and band definition

As seen in Figure 2.8, the bandpasses for multicolor operation can be defined by placing lumped-element filters in the transmission line from the antenna to the MKID absorber. These bands are defined by lumped element series LC and shunt C circuits in the niobium transmission line [59].

It is fairly straightforward to multiplex the filters to allow several MKIDs to receive different colors from the same antenna. In such a circuit, the antenna feedline is divided into several, typically two or four, separate microstrips each leading to a separate filter. If the bandpass filters are physically close enough together, the transmission through the correct bandpass is high. This type of junction feeding multiple filters is seen in Figure 2.9. The difference in the size of the series capacitors between the two filter bands is clearly seen in the figure.

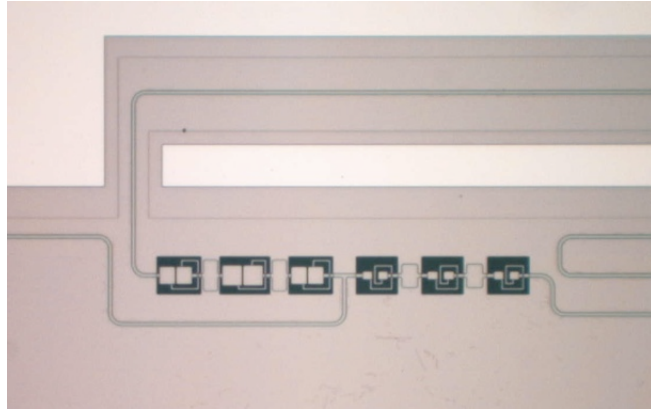


Figure 2.9: An antenna feed junction, dividing the signal into two different colored filters. The line is a microstrip feed from the antenna. After the junction, the light is fed through the bandpasses to two separate resonators. This specific filter junction comes from the first device used to test antenna-coupled MKIDs, using an aluminum groundplane, the discussion of which is beyond the scope of this thesis.

### 2.2.4 MKID readout

Up to this point we have considered the physical MKID devices, and how they operate. Here is discussed how MKIDs are read out, and in particular how they are multiplexed. This primarily relates electronics operating at room temperature, and how it can measure the small frequency and dissipation changes in a resonator, or many resonators.

#### 2.2.4.1 Basic readout principle

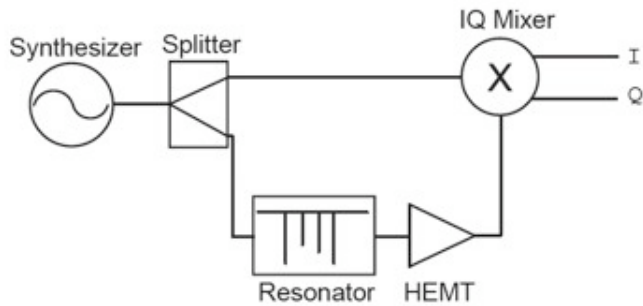


Figure 2.10: The approach of analog readout [76].

The technique for reading out the response of MKID detectors to small changes in optical loading is called homodyne mixing, shown in Figure 2.10. Unlike heterodyne mixing, here one signal (a generated sine wave) is mixed with a copy of itself. A probe signal at a characteristic frequency is divided into two copies by a microwave -3dB splitter (or combiner in reverse). One copy goes into the cryostat, where it couples to the resonator of interest, and receives a phase shift and amplitude change from the impedance of the coupled resonator. This copy is then mixed back together in the RF port of an IQ mixer. The copy which did not go into the Dewar is fed directly into the LO port of the IQ mixer. The IQ mixer multiplies the two signals to get the in-phase and quadrature components, or the amplitude and phase of the signal (e.g. [97]). The mixed signal is given by

$$I = C(1 + \delta A(t)) \cos(\omega_{RFT} t + \phi(t)) \cos(\omega_{LOT}) \quad (2.26)$$

and

$$Q = C(1 + \delta A(t)) \sin(\omega_{RF}t + \phi(t)) \cos(\omega_{LO}t) \quad (2.27)$$

where  $C$  is some constant related to the transmission of the IQ mixer. Here  $\delta A(t)$  and  $\phi(t)$  simply correspond to amplitude and phase fluctuations with time. Simplifying by knowing that  $\omega_{LO} = \omega_{RF}$  and only including results at audio frequencies (i.e. throwing away terms mixed to higher GHz frequencies), we have

$$I + iQ = \frac{C}{2}(1 + \delta A(t))e^{i\phi(t)}. \quad (2.28)$$

For small changes,  $I$  and  $Q$  correspond to amplitude and phase shifts, given by  $I+iQ=C(\delta A(t) + i\phi(t))$ . If we divide out the carrier, this is equivalent to the change in  $S_{21}$  given in Equation 2.4.

At audio frequencies much smaller than the probe frequency, the high frequency sine wave averages out, leaving pure measurements of amplitude and phase. While the outputs of the IQ mixer are generally not correctly separated into phase (imaginary) and amplitude (real) components, it is straightforward to project the combined signal of the two outputs by applying a simple rotation matrix, i.e.  $I+iQ = e^{i\theta} [I_{raw}+iQ_{raw}]$ . With this projection, two timestreams are generated from the same detector, one of amplitude and one of phase. These can later be combined to generate the optimal signal-to-noise ratio.

#### 2.2.4.2 Digital multiplexed readout

Detector readout becomes somewhat more complicated when considering tens or hundreds of detectors at multiple frequencies. The general strategy is to design all detectors to fall within a given frequency bandwidth,  $w$ , such that they fall in a range  $[f, f + w]$ . Then, a single tone can be generated corresponding to each resonance within that bandwidth, with frequencies in between 0 and  $w$ . These tones are mixed with a local oscillator signal to higher frequencies, such that the tones also fall into the bandwidth  $[f, f + w]$ . Each tone is then at the frequency of a given resonator. After going through the device, the tones are mixed back down to baseband. The system for upconverting and downconverting, consisting of a frequency synthesizer and IQ mixers, is called

the IF system (or Intermediate Frequency system). Once through the IF system, the signals are converted into digital format, then mixed in a way analogous to standard homodyne mixing method [74]. The digital readout is represented in Figure 2.11.

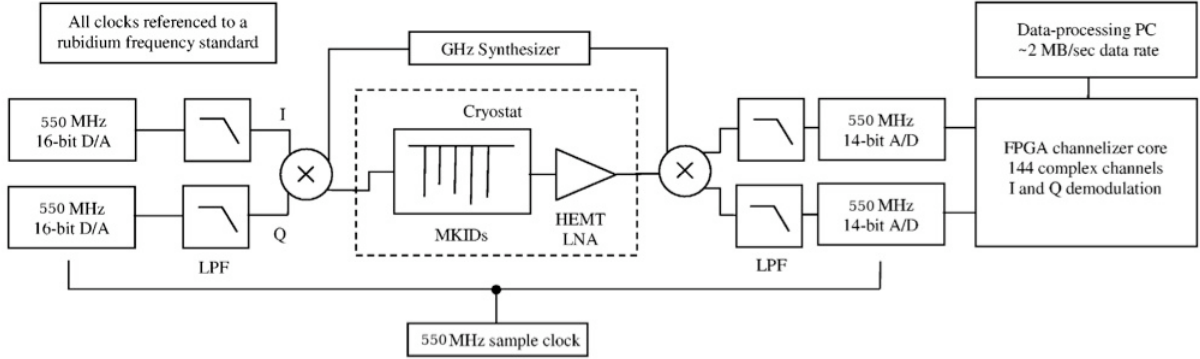


Figure 2.11: A schematic of the approach of digital multiplexed readout, from Ref. [68]. In this system a digitally generated buffer of probe signals is converted to analog, mixed up to the band of resonator frequencies, and sent into the cryostat. After probing the MKIDs, the signals are mixed back to base and converted back to digital.

In this process, the tones are most easily generated digitally and converted to analog to probe the resonator. A fast D/A computer card must generate signals within a given bandwidth, typically several hundred MS/s. This defines the frequency range, as the frequencies sent in must be Nyquist sampled. For example, a single 100 MS/s card could only generate frequencies up to 50 MHz, because at higher frequencies there are not enough points to define the effective sine wave.<sup>6</sup> Thus, the maximum range is given by the speed of the card, modulo unusable space for the effect of anti-aliasing filters. After the homodyne mixing stage, the outputs are converted by fast A/D cards into digital format. These signals can be resampled to any data rate desired, which in the case of submillimeter astronomy is typically on the order of 100 Hz. In this process, it is imperative to retain enough bits of resolution, or the signal-to-noise ratio will degrade due to digitization effects.

The problems faced in achieving good signal-to-noise ratios for numerous tones are significant. One must generate a combination of very large probe signals, while the readout is searching for very small shifts in the amplitude and phase of these signals once through the IF system and cryostat.

<sup>6</sup> In the case of a frequency at exactly half the sampling rate, the actual signal sent in would be a square wave.

Thus, astounding levels of signal-to-noise are required for the probe signal generation. The dynamic range, the range of power levels in the output signal relative to the noise floor, is set by the DAC and determines this signal-to-noise ratio. With multiple probe sine waves at different frequencies, however, the amplitude can exceed the largest allowable level at certain points. This effect is known as clipping. The signals are recoverable, but this highlights the difficulty in using many probe signals in a single frequency bandwidth. In general, more probes lead to reduced signal-to-noise, as more signals require a decrease in each signal's amplitude with a fixed dynamic range. Additionally, noise can arise at the DAC due to poor voltage regulation in converting the digital signals to a transmitted signal in physical volts. This generally would manifest itself as excess  $1/f$  noise in the probe signal voltage. Luckily, this noise is largely correlated among different probe signals because the conversion from digital to analog is common to all, so it is in principle removable.

In general, a buffer is created which is the sum of the probe signals as a function of time. The sine waves comprising the buffer must be added in such a way that they are cyclical over the buffer size. This means that only certain frequencies can be set with probe signals. For example, with a DAC generating signals at 16 MHz with a 64-point buffer, the minimum spacing between probe signals would be 250 kHz. With a 550 MHz DAC and a buffer of  $2^{17}$  points, the minimum frequency spacing is under 5 kHz. The latter spacing is usable for probing MKIDs with minimal flux reduction, as is shown in Appendix D.

### **2.3 Parameters and measurements necessary to understand MKID Camera performance**

To understand the operation of MKIDs in ground-based sub/millimeter cameras, and to diagnose problems, several parameters must be measured. Below, we list the important parameters having to do with the operation of MKID cameras.

### 2.3.1 Optical efficiency

A primary consideration involves how efficiently a camera can convert a change in sub/millimeter loading into a change in signal. This efficiency includes several independent effects: the efficiency of the optics, the efficiency of the coupling to the detector (antenna efficiency, in the case of antenna-coupled MKIDs), and the quasiparticle creation efficiency. Because it is difficult to decouple these effects, we generally consider an overall efficiency,  $\eta$ . To find this, we start with the generation-recombination equation for quasiparticles under the load of some power,  $P$ , comprised of photons with energy greater than gap parameter,  $\Delta$ , given in Equation 2.23. This relationship is

$$\frac{n_{qp}}{\tau} = n_{qp} \left( \frac{1}{\tau_0} + Rn_{qp} \right) = \frac{\eta P}{V\Delta} + \frac{n_{thermal}}{\tau_{thermal}} \quad (2.29)$$

where the thermal quasiparticle term is generally negligible compared to the loading. Neglecting the latter term, we can solve for the total efficiency, yielding

$$\eta = \frac{V\Delta}{P} \left( \frac{n_{qp}}{\tau_0} + Rn_{qp}^2 \right). \quad (2.30)$$

This shows that, to know efficiency as a function of quasiparticle density, one must measure  $\tau_0$ ,  $R$ ,  $\Delta$ ,  $V$ , and the load power. To parameterize in terms of frequency shift per unit power, one must also know  $\alpha$ . With these parameters, by measuring a frequency shift under known loads, one can determine the optical efficiency.

### 2.3.2 Excess load

MKIDs, like all sub/millimeter detectors, become less sensitive under large optical load. In addition to the expected loads coming from antenna-coupling to sources (e.g. sky load), there may be additional loading on the detectors. This light is generally caused by stray light coupling into the detectors, creating a higher load temperature. This excess loading, as well as the overall load, is generally expressed in Rayleigh-Jeans temperature for a single polarization,  $T_{load} = P_{load}/\eta k_B(\Delta\nu)$ .

Excess loading can generally be determined from two sources - measurements of the recombination time for quasiparticles, and from measurements of  $Q_i$  in Network Analyzer sweeps. In principle these two methods should give identical results.

To find excess load from lifetime measurements, we need to know the lifetime corresponding to this base temperature, as well as the lifetime at  $T = 0$  ( $\tau_0$ ). In this case, the generation/recombination equation (Equation 2.29) becomes

$$\frac{\frac{1}{\tau} - \frac{1}{\tau_0}}{R\tau} = \frac{\frac{1}{\tau_{thermal}} - \frac{1}{\tau_0}}{R\tau_{thermal}} - \left(\frac{\eta}{V\Delta}\right)P_{load}. \quad (2.31)$$

If all we are interested in is the ratio of  $P_{load}$  looking at a 77 K and 300 K blackbodies, then the parameters  $V, R, \Delta$  and  $\eta$  drop out.

$$Const \times P_{load} = \frac{1}{\tau^2} - \frac{1}{\tau_{thermal}^2} - \frac{1}{\tau_0} \left( \frac{1}{\tau} - \frac{1}{\tau_{thermal}} \right) \quad (2.32)$$

This is a valid method for finding the excess load providing the data is precise enough and good fits to the lifetimes can be obtained.

A second case involves finding the excess load from network analyzer frequency sweeps. This method, while much easier to fit, is much less ideal because it requires the invocation of Mattis-Bardeen theory. Let us consider the case of  $1/Q_i$ , which is effectively proportional to the measured frequency shift,  $\delta f/f_0$ . If the quasiparticle density can be assumed to be uniformly distributed across the resonator, then  $1/Q_i$  should be proportional to the quasiparticle density by some factor, which we arbitrarily call  $A$ . The generation-recombination equation then becomes

$$\frac{A}{Q_i} \left( \frac{1}{\tau_0} + R \frac{A}{Q_i} \right) = \frac{A}{Q_{i,thermal}} \left( \frac{1}{\tau_0} + R \frac{A}{Q_{i,thermal}} \right) + \left( \frac{\eta}{V\Delta} \right) P_{load} \quad (2.33)$$

If  $\tau_0$  can be assumed to be very large compared to the operating lifetime, then we can absorb the  $A$ 's into a “vacuum” for constants, and the equation becomes

$$Const \times P_{load} = \frac{1}{Q_i^2} - \frac{1}{Q_{i,thermal}^2}. \quad (2.34)$$

This in turn gives the “naive” excess load calculation between two loading powers as

$$T_{exc} = \frac{\frac{T_2}{Q_{i,1}^2} - \frac{T_1}{Q_{i,2}^2}}{\frac{1}{Q_{i,2}^2} - \frac{1}{Q_{i,1}^2}}. \quad (2.35)$$

This definition is used in the calculation of excess load throughout the thesis.

### **2.3.3 Beam maps and point source response**

To ensure good coupling to point sources in astronomy, it is helpful to map out the response of detectors to a source as a function of angle, known as a beam map. These are maps of detector response to a chopped blackbody source. For downward-facing Dewar windows, the source is placed some vertical distance away from the camera window, and stepped in a grid pattern at that distance. The average detector response at each location gives a map of the response as a function of angle. This can be compared to simulation of the optical path of the system, to ensure the optics and detectors are behaving as expected.

With beam maps, one can ensure good coupling to point sources, as defined by the beam. A beam map without good directivity (highly peaked angular response) will not respond well to point sources. In a sense, observing astronomical sources constitutes a beam map of a point source in the extreme far field. Knowing the calibrated response to these point sources is essential to the operation of MKIDs as astronomical detectors.

### **2.3.4 Spectral bandpass measurements**

One must ensure that the spectral bandpasses are correct for astronomical measurements for two reasons: to understand the spectral flux of astronomical sources, and to avoid increased loading from atmospheric water lines. It is helpful to measure detector response as a function of frequency of sub/millimeter radiation in the laboratory. The most straightforward method is to use a millimeter-wave source, or microwave synthesizer combined with frequency multipliers, tuned to precise frequencies, and measure the detector response as a function of frequency. However, it is generally difficult to calibrate the relative power outputted, from frequency to frequency, from such sources, making calibrated bandpass measurement difficult. Another method is to use a Fourier Transform Spectrometer (see e.g. [1]). This method is used much more often in millimeter-wave instrumentation, including in this thesis, as the frequency-to-frequency relative calibration is straightforward.

### 2.3.5 Resonator internal and external noise

To assess the performance of an MKID Camera, it is very helpful to differentiate noise sources internal to the resonator from external sources, such as amplifiers and electronics. These noise sources are shown in Figure 2.12. The former sources constitute frequency or dissipation noise,

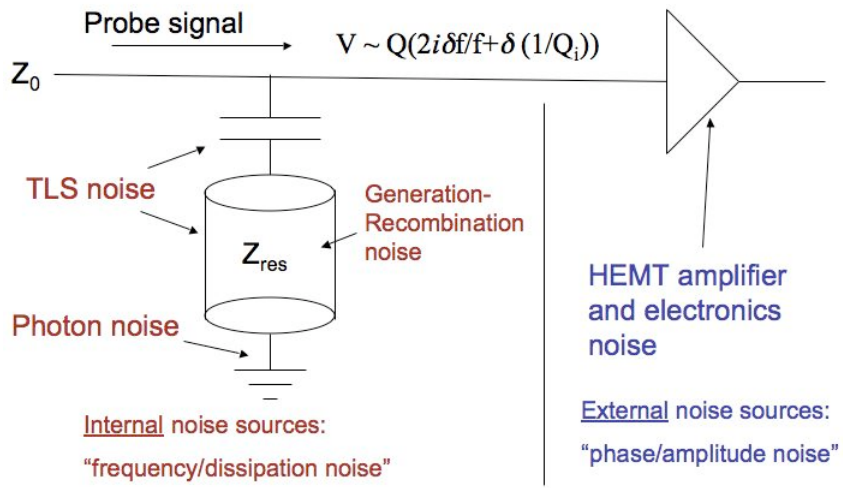


Figure 2.12: A diagram of internal and external noise sources. Internal noise sources manifest themselves as frequency or dissipation noise, while external sources include phase and amplitude noise.

while the latter constitute phase and amplitude noise. To understand the camera, one must know if there is excess photon noise within the resonator, which may come from the sources of excess load. To understand the external noise, one may find the noise level off-resonance, typically in units of  $\text{V}^2/\text{Hz}$ . This noise can be compared to what is seen in internal noise sources. A discussion of external noise sources, and their effect on camera performance, is discussed in more detail in Chapter 7.

### 2.3.6 Systematic effects

For optimal performance, one must understand any systematic effects associated with the camera and detectors. There are several important systematics, all discussed in detail in the ensuing chapters. The first such effect is the nonuniform absorption of quasiparticles from the antenna: power tends to be absorbed toward the grounded end of the resonator, biasing the measured efficiency lower. Another significant effect is pickup not through the antenna, or out-of-band direct pickup. This can occur due to leakage in the bandpass filtering, or by radiation bypassing the antenna altogether. A third effect is the heating of the array under load, creating thermal quasiparticles which resemble excess load, or optical response. A fourth effect is the change in resonance frequency and  $Q$  associated with changes in magnetic fields. Finally, there may be significant crosstalk among detectors, yielding a more uniform responsivity from detector to detector (or band-to-band) than one would expect. Although this list is not necessarily exhaustive, all these aspects have been observed in MKID camera testing, and can bias the evaluation of the performance of MKID detectors.

### 2.3.7 MKID performance as a function of readout power

In Section 2.1.3, it is discussed that using high readout power can improve the sensitivity of MKIDs by reducing the noise. All else being equal, increasing the readout power will improve the signal-to-noise ratio. The limits to this assertion must be found, as one may expect a decrease in responsivity at high readout power, due to the creation of quasiparticles by the readout power or the heating of the quasiparticle population created from a sub/millimeter load. It is important, as well, that the readout power does not make the small-signal response nonlinear.

## Chapter 3

### MKID NEP and mapping speed optimization

It is useful to consider what parameters influence MKID design and optimize sensitivity. From first principles, it is useful to know what design characteristics will maximize detector sensitivity, as well as mapping speed for a large number of detectors on the sky. This chapter breaks down MKIDs to the fundamental parameters in different noise-limiting environments, then finds what design parameters would work best in large arrays. The majority of the chapter considers the case in which microwave power will create quasiparticles with some efficiency; we consider the case in which the dominant effect is the effective heating of quasiparticles by readout power, but its consequences are difficult to calculate from first principles.

#### 3.1 Responsivity

As MKIDs are pair-breaking detectors, the responsivity depends on the relationship between quasiparticle density and applied power, e.g. submillimeter loading. If quasiparticles can be created through both submillimeter radiation coupled through the antenna and microwave readout power, the quasiparticle density in Equation 2.29 becomes

$$n_{qp} = \frac{-1/\tau_0 + \sqrt{1/\tau_0^2 + 4R \left( \frac{\eta_o P_{submm}}{\Delta V} + \frac{\eta_r P_{read}}{\Delta V} \right)}}{2R}. \quad (3.1)$$

Here  $\eta_r$  is the efficiency of the readout power at creating quasiparticles, which has been found to be nonzero, and at higher resonant frequencies may be not too far from the submillimeter efficiency. The parameter  $\eta_o$  includes efficiencies of the Dewar optics, antenna, bandpass filters, and  $\eta_{abs}$ , the

submillimeter power absorption efficiency for quasiparticle creation. For the purposes of finding the responsivity to a given power, we must know how the resonant frequency shifts with quasiparticle density, and how the quasiparticle density shifts with power. For simplicity, we'll take the total power in the resonator which is translated into pair-breaking to be

$$P_{tot} = \eta_o P_{submm} + \eta_r P_{read} = P_{submm}(\eta_o + \xi\eta_r). \quad (3.2)$$

We here define  $\xi$  to be the ratio of readout power at the device to the incident submillimeter power at the Dewar window. Note the definition of these parameters:  $\eta_o$  is defined as the total Dewar optical efficiency, but  $\eta_r$  is just absorption efficiency. If we take the ratio of these two to equal 1, we are inferring that the absorption is lower in microwave compared to submillimeter. This way of defining things makes it easier to relate to measurements, but less fundamental.

Taking the derivative of Equation 3.1 with respect to power gives

$$\frac{dn_{qp}}{dP_{tot}} = \left( \frac{\Delta^2 V^2}{\tau_0^2} + 4RP_{tot}\Delta V \right)^{-1/2}. \quad (3.3)$$

The fractional frequency shift<sup>1</sup> per quasiparticle, as seen in Section 2.1, is given by

$$\frac{df/f}{dn_{qp}} = \frac{\alpha}{2} \frac{d\sigma_2/\sigma_2(0)}{dn_{qp}}. \quad (3.4)$$

From Mattis-Bardeen theory, we can express this as

$$\frac{d\sigma_2/\sigma_2(0)}{dn_{qp}} = \frac{1}{2N_0\Delta_0} \left( 1 + \sqrt{\frac{2\Delta_0}{\pi kT}} \exp\left(\frac{-\hbar\omega}{2kT}\right) I_0\left(\frac{\hbar\omega}{2kT}\right) \right) = c(\Delta_0, T, \omega) \quad (3.5)$$

This expression is exact in the limit of  $T \ll T_c$  and  $\hbar\omega \ll \Delta$ , which is true in the normal operation of MKIDs. This shows that in this limit, the fractional frequency change per quasiparticle is constant at fixed gap parameter, physical temperature, and the resonant frequency. The total responsivity then can be described as

$$\frac{df/f}{dP_{tot}} = \frac{d\sigma_2/\sigma_2(0)}{dn_{qp}} \frac{dn_{qp}}{dP_{tot}} = \frac{\alpha}{2} c(\Delta_0, T, \omega) \frac{1}{\sqrt{\frac{\Delta^2 V^2}{\tau_0^2} + 4RP_{opt}\Delta V}} \quad (3.6)$$

---

<sup>1</sup> Here fractional frequency shift is labeled as the change in frequency  $f$ . In Mattis-Bardeen, the convention is to use the angular frequency,  $\omega$ , though the fractional shifts are equivalent.

This is the final equation we need detailing the responsivity to power absorbed in the resonator. It simply shows that the response to changes in power goes down with the square root of the load, as expected. In addition, higher kinetic inductance fraction and lower recombination constant or volume increase the responsivity. As discussed earlier,  $\alpha$  changes as a function of superconductor thickness, which is proportional to volume. In the limit of high steady-state quasiparticle densities, the responsivity will scale as  $\alpha/\sqrt{V}$ .

We simultaneously detect the change in surface resistance through the change in internal  $Q$ . For a given gap parameter, temperature and frequency, there is a set ratio between the two responses, given by Equation 2.18. With this constant relating  $Q$  to  $\delta f$ , we know the responsivity of  $Q_i$  to power is simply

$$\frac{d(1/Q_i)}{dP_{tot}} = 2(\tan \psi) \frac{df/f}{dP_{tot}} \quad (3.7)$$

The factor of 2 here comes from Equation 3.4, and originates because the fractional frequency response goes as the square root of the reactance, while the dissipation goes linearly with resistance.

It is essential for NEP calculations involving dissipation response to know the exact dependence of the total  $Q_i$  at a given load. We can then express the internal  $Q$ , which is proportional to  $n_{qp}$ , as

$$\frac{1}{Q_i} = (\tan \psi) \alpha c(\Delta_0, T, f) \frac{-1/\tau_0 + \sqrt{1/\tau_0^2 + 4R \left( \frac{P_{tot}}{\Delta V} \right)}}{2R}. \quad (3.8)$$

Equation 3.8 implicitly assumes that other sources of loss (e.g. TLS loss) are negligible, but they can be accounted for by simply adding another loss term. For applications with significant background loads,  $Q_i$  is often an order of magnitude lower than the “unloaded”  $Q_i$ , so this approximation is generally valid.

For noise with amplitude  $S$  (in squared fractional frequency per Hz), the square of the NEP is

$$(NEP)^2 = 4S \frac{\left( \frac{\Delta^2 V^2}{\tau_0^2} + 4RP_{submm}(\eta_o + \xi\eta_r)\Delta V \right)}{\alpha^2 c^2(\Delta_0, T, f)} \quad (3.9)$$

We only need to know the form of the noise sources to find the NEP’s dependence on these parameters. This NEP is for power absorbed in the detector; astronomical NEPs, involving the power

projected back onto the sky, will be denoted  $(NEP)_{astro}$ , and can be found by dividing the NEP by the optical efficiency.

Noise sources often need to be scaled with  $Q$  as will be seen in the following sections. In this note, whenever  $Q$  is given as a parameter, we assume critical coupling, or  $Q_c=Q_i$ , which implies  $Q = Q_i/2$ . A review of departures from critical coupling are discussed in Section 3.5.1.

## 3.2 Noise-limiting cases

### 3.2.1 NEP in the substrate TLS noise limit

Noise which is observed as a jitter in the resonance frequency can come from several sources such as substrate noise and quasiparticle generation-recombination noise. In practice, TLS noise from the substrate will dominate; the specifics of these are discussed in Ref. [36]. This noise scales to phase in the same manner as the frequency response; thus, if this noise dominates, we can find the NEP entirely by looking at fractional frequency shifts.

The NEP is defined in this case as

$$(NEP)^2 = \frac{S_{\delta f/f}}{\left(\frac{df/f}{dP_{tot}}\right)^2} \quad (3.10)$$

In dealing with the device noise, maximizing the readout power minimizes the noise. As discussed in Section 2.1.3, the fractional frequency shift noise power spectrum goes as

$$S_{\frac{\delta f}{f}} = k/\sqrt{P_{int}} \quad (3.11)$$

where  $k$  is some constant of proportionality, which is best determined experimentally. The internal power in the resonator scales with readout power as

$$P_{int} = \frac{2}{\pi} \frac{Q^2}{Q_c} P_{read} \sim \frac{Q}{\pi} P_{read} \quad (3.12)$$

This makes sense intuitively if we consider the resonator as a lossy cavity weakly coupled to a power source via a transmission line. The waves which couple to the cavity will resonate there, and the

effective power in the resonator will go as  $Q$  times the feedline power. With this increased power, we can write Equation 3.11 in terms of internal and coupling  $Q$  and submillimeter power, yielding

$$S_{\frac{\delta f}{f}} = k \sqrt{\frac{\pi}{2}} \frac{Q_i + Q_c}{Q_i \sqrt{Q_c \xi P_{submm}}} \sim \frac{k}{\sqrt{Q \xi P_{submm}}}. \quad (3.13)$$

So we are in luck – we get a factor of  $Q^{-1/2}$  reduction in the fractional frequency noise power spectrum for free. Putting this noise into Equation 3.9, the NEP becomes

$$\begin{aligned} (NEP)^2 &= \frac{k}{\sqrt{\xi P_{submm} \frac{Q_i^2 Q_c}{(Q_i + Q_c)^2} \left( \frac{df/f}{dP_{tot}} \right)^2}} \\ &= 4 \frac{k}{\alpha^2 c^2 (\Delta_0, T, f) \sqrt{\frac{Q_i^2 Q_c}{(Q_i + Q_c)^2} \xi P_{submm}}} \left( \frac{\Delta^2 V^2}{\tau_0^2} + 4 R P_{tot} \Delta V \right). \end{aligned} \quad (3.14)$$

We then substitute Equation 3.8 into Equation 3.14 to get the explicit dependences on the basic parameters. In order to clean up the expression to better see the dependences on parameters, we will make the assumptions of critical coupling and assume that  $\tau_0$  is large compared to the loaded quasiparticle lifetimes. Including these, and dividing by  $\eta_o^2$  to find the NEP of the device projected back upon the sky, we find

$$(NEP)_{astro}^2 = 4\sqrt{2\pi} k \frac{(\eta_o + \xi \eta_r)^{5/4} (P_{submm} R V \Delta)^{3/4} \tan^{1/2} \psi}{\xi^{1/2} \eta_o^2 \alpha^{3/2} c^{3/2}}. \quad (3.15)$$

This tells us that for single pixel sensitivity in the detector frequency noise limit, we want to make the detectors as thin as possible. As the volume decreases, the kinetic inductance fraction increases, giving a significant reduction in NEP. Other parameters can be difficult or impossible to control, so depositing less aluminum (or whatever the absorber is) is the simplest way to decrease NEP.

### 3.2.2 NEP in the amplifier noise limit

The HEMT noise occurs outside the device, and thus cannot be considered a noise source intrinsic to the device, like substrate noise or sky noise, which are independent of  $Q$ . It is in fact a voltage noise added to the  $S_{21}$  voltage going through the circuit. Instead of just considering the response of the resonance frequency, we must consider the response of  $S_{21}$  and relate that to the

noise. In the limit of small perturbations, phase response then scales as  $\frac{2Q^2}{Q_c}$  times the fractional frequency shift, while amplitude can be shown to scale as  $\frac{Q^2}{Q_c}$  times  $\delta\frac{1}{Q_i}$ . This is discussed in Appendix B. The factor of 2 here compensates for the factor in Equation 3.7, so the phase-to-amplitude ratio is still given by  $\tan \psi$ .

The noise is given by

$$(\delta V_\theta)^2 = 4k_B T_n Z_0 \quad (3.16)$$

in units of  $V^2/\text{Hz}$ , where  $T_n \sim 5 \text{ K}$  and  $Z_0 = 50 \Omega$ . Here we assume only a noise temperature; other sources of noise, such as amplifier gain and phase fluctuations, are assumed to be removable as they are correlated among probe signals. This effect is explored in greater detail in Chapter 7. We want to maximize readout power in this case as well, in order to minimize the fractional noise. In keeping with the above example, we have  $P_{opt} \sim V_\theta^2$ , as  $P_{read} = 4V_\theta^2/Z_0$  for an optimally coupled detector (i.e. where half the signal is transmitted past the resonator).

The HEMT is external to the resonator, thus what it sees is a transmission on the feedline where we are measuring a phase shift. Therefore, we must scale the noise to make it the same type as frequency noise. For small perturbations, we can approximate this effect by simply scaling the voltage response by  $2Q^2/Q_c$ , or equivalently  $2Q_i^2 Q_c / (Q_i + Q_c)^2$ . This noise term is then

$$S_{HEMT} = \frac{4(Q_i + Q_c)^4}{Q_i^4 Q_c^2} \left( \frac{\delta V_\theta}{V_\theta} \right)^2. \quad (3.17)$$

The NEP then becomes

$$(NEP)^2 = \frac{4(Q_i + Q_c)^4}{Q_i^4 Q_c^2} \frac{\left( \frac{\delta V_\theta}{V_\theta} \right)^2 \left( \frac{\Delta^2 V^2}{\tau_0^2} + 4RP_{submm}(\eta_o + \xi\eta_r)\Delta V \right)}{\alpha^2 c^2 (\Delta_0, T, f)}. \quad (3.18)$$

Let us now include the efficiency projected onto the sky, that is divide by  $\eta^2$ , and eliminate the explicit  $Q$  dependence by assuming optimal coupling ( $Q_i = Q_c$ ) and replacing  $Q_i$  with the response in Equation 3.8. Equation 3.18 becomes

$$(NEP)_{astro}^2 = \left( \frac{\delta V_\theta}{V_\theta} \right)^2 \frac{4P_{submm}^2(\eta_o + \xi\eta_r)^2 \tan^2 \psi}{\eta_o^2} \quad (3.19)$$

This shows that everything cancels except for the power. However, we are not quite finished. If we

relate  $V_\theta^2$  to the readout power we find

$$(NEP)_{astro}^2 \propto \frac{(\delta V_\theta)^2 P_{submm} (\eta_o + \xi \eta_r)^2 \tan^2 \psi}{\eta_o^2 \xi}. \quad (3.20)$$

Thus the final equation only depends on overall optical efficiency in its relation to the absorption efficiency of the readout power. So if we are already HEMT noise-limited, further increases in detector responsivity, such as by decreasing the absorber volume, simply do not matter. The only way to improve is to find less noisy amplifiers, to decrease sky or excess loading, or to use more readout power without creating too many quasiparticles.

### 3.2.3 NEP in the photon noise limit

Here we must take into account the Bose term and the usual Poisson term when considering the photon noise from the atmosphere[122, 102]. The Poisson term is simply due to fluctuations in the number of photons, while the Bose term arises because, with large numbers, photons will tend to bunch into the same state. As we are taking all responsivities to be at the front of the Dewar, we must only consider the efficiency of the telescope optics. Including the Bose term, and assuming that we are operating in the Rayleigh-Jeans limit<sup>2</sup> with a detector sensitive to a single polarization, the photon noise NEP is given by

$$(NEP)_\gamma^2 = \eta_{tel} k T [h((\nu_0 + \frac{\Delta\nu}{2})^2 - (\nu_0 - \frac{\Delta\nu}{2})^2) + \eta_{opt} \Delta\nu k T] \quad (3.21)$$

where we have integrated an assumed square bandpass with width  $\Delta\nu$ . The optical efficiency,  $\eta_{opt}$ , includes both Dewar optics and the device.

### 3.2.4 Combined NEP

NEPs generally add in quadrature. However, in this case we have both an amplitude and phase readout, and we can optimally combine the two to optimize the signal-to-noise ratio. The

---

<sup>2</sup> Generally, we find an effective RJ temperature corresponding to the exact load. Generally, the sky at Mauna Kea is approximated by a 260 K blackbody with variable emissivity, which we convert to an effective temperature including telescope emissivity for convenience.

NEP given this optimization becomes

$$(NEP)_{comb}^2 = \frac{1}{\frac{1}{(NEP)_{HEMT}^2 + (NEP)_{df}^2} + \frac{1}{(\delta\sigma_2/\delta\sigma_1)^2(NEP)_{HEMT}^2}} + (NEP)_\gamma^2 \quad (3.22)$$

. Figure 3.1 shows the results of such a combination as a function of  $Q$  under load. This can also be thought of as plotting against  $\alpha/\sqrt{V}$  (or just  $\alpha$ ), as this is effectively a single valued function of detector  $Q$  given constant  $R$  and large  $\tau_0$ . The responsivity is taken from device measurements of hybrid CPW resonators, but the results should be independent of the exact resonator form. The photon limit assumes regular atmospheric conditions at the telescope ( $\tau_{225GHz} = 0.1$ ) and some small Dewar excess load. The readout power is optimized with a 10% efficiency for creating quasiparticles assumed. Phase noise is taken from initial measurements of IDC resonators. The projected relationship between the photon noise and detector noise depend heavily on the assumed parameters and the effective power which can be used in readout.

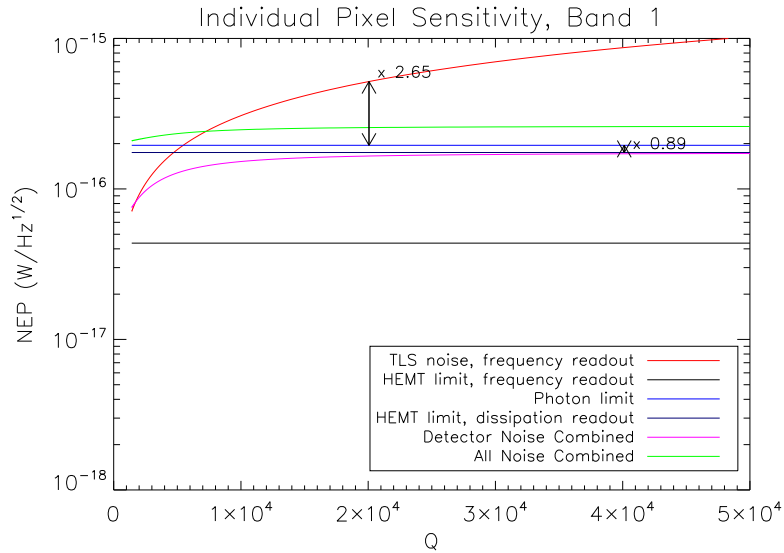


Figure 3.1: The NEP as a scaled function of  $Q$ , with responsivity dependence taken from a hybrid CPW-on-Sapphire device, scaled down to 3.5 GHz. Noise is from previously measured IDC geometries. The TLS noise limit assumes frequency response, and all noise combined includes both frequency and dissipation response combine optimally. Here we assume a 10% efficiency for readout power to create quasiparticles.

### 3.3 Mapping speed optimization

From the NEPs derived above, we are interested in finding the conditions which produce the best mapping speed. The mapping speed is defined as

$$MS = \frac{N_{pix}}{(NEP)^2} \quad (3.23)$$

assuming an independent pixel for each beam.<sup>3</sup> Our primary limitation in increasing the number of pixels is due to having a fixed readout bandwidth, and trying to fit all the resonators in while minimizing the effect of crosstalk. In this limit,  $Q$  becomes very important for the number of detectors that can be read out, as well as for responsivity. If we take  $Q = f/\Delta f$ , and we want a number  $N_{fw}$  total FWHMs between resonators determined by the minimization of crosstalk, then each resonator requires  $N_{fw}f/Q$  space. The total number of pixels we can fit in is  $N_{fw}Qf$  divided by the total bandwidth, which we call  $w$ . So the mapping speed is given by

$$MS = \frac{wQ}{fN_{fw}(NEP)^2}. \quad (3.24)$$

First, let us consider the case of the frequency noise limit. In the limit of infinite bandwidth, in which pixel count does not vary with  $Q$ , we would want a  $Q$  value as small as possible to maximize single-pixel NEP. However, we must consider how to optimize the mapping speed. The frequency-limited mapping speed is given by

$$MS = \frac{wQ}{fN_{fw}} \frac{\xi^{1/2} \eta_o^2 \alpha^{3/2} c^{3/2}}{4\sqrt{2\pi} k (\eta_o + \xi \eta_r)^{5/4} (P_{submm} R \Delta V)^{3/4} \tan^{1/2} \psi} \quad (3.25)$$

or, equivalently,

$$MS_{astro} = \frac{w}{fN_{fw}} \frac{\xi^{1/2} \eta_o^2 \alpha^{1/2} c (\Delta_0, T, f)^{1/2}}{8\sqrt{2\pi} k (\eta_o + \xi \eta_r)^{7/4} P_{submm}^{5/4} (R \Delta V)^{1/4} \tan^{3/2} \psi} \quad (3.26)$$

We have taken the NEP values for this formula from Equation 3.15 above. This equation is somewhat dense, so in order to see what is truly going on, we look at only the terms depending on

---

<sup>3</sup> This is a reasonable assumption, because the platescale is fixed by the optical design, and we are simply determining what number of detectors of the total to read out in a given bandwidth. An alternative approach would be to change the size of the pixels with fixed  $N_{pix}$ . However, this is not explored as the devices are built to conform to the optical design.

the incident power and thickness (discarding efficiency terms as effective prefactors), and find

$$MS \propto \frac{w\alpha^{1/2}c(\Delta_0, T, f)^{1/2}}{kP_{submm}^{5/4}V^{1/4}} \quad (3.27)$$

This formula shows that one's tendency to want to increase the signal-to-noise ratio by maximizing  $Q$ , and thus the pixel count, is not verified. Indeed, to maximize responsivity in the absence of other noise sources, one wants to maximize  $\alpha$  and correspondingly minimize thickness, which makes  $Q$  under load small as the dissipative response increases.

Let us now consider the HEMT-limited case. Then the mapping speed is

$$MS = \frac{wQ\eta_o^2\xi}{fN_{fw}(\delta V_\theta)^2(\eta_o + \xi\eta_r)^2P_{submm}} \quad (3.28)$$

up to the point at which  $Q$ s are high enough to allow for the maximum number of pixels, which in our case is 36 in each band. Then the mapping speed for DemoCam in each band will go as

$$MS = \frac{36\eta_o^2\xi}{(\delta V_\theta)^2(\eta_o + \xi\eta_r)^2P_{submm}}. \quad (3.29)$$

What does this tell us about  $Q$ s in the HEMT noise limit? It says that they effectively don't matter. In effect, we should go with the thickest aluminum available, as long as we remain in this limit outside of the phase noise regime. In this regime, thicker aluminum will not degrade the signal-to-noise ratio, but it will allow the maximum number of detectors in the same bandwidth. However, this limit is highly idealistic, as seen in the following section.

### 3.4 Scatter in resonance frequency spacing

In general, we will not be able to predict the exact resonance frequencies due to small variations in Aluminum thickness and the correlated kinetic inductance fraction. Therefore, we must factor in resonator “collisions,” or the probability that any number of resonators will have crosstalk above some threshold value. There are several parameters which must be considered: the spacing between resonators beyond which it is considered a “collision,” the RMS scatter between designed and observed resonance spacing, and the designed spacing between resonators. Figures

3.2 shows the effect of the projected number of resonators which we expect to have which have not collided as a function of  $Q$ . Figure 3.3 combines this information with Figure 3.1 to show the best mapping speed at the CSO as a function of  $Q$ . Note that the combined mapping speed is largely independent of  $Q$ , leading us to large  $Q$ s to maximize the number of detectors. However, at very high  $Q$ , the responsivity drops to where the generation-recombination noise limits the NEP, making this strategy infeasible.

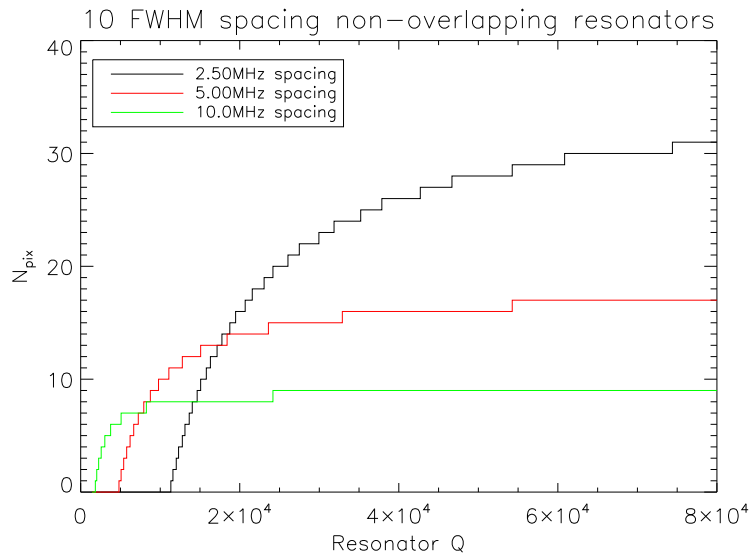


Figure 3.2: The number of usable detectors assuming a 5 MHz RMS scatter and a 10 FWHM crosstalk criterion (corresponding to  $\sim 1\%$  crosstalk level) as a function of  $Q$ . Here we assume a maximum of 36 detectors in a 90 MHz bandwidth.

Tables 3.1 and 3.2 show the results of these simulations for resonators at 240 GHz band center. We have assumed a 360 MHz bandwidth for four colors, or 90 MHz for each band. Similar optimizations are obtained at other bands, with lower bandwidth but higher background loading expected in observing conditions. These tables include the assumed scatter in detector resonance frequencies, the microwave quasiparticle creation efficiency, and the responsivity we would expect from hot/cold tests in the lab. The results can be seen from this data: for a reasonable crosstalk criterion for collision of a few percent, the mapping speed is generally optimized by scenarios that include more detectors, and therefore push toward higher  $Q$  and less responsivity. These results

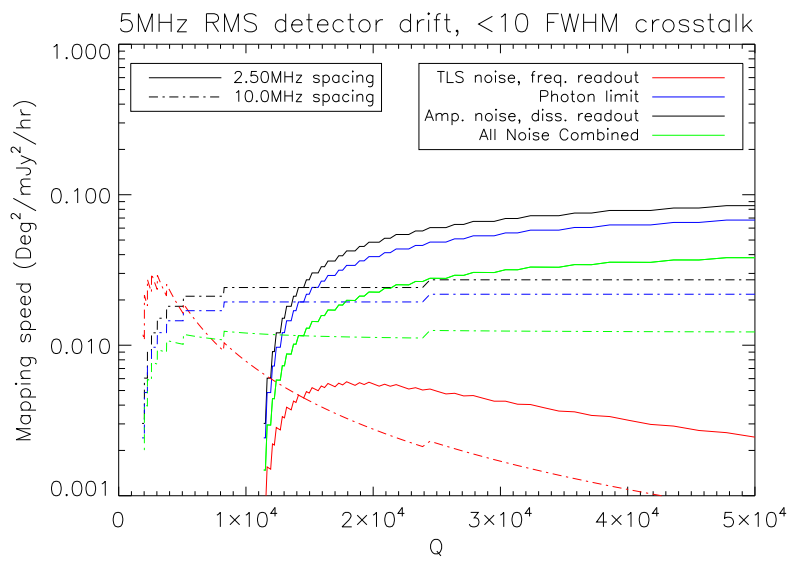


Figure 3.3: The mapping speed for different detector spacings as a function of  $Q$ . Plotted are the three cases for NEP: frequency readout in the TLS noise limit (red), dissipation readout in the 5 K HEMT noise limit (black), and the total response in the photon noise limit (blue). The mapping speed combining all noise sources and all responsivities is given in green.

are taken from finite grids of  $Q$ , over which only a reasonable range was tested. Note, again, this assumes that all  $1/f$  noise due to the amplifier can be completely removed; if this is not true, then the NEPs will be increased in the dissipation direction, and this may change the optimization.

### 3.5 Other effects on sensitivity

In the above sections, we have assumed optimal conditions under which the resonators operate. This includes optimized readout power, optimal coupling, and uniform absorption of submillimeter light. Here, we look at the assumptions in these optimizations, and find what effect these have on optimizations above.

#### 3.5.1 Critical coupling

If  $Q_i$  is fixed, as by loading, we want to make  $Q_c$  which matches it. For a  $Q_i$  determined by optimal responsivity, this will guarantee the largest phase shift per unit power absorbed by the detector. This can be seen in Equation 2.4 – for a fixed  $Q_i$ , the factor  $Q^2/Q_c$  is largest when  $Q_i = Q_c$ , leading to the largest response. This is easier to see when one rewrites this factor as  $\frac{Q_i^2}{Q_i + Q_i^2/Q_c}$ .

In the cases of substrate noise and HEMT noise, both depend on critical coupling where  $Q_i = Q_c$ , but the dependence arises from different causes. In the phase noise case, the only way the term enters is due to the internal power dependence upon  $Q$ . This is a square root dependence, so it depends weakly on coupling. The HEMT noise limit depends more strongly on coupling, because the noise enters in after the resonator change has been converted into a change in the probe signal. Thus, the responsivity will go down exactly as  $Q^2/Q_c$  decreases. In neither case is it absolutely necessary to have optimal coupling. For example, a factor of 2 error in the coupling  $Q$  will lead to a 20% reduction in sensitivity in the HEMT noise case, while in the phase noise limit the error will be half that. For an internal  $Q$  fixed by the total NEP, we will suffer this error if the coupling  $Q$  is not matched properly. However, the effect is very shallow, particularly for the substrate noise limited case.

Table 3.1: A list of the best  $Q$ s to shoot for in Band 1 (240 GHz) , overlap condition of 1% to be considered to not have collided. The multiple appearances of several values are due to the finite grid of  $Q$ 's considered hitting their limits; it would be impractical to design  $Q$ s outside this range.

Spacing (MHz)	RMS (MHz)	$\eta_{\mu w}$	Q	Q range	Lab Resp (kHz/K)	MS $\frac{arcmin^2}{mJy^2hr}$	$N_{res}$ in Band 1
2.5	1.0	1	21807	8799-125388	0.62	18.6	29
5	1.0	1	5936	3981-59006	2.29	19.4	16
10	1.0	1	2377	1907-7898	5.73	18.3	9
2.5	1.0	0.05	100310	10671-125388	0.13	109	35
5	1.0	0.05	9119	4197-125388	1.49	59.5	18
10	1.0	0.05	2377	1907-125388	5.73	34.3	9
2.5	3.0	1	111456	15199-125388	0.12	17.2	33
5	3.0	1	9932	4754-125388	1.37	10.7	12
10	3.0	1	3068	1959-16718	4.44	12.5	7
2.5	3.0	0.05	111456	18926-125388	0.12	103	33
5	3.0	0.05	125388	6918-125388	0.10	56.0	18
10	3.0	0.05	7961	2121-125388	1.71	30.1	9
2.5	5.0	1	125388	17295-125388	0.10	17.1	33
5	5.0	1	15199	5798-125388	0.89	9.4	13
10	5.0	1	3771	2259-66874	3.61	9.6	6
2.5	5.0	0.05	125388	20898-125388	0.10	103	33
5	5.0	0.05	55728	7961-125388	0.24	53.0	17
10	5.0	0.05	24466	2579-125388	0.55	28.5	9
2.5	9.0	1	125388	17598-125388	0.10	17.1	33
5	9.0	1	26397	6389-125388	0.51	9.1	15
10	9.0	1	5252	2477-125388	2.59	7.9	6
2.5	9.0	0.05	125388	21343-125388	0.10	103	33
5	9.0	0.05	62694	9739-125388	0.21	53.0	17
10	9.0	0.05	37152	3355-125388	0.36	28.3	9

Table 3.2: A list of the optimal  $Q$  values in Band 1 (240 GHz), overlap condition of 10%. The multiple appearances of several values are due to the finite grid of  $Q$ 's considered hitting their limits; it would be impractical to design  $Q$ s outside this range.

Spacing (MHz)	RMS (MHz)	$\eta_{\mu w}$	Q	Q range	Lab Resp (kHz/K)	MS $\frac{\text{arcmin}^2}{\text{mJy}^2 \text{hr}}$	$N_{res}$ per band
2.5	1.0	1	4666	2565-125388	2.92	35.2	25
5	1.0	1	2031	1419-7776	6.71	36.8	17
10	1.0	1	1419	1419-5866	9.60	22.0	9
2.5	1.0	0.05	91191	3096-125388	0.14	112	36
5	1.0	0.05	2741	1419-125388	4.97	67.0	18
10	1.0	0.05	1419	1419-125388	9.60	36.0	9
2.5	3.0	1	8222	3888-125388	1.65	22.8	23
5	3.0	1	2968	1513-21343	4.59	21.9	12
10	3.0	1	1419	1419-7064	9.60	19.5	8
2.5	3.0	0.05	77162	5393-125388	0.17	109	35
5	3.0	0.05	38581	1893-125388	0.35	56.5	18
10	3.0	0.05	2377	1419-125388	5.73	34.3	9
2.5	5.0	1	9645	4233-125388	1.41	21.7	24
5	5.0	1	3843	1861-77162	3.54	19.0	12
10	5.0	1	1527	1419-9203	8.92	16.7	7
2.5	5.0	0.05	83592	5901-125388	0.16	109	35
5	5.0	0.05	50155	2383-125388	0.27	56.0	18
10	5.0	0.05	2477	1419-125388	5.50	30.3	8
2.5	9.0	1	9834	4305-125388	1.38	21.5	24
5	9.0	1	4269	2051-125388	3.19	17.8	12
10	9.0	1	2200	1419-11664	6.19	14.7	7
2.5	9.0	0.05	83592	5971-125388	0.16	109	35
5	9.0	0.05	55728	2640-125388	0.24	56.0	18
10	9.0	0.05	11023	1419-125388	1.23	29.4	9

### 3.5.2 Non-uniform power absorption

Up to this point, we have considered the case in which the submillimeter power is distributed evenly in the resonator's volume. However, for an antenna-couple MKID, this is very unlikely to be the case. A non-uniform distribution of power absorption would decrease the responsivity, as larger power in some sections would lead to fewer quasiparticles per unit power. It is beneficial to see how the responsivity would be reduced.

Let us consider the absorptive section of the resonator as a sum of infinitesimal lengths  $(z, z + dz)$  in which  $P(z)$  is absorbed and turned into  $n_{qp}(z)$ . Here, as in the actual resonator, the distribution is uneven along the long axis of the resonator volume, as this is much longer than the electron mean free path. In such a case, the responsivity for each “bin” goes down as  $P^{-1/2}$ , as it does for the entire resonator under the assumption of uniform absorption and high quasiparticle density (as in Equation 3.6). The resonant frequency, if the current is uniformly distributed throughout the resonator (which is nearly true in the case of quarter-wave resonators), does not care where the quasiparticles are created, just that they are there. Then the only term that matters is the one describing the quasiparticle creation rate with respect to power.

In an antenna-coupled MKID camera, we have the specific case in which an antenna dumps power from a feed microstrip along the length of a resonator. If the absorption is purely due to resistive loss in the resonator, or by the breaking of Cooper pairs, we would expect an exponential profile of how the power is dissipated into the resonator. If we consider the simplified power profile to be  $P = A \exp(-z/z_0)$ , then the quasiparticles created go as  $n \sim \frac{1}{\sqrt{A} \exp(-z/2z_0)}$ . If we vary the submillimeter power level, but keep the power profile the same (as it should only depend on such things as resistivity and diffusion constants), then this should give the same scaling for different powers. Then, all we need is an overall fudge factor giving the amount by which the responsivity is reduced compared to the uniform absorption case, i.e. the ratio between the average quasiparticle density in the exponential and uniform case. For example, for a value of  $z_0 = 0.1$  mm in a 1 mm long absorber strip, the response decreases by a factor of about 0.6. The optimal NEP found for

any simulation should be divided by this number. We can think of this in the same way we have “effective” kinetic inductance fractions for hybrid resonators, as in both cases the effective factor arises from not using the full length of the resonator. However, this factor cannot be determined from dark temperature sweeps, but must be inferred from optical data. Note that, given that Section 3.4 comes from extrapolations from real data, this has already been accounted-for in the optimizations shown in that section. This factor will bias any value of optical efficiency, giving an artificially low value.

### 3.5.3 Excess power driving: “distortion” and “saturation” of MKIDs

In Section 3.4, the optimizations are done assuming the optimal readout power level is used, calculated to maximize the signal-to-noise ratio given an assumed efficiency. However, it is also possible that this is not the dominant effect on the responsivity. Although large amounts of readout power below the gap energy are known to create quasiparticles, this effect becomes smaller as the drive frequency decreases relative to  $\Delta/h$ . Thus, it is possible that the dominant effect we see is not from quasiparticle creation, but from quasiparticle *heating* of the steady-state population. While microwave power can create quasiparticles, a 3 GHz signal could be much more likely to slightly excite free electrons than to create quasiparticles when the gap is  $\sim 30$  times as large. There is no definitive experimental evidence, but power at higher frequency may be more efficient at creating quasiparticles [111]. In fact, the effect of high powers on the energy distribution of quasiparticles is highly complicated, but we consider the analogy of raising the quasiparticle temperature which has a similar result. As the steady-state quasiparticle population increases in energy, we expect the resistance to decrease, and thus the  $Q$  to increase. This can be seen from the Mattis-Bardeen equations, but it is also an intuitive effect on the real conductance. As free electrons which cause the resistance are heated, they go well over the Fermi energy, and thus the occupation of any energy state is lowered. With fewer fermions occupying each energy, the resistance is lowered. Unfortunately, this should also decrease the dissipation response, as any additional quasiparticle added will not create as much resistance as before. The dominant noise in the dissipation direction

comes from the amplifier, it is still possible to increase the signal-to-noise ratio by going to higher readout powers.

The effect of an increase in temperature on the frequency, or on the imaginary conductivity, is less intuitive. However, the Mattis-Bardeen equations can effectively guide us here, where we do not have a good physical picture.<sup>4</sup> In Figure 3.4 the effect of temperature on the response of real and imaginary components to a change in quasiparticle density is plotted. The real responsivity drops significantly, as we would expect from lowered resistance due to high temperature. The imaginary component also decreases at high temperatures, but much more slowly. This is consistent with what is seen in Figure 2.3.

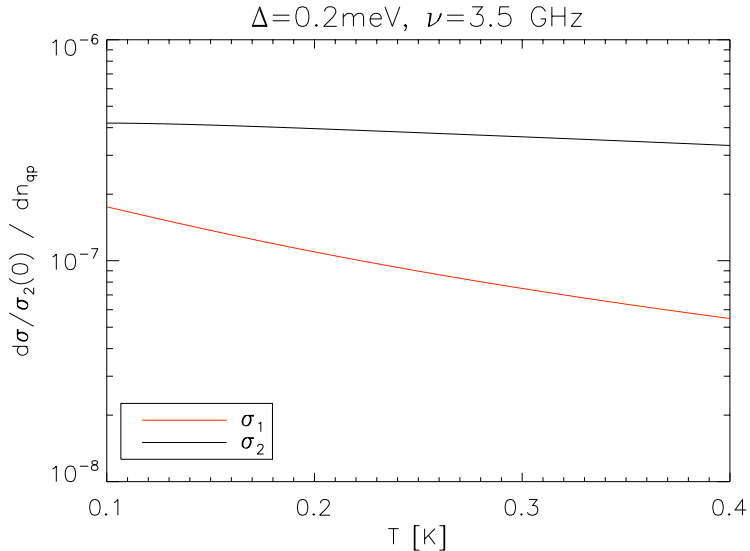


Figure 3.4: The fractional change in complex conductivity with respect to quasiparticle density as a function of temperature, assuming no optical load.

Driving resonators into the distorted regime, however, can put the resonator into a nonlinear regime, which shifts the point of maximum response away from the low power resonance. The linearity of the response is unproven, but for small enough signals this should not be an issue - effectively any response is linear at the level of a small astronomical signal. The primary concern

<sup>4</sup> As Fermi said to Dyson: “One way [to do calculations], and this is the way I prefer, is to have a clear physical picture of the process that you are calculating. The other way is to have a precise and self-consistent mathematical formalism.” [32] This, of course, was followed by the statement, “You have neither.”

at very high powers is the driving of resonators into saturation - the point at which there are discontinuities, or a bifurcation, in the resonance loop [116]. In this regime, the resonance point is effectively cut off as the loop becomes double-valued at some frequency points. While this saturation would be useful for an effective digital amplifier [113], the fact that it cuts off the resonance point most sensitive to changes in loading limits its utility for submillimeter detectors.

In summary, using a large amount of power compared to the submillimeter loading has several effects which can both help and harm the use of MKIDs as detectors. The heating of quasiparticles, and the low-level creation of new quasiparticles, limits the sensitivity, particularly the resistive responsivity. However, driving into distortion can amplify the signal, and increased power suppresses the effects of two-level systems and decreases the relative effect of HEMT noise. How these effects work out empirically is explored in subsequent chapters.

## **Chapter 4**

### **DemoCam design and laboratory testing**

Here we discuss the design, assembly, and testing of the DemoCam and its detector arrays in the first iteration of MKIDs for submillimeter astronomy. The main goal of this chapter is to explain our understanding of optical responsivity in these antenna-coupled MKID devices, and to explain the tests that have been done to understand their responsivity characteristics. This is done by examining individual detectors in detailed analysis, and by finding the properties of resonators relative to each other. We include the effects of optics modifications on our tests, and examine the effect of such physical alterations.

This chapter covers testing from March 2007 to January 2009. The cryostat assembly, however, began in September 2006. The initial months of testing were spent diagnosing cryogenic difficulties and redesigning the optical layout. Dedicated testing of the final optical design began in March 2007.

#### **4.1 Dewar Assembly**

##### **4.1.1 Device Layout**

Early MKID testing in 2006 had determined the efficacy of the antennas and bandpass filters [59]. In the DemoCam, second generation designs were used to produce a uniform tile while eliminating effects of pair braking by sub/millimeter photons in an aluminum groundplane. Three separate devices were tested in the DemoCam instrument, with the dates of testing shown in Table 4.1. The first device involved hybrid aluminum/nobium CPW resonators on a silicon substrate.

Table 4.1: Devices tested, and dates of testing, in the original DemoCam configuration. Here are given the dates of the testing of the different devices, as well as notes on the changes in configuration. Device 3 was dark-tested in a dilution refrigerator, courtesy of Peter Day.

Device	Testing type	Start Date	Notes
1: Silicon	Light	Mar. 2007	Metglas™ magnetic shielding added
1: Silicon	Light	Nov. 2007	In-depth, post-run testing
1: Silicon	Dark	Apr. 2008	
2: Sapphire	Dark	May 2008	
2: Sapphire	Light	Sep. 2008	Telescope configuration
2: Sapphire	Light	Nov. 2008	Wide-window configuration
3: 30 nm Al on Si	Dark	Dec. 2008	Not tested in DemoCam
3: 30 nm Al on Si	Light	Jan. 2009	Wide-window configuration

This device was used for telescope observations. This design consisted of 3 mm × 3 mm square antennas, consisting of 16 slotlines, each with 16 RF shorts. A feed network of Nb/SiO<sub>2</sub>/Nb microstrips combined the signals, and delivered the optical signal to the dissipative resonator. The antenna network and the overall layout can be seen in Figure 4.1. In Figure 4.1b, the blue sections represent niobium ground plane, while red represents aluminum, gray represents microstrip wiring, and white represents gaps in the ground plane. The aluminum part of the resonator is 60 nm thick before etching, and the exact thickness after etching is unknown. The resonator is a 6 μm wide center strip with 2 μm wide gaps; 1 mm of the length is the aluminum absorber, and the rest is niobium (approximately 3 mm). The coupler length was designed for  $Q_c=15,000$ .

The resonators were designed for two bands on each pixel - one centered at 240 GHz with a width of nearly 70 GHz (Band 1) and one centered on 350 GHz with a width of approximately 30 GHz (Band 3). Each antenna fed these two colors, giving 32 total resonators. The design frequency spacing was 10 MHz, to ensure a relative small number of collisions. However, the frequency spacing was not uniformly increasing across the array. In order to have the option of reading out all same-color detectors or multiple colors in a 50 MHz window, the resonators were spaced in a nonsequential manner, such that adjacent resonators in frequency were not necessarily nearby in physical location [59].

Beyond the silicon substrate device (Device 1 or “Silicon Device”) used for first light at the

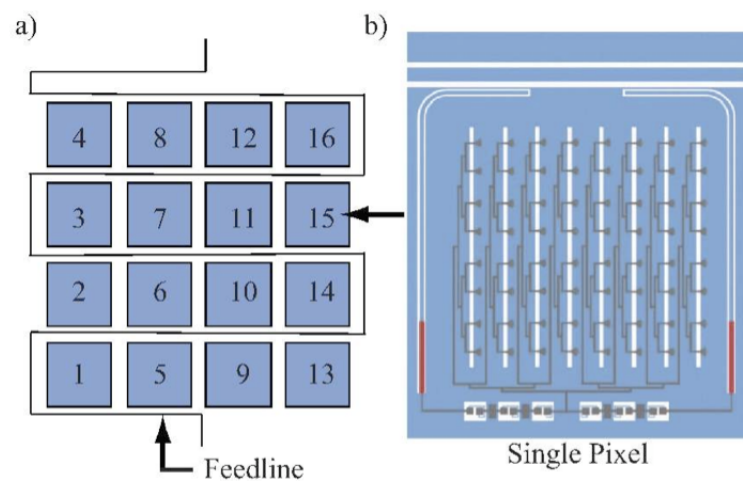


Figure 4.1: a) The layout of the antennas on the focal plane, a  $4 \times 4$  pattern with a meandered feedline. b) a view of an antenna coupled to two different-colored resonators. From [59]

telescope, several other iterations were made on the same design. The first iteration (Device 2 or “Sapphire Device”), used sapphire as the substrate, which had been demonstrated on past devices to have less phase noise than a silicon substrate. The second iteration (Device 3 or “Thin Al Device”) involved using 30 nm-thick aluminum (before etching) in order to measure the change in absorption efficiency and responsivity. The tests run on these devices are the same as those described above; thus, only the results are presented.

#### 4.1.2 Cryostat Assembly

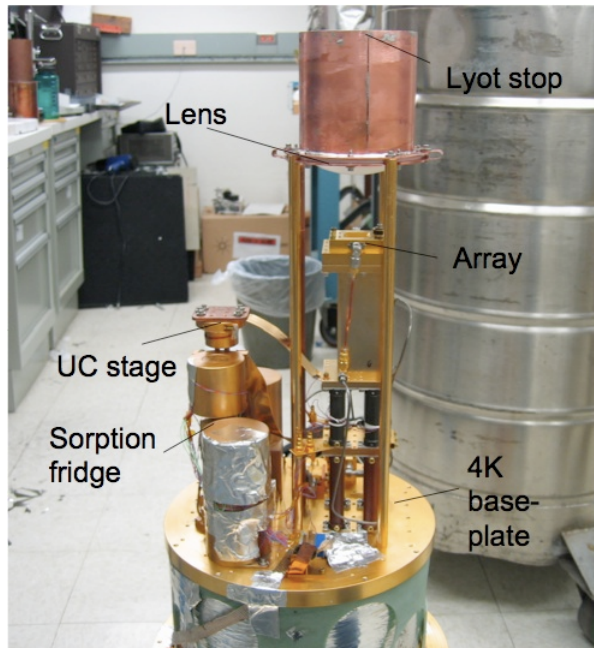


Figure 4.2: The DemoCam cryostat in its first iteration.

The cryostat used for the DemoCam is adapted from a spare Dewar used in the Kuiper Airborne Observatory. This cryostat was originally designed to use 5 liters of LN<sub>2</sub> and 5 liters of LHe to cool a receiver to 4.2 K in flight. The cryostat needed to be adapted to have a cold stage at <250 mK, and enough length to contain the cold optics used in the Bolocam system. To this end, a three-stage Helium sorption fridge made by Simon Chase [11] was added, and was found to cool the ultracold (UC) stage to approximately 215 mK under no optical load. To accommodate the new



Figure 4.3: The DemoCam cryostat, including coax inputs and internal Metglas™ magnetic shielding.

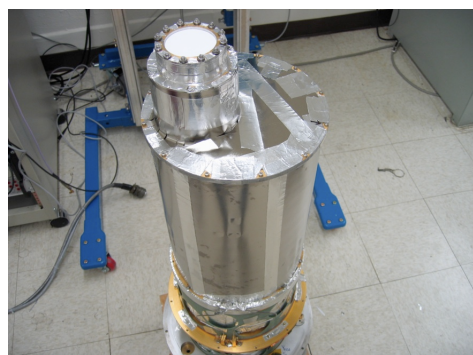


Figure 4.4: The DemoCam with the 4K shield, including snout and Metglas™ magnetic shielding.

cooling system and optics, the height of the cold stage (between the baseplate and top radiation shield) was extended from 4 to 14 inches, and additional height was added for the optics and filter stack. The optical system used consisted of a single Teflon lens, used to focus light onto the array for the appropriate coupling to the antenna beams. A Lyot stop several inches beyond the lens was used at the location at which all the beams uniformly sample the space.<sup>1</sup> The Lyot stop at this location truncates the beams to avoid beam spilling at the telescope beyond the primary dish; a diameter of 1.8 inches was chosen to duplicate Bolocam's illumination pattern. The optics represent a very small  $f/\#$ , approximately 1.5, to ensure good transmission through the Lyot stop, and relatively high responsivity. This gives us a relatively large platescale in astronomical observations compared with Bolocam.

Generous filtering was used to ensure a cold base temperature of the device using only dielectric filters. The vacuum window was made of Zote foam, which has good transmission below 400 GHz [46]. The 77 K filter consisted of 1 inch of Teflon PTFE to block large amounts of infrared radiation. The 4 K filter consisted of 0.5 inch thick blocks of Teflon sandwiching a 1.6 mm-thick piece of Fluorogold. The outside of all Teflon filters were also AR-coated with Zitex G108, which has a thickness and index of refraction nearly optimized for 300 GHz transmission. Finally, the lens was made of Teflon to provide extra out-of-band attenuation, and for ease of AR-coating.

These filters are shown to effectively filter near- and far-infrared radiation. Benford *et al.* [9] found the attenuation constant to go as  $6 \nu^4 \text{ cm}^{-1}$ . The Fluorogold is a strong blocker of radiation at  $\sim 1 \text{ THz}$  [8], and significantly reduces radiation which may create quasiparticles in niobium ( $2\Delta \sim 700 \text{ GHz}$ ).

The assembly changed several times in attempts to reduce excess loading and increase throughput. These optics are shown in Figures 4.5 and 4.6. If the windows in an optical configuration are too narrow, there may be significant coupling from the antenna beam to these surfaces,

---

<sup>1</sup> This is the location at which a time reverse ray of light at a given angle coming off the focal plane, from any physical point on the array, will converge to the same place. The fact that there is such a place ensures that all the beams at a given wavelength have the same profile at the aperture, and the amount of each beam truncated is uniform from detector to detector

creating a significant excess load. The changes involved widening the 4 K window from 2 to 2.5 inches, the 77 K window from 2.5 to 3.25 inches, and the vacuum window from 3 to 4.75 inches in diameter, while holding the diameter of the cold Lyot stop constant. The replacement of the vacuum window may have also helped increase the efficiency, as it is possible that Zote foam loses efficiency over time by the slow absorption of water when used as a vacuum seal. The results of this window change, which was investigated only in the lab, are discussed below.

## 4.2 MKID device testing

### 4.2.1 Resonator fitting routine

The extraction of fundamental MKID parameters depends upon fitting the resonance - the  $S_{21}$  as a function of frequency around the resonance frequency. This fitting directly finds several parameters -  $f_0$ ,  $Q$ , and  $Q_c$  – required for determining responsivity (both directly and indirectly, without knowing the total optical efficiency), excess loading, and frequency-to-dissipation response ratio. This technique is necessary for finding the quasiparticle density with and without optical load, and the frequency shift per quasiparticle created.

To get all this information, we must fit the resonances under a variety of conditions, which requires a robust fitting routine. There are generally two fitting approaches: fitting the resonance loop of complex  $S_{21}$  data with frequency, or fitting  $|S_{21}|$ . It is not clear that one method is significantly better than another, but the results are similar [86]. The former routine involves making use of all the available data, but the latter involves fitting to fewer parameters. In this thesis, we use the latter approach.

One last obstacle involves the background transmission (i.e. transmission in the absence of a resonance) level. One method of dealing with this is to measure the transmission at high temperature (typically 1 K or so for aluminum resonators), at which point the resonators have become so lossy as to have disappeared. This provides information on the background transmission, allowing one to account for the variable transmission over the frequencies around the resonator.

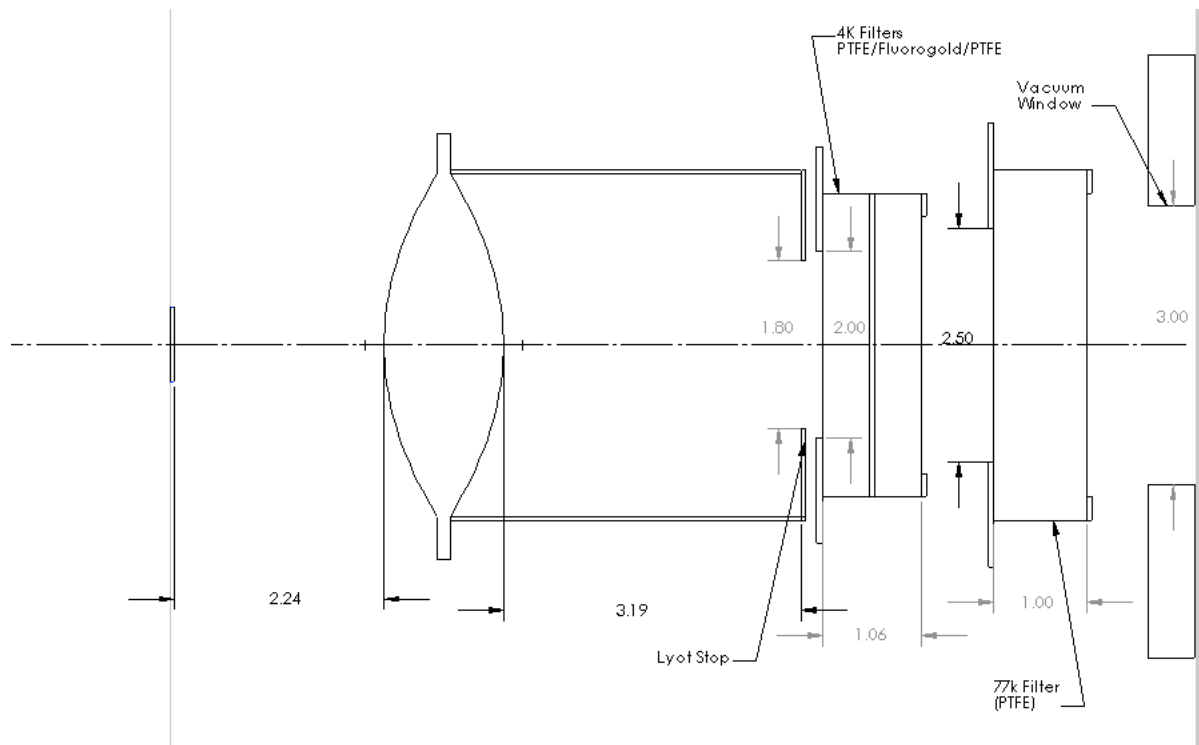


Figure 4.5: The DemoCam optical train in the configuration taken to the telescope. Dimensions are in inches

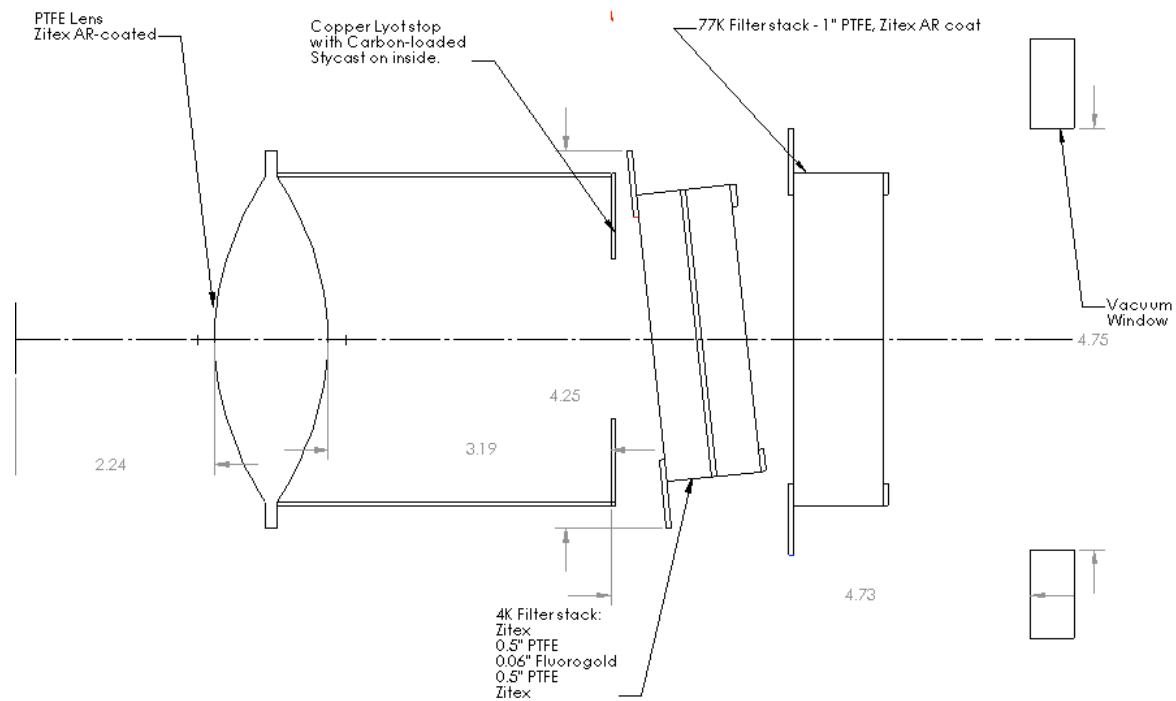


Figure 4.6: The DemoCam optical train in the configuration with wider windows intended to reduce excess loading, and one filter tilted to reduce standing waves in the optics. Note that focusing optics and Lyot stop are unchanged.

However, this data is not always available, and the technique is not always necessary. In general, the background level changes slowly enough to be easily accounted-for with a background term in the resonator fit. We fit the transmission to the equation

$$|S_{21}| = \sqrt{a_1 + b_1 dx} \left| \frac{Q}{2Q_c} \left( 1 - \frac{2}{1 + 2iQdx} \right) e^{i\phi} + 1 - \frac{Q}{2Q_c} \right| \quad (4.1)$$

where  $dx = df/f$ . This is an extension of Equation 2.3 including three effects: the background transmission; the rotation angle of the resonance loop  $\phi$ , which causes the distortion from a true Lorentzian; and put in terms of the  $Q/Q_c$  ratio, which determines the depth of the resonance. These effects and an alternate fitting routine are described in greater detail in Appendix E of Ref. [36]. In the limit of  $\phi = 0$  and unity background transmission, this reduces to Equation 2.3. Knowing  $Q$  and  $Q_c$  from the fit, one can calculate  $Q_i$ , and find its variation. This fitting routine works best on well-calibrated instruments. Therefore, most sweeps were taken with an HP 8722ES Vector Network Analyzer.

An example of a fit is given in Figure 4.7, and the residual as a fraction of the average background transmission is seen in Figure 4.8. The residuals generally show no systematic effects, and leave residual scatter at low levels of a few percent to fractions of a percent, depending upon the readout power used.

#### 4.2.2 Measurement of fundamental MKID parameters - Dark Testing

As discussed in Section 2.1, there are three fundamental parameters for the understanding of MKID response: the kinetic inductance fraction,  $\alpha$ , which determines the frequency shift per quasiparticle; the gap parameter,  $\Delta_0$ , which determines the number of quasiparticles created; and the quasiparticle recombination constant,  $R$ , which determines the quasiparticle lifetime. As shown in Chapter 3, the only other fundamental parameters which contribute to responsivity are the single-spin density of states ( $N_0$ ), volume and the resonant frequency (which simply determines the ratio of frequency-to-dissipation response). The latter two parameters are effectively controlled in design, and the density of states is a measured parameter. For aluminum, the value of  $N_0$  is

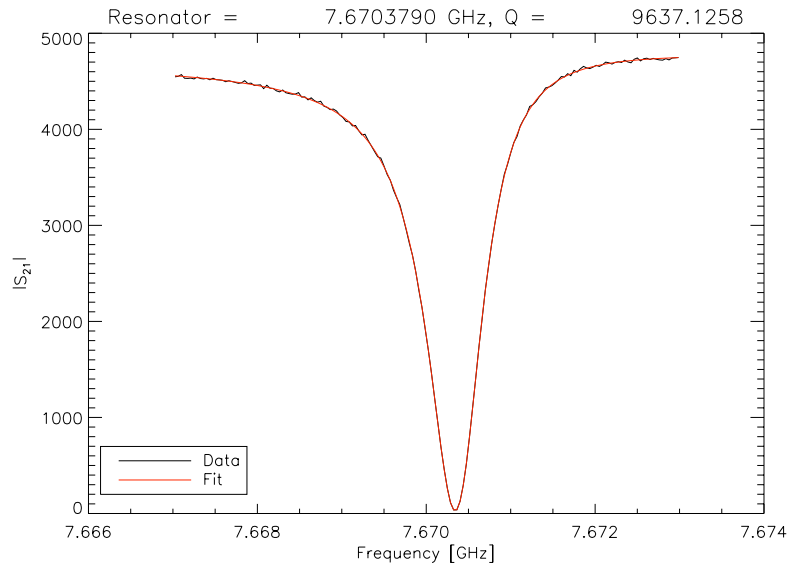


Figure 4.7: The fit of a resonator to the resonance curve.

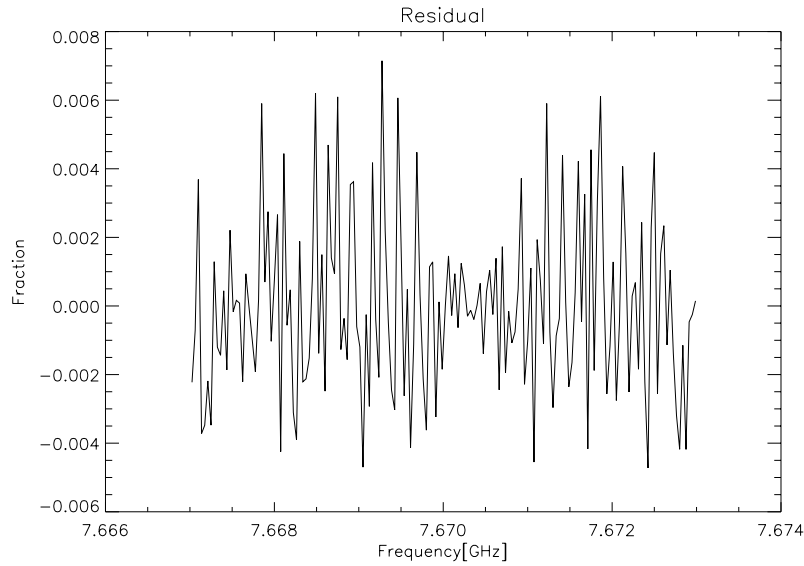


Figure 4.8: The residual of the resonance fit. The residual noise generally shows no structure, and has an RMS determined by the input power. The noise-to-carrier ratio is higher on-resonance (worse signal-to-noise ratio), but is lower here because the transmission is smaller on-resonance.

variously reported as 1.2 and  $1.72 \times 10^{10} \text{ eV}^{-1} \mu\text{m}^{-3}$  [35, 76, 36, 77]. Throughout this thesis we assume a value of  $1.72 \times 10^{10} \text{ eV}^{-1} \mu\text{m}^{-3}$ .

#### 4.2.2.1 Temperature sweeps - measuring $\alpha$ and $\Delta_0$

The fitting of  $\alpha$  and  $\Delta_0$  can be done simultaneously, and can yield confidence intervals on both parameters. The method relies on finding from Equations 2.16 and 2.11 the expected frequency shift as a function of temperature under no optical load. We generate a grid of  $\alpha$  and  $\Delta_0$  in order to find which parameters fit the observed data best. We then perform a  $\chi^2$  test to find the best-fit parameters, and extract the uncertainty in these parameters. The frequency uncertainty is known from the resonance fitting routine above. In addition, we take into account the temperature uncertainty in the GRT sensor of  $\pm 0.5 \text{ mK}$  [61] for each  $\alpha/\Delta_0$  combination.<sup>2</sup> Based on these values, the temperature errors will translate into different frequency errors. Thus, for different grid points, the same data necessarily has different error bars.

A serious problem arises in that the temperature data typically only goes as low as 220 mK, which is significantly shifted from the  $T = 0$  resonance frequency. Dilution fridges are capable of going to lower temperatures, but below about 200 mK (or approximately 1/6th of the transition temperature) the frequency shift due to two-level systems becomes significant [58], restricting our ability to find the true resonance frequency at zero temperature in the absence of such effects. Therefore,  $f_0$  is treated as a free parameter in the fits, and is allowed to vary. With the error bars calculated for an  $\alpha/\Delta_0$  combination, we fit out the most likely  $f_0$  which minimizes the mean-square residual for that combination. This process is the only method to ensure an optimal fit to the data.

Once the data are fit, a grid of  $\chi^2$  values is generated. These fits depend heavily on the device as to their accuracy, as some datasets do not match the theoretical predictions as well as others. The hybrid resonator devices typically give radically different answers depending on whether temperature errors are taken into account, as the high temperature data is given much less weight

---

<sup>2</sup> This value likely overestimates the error, as it causes the  $\chi^2$  per degree of freedom to be significantly lower than unity. For  $\chi^2$  confidence regions, these values are retained because the error is still significantly smaller than the resonator-to-resonator scatter.

in this case. It is possible that the low temperature data corrupt the fit through a non-negligible two-level system contribution. This is consistent with the effect being much more pronounced in the device with a silicon substrate, as such devices have been measured to have greater TLS effects than devices with a sapphire substrate [36].

To deal with this effect, there are two options: to simultaneously fit to a TLS model for frequency shift versus temperature, or to exclude the low temperature data from a fit. The former involves much more difficult fitting procedures, with several additional parameters, and the lack of data at very low temperature is a large obstacle. Thus, this method is not preferred. The latter approach requires good fits to the high-temperature data ( $\chi^2/\nu \simeq 1$ ), and results that show the parameters returned are not affected by the cutoff. To this end, we can use results from the sapphire device with various cutoff temperatures, and see where the measured parameters become noticeably affected. This is plotted in Figure 4.9. It is clear that the measured parameters do not significantly vary up to 300 mK for any resonator. It should hold for other devices, as well, that including data only down to this temperature level will not bias the results in any significant manner.

Examples of optimal fits for the silicon and sapphire device, respectively, are seen in Figures 4.10 and 4.12, and the residuals normalized to each point's standard deviation error are seen in 4.11 and 4.13. The silicon device data has been fit to only data above 280 mK, as the lower temperature points are likely corrupted by TLS effects. The large divergence can be seen in the residuals at low temperature in Figure 4.11. If points below that temperature are included, the fit becomes much worse and gives unphysical results for the gap parameter. This fit is seen in Figure 4.14, and the residual in Figure 4.15.

From the  $\chi^2$  contours, we can find the marginal  $1\sigma$  errors for each parameter by taking the extrema of the  $\Delta\chi^2 = 1$  contour. Plotted in Figures 4.16 and 4.17 are the  $\Delta\chi^2=2.7$ , 6.17 and 11.3 contours, which enclose 68, 95 and 99% of the likelihood, respectively, for the two parameters fit. The high degeneracy between  $\alpha$  and  $\Delta_0$  is clearly seen in the graph. However, the likelihood of the values gives a reasonable estimate of both parameters. The contours put error bars on  $\alpha$

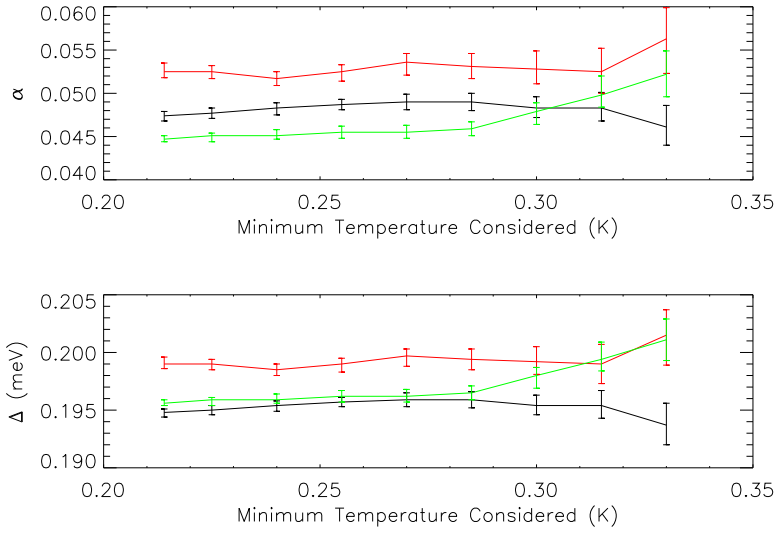


Figure 4.9: Best-fit values as a function of minimum temperature considered. The top plot shows the kinetic inductance fraction and the bottom the gap parameter. Error bars given correspond to temperature errors of 0.15 mK ( $1\sigma$ ), lower than the referenced values, but found to give  $\chi^2/\nu \simeq 1$ . Different colors correspond to three fitted resonators, at 7.026 GHz, and 7.103 GHz, and 7.112 GHz.

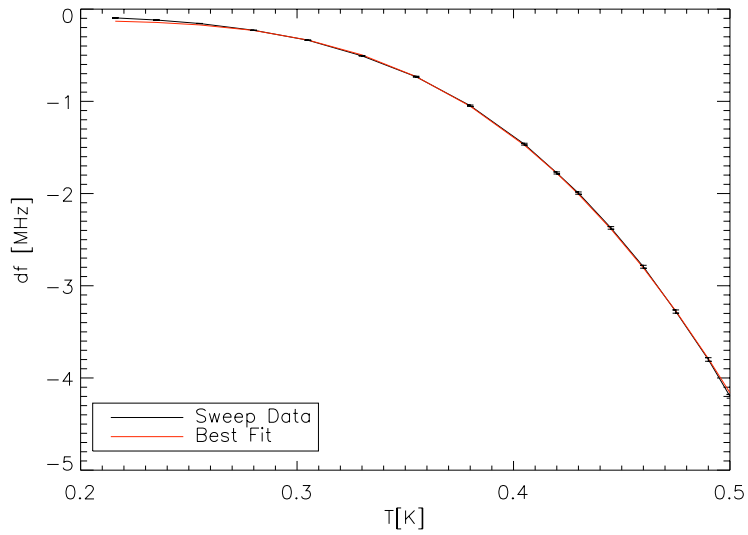


Figure 4.10: A fit to all temperature sweep data above  $T = 280$  mK for a silicon device (Device 1) resonator. The residual is much smaller for the high temperature data, and is shown in Figure 4.11.

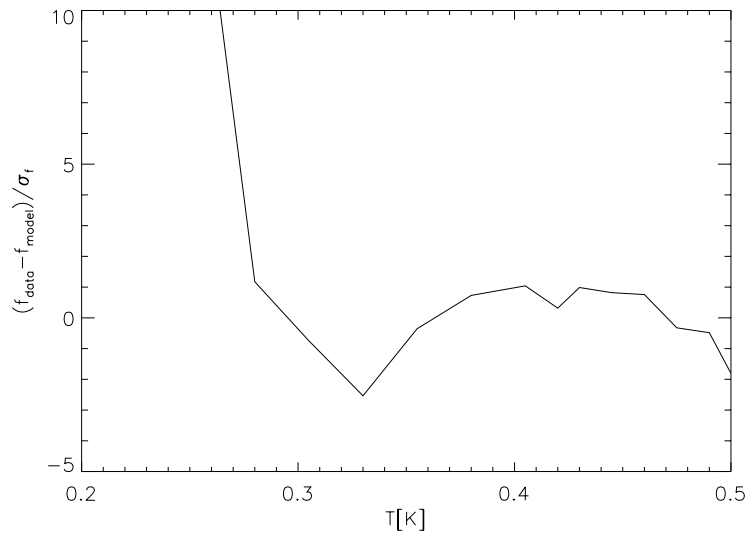


Figure 4.11: The residual of the fit in Figure 4.10, divided by the error at each point. Note the divergence at low temperatures not included in the fit due to TLS effects.

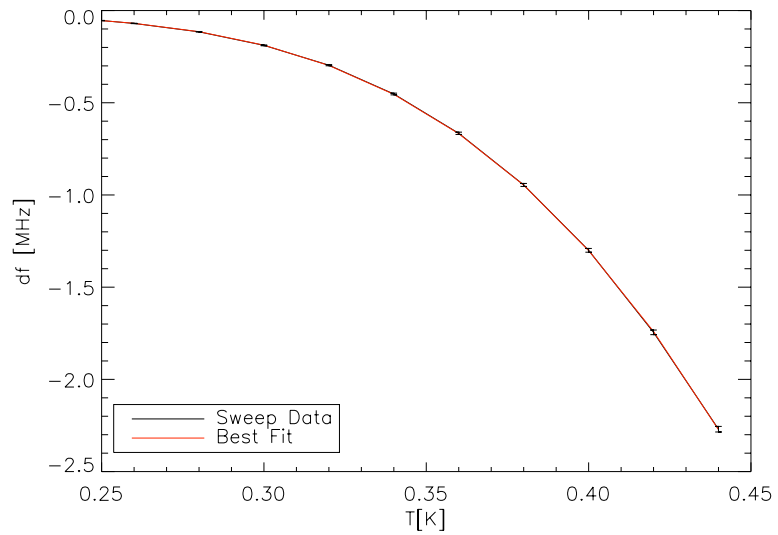


Figure 4.12: A fit to all temperature sweep data above 250 mK in a sapphire device (Device 2) resonator.

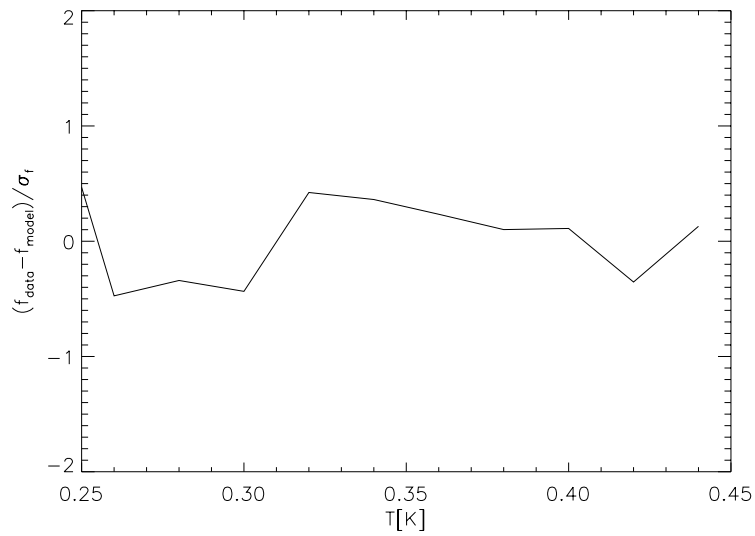


Figure 4.13: The residual of the fit in Figure 4.12, divided by the error at each point.

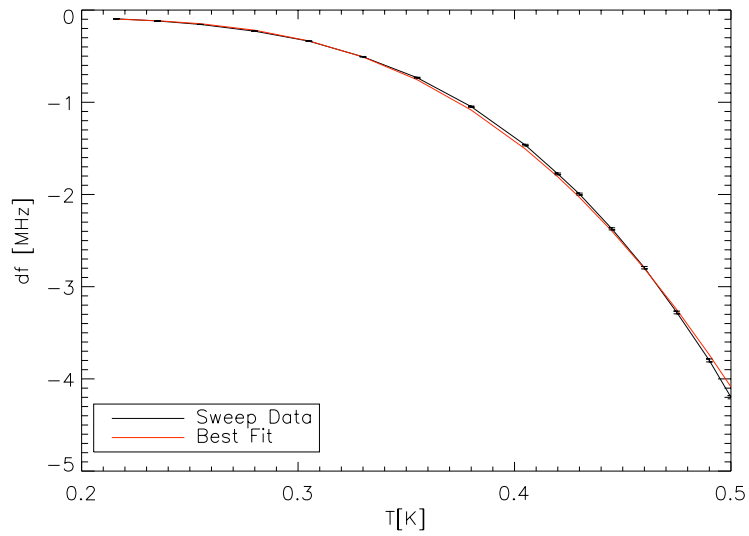


Figure 4.14: A fit to all the temperature sweep data, including low temperatures, from a resonator on the silicon DemoCam device (Device 1) at 7.624 GHz.

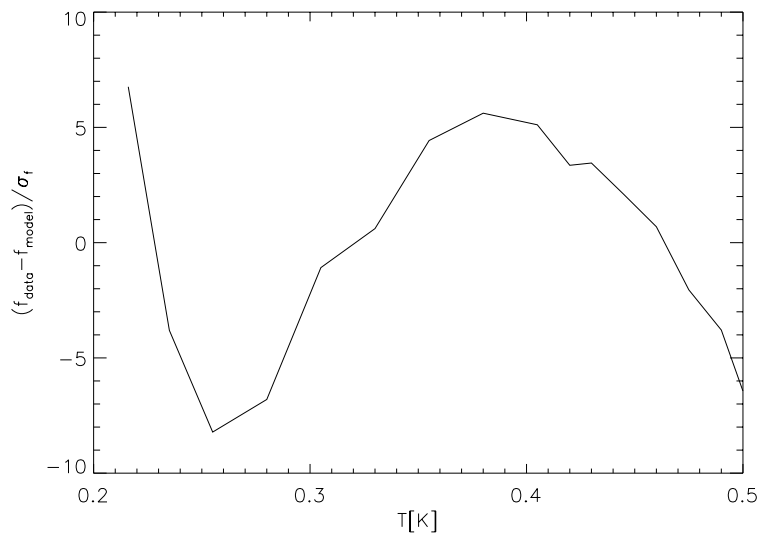


Figure 4.15: The residual of the fit to all data of the silicon device (Device 1) resonator at 7.624 GHz. There is a clear structural correlation with  $T$  due to the systematic effects of TLSs at low temperature.

of a few percent, easily good enough to use in finding optical properties. The figures show the results of several of these fits to resonators on the same device. These display the high degeneracy between  $\alpha$  and  $\Delta_0$ , but do not have overlapping confidence regions. This is most likely due to aluminum thickness variations across the array, which can cause significant variations in both parameters. Though the real scatter among resonators is larger than the confidence regions for a single resonator, the scatter in the fitted parameters is at the level of only a few percent, shown in Table 4.2.

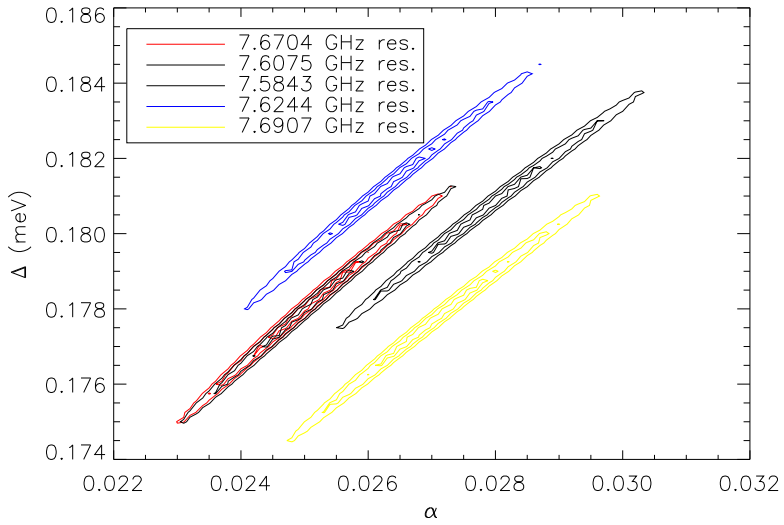


Figure 4.16: Confidence regions for  $\alpha$  and  $\Delta_0$  from  $T \geq 280$  mK data in the silicon device (Device 1) for several resonators at different resonance frequencies. The frequency of each resonator is given in GHz in the legend. Lack of overlap is likely due to thickness variations across the array.

It should be noted that this method cannot determine the absolute kinetic inductance fraction for a length of aluminum CPW. It instead determines an effective  $\alpha$ , which basically accounts for the fraction of the current actually seen in the aluminum detector length. However, this is the value we want in fitting out the optical properties of the camera. Table 4.2 gives the values used to determine optical efficiency. In a later device, all-aluminum  $\alpha$  test devices were used as a check on this method. Their agreement is discussed in Chapter 6.

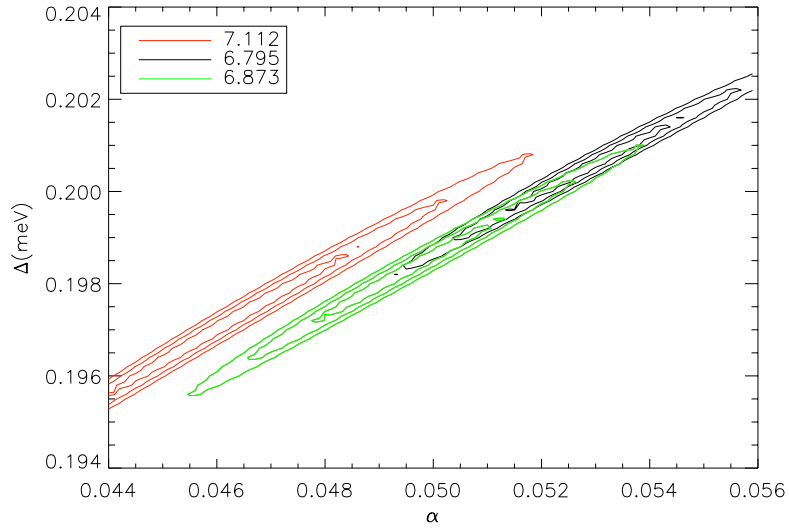


Figure 4.17:  $\alpha/\Delta_0$  confidence regions for the sapphire device (Device 2). Three different resonators are plotted, denoted by their resonance frequency in GHz.

Table 4.2: Average parameters  $\alpha$  and  $\Delta_0$  across several resonators. Statistical errors are shown, based on resonator-to-resonator dispersion given a sample of several resonators in each case (between 5 and 10 for all devices).

Device	$\alpha$	$\sigma_\alpha$	$\Delta_0$ (meV)	$\sigma_\Delta$ (meV)
1: Silicon	0.0262	0.0012	0.1791	0.0017
2: Sapphire	0.0496	0.0035	0.1987	0.0018
3: 30 nm Al on silicon	0.114	0.0126	0.1858	0.0047

#### 4.2.2.2 Quasiparticle lifetimes – finding the recombination constant

The determination of parameters from quasiparticle recombination time measurements are essential to finding the correct responsivity. As discussed in Section 2.1.2.5, the recombination constant,  $R$ , will greatly affect the responsivity in high-loading applications like ground-based astronomy. This value will typically have a much greater effect than the unloaded lifetime,  $\tau_0$ . To measure this value, we must fit a curve of lifetimes versus known quasiparticle density. The densities can be computed from the base temperature and the fitted gap energy. There are two effective methods for determining the lifetimes used here: fitting the decay time to a response from either a microwave pulse or a millimeter-wave optical pulse.

The microwave pulse can be sent in on the third harmonic, where it may be more likely to create quasiparticles due to the higher frequency being a more substantial fraction of the gap frequency. The pulse cutoff time must be small compared to the microwave recombination in order to measure the true response. Averages are taken of a series of pulses, and the data stored digitally with a fast ADC card. The exponential response can be fit, giving the lifetime. This can be repeated at different base temperatures, and the quasiparticle densities can be inferred from the measured gap parameter. This method can be performed while dark or open, in which case it can measure the difference in lifetimes between loads. One caveat to this method is that it creates quasiparticles along the third harmonic current distribution, which is not uniform and is distinct from the quasiparticle distribution from the optical loading. Thus one must be careful in accounting for these effects. This correction is small if the steady-state quasiparticles are uniformly distributed and the created quasiparticle density is small compared to the steady-state population. These are generally the case under dark base temperature sweeps.

In this case, one must be careful about fitting to the correct effect. Power below the gap frequency can heat up the quasiparticles in the material, as well as creating new ones. Thus, when the third harmonic driving wave is sent in, one can see the effective change due to quasiparticle heating, and then the longer-term effect of quasiparticle recombination. This can be particularly

difficult for high temperature data where recombination times are small, and thus the signal-to-noise ratio is low at longer timescales. In general, it is best to try multiple starting points in time samples after the signal is turned off, and find where the best fit starts to converge. This method guarantees low contamination from the short-term heating effects, and allows the best signal for the longer timescale recombination.

The second method is to create quasiparticles optically with a millimeter-wave source tuned to the specific band. In this method, the perturbing signal comes through the antenna, and creates quasiparticles according to the same profile as the optical load. However, this method can only be used during optical tests, and given the uncertainty of the quasiparticle distribution, is not feasible for constraining  $R$ .

Once  $\Delta_0$  has been found through the temperature sweep data, it is easy to compute the quasiparticle density as a function of base temperature under no optical load. We can easily fit for the two unknowns,  $\tau_0$  and  $R$ , with the equation  $1/\tau = Rn_{qp} - 1/\tau_0$ . With lifetimes found at several temperatures under no optical load, it is straightforward to fit for these parameters. The results of a fit to silicon device resonators are found in Figure 4.18, with  $R \simeq 7.5 \mu\text{m}^3\text{s}^{-1}$ . It is encouraging that, for this device, the inverse lifetime is linear with quasiparticle density, as one would expect from Equation 2.24. We must compare these data to values obtained from other sources. Most literature refers to  $\tau_{e\omega}$ , the electron-phonon relaxation time, so we must use Equation 2.25 to convert to  $R$ . This timescale has been computed theoretically by Kaplan *et al.* [56] to be  $\tau_{e\omega} = 438 \text{ ns}$  for aluminum, with the equivalent  $R$  of  $8.1 \mu\text{m}^3/\text{s}$ , given reasonable assumptions of  $\Delta_0 = 0.18 \text{ meV}$ . Other assumed constants lead to a computed value of  $9.6 \mu\text{m}^3/\text{s}$  [35]. More recent analyses have found dependences on substrate material and superconductor thickness in thin films, and found  $\tau_{e\omega} = 687 \pm 6 \text{ ns}$  for aluminum thickness of  $150 \mu\text{m}$  on silicon substrate [3]. Using the values assumed above, this yields  $R = 5.2 \mu\text{m}^3/\text{s}$ . However, by scaling with the lifetimes obtained in the same analysis for  $100 \text{ nm}$ -thick aluminum, the value becomes  $R = 8.3 \mu\text{m}^3/\text{s}$ . This would suggest that the best-fit values in Figure 4.18 are reasonable.

In much of the data, in particular for the sapphire device, it was difficult for the author

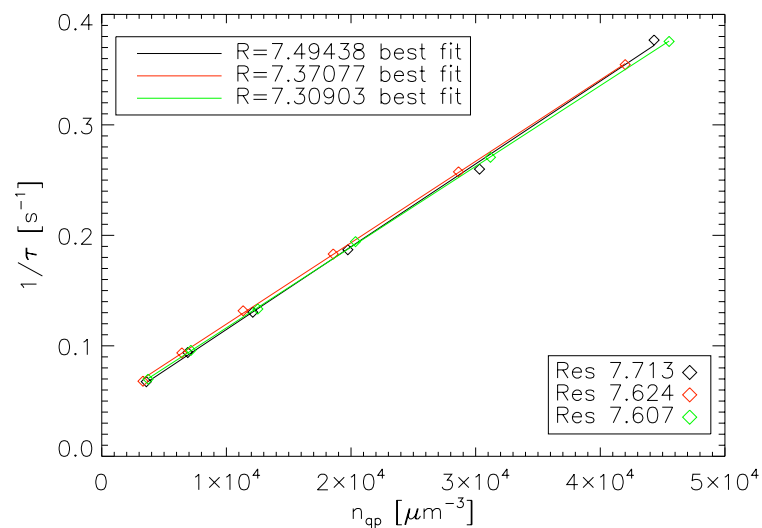


Figure 4.18: Lifetime as a function of quasiparticle density, inferred from the measured gap parameter of each detector.

to decouple the effects of initial heating from the exponential recombination. Future analysis by collaborators may yield reliable measurements of  $R$  from these data. However, it is currently impossible to find if the measurements of  $R$  are consistent across multiple devices, substrates and multiple aluminum thicknesses. Because this is unknown, analyses of responsivity assume a fixed value for all devices.

#### 4.2.2.3 Frequency and dissipation response

The ratio of frequency-to-dissipation response is particularly important because of the excess noise along the frequency direction. The lower the ratio, the higher the amplitude signal-to-noise ratio. Thus it is important to find if these values follow Mattis-Bardeen predictions. The results can be seen in Figure 4.19. At low temperatures the ratio lies significantly above predictions; this is likely a systematic effect due to the difficulty in precisely fitting small changes in high  $Q_i$  (typically  $>100,000$ ) while  $Q_c$  is much smaller ( $\sim 10,000$ ). It may also be affected by the loss associated with two level systems, which is most prominent at low temperature. This trend is seen to follow the same path for both dark and open-window data.

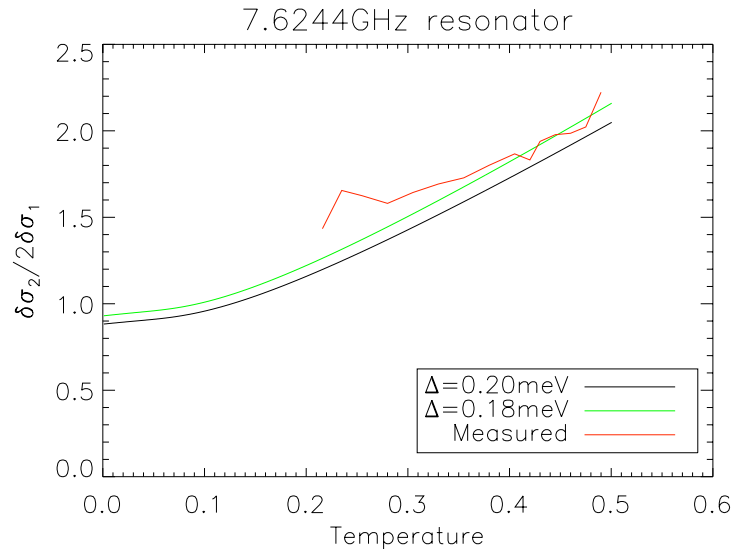


Figure 4.19: The measured ratio of response between frequency and dissipation, plotted over the Mattis-Bardeen predictions.

#### 4.2.2.4 Power dependence of response

As established in Chapter 3, the readout power available to use is of fundamental importance in maximizing MKID sensitivity. In that chapter we assumed that the primary effect of readout power was to create quasiparticles that limit sensitivity. This assumption was made because we know microwave power can create quasiparticles, but the assumption is somewhat simplistic in that it ignores the effects of nonlinearity and distortion. It has been observed that a resonator driven into a nonlinear regime can act as an amplifier [110, 113]. The primary limitation to a more involved model is the lack of understanding of the behavior of MKIDs at high powers. That is, how do the nonlinear effects of high drive powers, which can cause increased responsivity (i.e. a larger response in V/W), balance out with the effects of quasiparticle heating and creation, which decrease responsitivity? We therefore look at frequency shifts due to temperature changes to find how this response varies.

While it is difficult to find the change in resonance frequency at high powers because of the difficulty in fitting, it is possible to look at the response in the IQ plane of a frequency point. Looking at frequency sweeps taken at two base temperatures and finding the difference gives the response as a function of frequency - i.e.  $\delta S_{21}$  as a function of frequency. These sweeps can be taken at different powers, and the responses compared to find how power affects responsivity. This is seen in Figure 4.20 . For a non-distorted loop in which the frequency shift between the two base temperatures is small compared to the resonance width, the response as a function of frequency should be a Lorentzian with the same width as the resonance. It should be noted here that by measuring  $\delta S_{21}$  we actually find the magnitude of the phase and amplitude response, such that resonators with mismatched  $Q_c$  show appreciably smaller  $|\delta S_{21}|$ .

In Figure 4.20, high power makes the total response decline. However, Figures 4.21 and 4.22 show the same plots at higher temperature, and show an increase in responsivity with power. This suggests that the negative effects of power, quasiparticle creation and heating, are effectively lessened in resonators with a large, steady-state population. As these effects decrease, the gain in

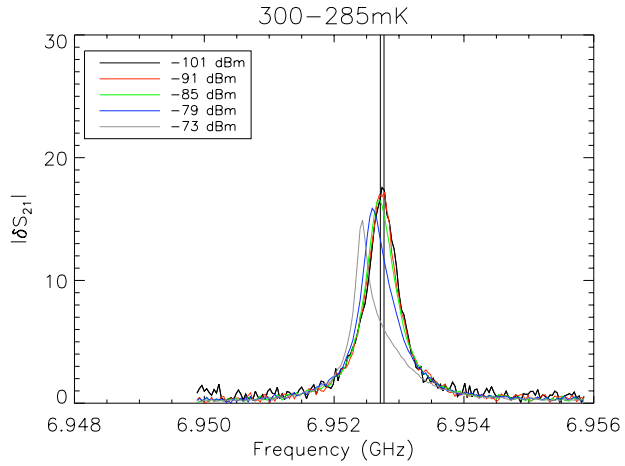


Figure 4.20: The total response of a resonator as a function of frequency for several readout powers [103]. Here is shown the response between 300 mK and 285 mK base temperature under no optical load. At high powers, the magnitude of the response decreases.

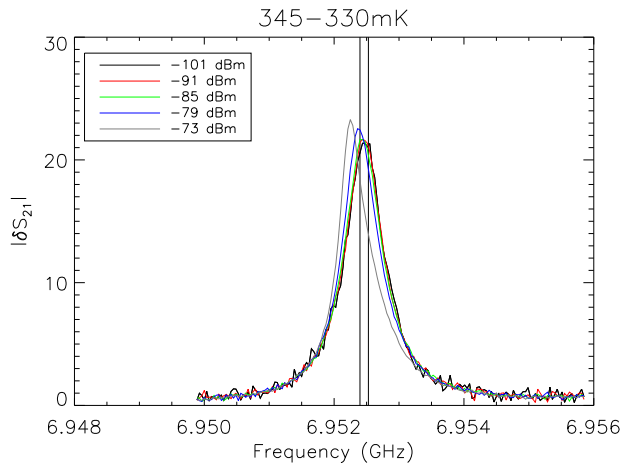


Figure 4.21: The total response of a resonator as a function of frequency for several readout powers. Here is shown the response between 345 mK and 330 mK base temperature under no optical load. At high powers, the magnitude of the response increases.

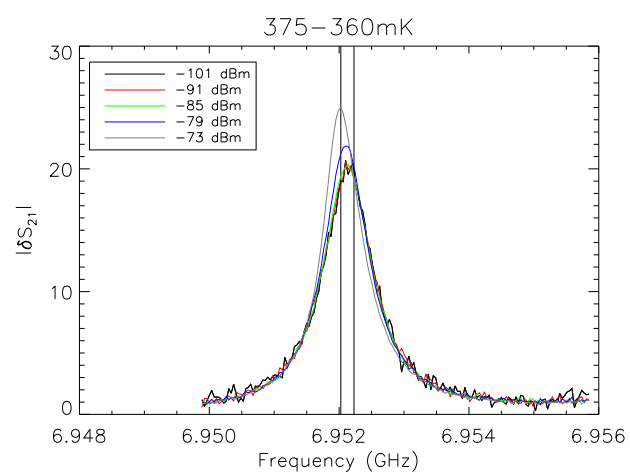


Figure 4.22: The total response of a resonator as a function of frequency for several readout powers. Here is shown the response between 375 mK and 360 mK base temperature under no optical load.

response from a nonlinear resonator can be realized.

In addition to finding the total response, we can decompose the response into phase and amplitude directions, to find how both change as a function of frequency. The width of the response can give an approximation of the effective  $Q$ ; however, we are only particularly interested in the behavior of the point of peak response, the effective resonance frequency. We track this point in IQ space to find its projected response in either direction. The frequency direction, which by definition suffers noise due to TLS effects, is given in all cases by the tangent to the distorted loop. This is simply because the loop defines the frequency direction, as it is itself a sweep in frequency. The dissipation is given by the orthogonal direction. Figure 4.23 shows the maximum response in these directions as a function of readout power estimated at the device for a sapphire device resonator. One can see that the frequency response is relatively stable at high power, and that the dissipation tends to decline. At higher quasiparticle densities, the relative dissipation decline is somewhat smaller (Figure 4.24). This, combined with the narrowing resonance widths at high readout power, suggest that the effect of quasiparticle heating dominates over the creation of additional quasiparticles.

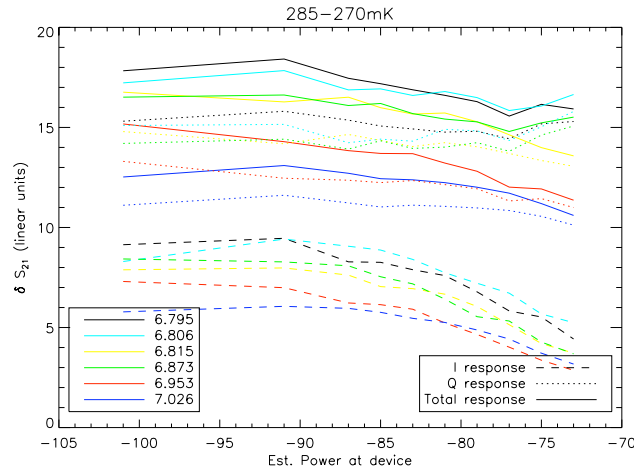


Figure 4.23: The total response, and the response in I (amplitude) and Q (phase), as a function of power for several resonators. The dispersion in response is due to variations in  $Q_c$ . Note the relatively low temperature and associated quasiparticle density.

These analyses have all been done for dark data, in which the response is due to a base tem-

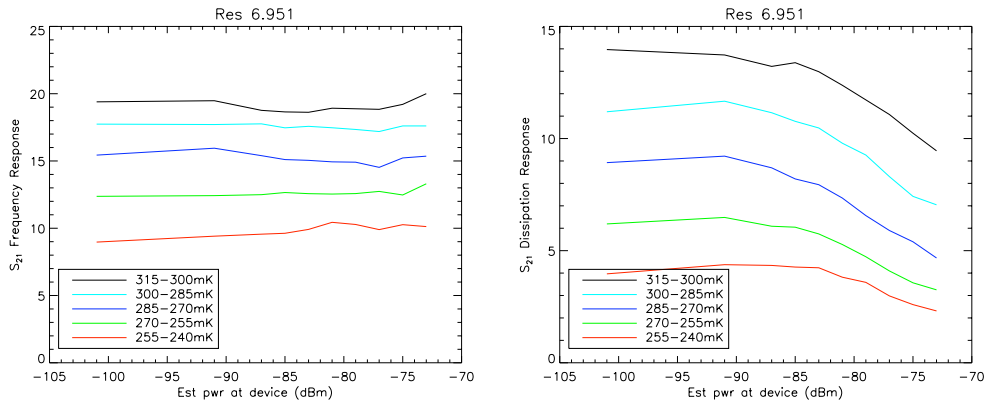


Figure 4.24: The I (amplitude, right) and Q (phase, left) response as a function of temperature. At higher temperatures, the fractional amplitude dropoff decreases somewhat, as is qualitatively expected for higher quasiparticle densities. Higher temperatures than this could not be considered, as the larger quasiparticle density changes would make it impossible to decouple frequency and dissipation response.

perature change. Given the likelihood of non-uniform quasiparticle absorption from sub/millimeter light, it would be ideal to test this again with optical sources. However, as the typical optical test involves large shifts from beam-filling blackbody loads (described below) the response is highly non-linear and it is difficult to separate frequency and dissipation response. This issue is fundamental for the optimal operation of MKIDs, and is therefore addressed further in Chapter 7.

#### **4.2.3 Optical measurements**

##### **4.2.3.1 Blackbody tests of responsivity**

The responsivity is measured by hot/cold loads of Eccosorb<sup>TM</sup> submerged in LN<sub>2</sub> at 77 K, and at room temperature, typically around 297 K. These are placed directly below the vacuum window, and should fill the entire beam. Network analyzer sweeps are performed over the array under these two optical conditions. These allow the measurement of the shift in frequency, giving us the detector responsivity for a beam-filling load. An example of this is seen in Figure 4.25, with the sapphire device (Device 2) in the wide-window configuration (see Figure 4.6). Figure 4.26 shows the responsivities for the silicon device (Device 1) in the telescope configuration (see Figure 4.5). Both these examples show significantly more response in the wider Band 1 than the narrow Band 3, as expected. The responsivities measured in these tests can be used to find the responsivity at any given load temperature, and applied toward NEP (see Appendix C). Hot/cold blackbody tests also form the basis for the determination of excess loading and optical efficiency, discussed later in this section.

##### **4.2.3.2 Beam maps**

The beam map data was taken by Tasos Vayonakis and Nicole Czakon. It was then compared to simulations for beam width. Figure 4.27 shows the beams in the near field of the Lyot stop for the two bands. As can be seen, the beam shapes depend upon the band, as the beam pattern in the near field is heavily frequency dependent. The higher frequency bands have central peaks, while the lower frequency bands have dips. These shapes evolve as one goes into the far field, as

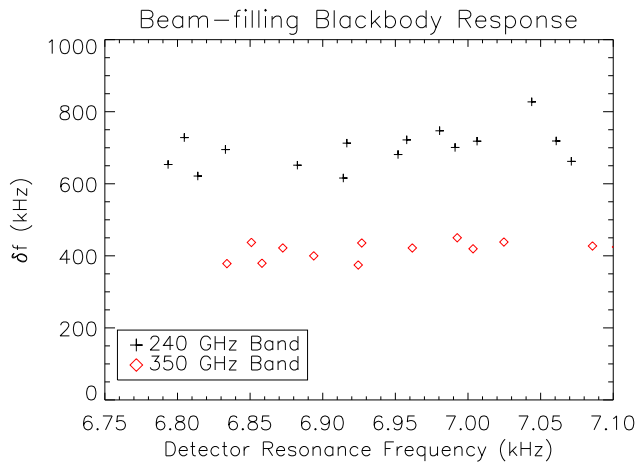


Figure 4.25: Sapphire device (Device 2) responsivity in frequency shift, in kHz. when exposed to 300 K and 77 K blackbody loads.

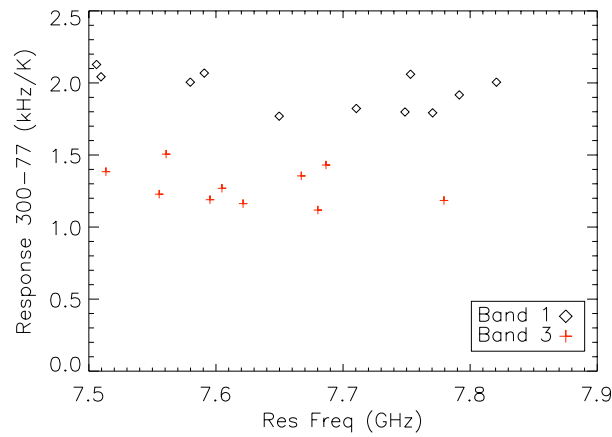


Figure 4.26: Silicon device (Device 1) responsivity in frequency shift in kHz per Kelvin, in telescope configuration. The response is the average over the range of 77 K and 300 K beam-filling loads.

is expected from simulations using Zemax<sup>TM</sup>. The exact shape is difficult to compare to Zemax calculations due to the finite resolution of the physical optics propagation, but the FWHM of the beam has a similar width.

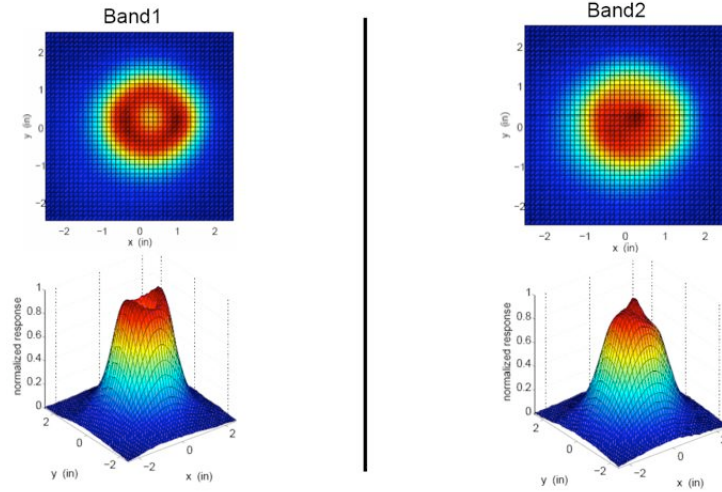


Figure 4.27: Beam maps of two colors (240 GHz left, 350 GHz right) from the silicon DemoCam device (Device 1). Figure courtesy of Tasos Vayonakis.

#### 4.2.3.3 Fourier Transform Spectroscopy

FTS data were taken by Tasos Vayonakis and Nicole Czakon, and are necessary for determining the effective bandwidth, and testing for out-of-band response. In the first iteration of devices, these data confirmed sensible bandpasses with poor coupling to out-of-band radiation (i.e. negligible response out of band). However, as has been endemic of these devices, a high degree of fringing is observed. It is unlikely to be caused by the optics due to the antireflection coatings applied, and may relate to standing waves in the antenna feed network. However, the exact cause is unknown. Examples of the two bands, superposed upon the atmospheric transmission at Mauna Kea, are shown in Figure 4.28

In all calculations of sensitivity, the bandwidth is found from the FTS measurements, but the bandpass is assumed to be perfectly square. Thus, the effects of nonuniformity and standing

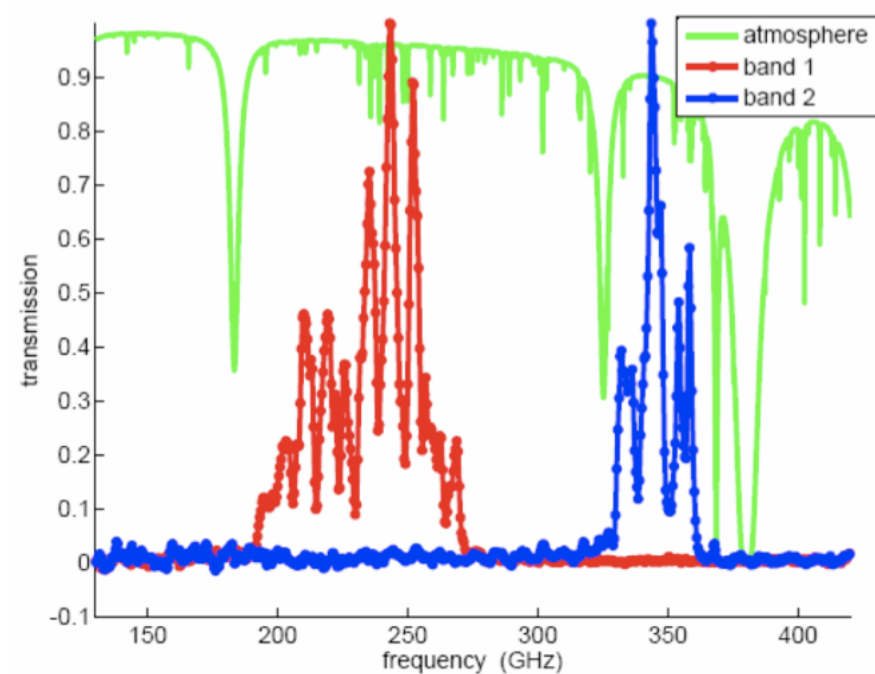


Figure 4.28: FTS spectra of bandpass measurements of bands on the silicon device, normalized to unity peak responsivity [104]. Overplotted is the transmission at Mauna Kea assuming 0.5 mm of precipitable water vapor.

waves are lumped into the optical efficiency term.

#### 4.2.3.4 Excess load

The excess load, discussed in Section 2.3.2, is an important factor in determining the expected sensitivity of MKIDs. This can be easily calculated using Equation 2.35, assuming  $\tau_0$  is large. But is it a valid assumption to ignore  $\tau_0$ ? The best fits indicate  $\tau_0 = 23 \mu\text{s}$  for the silicon device, much smaller than other devices, while typical fits looking at loads of 77 K give  $\tau \sim 7 \mu\text{s}$  in band 3 and  $\sim 5 \mu\text{s}$  in Band 1. This effect is fairly small, particularly for devices with long dark lifetimes. However, to calculate the effect exactly, we must use Mattis-Bardeen to find the value of  $A$ .

If the effect of  $\tau_0$  is small, we would not need to know anything other than the proportionality between  $1/Q_i$  and  $n_{qp}$ . If this is linear from dark temperature sweeps, then the method should be valid in determining excess load. While from Mattis-Bardeen theory it is not linear, as the frequency shift and change in  $1/Q_i$  per quasiparticle are both temperature dependent, it is nearly so over the range of interest. In Figure 4.29, we see the results of the fit are linear to good approximation in the region of higher quasiparticle densities expected under load.

Now let us consider the effect of a higher absorption by the grounded end of the resonator. We assume that there is some excess loading temperature,  $T_{exc}$ , which is causing the load through the antenna (for example, millimeter-wave radiation through window vignetting). The effect of this load will be a diminished frequency response, or a diminished response in  $Q_i$ . This occurs because, at the area of absorption, the quasiparticle density is higher, and thus the energy is less likely to be transferred directly to broken pairs.

Now consider the effect of raising the base temperature. This should create a uniform quasiparticle density everywhere in the resonator, on top of which the optical loading creates a non-uniform density. In effect, the base temperature contribution is more heavily weighted in  $Q_i$  than the optical contribution. This leads to a decrease in responsivity, found from the difference in  $1/Q_i$  between the blackbody temperatures.

Consider that the effective efficiency towards radiation decreases as either base temperature

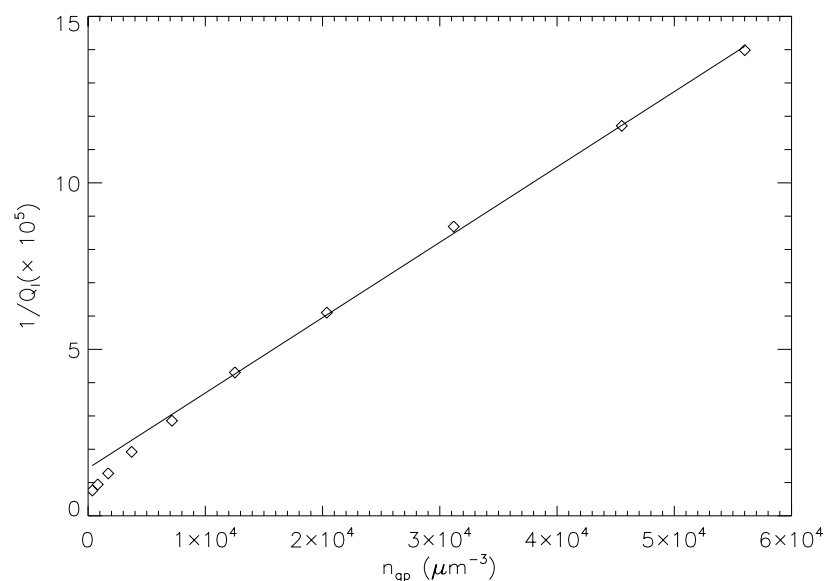


Figure 4.29: Internal  $Q$ 's inverse plotted against quasiparticle density, which is found from dark temperature sweeps.

or loading increase. The change in efficiency with base temperature when looking at 77 K will be greater than the change in efficiency when looking at 300 K (because, as the quasiparticle density increases, it tends to saturate toward a more or less constant responsivity). Thus, if we have an excess temperature seen in both bands, it will be seen more efficiently at 77 K, and less efficiently at 300 K. This could create a larger-than-expected excess temperature, since it is a smaller effect in the 300K data compared to 77 K. Thus, as base temperatures increase, this effect should get smaller, as the relative effect of the excess load diminishes.

The only true method to find the excess loading is to simulate the effects of nonuniform absorption. Figure 4.30 shows the effect of the excess load.<sup>3</sup> Plotted is the “naive” excess load method, following Equation 2.35, as a function of base temperature for resonators in the narrow-window (January 2008) and wide-window (June 2008) configurations. Here the elevated base temperature creates thermal quasiparticles, which appears as an effective excess load. The wide-window data has much smaller excess, and both rise with base temperature, as expected. Along the data are fitted curves assuming Mattis-Bardeen parameters measured dark, with an assumed excess load of 130 K. The nonuniform absorption line assumes power from the antenna is distributed along the resonator as an exponential with a constant of  $z_0 = .05$  mm. Two additional parameters in this plot, thickness (50 nm) and “true” optical efficiency (0.3), were adjusted to give a good fit to the data. At various base temperatures, the anticipated excess load to be measured is found for both uniform and nonuniform cases. It is clear that a nonuniform absorption is easier to fit than the nonuniform case.

However, there are many assumptions that go into this that preclude this method from giving a correct answer for the excess load value. The method can be used as a guide to show that the “naive” method gives reasonable answers, and that a nonuniform power absorption of some kind is a better fit to the data. Thus, Figure 4.30 is more useful as a guide than a strict determination of

---

<sup>3</sup> The January 2008 data was taken during a long cooldown that experienced significant optical responsivity decline and increase in excess load with time. Thus, the excess load for a resonator in January is 120 K at base temperature, much larger than that measured in the initial optical configuration. This data is presented because it includes the most extensive measurements of responsivity with base temperature.

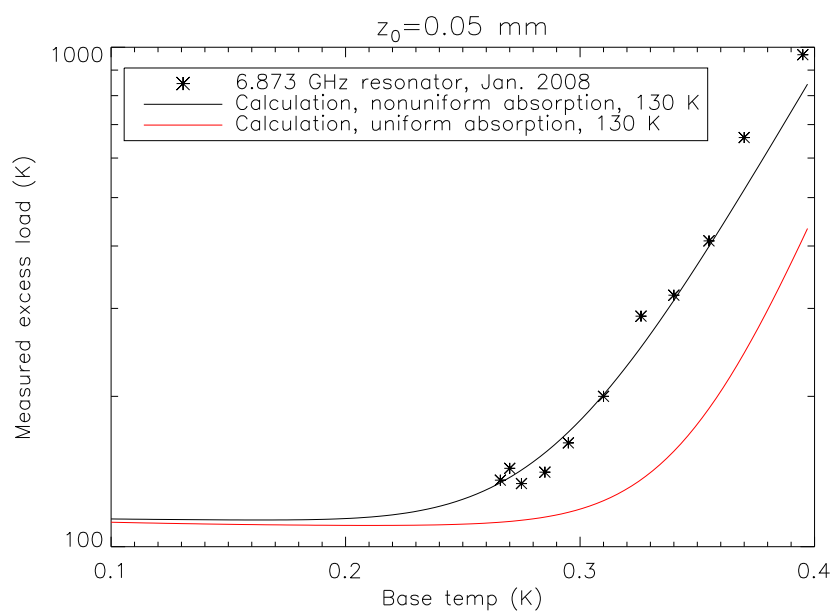


Figure 4.30: Measured excess loading for a Band 1 resonator from the sapphire device (Device 2) as a function of temperature in the small window configuration. Two cases are plotted, one assuming completely uniform absorption of power throughout the resonator, and one case involving a sharply peaked exponential distribution.

excess load. Due to the difficulty of determining the true excess and the reasonable performance of the “naive” method, all further references to excess load are calculated by Equation 2.35.

Now, let us look at the results of different excess load tests. The first is excess load in the original telescope configuration seen by the silicon device, in which the two bands see clearly distinguishable values of excess load. This is seen in Figure 4.31. Next, we can see the reduction in

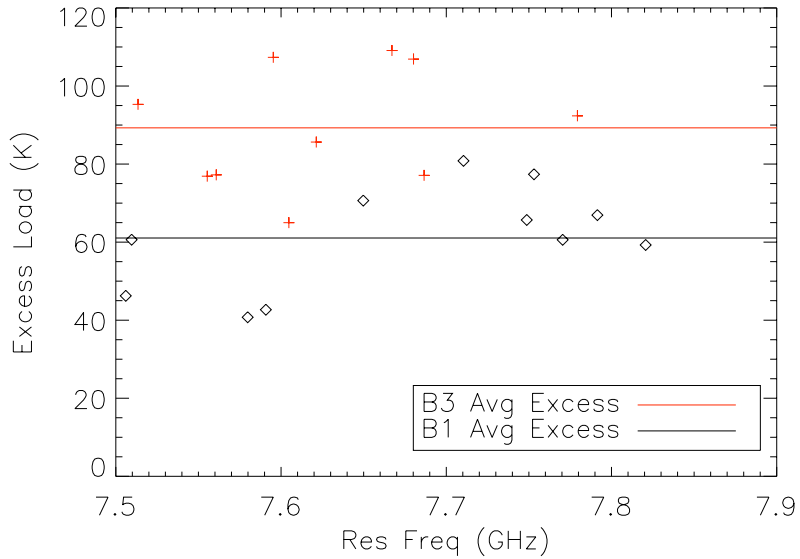


Figure 4.31: Excess loading in both bands of silicon DemoCam device (Device 1) in telescope optics configuration, seen in Figure 4.5.

excess loading by changing and widening the Zotefoam vacuum window with the sapphire device. The narrow window data was taken with a tilted 4 K filter, unlike the telescope configuration, but with a small vacuum window, while the wide window data is from the configuration of Figure 4.6. This reduction is seen in Figure 4.32 below. The final  $<20$  K level of excess is in the acceptable range for ground-based astronomy, as the sky background will generally dominate the loading. There are two likely reasons for the reduction in excess load: either a portion of the beam had been terminating on warm surfaces inside the Dewar, or the old Zotefoam had degraded in transmission over time. It is not possible to strictly differentiate the two possibilities. It was noted that responsivity degraded significantly over the course of a long cooldown, which gives some evidence for the hypothesis of

window degradation. However, conclusive evidence is lacking.

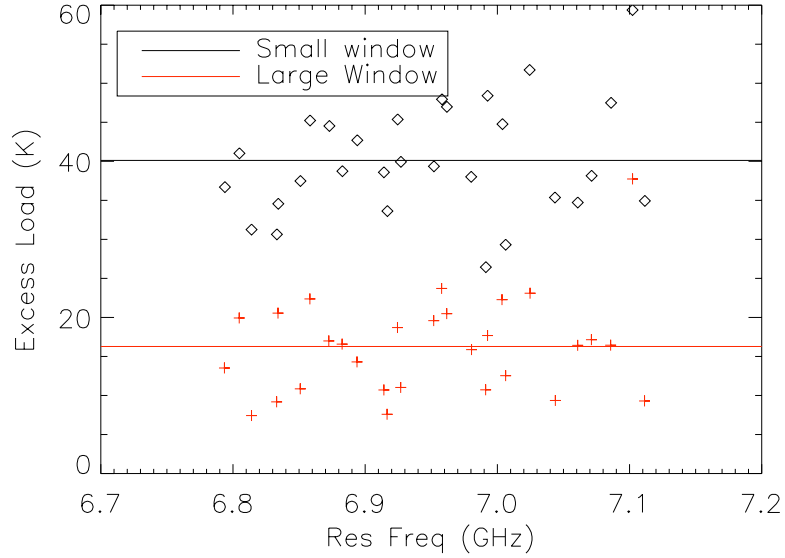


Figure 4.32: Excess loading for all resonators in two different configurations. Diamonds represent small window configuration seen in Figure 4.5, and pluses represent large window configuration in Figure 4.6

#### 4.2.3.5 Optical efficiency

The optical efficiency of the entire system is critical in the optimization of the mapping speed of the camera. Thus, having a precise knowledge of the efficiency of the system, and its components, is vital to optimization of the instrument. Ultimately, we are limited by two factors in regard to the understanding of the response - the lack of knowledge of the aluminum film thickness, and the unknown parameter of the absorption profile of power coupled through the antenna as a function of distance along the resonator (discussed in Section 3.5.2). However, we can make reasonable guesses as to the effect of these two parameters, which are largely degenerate in terms of response. We can plot effective aluminum thickness versus optical efficiency, as seen in Figure 4.33. This efficiency does not take into account the fudge factor due to the nonuniform absorption of power; even knowing the volume, which one would guess is likely to be in the 40-50 nm range for 60 nm of deposited aluminum, it is impossible to know the true optical efficiency decoupled from the

effect of nonuniform absorption. To take this extra value into account, one must divide the derived efficiency by the square of the fudge factor. If the factor is found through some means to be 0.6, then the optical efficiency should be multiplied by 1/0.36 because the responsivity (e.g. in kHz/K) is proportional to the square root of the efficiency in the limit we consider. Here we consider the effect of non-uniform absorption as a component in the total efficiency of the system. Knowing the thickness of the aluminum is therefore the only component required to find the exact efficiency of the optics.

We can still determine efficiency as a function of the unknown thickness simply by considering the quasiparticle generation and recombination, as in Equation 2.29. This can be done without measuring quasiparticle lifetimes, but requires an assumption about the recombination constant, and that  $\tau_0$  is large compared to  $1/Rn_{qp}$ . This is the assumption that the optical power is large enough that the quasiparticle density alone sets the recombination time. This assumption should not cause a great error in the calculation; using the silicon device (Device 1) parameters in calculating this effect, even with the relatively small  $\tau_0$ , the efficiency was found to be overestimated by less than 2% of the value. From measured internal  $Q$ s, we know the excess loading (assuming the excess couples at the same efficiency as the optical response), and can use this to find the frequency shift response if there were no excess load whatsoever, which can be related to the efficiency. Measured from hot/cold loads in the limit of large  $\tau_0$ , the total efficiency from a hot/cold measurement is given by

$$\eta = \left( \frac{\frac{\delta f}{\delta T}(\sqrt{77 + T_{exc}} + \sqrt{300 + T_{exc}})}{\frac{df}{dn_{qp}}} \right)^2 \frac{RV\Delta}{k_B(\Delta\nu)}. \quad (4.2)$$

Here  $\frac{\delta f}{\delta T}$  represents the hot/cold response in kHz/K. The frequency shift's reliance on the kinetic inductance fraction is contained in  $\frac{df}{dn_{qp}}$ . It is straightforward to incorporate  $\tau_0$  into Equation 4.2, though it has been left out here for simplicity. From knowing these parameters, one can calculate efficiency. The volume is the only parameter not easily measurable in operation. This method allows the comparison of the efficiency among devices in the same optical configuration, as is seen in Figure 4.33.

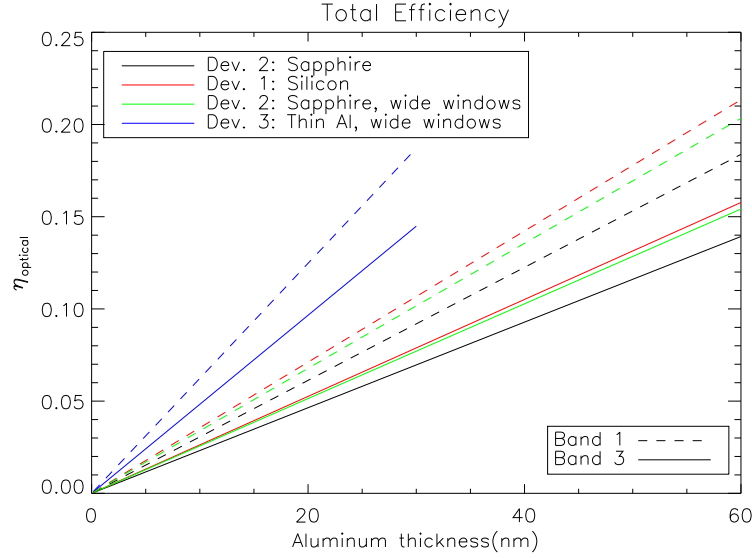


Figure 4.33: Optical efficiency as a function of resonator thickness. The “thin aluminum” device (Device 3) was originally 30 nm aluminum thickness sputtered, all other devices were 60 nm thick. The exact thickness removed by etching is unknown. Here we have assumed  $R=7.5 \mu\text{m/s}$ , that measured for the silicon device (Device 1), but we assume it is constant for all devices. The effect of non-uniform power absorption is included in the efficiency, rather than being explicitly removed. Device 3 gives similar efficiency values for both Band 1 and Band 3, as shown.

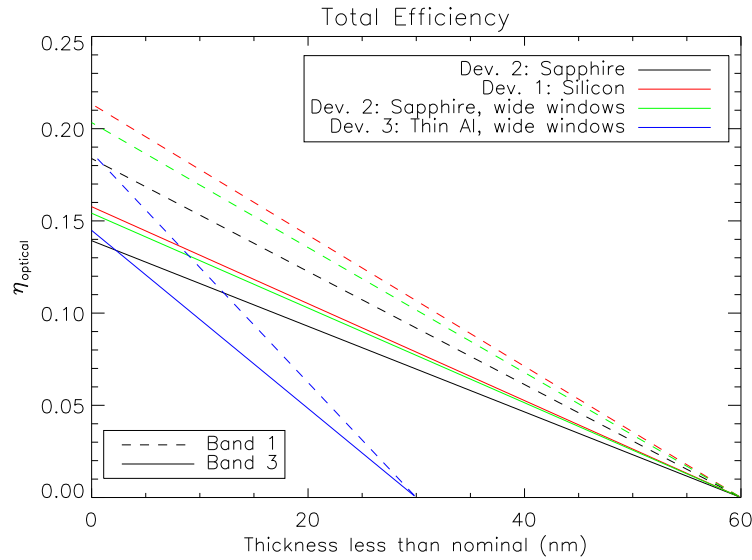


Figure 4.34: Optical efficiency as a function of thickness etched away. The amount etched is unknown, and depends upon many device-specific parameters. Here we assume  $R=7.5 \mu\text{m}^3/\text{s}$ . The effect of non-uniform power absorption is included in the efficiency, rather than being explicitly removed.

Figure 4.33 plots the efficiency of three devices, using responsivity averaged over all the detectors in each band. An immediate conclusion one may jump to is that the silicon device has an inherently better efficiency than the sapphire device (Device 2). However, one must be very cautious in making such interpretations. A more likely conclusion is that the silicon device has slightly thicker aluminum, and thus has a slightly more uniform power absorption profile due to its lower resistance. This efficiency represents the optical efficiency multiplied by the square of this fudge factor, so a small difference in this factor can lead to a significant discrepancy between devices.

In Figure 4.34, we see that thin aluminum device has *lower* apparent optical efficiency, assuming a similar amount etched away. At first glance, this is unexpected, as thinner aluminum implies higher resistivity ( $\rho \sim 1/t$ ) and higher surface resistance ( $R \sim \rho/t \sim 1/t^2$ ). A higher sheet resistance implies greater absorption of millimeter waves from the antenna microstrip. Yet here is shown that, assuming 10 nm etched away, the thin-aluminum resonators have 0.89 times the efficiency, and at 15 nm etched, this decreases to 0.74.<sup>4</sup>

There are two likely explanations for the reduced efficiency of the thin aluminum device relative to the sapphire device with wide windows (in the same optical configuration). As the aluminum becomes more resistive, the scale length for absorption of light from the microstrip becomes shorter, leading to a reduced “fudge factor.” A thinner device would thus give a lower overall efficiency. The second explanation involves the change in impedance between the lossless (real impedance) niobium portion of the microstrip and the lossy (complex impedance) aluminum portion, where quasiparticles are created. This difference in impedance along the microstrip transmission line causes a reflection, reducing the efficiency of the antenna. As the aluminum goes to higher sheet resistance, the reflection will increase. The combined effect of absorption and reflection as a function of sheet resistance is seen in Figure 4.35. Using a reasonable guess of  $0.2 \Omega/\square$ ,<sup>5</sup> and neglecting edge effects,

---

<sup>4</sup> This is corrected for the optical transmission difference, as due to problems during fabrication, the bandpass centers were shifted downward by tens of GHz. In addition, the Band 1 bandpass became narrower, and this effect is also corrected-for. This also assumes that the same amount is etched in both devices, which is not necessarily true.

<sup>5</sup> In 20 nm aluminum films, the sheet resistance has been found to be 1.1-1.4  $\Omega/\square$  [111], while in subsequently etched films with 70 nm of aluminum deposited, the sheet resistance has been measured to be 0.24-0.3  $\Omega/\square$  [101].

the reflection ranges from 8% at 200 GHz to 4.5% at 360 GHz. Without knowing specifics of the film thickness and sheet resistance in the devices, it is difficult to determine which effect is dominant. Assuming a factor of 3 increase in resistance due to etching effects (to  $0.6 \Omega/\square$ ), these values become 20.8% and 15.4% in Band 1 and Band 3, respectively. While these high reflections decrease the antenna efficiency, they are small enough for these moderate resistances to not primarily limit the antenna efficiency.

The discussion of optical efficiency is incomplete without considering what is expected given the known optical transmission elements. These are given in Table 4.3. If we include a rough guess at antenna efficiency of 0.6, the total expected efficiencies become 41% and 46% for Bands 1 and 3, respectively. While this is unlikely to be fully explained by non-uniform power absorption, it is still close to the expected value. If we take the Band 1 efficiency to be 15%, it would require a factor of 0.37 due to non-uniform absorption, and reflections, to explain the effect. While this is certainly not outside the realm of possibility, it likewise cannot preclude a somewhat less efficient antenna structure. Such a large factor is very difficult to explain with reduced antenna efficiency due to microstrip line reflections alone, but this effect likely contributes to the lower efficiency. The lower efficiency in Band 3, despite the more transmissive optics, is likely to be due to the antenna feed structure being less efficient at high frequencies (see Section 4.2.3.6 below).

One other considerations must be taken into account when comparing the extrapolated and expected efficiencies. First, the kinetic inductance fraction measured in dark runs will be larger than that from created quasiparticles. This is because the optically-generated quasiparticles are created only on the center aluminum strip, while there is a small amount of aluminum on the ground plane side. This aluminum is present because it is easier to create a resonator of the correct dimensions through etching rather than through precise deposition. Although the magnitude of the effect is unknown, as it depends on the relative penetration depths of the aluminum and niobium, and thus their thicknesses, it is likely to be a small effect which would bias the calculated efficiency low.

---

Without knowing the precise thickness of the latter, it is difficult to establish if  $R \sim 1/t^2$ .

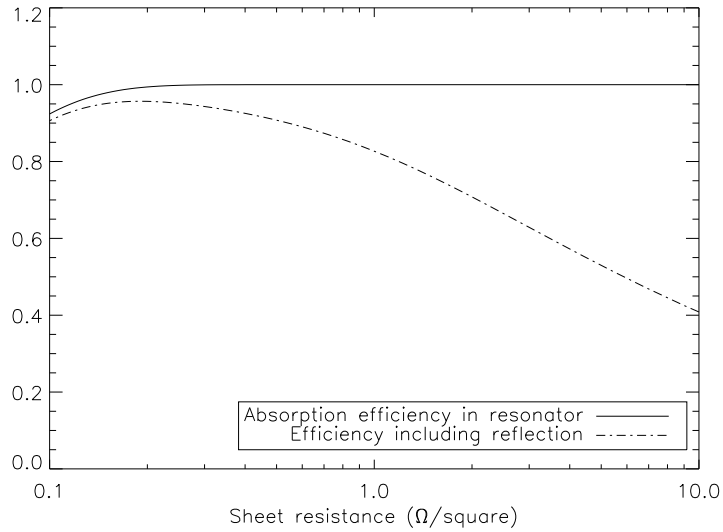


Figure 4.35: Absorption efficiency from a microstrip as a function of sheet resistance. This includes first-order values for the inductance and capacitance per unit length ( $2 \times 10^{-7} \text{ H/m}$  and  $2.5 \times 10^{-10} \text{ F/m}$ , respectively, for a  $2.5 \mu\text{m}$ -wide microstrip with  $0.4 \mu\text{m}$  dielectric of  $\epsilon=4.5$ , neglecting edge effects). Efficiencies shown here correspond to 350 GHz radiation. The solid line indicates the absorption efficiency for radiation in the lossy portion of the microstrip, while the dashed line includes the effect of reflections at the interface with the lossy portion.

Table 4.3:

Band	Lyot	Filters	Window	Total
1 (240 GHz)	0.76	0.91	0.99	0.68
2 (350 GHz)	0.95	0.84	0.96	0.77

Unfortunately, unless there are measurements of the thickness and the normal-state resistivity of the aluminum, there is very little else we can say about the absolute optical efficiency. These measurements were typically easy given devices using an aluminum CPW feedline. With niobium ground planes, this simple measurement becomes more difficult because one cannot find the resistivity of aluminum from the feedline transmission. This remains a major limitation to the practical understanding of MKIDs.

#### **4.2.3.6 Out-of-band pickup**

Determining the out-of-band pickup can be quite tricky, but is imperative for two reasons. The first reason is that out-of-band pickup can lead to excess loading, which severely degrades detector sensitivity, particularly in the amplifier noise limit. The second concern is out-of-band coupling to the sky or astronomical sources in ways difficult to differentiate from the on-chip antenna beam. This can lead to improper measurement of the source flux in-band and high sensitivity to atmospheric water lines. In addition, in beam-filling blackbody responsivity measurements, these can lead to an overly optimistic detector responsivity.

The out-of-band pickup may be caused by direct pickup in the aluminum portion of the resonator, by substrate heating, by the resonator and coupler acting as an antenna, or by leaks in the on-chip bandpass-filters. Direct pickup will have a large beam pattern due to the small size of the aluminum resonator portion, and it is unlikely to couple well to the incoming radiation from the telescope. The whole resonator may act as a dipole antenna (if a CPW resonator) or may act as a more complicated antenna (IDC resonator) which deposits the radiation in the lossy aluminum section. Although this process will not be as efficient as the antenna, it is a dangerous source of pickup because it can be very wide-band. Finally, leaks in the filters can be present, which can only be remedied by enhanced optical filtering. It is fairly clear for the devices studied in this chapter that the pickup from all of these sources is not the dominant method of coupling to radiation because of the large differences between Bands 1 and 3. In addition, the similar efficiencies calculated for the two bands, despite the large difference in antenna bandwidth, suggest large loading differences

consistent with coupling primarily through the antenna and bandpass filters.

There are several ways to approach the problem of finding out-of-band response, though none are completely satisfactory. The first method is to simply look for out-of-band response in the FTS data. This can be misleading, as it involves coupling to a fairly narrow beam. However, if the out-of-band response here is non-negligible, it is likely that coupling to the telescope beam is also non-negligible. This method is the best for finding out-of-band filter leaks as well due to the good coupling, though no significant leaks have ever been found.

A second method to determine out-of-band pickup is to use the single-polarization nature of the antennas to test if extra pickup comes from polarization along the antenna slotlines. A single-polarization millimeter-wave source can find the response to both polarizations by tilting the source 90 degrees. If the source responds significantly to both polarizations, then the pickup is likely not directly through the antenna. However, this method is somewhat useless if the out-of-band pickup is also coupled to the same polarization as the antenna. In the case of the first DemoCam devices, the resonators are largely along the same direction as the antenna slots. Informal tests showed pickup in the orthogonal direction to be less than 10% of the antenna polarization direction.

A third method can be used to quantify direct pickup. If one knows the relative antenna efficiencies between two bands, one can compare this to the measured relative efficiencies to quantify the direct pickup efficiency. The theoretical antenna feed network efficiencies over the bands have been simulated by Dr. Peter Day, with a ratio of 0.44 from Band 3 to Band 1. Decoupling the optical efficiencies from the measured efficiencies, the measured ratio is 0.76 for the sapphire device, and 0.74 for the silicon device. Including the effects of calculated optical efficiency, this implies that the efficiencies presented above are overestimated by a factor of  $\sim 1.18$  and  $\sim 1.80$  in Bands 1 and 3, respectively, due to non-antenna pickup. This method for determining pickup relies on simulation and the loss in the microstrip lines being well understood, as well as on the simulation representing the physical antennas perfectly. It is therefore too far-removed from direct measurement to be a definitive measure of the direct pickup.

Other methods include using metal-mesh filters and checking the response. This can show

if there is major out-of-band pickup, but requires knowing the exact filter transmission, which may degrade over long time periods. The only filters available for tests in the first DemoCam configuration were older, possibly degraded metal meshes, so the responsivity change could not be trusted. However, this experiment showed little change in excess load (as would be expected if wide-band pickup landing on warmer surfaces causes some of the excess), so it is unlikely out-of-band coupling was a dominating factor in the first generation devices. A more thorough and systematic check of out-of-band pickup was performed on later devices with resonators not coupled to antennas; this is discussed more fully in Chapter 6.

#### **4.2.4 Resonance frequency scatter**

As the location of the relative resonant frequencies compared to the design frequency can limit the number of uncollided detectors, it is important to find the scatter in designed versus actual frequencies. This can be achieved by making beam maps, discussed in Section 2.3.3, of all the detectors on a device. A new map was made for each resonator, one at a time, primarily by Tasos Vayonakis. This task was performed with the sapphire device, which should be representative of all devices. Figure 4.36 shows the difference between intended and actual locations for these devices. After subtracting out a second-order polynomial fit to account for non-random effects, the scatter is found to be 8.1 MHz.

In future devices, the strategy of having physically proximate resonators far apart in frequency (thus causing more collisions from aluminum nonuniformities across the array) was dropped – nearby resonators were then also close in frequency. The results of this approach are discussed in Chapter 6.

### **4.3 Summary**

From these various dark and optical tests, we understand the device and optical system well. Dark parameter measurements, such as the recombination constant, kinetic inductance fraction and gap parameter, as well as the ratio between dissipation and frequency response, seem largely in line

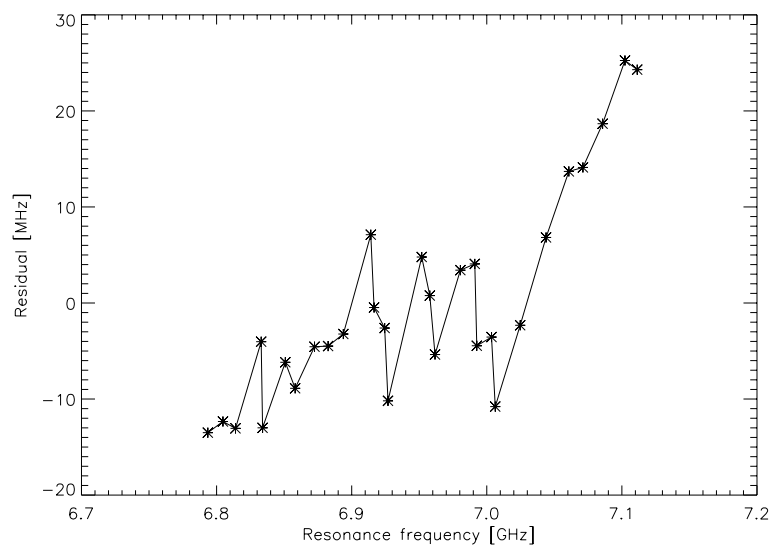


Figure 4.36: Scatter of intended versus actual resonance frequency spacings between detectors.

with expectations. In addition, beam maps and bandpass spectra appear to behave as expected. However, the complex physics of MKIDs, including the difficult-to-measure parameters of thickness and absorption, make it difficult to fully understand the system. The numbers measured are consistent with everything working as well as we can expect. The excess load appears manageable, at the level of 10s of Kelvin, and not significantly in excess of what is found in similar cameras. The bands have clearly different responsivities, indicating that the bulk of the responsivity is through the antennas and bandpass filters.

Other measurements, such as the effect of readout power, are left to later analysis to find how to optimize the system in telescope operation. From these data, the response appears to depend on the quasiparticle density. It will be left to later experiments to determine whether this is true under telescope loading conditions.

## Chapter 5

### MKID DemoCam Telescope Data - First Light with KIDs

The MKID camera was brought to the Caltech Submillimeter Observatory in April 2007. The purpose of the observing run was to demonstrate the viability of MKIDs as an astronomical detector, to measure the response to point sources, to determine our ability to do multicolor as well as spatial sky subtraction, and to discover systematics. Additionally, we were able to test differences in readout schemes and test how the MKID response varies with orientation due to the Earth's or any local magnetic field.

#### 5.1 Optical Design/Telescope Interface

The MKID camera was brought to the CSO, a 10.4-meter diameter Cassegrain telescope. The DemoCam was mounted directly behind the Cassegrain focus. The Bolocam optics box, consisting of an ellipsoidal mirror, two flat mirrors, a final ellipsoidal mirror, creates a near image of the primary mirror at a given height above the final mirror. The schematic for the optics box attaching to the telescope is seen in Figure 5.1. The cryostat bolts onto the top of this, seen in Figure 5.2 such that the image forms at the focal plane.

The optical design used for the MKID DemoCam project was very similar to Bolocam. The optics are designed to take advantage of a large field of view. The design, from Zemax simulations, yielded a platescale of 13.6 " /mm.

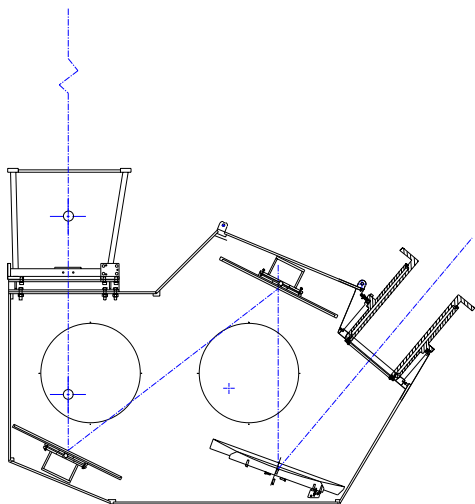


Figure 5.1: The Bolocam optics box. Light from the telescope's secondary mirror bounces off two flat mirrors and an ellipsoidal, then into the cryostat window (right). Figure courtesy of Sunil Golwala.

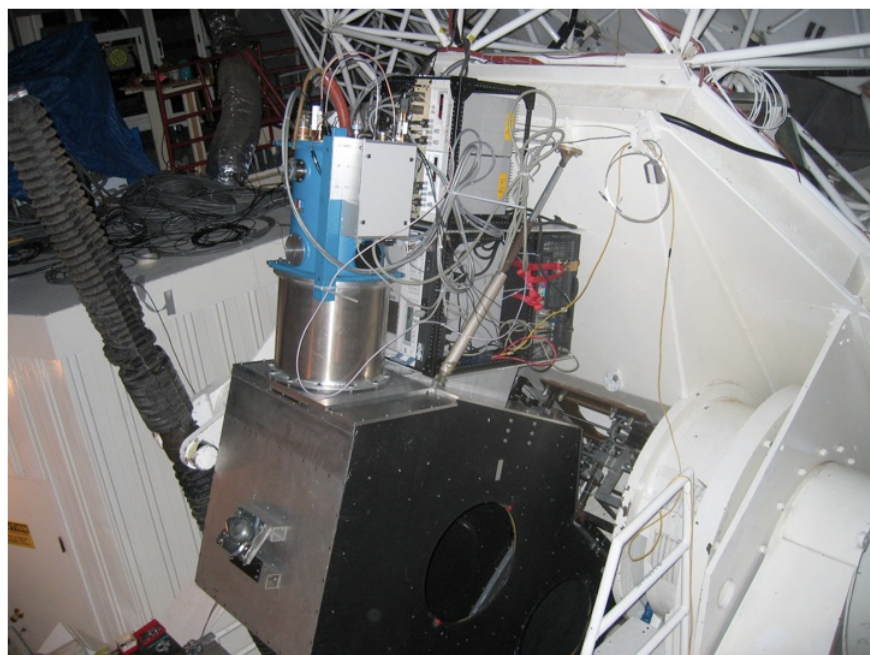


Figure 5.2: The DemoCam mounted to the Bolocam optics box at the CSO.

## 5.2 Description of observing mode

In submillimeter observations using cameras with large arrays, the typical method is to scan over an astronomical field, recording timestreams of data as well as information on the pointing of the telescope. Maps of the fields are made by adding the contributions of detectors at the same point on the sky into bins, which in this run were typically  $10''$  on a side. We used two types of scan patterns - raster scan, in which the scan puts the signal band above sky  $1/f$  noise, and drift scan, in which the telescope is stationary as the sky rotates. In this observing run we used a digital MKID readout combined with the existing Bolocam pipeline for analysis. The Bolocam pipeline allows detector timestreams to be cleaned and converted into astronomical maps. To do this, it merges data from the telescope, such as the azimuth and elevation to which the dish is pointed, with data from the detectors in real time. With these data together, it is set up to track the location of any detector on the sky as a function of time. In addition, it allows data to be cleaned of sky noise by using the response of many detectors in an array to form a sky template, which can be subtracted from all detectors [102]. The pipeline works best in modes in which the telescope is scanning over a source, thus putting the point source signal at several Hertz of frequency rather than at DC.

In the DemoCam run of 2007, most of the work in the readout, recording and projecting of data was done by Dr. Ben Mazin, then of JPL, and is described here. The timestream data was taken using Pentek boards [74] which sampled at 10kS/s, with buffer size of 16,384 points. The challenge was to merge this data, which was taken in less than 30 minute increments, with the continuous telescope pointing data at 1 Hz and 100 Hz. This is necessary to ensure that the telescope is pointed in the correct position corresponding to the resonator data at that time, as discussed in Section 5.3 below.

The first step for each observation is to determine the resonant frequencies for each observation. This is generally done by taking a 60 second integration, during which the LO frequency was varied to create an effective frequency sweep around the guessed frequencies. The first step in determining these parameters is to find and take out the cable delay,  $\tau$ . This is corrected for by

Table 5.1: The parameters involved in quick fits to resonator IQ sweeps.

Parameter	Meaning
$Q$	resonator quality factor
$dx$	fractional frequency off resonance
$dA$	fractional amplitude change
$A_{leak}$	amplitude leakage
$\phi_1$	leakage phase shift
$\theta$	rotation angle of data
$g$	gain
$I_{off}$	offset of loop in I direction
$Q_{off}$	offset of loop in Q direction

transforming  $S_{21}$

$$S_{21,corr} = S_{21}e^{2\pi if\tau}. \quad (5.1)$$

If the cable term is correctly removed, the resonant loops are nearly circular. These sweeps were then fit using IDL's mpfit routine. Nine parameters are simultaneously fit in this program, according to a resonance loop projection. The loop is fit to the equation

$$S_{21} = (I_{off} + iQ_{off}) + ge^{-i\theta} \left( dAdx + \frac{2iQdx}{1 + 2iQdx} - \frac{1}{2} + A_{leak}(1 - e^{idx\phi_1}) \right). \quad (5.2)$$

These values are described in Table 5.1.

After fitting, the next step is to project out I and Q so that these timestreams correspond to fractional amplitude changes and phase shifts, respectively. To project the I and Q correctly, the resonance circle is translated so that it is at the center of the I/Q plane (by subtracting out the fitted parameters  $I_{off}$  and  $Q_{off}$ ), then rotated about its axis (from  $\theta$ ) so that I and Q represent amplitude and phase. This projection is all done after each observation, when the data from the original I and Q directions is in hand. The I and Q data from the observation, which are taken without any processing, are then shifted and rotated accordingly. In theory, the data is now in units of voltage of the overall signal. Dividing out by the mean of the amplitude signal puts these two quantities into units of fractional amplitude and radians for I and Q, respectively.

At this point, the data from the previous observation must be formatted and merged with the telescope data stream. This data stream included the array temperature, source acquisition,

tracking, and observation number logic signals. These are all taken at 100 Hz. The signal data, now at 10 kHz, must match up with these signals fed from the telescope. These are then stored at 50 Hz. The first step was to re-bin the 10 kHz data down to 500 Hz, which effectively is done by averaging. The procedure then uses a downsample filter, a multi-pole frequency space filter to avoid ringing associated with pure averaging to go all the way down to 50 Hz timestreams. This avoids aliasing noise into lower frequency bands. The data are then combined into binary files with all this information included in the Bolocam format, and the Bolocam pipeline acts the same way as it would for a standard run. The readout system could not run continuously, as it had to be interrupted to perform IQ-sweeps and change frequencies.

### 5.3 Integration with Bolocam pipeline

The details of the Bolocam pipeline can be found elsewhere (e.g. [102, 63]); however, some details of the process are described here. The first step is the merger of data from the telescope, including pointing information, with information from the detectors, taken at 100 Hz. In practice, working with this is particularly challenging because the Bolocam pipeline is built around receiving a continuous bolometer timestream throughout the night. The solution used involves “filling the gaps” - creating fake data anytime the electronics were not recording to ensure proper merging and slicing. The data are merged in 1-minute files, placed in netCDF format which incorporates all data together. As data needs to be fed in continuously at the telescope, additional “junk” data is added in between observations of the merged files to keep the Bolocam pipeline from crashing on blocks of time without data. These merged files, at the completion of an observation, are sliced into files including only the scans corresponding to that observation. This is the raw data file for the observation.

Further in the pipeline, files are generated to plot the location of the pixels on the sky relative to each other, and to an absolute pointing offset, and also find the measured platescale (in ”/mm) of the run. Further information is added by hand in the files, detailing the band (Band 1, 240 GHz center or Band 3, 350 GHz center) and resonant frequency used. This information is used by the

cleaning algorithms, which turns the timestreams into pixelated maps, which can correspond to one detector or a coaddition of many detectors. These maps are the end product of the pipeline.

From observation to observation, several variables could be changed, including the resonator frequencies within the 50 MHz window, the length of the scan, and the power sent in on each readout channel. In practice, the readout power was generally fixed at an estimated level of -88 dBm at the device, which was shown in the lab to be conservative and not drive the resonators into saturation.

The run was severely limited, however, by severe problems with the Pentek boards' data acquisition system. It was discovered after the observing run that the unprojected Q data for every other buffer size of 16384 points, corresponding to over 1.6 seconds at 10 kHz, was overwritten by the data from the previous buffer. The unprojected I data were still available, but were effectively useless without its counterpart. Every 1.6 seconds with repeated data were flagged as unusable, effectively creating a hole in the timestream.

## 5.4 Telescope data

### 5.4.1 Data cleaning - sky subtraction and magnetic field cleaning

The raw data was heavily corrupted by magnetic field effects, and thus required cleaning to see sources dimmer than the brightest sky sources (i.e. Jupiter and Saturn). The observing strategy was to perform raster scans in right ascension and declination, which changed the angle of the Earth's magnetic field relative to the focal plane, causing a shift in the resonance frequencies. It was necessary to remove this signal to see the true flux of the sources. To this effect, two cleaning modules were devised and applied. The first module consisted of azimuth regression - effectively taking out a linear fit of the scanning mode with azimuth. The second method involved the simple subtraction of the average signal among detectors in the same band. This average subtraction, however, cannot include any source signal. Thus, an area around bright sources, like Jupiter, is masked off, and does not contribute to the average template. This average subtraction was shown

to be vital in improving signal-to-noise ratio to make dimmer sources detectable.

Several other types of sky noise removal were attempted. Principal component analysis was tried for several observations, but failed due to the small number of usable detectors. In addition, multicolor average sky subtraction fit was attempted for observations with two pixels in two colors. However, due to the extreme discrepancy in optical efficiency between bands (discussed below), this had no significant effect on the noise.

Co-addition of scans across different observations proved difficult due to the lack of a pointing model. It was difficult to measure sources at known coordinates to sufficient signal-to-noise ratio to develop a sufficient model. Thus, this attempt was dropped and only scans from the same observation were coadded.

#### 5.4.2 Beam sizes

Observing point sources and planets enables one to find the effective beam sizes for the different bands, effectively the angular resolution of the band. The beamwidths are straightforwardly measured by fitting the source profile to a Gaussian and finding the best FWHM of the fit. The best sources to use for beam-width measurements are the planets with sufficient signal-to-noise to fit correctly. These are expected to be non-Gaussian, as they represent the convolution of a Gaussian and a radial step function with the observed planet's diameter. However, a Gaussian can generally yield a good enough approximation to sufficiently find the FWHM.

Plotted in Figure 5.3 are the measured beam FWHM, and the size of the beam which, convolved with the source, would yield the observed beam size. In other words, it is the width of the measured Gaussian versus the beam size one would measure if it were a point source. During the run, Saturn had an average diameter of 18", while Jupiter's diameter was 40" [16]. For simplicity, the effective real beam sizes were found by numerically convolving a predicted Gaussian beam with a cylindrical top-hat function representing the source. The effect of the non-Gaussianity of the actual beam should be small, and the errors are dominated by the ability to fit the observed planets with a Gaussian. This leads to a significant observation-to-observation standard deviation

in the observed width.

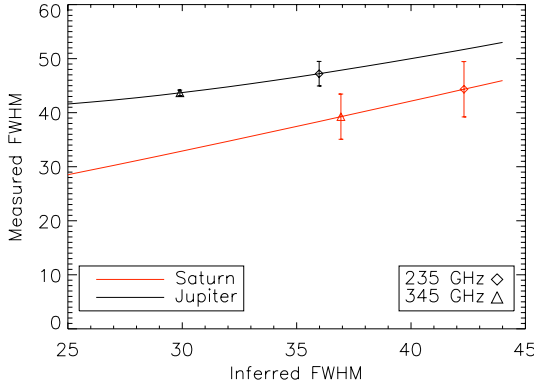


Figure 5.3: The beamsize found from observations of planets, with standard deviations from observation-to-observation scatter. Given the large scatter in measured beam sizes, largely due to unusable data in the observations, the results from the two planets are largely consistent.

Due to the lower scatter in the measurements, the FWHM from the Jupiter observations (30" in Band 3, 36" in Band 1) will be used in responsivity calculations. This will result in a greater sensitivity than using the Saturn numbers, as they incorporate fewer Janskys in a smaller beam, leading to a larger effective responsivity. However, the effect is a small correction, and the Jupiter numbers are closer to the values expected.

It must be emphasized that, due to the large gaps in the data, this method of finding the beam sizes is very imprecise. Most observations had scant coverage over the majority of the beam, making true Gaussian fits relatively suspect. This increases the uncertainty in the derived parameters, both width and peak heights, from the majority of observations.

#### 5.4.3 Responsivity

The responsivity is obtained by observing sources of known brightness, either calibrated sources or planets, and calibrating the response in either phase or fractional amplitude change per unit flux or flux density. The peak fluxes were measured by fitting the map to a Gaussian profile for the source, and finding the best-fit peak value.

The planets observed were generally not small enough compared to the beam size to be

treated as point sources. In order to correctly calibrate the detector, we must know the flux expected in a beam from a non-point source. The correction factors are discussed in Appendix C. This depends on the beam size for extended sources.

Plotted in Figures 5.4 and 5.5 are the calibration of Band 1 from planetary observations. The calibration varies significantly from observation to observation, and relative responsivity of detectors within each observation is highly variable. This is likely due to magnetic field effects, but also to atmospheric conditions changing the load, and therefore detector responsivity. This may be partly caused by the gaps in the data causing uncertain fits, as discussed above.

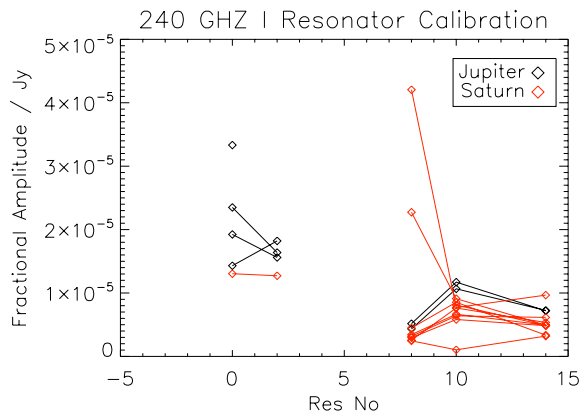


Figure 5.4: The I (projected) responsivity at the telescope. Lines joining points together indicate the calibration is from the same observation.

It is possible to also find the responsivity in kHz/K to a source like Jupiter or Saturn by finding  $Q$  and  $Q_c$  of the resonator during the observation. This is not a direct comparison to the lab responsivity, as the background load is not the same.<sup>1</sup> However, at high loading the response varies slowly with increased effective loading temperature. Again, we assume that the fits are done perfectly, and that the phase direction is correctly projected throughout the scan. With all these caveats, it is still useful to find the responsivities, as they are useful in determining if the responsivity is at least on the correct order of magnitude. These are found in Table 5.2.

As is clear from the table, there is a large discrepancy in Band 1 to Band 3 responsivity.

---

<sup>1</sup> It is also impossible to calibrate out the background load, as this would require measuring  $Q_i$  due to quasiparticles alone. The large magnetic field effects prevented this calibration.

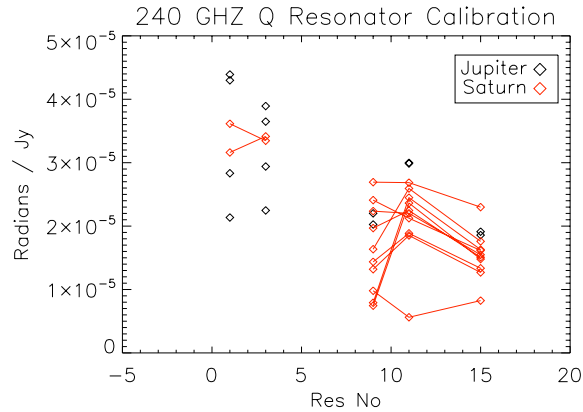


Figure 5.5: The Q (projected) responsivity at the telescope. Lines joining points together indicate the calibration is from the same observation.

Table 5.2: The response in several resonators to observations of Jupiter. Data comes from projecting the phase response back into frequency shift using  $Q$  and  $Q_c$  from the pre-scan IQ sweep.

Resonator	Band	Jupiter Resp (kHz/K)
7.579 GHz	1	2.363
7.589 GHz	1	1.932
7.603 GHz	3	0.287
7.620 GHz	3	0.155

Band 3 detectors generally had many fewer resonators due to assorted difficulties in fitting the data properly, and that the standard deviations are extremely high. The difference in responsivity, as seen here, is close to a factor of 10. The reason for the magnitude of the discrepancy is not understood, but is likely influenced by several factors. As planets are significantly brighter in Band 3, we generally do not see a factor of 10 discrepancy in the significance of detection. Part of the discrepancy comes from the very fast optics not being optimized for the high-frequency band: the Band 3 illumination of the primary mirror is much smaller with the given platescale than that of Band 1. This, combined with the lower Band 3 hot/cold response, accounts for much, but not all, of the discrepancy.

It must be noted that for the brightest sources observed, the individual response in phase or amplitude is so large as to be nonlinear with source flux density. This is fairly difficult to account for due to the very different effect on the phase and amplitude data, the projection of which is imperfect and likely changes over the course of an observation. The response should not vary by more than a factor of two due to this effect, which causes an increase in amplitude response and a decrease in phase response. A combination of the two would lead to a calibration closer to the actual result, although the total responsivity per unit flux decreases with source brightness.

#### **5.4.4 Total sensitivity - noise equivalent flux density**

From those observations with the best IQ loops, we can infer the total sensitivity by comparing finding the noise level reached in a certain amount of time. This can only be done in fields with bright sources to use for calibration, as magnetic fields prevented a global calibration model for the entire run. We assumed over a short integration that the calibration did not change drastically.

The noise in these observations involved finding the RMS deviations over areas in the map not containing sources. The map pixels, which were binned at 10" resolution, are each assigned the number of time samples for which a detector was centered on the pixel. The Noise Equivalent

Flux Density is calculated from this information by

$$NEFD = \frac{F\sqrt{2\delta t}}{(S/N)}. \quad (5.3)$$

Here  $F$  is the source flux density,  $\delta t$  is the time of observation, and  $(S/N)$  is the observed signal-to-noise ratio. The NEFD was found from raster scans of Jupiter (seen in Figure 5.7) and Saturn to be  $1.3 \text{ Jy s}^{1/2}$  at 240 GHz and  $8 \text{ Jy s}^{1/2}$  at 350 GHz. From G34.3 drift scan observations, as seen in Figure 5.6, the NEFD is found to be  $1.6 \text{ Jy s}^{1/2}$  at 240 GHz and  $14 \text{ Jy s}^{1/2}$  at 350 GHz, given the flux calibration from Sandell [98]. This NEFD is expected to be lower, as the effective scan speeds are lower, pushing the signal into a noisier part of the spectrum. The discrepancies in Band 3 are likely caused by the relatively low-level detection of G34.3, as well as a slightly increased skynoise contribution from operating in drift scan mode, which leads to higher atmospheric  $1/f$  noise. The main discrepancies between Band 1 and Band 3 NEFD is caused by the differences in responsivity.

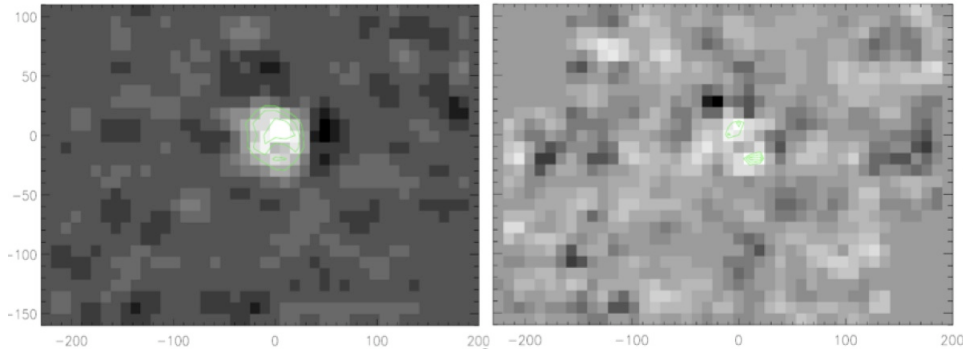


Figure 5.6: An image of G34.3 in drift scan mode, observed with two pixels in two colors. The Band 1 image (left) is detected at  $25\sigma$ , and Band 3 (right) at nearly  $5\sigma$ .

The total sensitivity in Band 1 was found to be on the order of 20 times worse than necessary for background limit, while Band 3's value is on the order of 100 times worse, as calculated from Equation 3.21 and assuming proper illumination of the primary telescope mirror (i.e. the collecting area is what is expected). Given that the optical efficiency in Band 1 is on the order of the expected value, the noise is the limiting factor.

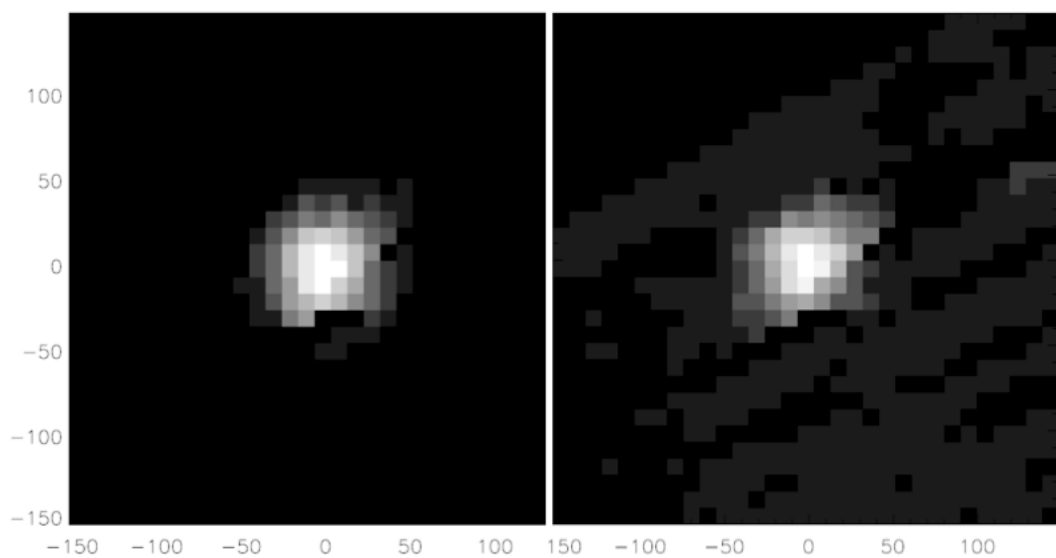


Figure 5.7: Jupiter in 2 bands from the same observation. Both detections are greater than  $1,000\sigma$ .

#### 5.4.5 Magnetic response

The magnetic fields ruined any chance at an overall calibration curve for the run, due to the constant, large changes in resonant frequency and  $Q$ . However, for single scans including a detected source of known flux, we can estimate the magnetic susceptibility. It is possible to project these into I and Q directions; however, the magnetic fields change this projection significantly even over the course of an observation, so the distinction is somewhat misleading. When calibrated, the average shift for the detectors was found to be approximately 590 Jy per degree of azimuth in the I direction and 1380 Jy/degree in the Q direction. These values should be considered with caution, as the both the standard deviations among detectors and the standard deviation for a detector from observation-to-observation are comparable to the average values. While the exact values are difficult to pin down due to calibration uncertainties and the poor state of the data, this shows that one would need to reduce the effect of magnetic fields by a factor of  $10^6$  to put the deviations at the 1 mJy level, which is the typical RMS noise level expected from future surveys. A higher magnetic field susceptibility may be tolerable for point source observations, as the effect of the field varies slowly, and can be removed from the data without significantly harming point-source sensitivity.

The question then becomes what is required for future MKID cameras. The ideal should be to have the effect of the magnetic fields below the ultimate noise level of a typical survey. This does not imply that a magnetic shield capable of 60 dB attenuation is necessary in MKID camera designs. It has been shown that superconducting microwave resonators respond to magnetic fields as  $H^2$  rather than linearly with  $H$  [48]. Thus, a shielding factor of  $10^3$  would put the MKID response at the mJy level if the responsivity is not changed. However, a significant amount of shielding has been shown to be absolutely necessary for MKID cameras which change orientations during observation.

## 5.5 Discussion - contributing factors to the sensitivity found

The sensitivity observed at the telescope was a factor of several worse than expected, and not all of this is fully understood. However, there are several contributing factors which likely worsened the sensitivity. The magnetic fields likely decreased the  $Q$ s of many detectors as had been seen in the lab. This would lead to decreased responsivity in both phase and amplitude directions. One additional factor involved being unable to take the optimal combination of I and Q. Generally, the I direction was found to have better sensitivity, but it was impossible to properly project the data over a scan due to magnetic field effects. Therefore, all sensitivities were found solely in the originally-projected I direction, a linear combination of frequency and dissipation which likely changed over the course of the observation. In addition, no attempt was made to optimize the readout power for sky loading conditions. To improve noise performance, higher readout power should be used. In addition, HEMT amplifier settings will be chosen for reduced gain fluctuations at low audio frequency (i.e., reduced  $1/f$  noise). More detectors, with proper projection, will be able to reject the effect of common-mode gain fluctuations. Thus, there is reason for optimism in large detector noise reduction even with the first generation detector designs.

The second major issue is the discrepancy between Band 1 and Band 3 sensitivity. Band 3, a factor of  $\sim 10$  lower in sensitivity, has many contributing factors which reduced it in comparison to Band 1. The sensitivity of Band 1 in the lab was approximately 1.5 times that of Band 3 (see Figure 4.26). The effective illumination of the telescope was smaller, which results in the same number of Janskys converting to fewer Watts at the detector. Finally, the efficiency of the dish and warm optics is likely worse in the higher frequency band. However, combining all these effects, there is still a large unexplained discrepancy between the responses in Band 1 and Band 3, with Band 1 much closer to the expected response. Both bands exhibited similar noise spectra, leaving the signal-to-noise ratio much higher in Band 1.

The purpose of the run was to demonstrate the viability of MKIDs as astronomical detectors usable in future instruments. In doing so it achieved the first light of MKIDs in any astronomical

observation. In all, there was a very limited amount we could learn from the devices in terms of sensitivity due to readout and magnetic field issues. It is not known if the noise level is truly device noise or some other effect due to its nonuniformity. Many of the questions of sensitivity would have to be saved for future cleaner observing runs with well-tested readout systems and significant magnetic shielding. This fulfilled the goal of a “quick and dirty” proof-of-concept, and while it accomplished the goal of demonstrating MKIDs as a feasible detector in the sub/millimeter. It demonstrated the basic idea of IQ sweeps to re-tune the probe frequencies before each observation as basically sound, and that multicolor MKID operation is a straightforward addition to the Bolocam operating model.

In the future, several of these problems could be corrected through improved readout and magnetic shielding. The readout power could be increased to lower detector noise. In addition, the removal of common mode HEMT drift would be easier with large numbers of detectors in each band, as there was likely much residual noise. So while the first run showed that MKIDs could be used successfully in the sub/millimeter, the demonstration of real sensitivity limits would have to wait for the next observing run.

## Chapter 6

### The MKID DemoCam rebuilt

In this chapter we discuss the second general design of MKID devices. We present the design changes for the rebuilt DemoCam instrument, descriptions of new device iterations, and results of testing (many of the methods of testing are discussed in Chapter 4). While individual devices discussed here differ significantly, the overall design in terms of pixel design, number of detectors, and tile size is largely the same. The goal of the tests here is to understand the optical properties of antenna-coupled MKIDs, and to identify and account for any systematic defects with the new large arrays of MKIDs.

This chapter generally focuses on several main themes: the validity of the  $\alpha/\Delta_0$  fitting applied in previous devices; the identification of the causes and solution to coupling between resonators; the identification and general solution to response to light not through the antenna; and the total efficiency of the devices and optics for astronomical use. The testing is described largely in chronological order, as these issues were encountered.

#### 6.1 Magnetic shield implementation and hardware changes

To reduce the intolerable sensitivity to magnetic fields, the DemoCam Dewar was completely rebuilt to incorporate a Cryoperm® magnetic shield. Fields orthogonal to the array were the primary concern, so the bottom end needed to be completely closed off, with as small a top aperture as possible. The physical constraints of the Dewar required a small diameter magnetic shield, and a change in the optical axis from 2 inches off-center to 1.5 inches. The shield was designed to lie

outside the 4 K optical train, consisting of a cylinder surrounding the lens, Lyot stop and array. This design had to account for a change in  $f/\#$  to as large as  $f/3$ , and is thus over 12 inches long. In addition, Amuneal suggested tubulations at the top of the magnetic shield to enhance shielding. However, these would have interfered with our expanding beams, and would require a larger aperture. A compromise was reached in using conical tubulations, which flare outward, to avoid vignetting. It is unknown what, if any, effect these tubulations have in reducing the magnetic pickup.

The shield was made out of .040-inch-thick Cryoperm-10®, which gives a larger field reduction factor than thinner varieties. The shield consists of two layers, effectively two separate shields, joined by OFHC copper rings for heat sinking. Including the copper, the shield weighs over 15 pounds, which may lead to pointing offsets in the telescope if the shield bends in different orientations. To minimize this, the shield is mounted to three large diameter copper rods which are in turn sunk to the baseplate. These rods mount to a copper ring in the middle of the shield, where the top (open ended, Lyot stop end) and bottom (closed end) shields join. All coaxes and wiring are fed through this break, and the optics and array are mated to the mount ring.

The shield mounting hardware is shown in Figures 6.1, 6.2 and 6.3. Figure 6.1 shows the inside of the lower half of the magnetic shield, but with the array and ultracold (UC) stage removed. The Teflon lens is shown attached via copper extensions to the copper ring, which is used as structural support and for heat sinking the magnetic shield. The top half of the magnetic shield (enclosing the Lyot stop) is seen at the bottom, attached to the copper ring.<sup>1</sup> Vespel posts keep the intercooler (IC) and UC stages thermally isolated, but rigidly supported structurally. NbTi superconducting coaxes can be seen avoiding the optical path as they connect the array to the outside world. Figure 6.2 shows an old device mounted in this configuration as is looking down the optical chain. The lens is not present here, but one can see the coaxes and thermal straps (connecting the stages to the appropriate fridge coldhead) bent to avoid the optical path and connect outside the shield.

---

<sup>1</sup> Here “top half” denotes the half closer to the window, or top half while the Dewar is upright, with the cold plate facing upward. When cold, the window is pointed downward, and the “top half” is the half closer to the window.



Figure 6.1: View of lens and coaxial cable mounts inside magnetic shield. At top is where the UC stage and focal plane would be mounted. Figure courtesy of Nicole Czakon.

This shows the entirety of the closed end, or bottom half of the magnetic shield, as viewed from the Lyot stop location. Figure 6.3 shows a new device stage, based on the previous design, capable

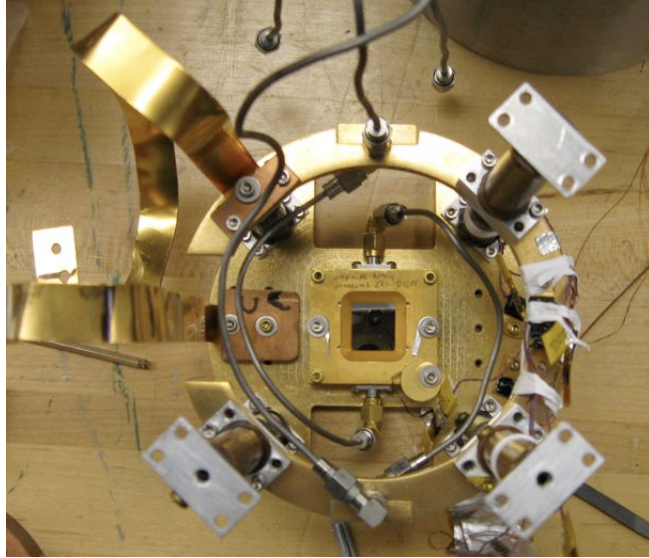


Figure 6.2: Sapphire device (Device 2) mounted in new DemoCam hardware. Here we see the view of the device from the location of the copper ring. This picture is taken from a point near the location of the Lyot stop once fully assembled. Figure courtesy of Nicole Czakon.

of mounting the new, larger tiles with IDC resonators. This takes the place of the stage in Figure 6.2. Finally, Figure 6.4 shows the assembled magnetic shield mounted in the DemoCam Dewar. The “conical tubulations” can be seen at the top of the magnetic shield.

As the purpose of DemoCam is to demonstrate final camera sensitivity, the optics were modified to match the platescale of 7 "/mm to be used in the final MKID camera. The optical train was extended to a length of approximately 11 inches to allow for both good Strehl ratios at the array and an even sampling of the primary image at the Lyot stop. Originally, the lens used was Ultra-high Molecular Weight Polyethylene (UHMWPE), with a higher index of refraction than Teflon. However, this proved problematic to anti-reflection (AR) coat, and a Teflon lens replaced it after initial testing of the magnetic shield. The new optical design with the Teflon lens is seen in Figure 6.5.

Initially, the design called for only Teflon IR-blocking filters, due to the large quantity of



Figure 6.3: A new  $6 \times 6$  device mounted on the new ultracold (UC) stage. Stage and mount designed by Matt Hollister.



Figure 6.4: The magnetic shield mounted in the DemoCam Dewar. Figure courtesy of Nicole Czakon.

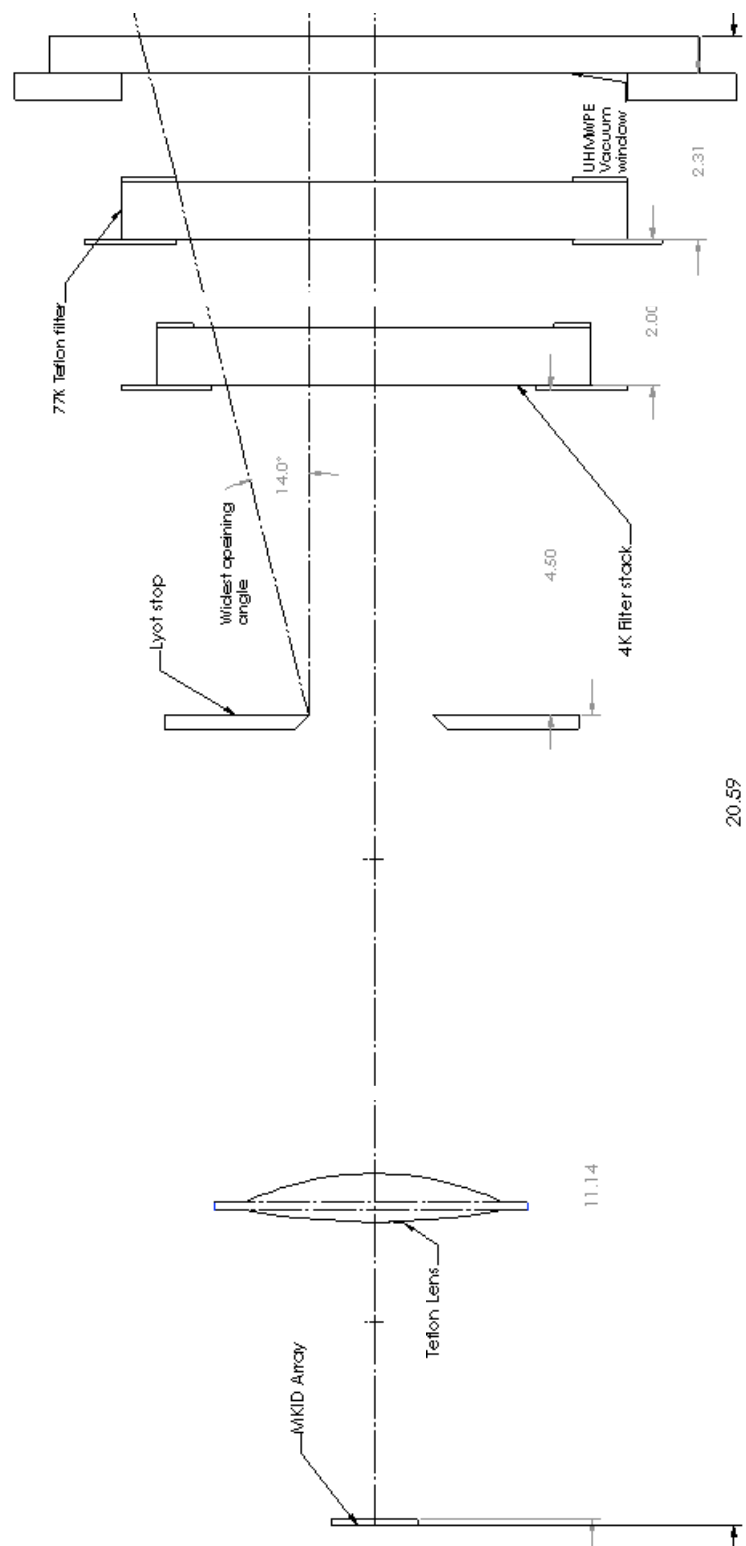


Figure 6.5: New optical design, with Teflon lens.

Teflon and the inability to quickly obtain Fluorogold. However, after initial tests found relatively large excess loads, a 1/8" thick sheet of Fluorogold was added in between two Teflon filters in the 4 K stack. As is discussed below, some tests also included a 420 GHz metal mesh low-pass filter<sup>2</sup> to test the effect of blocking high-frequency radiation.

## 6.2 New devices

### 6.2.1 General device design

In the previous devices, the designs remained effectively unchanged, with only substrate and aluminum absorber thickness varying from device to device. Due to the numerous mask iterations in the newer designs discussed here, it is best to consider the separate devices in chronological order to understand how things were developed, and why.

The new resonators feature a radical departure from the old design in the coupler to the feedline. These use interdigitated capacitors (IDCs), discussed in Section 2.2, as the effective capacitive section of the resonator. With the significantly lower frequency noise contribution, we expect markedly improved performance compared to previous designs. The responsivity is effectively the same, only changing due to the altered current distribution along the resonator.

The new designs all have several characteristics in common, which do not vary from device to device. The antennas are designed to be 4.2 mm long on a side, increased from the 3 mm length used before. These antennas have double the number of slotlines, and double the number of taps (RF shorts) on each slot, both from 16 to 32. This enables better high-frequency performance while allowing more of the space on the focal plane to be devoted to antennas as opposed to detectors. The larger pixels also allow for good coupling to a smaller platescale, such as the Bolocam-like 7 " /mm chosen for the final camera. The new designs also incorporate four resonators per antenna, as planned for the final array devices to be used. The new larger antennas provide more space on the focal plane to achieve a similar filling factor; it is easier to fit in the larger IDC resonators, used

---

<sup>2</sup> made by Dr. Peter Ade of Cardiff for the Bolocam instrument. When Bolocam was not in active use at the CSO, it was borrowed for testing in the DemoCam.

in some form on all newer devices, without a significant loss in efficiency. The devices are increased to  $6 \times 6$  arrays of antennas, from  $4 \times 4$ . In all devices made with this design, four resonators are associated with each antenna, for a total of 144 resonators. The resonators are coupled to the antenna through bandpass filters centered at 230, 290 and 350 GHz (Bands 1, 2 and 3); the fourth resonator is uncoupled to the antenna, and is considered “dark” for testing purposes.

Based upon the measured kinetic inductance fractions from previous devices, it was determined that the initially-deposited thickness should be greater than 60 nm to ensure high  $Q_s$  and few “collisions.” Therefore, the aluminum thickness is increased to 70 nm deposited. To match the expected value of  $Q$ , the coupling strength is reduced to an expected  $Q_c \sim 60,000$ . This was determined from simulation, and from experience with previous couplers. Due to the relative insensitivity of the bands to the  $Q_c$  value, the distance between the capacitor and the feedline is left the same for all bands for these devices.

### **6.2.2 Devices made and tested**

The device names given here are those colloquially assigned by those testing the devices in order to differentiate testing more easily without resorting to date of fabrication. Each device has its own iteration on the basic design. These changes, and the results from each device, are given in the following sections. For quick reference, a device number was given to each independent design to which a significant mask change was made. A list of devices tested is given in Table 6.1.

The fabrication and testing of each device motivated changes in the next device. Because of this linear progression in design, unlike the CPW devices, it is helpful to overview what was tried in each device, and why changes needed to be made. Device 4, the first IDC device, had two fundamental problems: resonator-to-resonator coupling causing crosstalk, and direct pickup to light through the capacitive section of the resonator. Device 5 was made with a new stepped-impedance filter to eliminate pickup from the capacitive portion, and with different resonator arrangement to limit crosstalk. In addition, half the resonators were CPWs in order to compare IDC and CPW direct pickup. However, yield issues largely limited this array’s usefulness, and it was primarily

Table 6.1: Devices of the new design tested in the new DemoCam.

Device Number	Resonator Type	Substrate Material	Aluminum Thickness	Comment
1	CPW	Silicon	60 nm	“Si device” - 32 res, 2 colors
2	CPW	Sapphire	60 nm	“Sa device” - 32 res, 2 colors
3	CPW	Silicon	30 nm	“Thin Al device” - 32 res, 2 colors
4	IDC	Silicon	70 nm	144 res, 3 colors, 1 dark
5	IDC/CPW	Silicon	70 nm	72 CPW, 72 IDC res
6	IDC/CPW	Silicon	70 nm	No transmission
7	IDC	Silicon	70 nm	No transmission
7b	IDC	Silicon	70 nm	No resonators visible
7c	IDC	Silicon	70 nm	144 resonators, 3 colors, 1 dark
8a	IDC	Silicon	70 nm	No transmission
8b	IDC	Silicon	70 nm	Gold wire bonds for heat sink

used to check bandpass filter performance. The yield issues were finally solved with Device 7c, made entirely of IDCs with stepped-impedance filters. This device showed dark resonators with significant response to hot/cold loads. It was determined that a majority of this pickup came from the heating of the array tile under load. Therefore, a final device was made – Device 8b – using gold wire bonds for improved heat sinking of the array. This final tile had reduced the effect of the three primary concerns: direct pickup, inter-resonator coupling, and tile heating, while also having a high detector yield.

### **6.2.3 Testing methods**

Here we show the results of testing similar to those seen in Chapter 4. Of particular interest are experiments with the hot/cold (300 K/77 K blackbody) response under different conditions, in order to find the total response of the system. Where possible, dark detector data was used to fit for fundamental parameters necessary for the experiment. One notable exception is the recombination constant,  $R$ . The IDC resonators are no longer quarter-wave resonators, and therefore no longer have higher harmonics one can use to create quasiparticles via microwave power. On-resonance probes generally are more efficient at quasiparticle heating than at creating quasiparticles at this low frequency, and the result is generally the saturation of the resonator with a very small quasiparticle contribution.

Optical tests of bandpasses (via Fourier Transform Spectroscopy) and beam maps were taken extensively. However, antenna and bandpass filter design, which these measurements primarily test, are generally beyond the scope of this thesis.

## **6.3 Device 4 - testing and parameters**

The first iteration  $6 \times 6 \times 4$  (36 antennas, 144 resonators) device was known as Device 4. In this device, resonators were nominally spaced 2.7 MHz apart from adjacent resonators, leaving the full set of resonators inside a 400 MHz bandwidth. In order to reduce the effect of thickness variations across the array on the scatter in resonance frequencies, the frequency scheme of the resonators was

re-done from the  $4 \times 4 \times 2$  designs. In a given column, adjacent resonators in frequency space are adjacent in physical space. In each new column, the frequencies then increase from the maximum of the previous column. Thus, slowly changing variations in superconductor thickness (and therefore kinetic inductance fraction) should have reduced effect in the dispersion in frequency between adjacent resonators.

This device was particularly useful in demonstrating several flaws in our initial design. These include, in particular, coupling between nearby IDC resonators and large amounts of “dark” pickup by the resonators. It also demonstrated basic functionality of design and understanding. Dark tests of the device showed all 144 resonators in the nominal bandwidth. In addition, several test resonators served as a double-check on our method of fitting for kinetic inductance fraction and gap parameter, which are essential for the calculation of optical efficiency.

### 6.3.1 Device Parameters

#### 6.3.1.1 $\alpha$ test resonators

In the IDC  $6 \times 6 \times 4$  device, there are two  $\alpha$  test resonators worthy of note: an all-aluminum with a 3-1 geometry and an all-aluminum 6-2 resonator. Here, a 3-1 (6-2) geometry refers to a 3 (6)  $\mu\text{m}$  wide center strip CPW with 1 (2)  $\mu\text{m}$  gap width between the center conductor and the ground plane. All the resonators are quarter-wave CPWs. As discussed in Section 2.1, the kinetic inductance (KI) fraction is given by

$$\alpha = \frac{L_k}{L_m + L_k} = \frac{L_k/L_m}{1 + L_k/L_m} \quad (6.1)$$

where  $L_k$  is the kinetic inductance and  $L_m$  is the geometric, magnetic inductance. It is shown in Ref. [36] that

$$\frac{f_i}{f_0} = \sqrt{\frac{L_0}{L_i}} = \sqrt{1 - \alpha_i} \quad (6.2)$$

where  $i$  represents the measured resonator index, and 0 represents values only accounting for geometric factors. Note that the error here is large if the kinetic inductance fraction is low.

Now, if we have two resonators with the same designed frequency (i.e. CPW length), but with different kinetic inductance fractions, we can find the KI fraction of both if we know their relative response (assuming the same  $\Delta$ ). The equation to solve becomes

$$\frac{f_2}{f_1} = \sqrt{\frac{1 - \alpha_2}{1 - \alpha_2 \frac{\alpha_1}{\alpha_2}}} \quad (6.3)$$

If we know  $\frac{\alpha_1}{\alpha_2}$  and  $\frac{f_2}{f_1}$ , we need only solve for one variable,  $\alpha_2$ .

In tests, we measure the response of all these resonators to temperature changes. If the gap parameter is the same, the only scaling should be due to a different kinetic inductance fraction. From Equation 2.11, we see that finding the average ratio of  $df/dT$  gives  $\frac{\alpha_{6-2}}{\alpha_{3-1}}$ . The only other parameter determining the shift,  $\Delta$ , should be the same. For the two aluminum resonators, this value was  $0.652 \pm 0.093$ . If we use this relative response, along with the frequencies taken at the lowest temperature in Equation 6.3, the result is  $\alpha_{3-1} = 0.230$  and  $\alpha_{6-2} = 0.150$ .

Scaling to the IDCs requires simulation. However, for a rough value, we can just use the ratio of the aluminum section length to the overall meander length. At the longest meander, this value is 3.1 mm, with 1 mm of aluminum (relative sizes are seen in Figure 6.15, later in this chapter). Thus we should expect about  $\alpha = 0.037$ , which is close to what we see from standard Mattis-Bardeen approach, discussed in Chapter 4, the results of which are given in Section 6.3.1.2 below.

A more direct way of finding the effective kinetic inductance fraction for the IDC resonators is to compare directly the frequency shifts of those resonators at the same temperature. There are two factors which must be applied to the relative frequency shift –  $\alpha$  and the relative responsivity of  $\sigma_2$  at the IDC resonator's frequency.

### 6.3.1.2 Mattis-Bardeen fitting for $\alpha$ and $\Delta_0$

The effective kinetic inductance fraction becomes much easier to fit at lower temperatures using the standard two-parameter Mattis-Bardeen approach. This is likely due to the reduced effect of the two-level systems in the IDC devices. An example of one such fit is shown in Figure 6.6, and the residual normalized to the error at each point are seen in 6.7. There is no significant residual

from incorporating all the data, so it is likely the effective kinetic inductance fraction is close to the optimal fit found. One device's optimal fit contours are seen in Figure 6.8, while a collection of resonators are shown in Figure 6.9. Table 6.2 shows the best fits to the Mattis-Bardeen method,

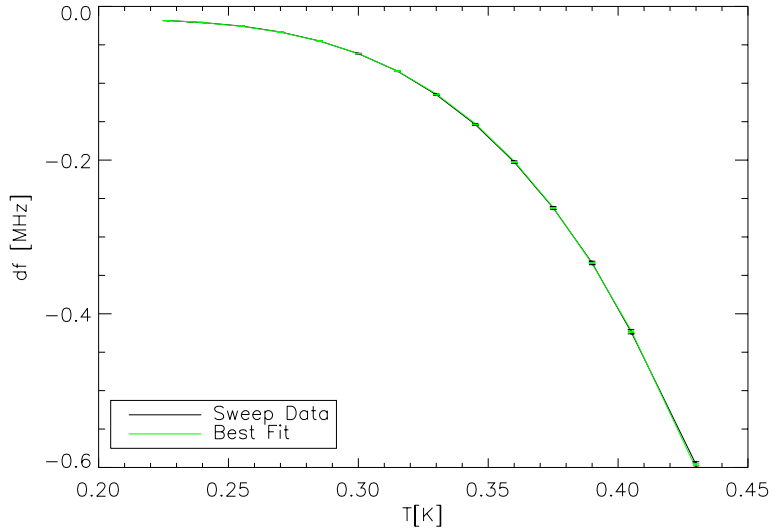


Figure 6.6: IDC resonator plot of best  $\alpha/\Delta_0$  fit with error bars (including temperature errors in green and without in black). From Device 4.

and using the  $\alpha$  test resonators. This shows that the two methods are generally consistent.

### 6.3.2 Inter-resonator coupling

A large scatter was observed in the values of  $Q_c$  among resonators, as seen in Figure 6.10. Given the precision of the distance between the capacitor of the IDC and the feedline, the main variable in determining  $Q_c$ , it is highly unlikely that an order of magnitude variation in  $Q_c$  can be explained by this variable alone. Thus, it stands to reason that the high variability is due to the coupling of nearby resonators in both frequency and on the array. In addition, it is difficult to explain the uniformity of response among all resonators (seen in the following section) given that they should have different bandwidths, and one quarter should be dark. We have seen the significant difference between bands on previous devices, so the uniform responsivity heavily indicates a method of coupling which evens out response between resonators.

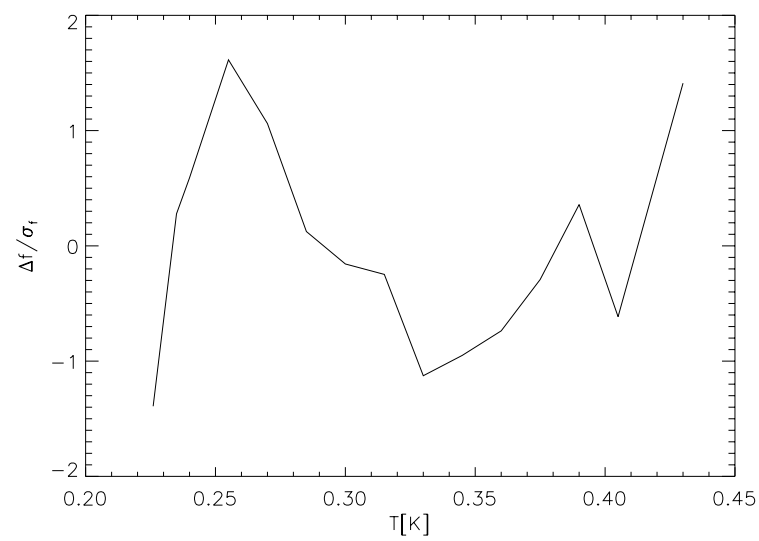


Figure 6.7: IDC resonator residual to best Mattis-Bardeen  $\alpha/\Delta_0$  fit.

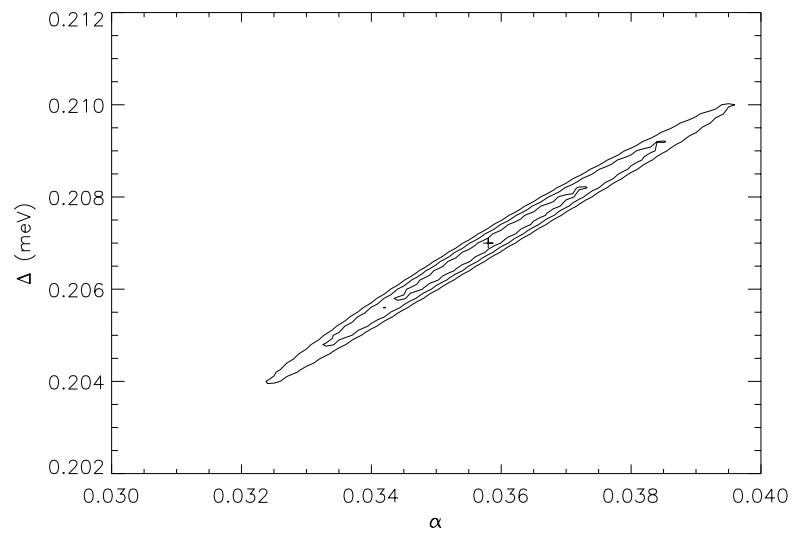


Figure 6.8: IDC resonator  $\alpha/\Delta_0$  contour plot.

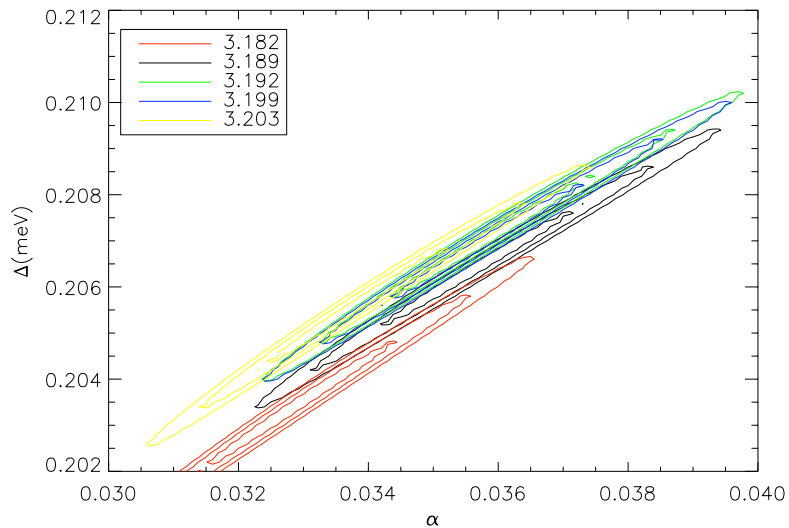


Figure 6.9: An assortment of  $\alpha/\Delta_0$  contour plots from Device 4. The resonance frequencies, in GHz, of the selected resonators are given in the legend.

Table 6.2: Results of the different versions of  $\alpha$  testing.

Res Freq.	$\alpha$ M.B.	$\Delta_0$ M.B. (meV)	$\alpha$ test
3.182	.0328 <sup>+.001</sup> <sub>-.0008</sub>	.2034	.0368
3.189	.0356 <sup>+.001</sup> <sub>-.0009</sub>	.2064	.0347
3.192	.0356 <sup>+.0012</sup> <sub>-.0009</sub>	.2068	.0341
3.199	.0338 <sup>+.001</sup> <sub>-.0008</sub>	.2056	.0340
3.203	.0357 <sup>+.0011</sup> <sub>-.0009</sub>	.2070	.0346

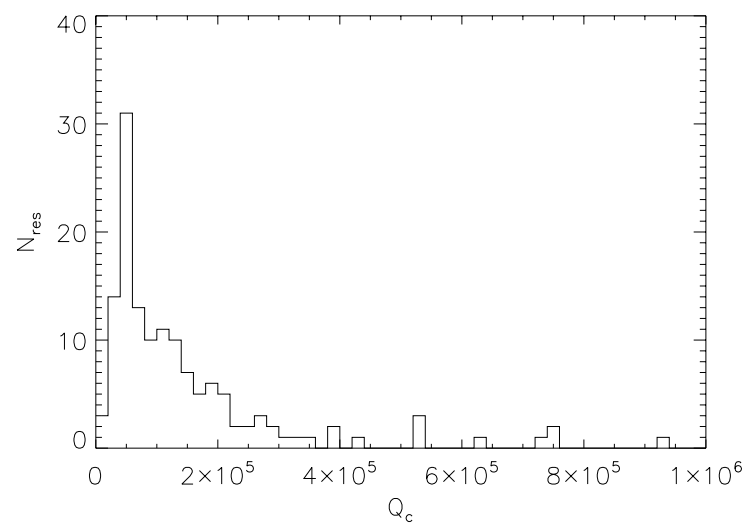


Figure 6.10: A histogram of  $Q_c$  for IDC resonators, with binsize of 20,000.

The best way to test this effect is to try driving a resonator with high levels of microwave power, and to look for the effect on nearby resonators, via a technique dubbed “pump-probe.” This is easily done by combining a signal at a fixed on-resonance frequency, the “pump” signal, with a Network Analyzer sweep of frequencies with nearby resonators, the “probe” sweep. As the pumped resonator is driven into saturation, we can see if the nearby resonators shift in  $Q$  or in resonance frequency. Because the coupled resonators are not themselves being saturated with readout power, they should remain in the standard Lorentzian profile, rather than being driven into a nonlinear regime. If the resonators are completely uncoupled, there should be no effect whatsoever.

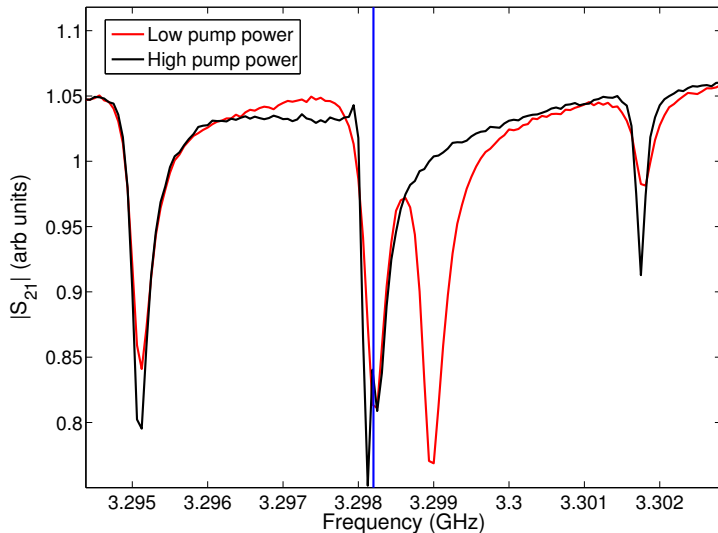


Figure 6.11: Results of “pumping” on a resonance, with frequency shown by the blue line. Plot shows  $|S_{21}|$  for different pump powers. Nearby resonators change significantly in  $Q$  and shift in resonance frequency under high pump power. In one case the resonance seems to disappear entirely.

Figure 6.11 shows the effect of this. If the resonators were uncoupled, we would see no change in the resonator profile of nearby resonators by the “pump” signal – it would be the equivalent of sending a very high power off-resonance, there is no response. If there is coupling, the primary resonator would saturate, due to the large amount of power. Other resonators, coupled but not receiving power, would shift in frequency but not become distorted. This is precisely the effect seen in Figure 6.11.

Additional information supported this conclusion, as well. In particular, in FTS measurements of bandpasses, resonators typically showed superpositions of multiple bandpasses for a single resonator. It appears that any response is a combination of responses from multiple resonators, and not an independent resonator response. This effect is seen in Figure 6.12.

### 6.3.3 Response, excess load and out-of-band pickup

Initially, the large detector response, and uniformity among detectors, led to speculation of the IDC capacitor acting as an antenna, coupling out-of-band radiation to the aluminum section of the resonator. The response to hot-cold tests was significantly more than predicted given the measured kinetic inductance fraction in the initial tests. The response is highly uniform among all detectors, as seen in Figure 6.13, which would not be expected if in-band pickup was the only response mechanism. Three separate filter stacks at 4 K were used to test the response and resulting excess load: 0.8 inches of Teflon only, Teflon plus a 420 GHz low-pass metal mesh filter, and Teflon plus 1/8-inch thick piece of Fluorogold. In the metal mesh configuration, the 4 K window aperture was reduced temporarily to a 3-inch diameter, but Zemax simulations showed this effect to be small ( $\sim 10\%$  for corner pixels, and effectively negligible for central pixels). Only the first 30 resonators were fitted, as this gave a large enough sample size, and it excludes effects from the low- $Q$  resonators at  $f > 3.4$  GHz. The response is significantly curtailed with more filtering, as is the excess load (Figure 6.14). These tests show clearly that some filter more aggressive than Teflon is required to reduce excess load and spurious response. The extra filtering is likely cutting into the broadband response from the IDC direct coupling, as this is unaffected by any bandpass filtering. This response can also be seen in the FTS data. Figure 6.12 in the previous section shows the nonzero out-of-band response, which is cut off by the 420 GHz low-pass filter. This response continues up to high frequency if not cut off by the metal mesh. This is particularly troubling, as it suggests significant out-of-band coupling to a chopped, point-like source, which would imply possible broad-band coupling to astronomical sources.

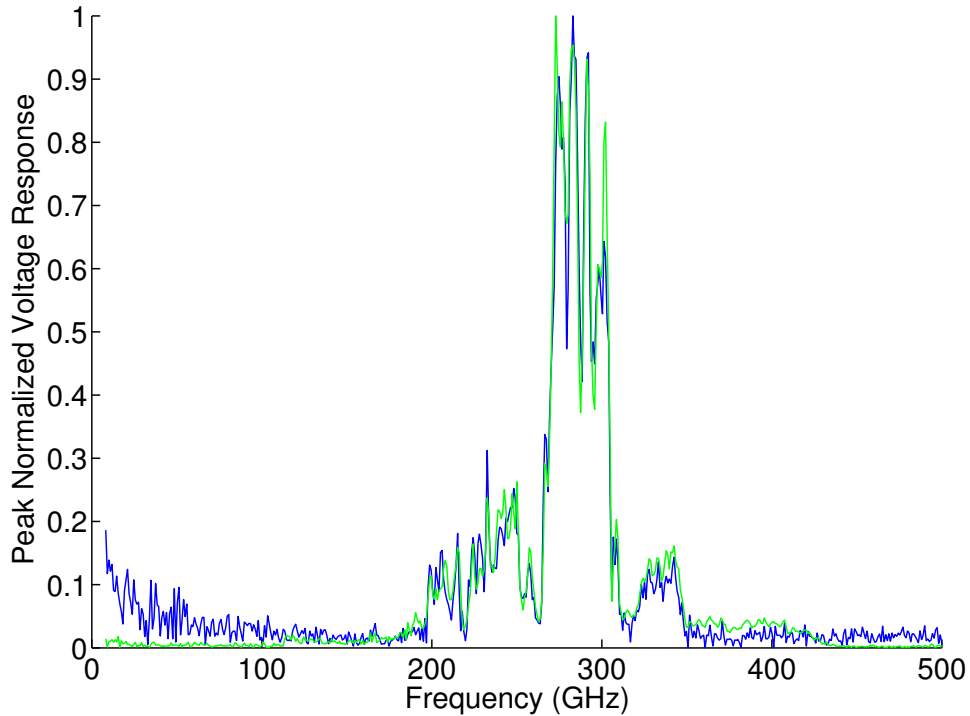


Figure 6.12: Typical response of Device 4 bandpasses in an FTS measurement. In one resonance is seen the superposition of the response of several resonators. Plotted are response with (green) and without (blue) a 420 GHz low-pass metal mesh filter in the filter stack. One can clearly see out-of-band pickup, which is cut off by the filter. Figure courtesy of Nicole Czakon.

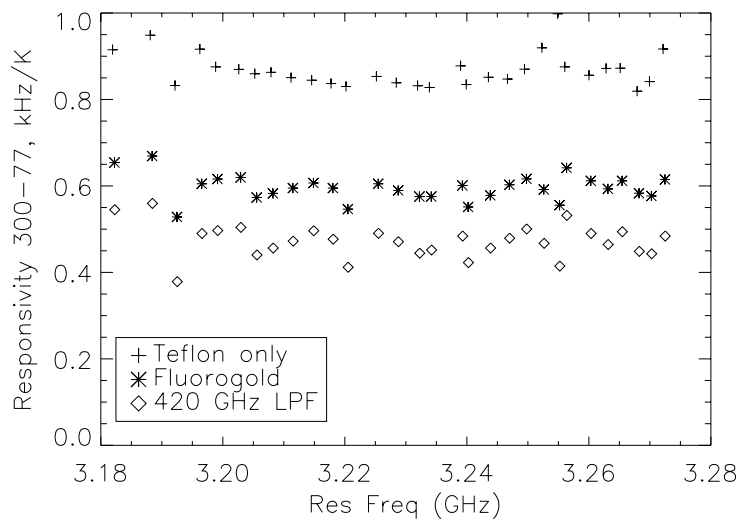


Figure 6.13: Responsivity of the first 30 resonators of Device 4, with different 4K filter materials.

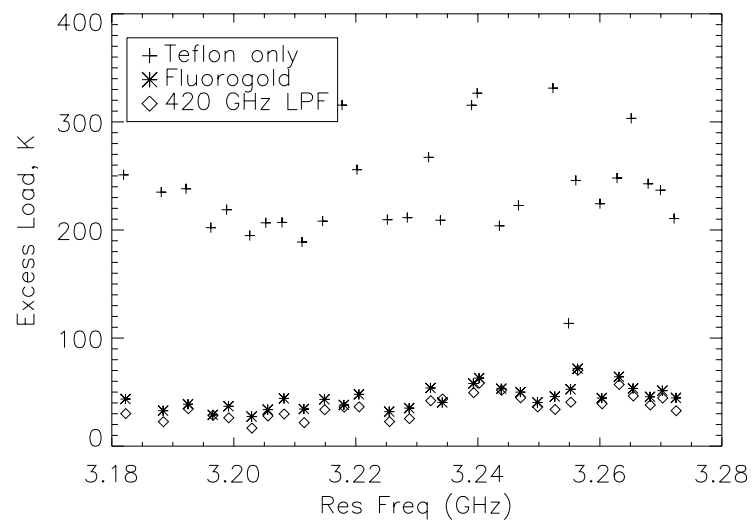


Figure 6.14: Excess load of the first 30 resonators of Device 4, with different 4 K filter materials.

## 6.4 Device 5 - A second iteration

### 6.4.1 Device design

In the iteration from the first IDC device try, several modifications were attempted to reduce systematic errors. The most major change was to split the array into two parts - half the array containing IDC resonators in the 3-3.4 GHz range, and half containing CPW resonators in the 5-5.4 GHz range for comparison, and to test bandpass designs.

First, to reduce the coupling between nearby resonators adjacent in frequency space, a new frequency scheme was adopted. This increased the spacing between resonators from 2.7 MHz to 5 MHz, roughly double that expected from the final configuration. In addition, the idea of nearby resonators being nearby in frequency was scrapped. The new configuration consisted of grouping of bands, such that the first 18 resonators were Band 2 ( $\sim$ 290 GHz band center), the next 18 Band 1 (center  $\sim$ 230 GHz), the next Band 3 (center  $\sim$ 345 GHz) and the last 18 dark. Thus, the nearest resonator in frequency would be three physical resonators away. This would also leave any residual coupling between the two as an effective “beam-smearing” instead of a color leakage.

The second major change involved the implementation of a “stepped-impedance” filter between the aluminum absorptive section of the resonator and the interdigitated capacitor [105]. This filter, shown in Figure 6.15 involves varying the width of the center strip of the CPW feed between the two points. Over the distance between the capacitor and the aluminum section, the width of the center strip varies between 1 and 16  $\mu$ m. This provides an effective filter against high frequency radiation by changing the impedance at millimeter-wave frequencies, while leaving the microwave frequencies effectively untouched. The design of the filter only blocked up to 700 GHz, as beyond that point Fluorogold has very good absorption in the filter stack.

Based on the previous device, bandpasses were tweaked to fit into the atmospheric windows properly. As in the case of the bandpasses discussed in Section 4.2.3.3, the bands were designed to fall within the atmospheric windows of low atmospheric absorption. Like the previous device, these bands were designed by Ran Duan for optimal sensitivity and low crosstalk. The IDC resonators

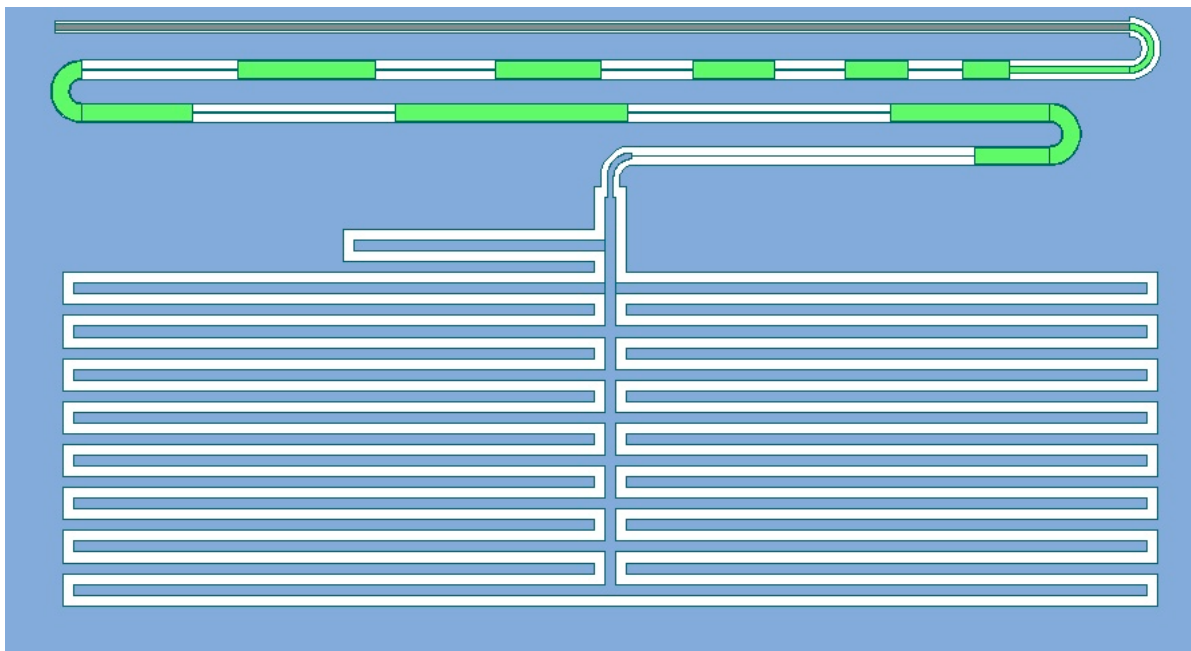


Figure 6.15: Design of IDC resonator with stepped-impedance filter [105]. Here blue represents niobium groundplane, gray represents aluminum, and white represents exposed substrate. The stepped impedance filter, also made of niobium, is shown in green. The filter varies between a canted width of 1 and 16 microns, inside a constant 18 micron-wide CPW section.

were designed to detect the same bandpasses in Device 4. Although Band 3 was found to be far too low in frequency (and in the middle of an atmospheric water absorption line) this was done for uniformity in assessment of improvements in this device. The CPW resonators, conversely, were used to test different bandpass designs. These included optimally modified bandpasses as well as designs both 15 and 30% from the optimal band center. The intention was find which design empirically fits in the correct band location.

#### **6.4.2 Device testing**

##### **6.4.2.1 Responsivity**

Device 5 was only tested with open windows to find its optical response. This is primarily because it was found to have several complications during testing. The number of IDC detectors between 3.0 and 3.4 GHz which could be easily fit was found to be only 19, while the number of CPW resonators between 5.0 and 5.4 GHz was only 20. In particular, nearly all Band 3 and dark resonators were missing from their IDC locations. Thus it was very difficult to determine dark resonator pickup. One resonator seemed to be located in the dark frequency range, and showed significant hot-cold response, but it was difficult to reach any conclusions with only one resonator. In general, the total response seemed to be on par with expectations, at the 0.6 kHz/K level for hot/cold measurements, as seen in Figure 6.16.

The paucity of detectors and clearly defined bandpasses, combined with a lack of dark data, did not allow for a clear test of systematics. In particular, the almost total lack of Band 3 and dark resonators made any complete study of the responsivity, in particular the response outside of the antenna response, impossible. These would be reviewed further in future devices.

##### **6.4.2.2 Inter-resonator coupling**

The new resonator scheme showed no significant response to pump-probe tests. In addition, the coupling  $Q$ s showed significantly reduced variation; the average  $Q_c$  was found to be 86,200 with a standard deviation of 33,300. This is significantly higher than the CPW standard deviation of

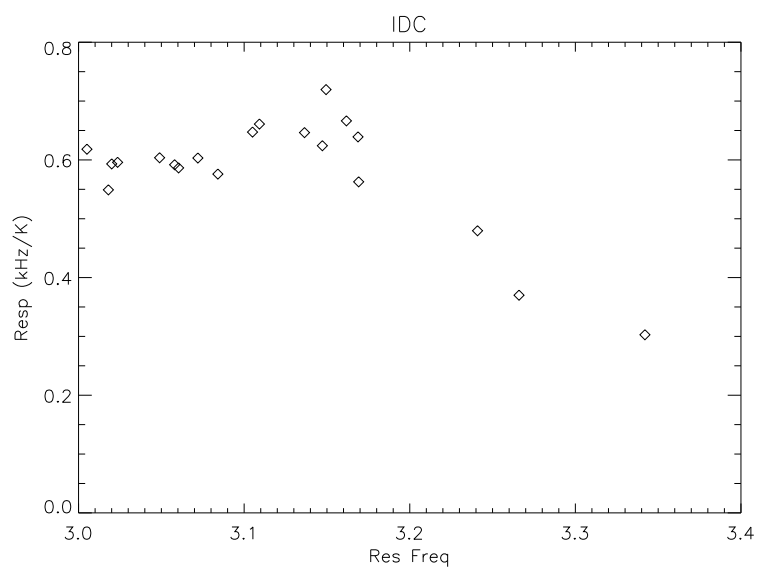


Figure 6.16: Hot/cold response for IDC resonators on Device 5.

7,900 with an average of 25,400, but much smaller than the deviation in Device 4. In particular, there was not tail to very high  $Q_c$ . With this new scheme, therefore, we do not consider inter-resonator coupling to be a significant problem, though this does not rule out the possibility for designs with resonators closer in frequency space.

#### **6.4.2.3 Power levels**

One troubling issue with many resonators on this device was the low saturation power, which limits the maximum power used in readout. In Figure 6.17 one can see the effects of power saturation on four resonators. This shows the magnitude of the response as a change in  $S_{21}$ . When it is driven into saturation, the resonance loop is effectively truncated before the resonance frequency, leading to a discontinuity and the apparent large response. This effective discontinuity is seen in Figure 6.18. In fact, this apparent response only comes because the saturation frequency is dependent upon quasiparticle density, which is greatly different between 77 K and 300 K loads. However, the distorted resonances shown at 3.005 and 3.020 GHz, can still be used effectively. Notice that the resonator at 3.014 GHz is already saturated at the lowest power setting, the 3.018 GHz resonator does not saturate until increased power is applied. It is unknown why different resonators of the same band would saturate at different powers, and could be related to some fabrication process, though this is purely speculative.

#### **6.4.3 Conclusions**

This device was primarily used to test bandpasses, and to test the effect of CPW and IDC resonators on the same chip. The specific bandpasses are not within the scope of this thesis, save to say that all variations had roughly the same effective bandwidth from detector to detector in the same band. The IDC and CPWs seemed to respond similarly, with higher frequency response in the CPW resonators likely due to a higher effective kinetic inductance fraction. It was impossible to make any conclusions about dark response from this device alone, due to the small number of resonators. However, this device did confirm the basic functionality of our fix to the inter-resonator

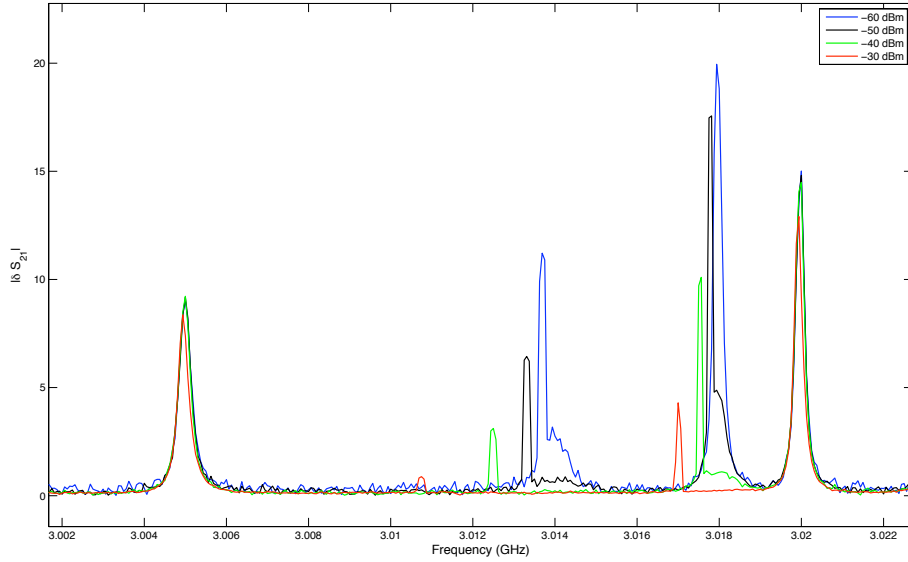


Figure 6.17: Hot/cold response for several IDC resonators on Device 5. This response is simply  $|S_{21}(77) - S_{21}(300)|$ , in uncalibrated units. Power levels refer to the input to the cryostat, approximately 43 dB larger than at the array. Discontinuities in the response indicate that the loop experiences a jump from one frequency point to the next, indicative of a saturated resonance.

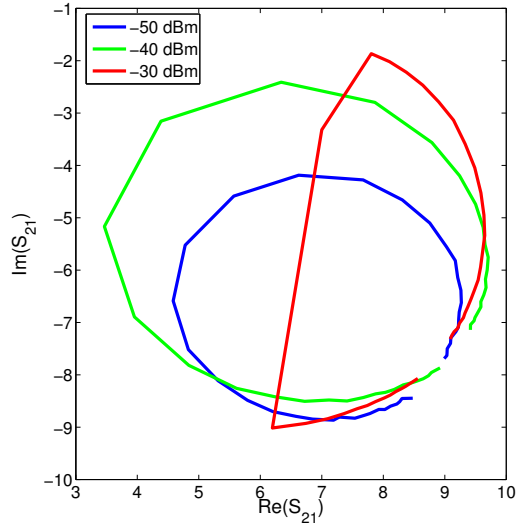


Figure 6.18: A resonance loop as it progresses to power saturation. Plotted is the loop in the plane of complex  $S_{21}$  transmission through the feedline. The loop has not had its cable term removed, and is thus arbitrarily oriented in the complex plane. Powers are given at cryostat input,  $\sim 43$  dB above the value at the array.

coupling.

## **6.5 Device 7 - the third iteration**

### **6.5.1 Changes in design**

In Device 7 iterations, the primary differences were tweaks in bandpass filter design, and the change to all-IDC devices. The changes in bandpass are not discussed here, save to mention that Bands 1 and 2 fell within the atmospheric window, while Band 3 had high detector-to-detector variability.

After several devices suffered from low or no pixel counts, combined with strange features which did not respond like typical resonances, a significant problem was found in the mask design. The overlap between niobium and aluminum portions of the IDC resonators was found to be smaller than originally thought, leading to the significant possibility of an effective open circuit between the niobium and aluminum portions of the resonator. This problem was recognized and resolved before Device 7c, leading to a much larger pixel count on that device. This device is the first working device after Device 5, with significantly higher yield.

### **6.5.2 Device 7c testing**

Device 7c was the first device with high enough pixel count to allow for significant testing. Here we describe the measurements made to understand its optical and systematic properties.

#### **6.5.2.1 Responsivity measurements**

In measuring this device, we generally concentrated on the lower 400 MHz band of detectors. Generally, this gave us an ample sample of resonators to test with. In addition, the higher band was contaminated by some features, although greatly reduced in number, which do not respond like MKIDs and would make measurement difficult. The lower band provided an adequate, uncorrupted set of resonances, and should have no reason to be different qualitatively from the higher band.

The hot/cold response was tested including a 420 GHz metal-mesh low pass filter, as well as without. The responsivities are seen in Figure 6.19. The highest frequency response points are the “dark” resonators in this figure (over 3.3 GHz), and are very uniform compared to the antenna-coupled response. Using dielectric filters only, the antenna response is effectively a small perturbation on the dark pickup. The situation improves dramatically when one introduces a metal-mesh filter, but the response is still unacceptably high. The excess load is shown in Figure 6.20. With the filter in place, the excess load appears to increase. This is because the responsivity, much of it dark, significantly degrades when the filter is in place. If the true excess loading creates the same number of quasiparticles, the load would appear to be higher based on the definition in Section 4.2.3.4, because the effective resonator efficiency has gone down. For the purposes of the excess load calculation, all pickup is assumed to be signal. To find the true excess loading, it is therefore imperative to remove the “dark” resonator pickup.

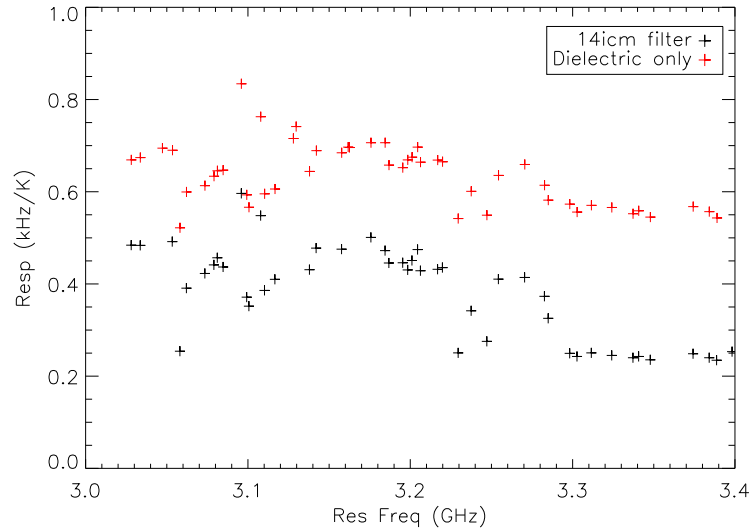


Figure 6.19: Device 7c detector hot/cold response. Dark resonators are those with resonant frequencies over  $\sim 3.3$  GHz. Here are plotted the results from optical filtering schemes of dielectrics only (Fluorogold and Teflon), and dielectrics plus a 420 GHz metal mesh low-pass filter. As the dark response decreases, the difference between the dark and light response becomes significantly greater.

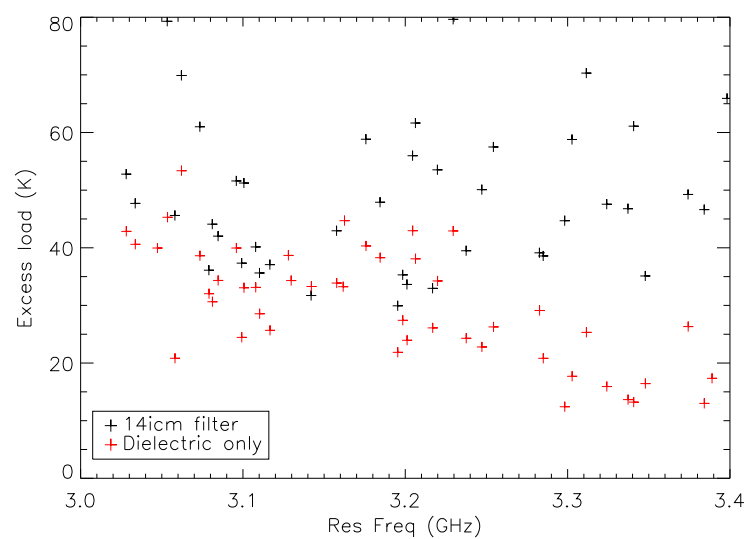


Figure 6.20: Calculated excess load for Device 7c detectors.

### 6.5.2.2 Evidence for tile heating

The response of the dark pixels leads to three plausible conclusions as to the origin of the “dark” pickup: direct absorption into the aluminum, pickup from the capacitor leaking through the stepped-impedance filter, and tile heating. It could also be some combination of these. Given the uniformity of the dark pixel response and the absorptive properties of the fused silica AR tile, it is likely that heating is a significant problem. The question is then, how can one measure this? The direct pickup in aluminum and from the IDC acting as an antenna are effectively indistinguishable except for beam pattern, which is very difficult to measure in a discriminating way. However, tile heating does have one measurable effect – at an elevated physical temperature (not the effective temperature based solely on quasiparticle density), the ratio of response between the dissipation and the frequency directions increases. This is due to quasiparticle heating lowering the effective resistance. By measuring  $Q_i$  and  $f_0$  for resonators under 77 K and 300 K loads, one can find the average temperature under optical load by comparing the ratio of the shifts in those quantities. In other words, finding  $\delta \frac{1}{Q_i} / \delta f$  gives the average temperature under the two optical loads. The results of such an analysis for Device 7c are shown in Figure 6.21. From this figure, one can see that this is not a precise measurement of the temperature, but the aggregate over many resonators can be useful in finding an approximate temperature. One can clearly see that a reduction in load from a metal mesh filter, and replacing the AR tile with a less absorptive version, reduce the ratio, as one would expect for the array becoming colder. In the metal mesh filter configuration, the average internal  $Q$ s of the dark resonators were consistent with a base temperature of 318 mK under 77 K load and 342 mK under 300 K load.

If heating is a reason for out-of-band pickup, one may ask, why was it not detected in previous devices? In CPW devices, there were clear breaks in response between the two bands. This indicates that the response due to tile heating must have been much smaller than the pickup through the antenna. In addition, the actual exposed tile area was much smaller, approximately 4 cm<sup>2</sup>, compared to the current exposed tile of ~9 cm<sup>2</sup>.

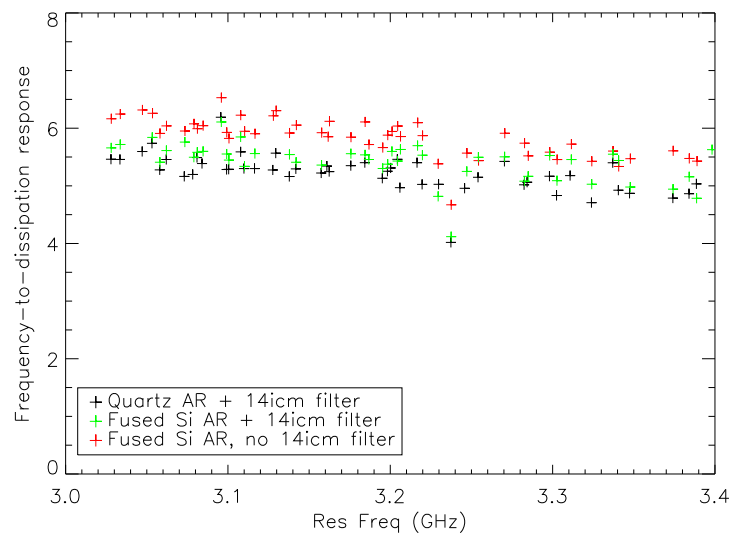


Figure 6.21: Ratio of the frequency and dissipation responses for optics with and without a metal-mesh low-pass filter, and including a crystal quartz anti-reflection coating to replace the previous fused Silica.

### 6.5.2.3 Antenna efficiency

From Figure 6.19, one can see that there is likely a very high dispersion in the optical response. Given that the optics are well understood, it is most likely due to a variable antenna efficiency. The range of bandwidths vary by a factor of several, which would give one the impression that there should be a clear distinction among bands. This is difficult to discern from the data. Therefore, it is instructive to see what the total efficiency is, and particularly the dispersion, and to find the implied antenna efficiencies.

The antenna efficiency is still not known because we do not know the thickness of the aluminum. In addition, due to the high dispersion in response, it is difficult to make a plot of average antenna efficiency versus thickness assumed (as done in Figures 4.33 and 4.34). However, if we assume a 55 nm thickness (15 nm etched away), we can see the approximate efficiency assuming the designed bandwidths, along with other parameters. The kinetic inductance and gap energy were measured as in Device 4. Again, fitting  $\alpha$  and  $\Delta_0$  to low temperatures yielded good fits, giving average  $\alpha = 0.0394$  and  $\Delta_0 = 0.2107$  meV, while the recombination constant was assumed to be  $7.5 \mu\text{m}^3/\text{s}$ , as in Chapter 4. Figure 6.22 shows this for two cases: assuming uniform absorption of power along the length of the aluminum absorptive section, and assuming an exponential absorption profile with a scale length of 100 microns. In both cases, the dark pickup has been accounted for as an effective temperature increase on the array. It is easy to see the large scatter in antenna efficiency; in the case of assuming uniform absorption, the average total efficiency through the entire system is  $0.027 \pm .015$ . The efficiencies by band are found in Table 6.3. This is nearly an order of magnitude decrease from the previous device design, when the expected decrease is only a factor of 2 in Band 1, and less in the higher frequency bands, due to the new optics. The low efficiency and large scatter suggest a problem perhaps involving the dielectric of the antenna feed network. However, the exact cause is unknown.

Again, these numbers mean little without proper context of expected efficiency. Table 6.4 shows the expected optical transmission for the new platescale and antenna sizes. Including antenna

Table 6.3: Calculated efficiency from measurements in the DemoCam. Here we have assumed a thickness of 55 nm, and  $R = 7.5 \mu\text{m}^3/\text{s}$ . The latter efficiencies simply come from the scenario in which the power absorption along the resonator follows an exponentially decaying profile with 100 micron scale length.

Band	$\eta$	$\sigma_\eta$	$\eta, z_0=0.1\text{mm}$	$\sigma_\eta, z_0=0.1 \text{ mm}$
1 (230 GHz)	0.024	0.004	0.040	0.008
2 (290 GHz)	0.032	0.018	0.053	0.035
3 (350 GHz)	0.020	0.018	0.030	0.028

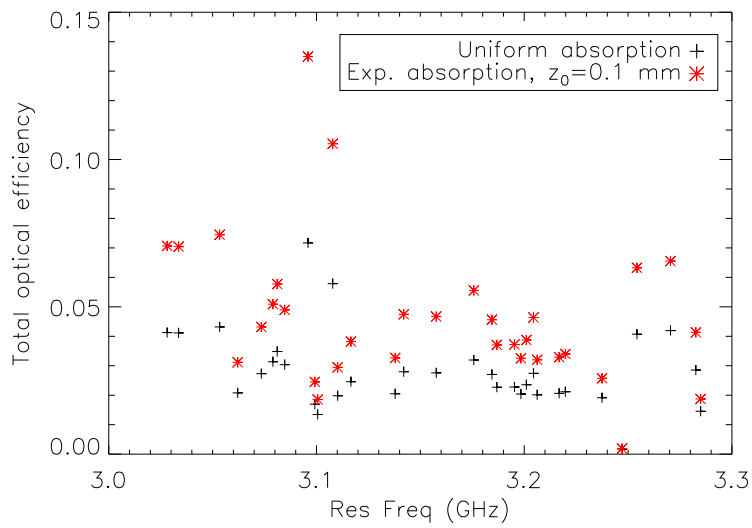


Figure 6.22: Optical efficiency inferred for light resonators. Here we assume a true thickness of 55 nm. The cases of an exponentially decreasing power absorption along the length of the aluminum section, and of a uniform absorption, are shown.

Table 6.4: Calculated efficiency from optical elements in the DemoCam. Here are tabulated the effects of transmission past the Lyot stop, through the filter stack and window in each band. Antenna efficiency is not included.

Band	Lyot	Filters	Window	Total
1 (230 GHz)	0.36	0.91	0.99	0.33
2 (290 GHz)	0.52	0.89	0.98	0.45
3 (350 GHz)	0.63	0.85	0.96	0.51

efficiency of 60%, these values become 20%, 27%, and 31% for Bands 1, 2 and 3, respectively.

### 6.5.3 Conclusions

There are two significant conclusions reached from this device. The first is that there is still significant dark response evidenced by detectors nominally uncoupled to the antennas. The second is the low and highly variable antenna efficiency. The first problem is, at least in part, likely due to tile heating, though secondary pickup mechanisms could not be ruled out. The latter problem is of unknown cause. Both these effects significantly limit the practical NEP achievable by these devices.

## 6.6 Device 8 - a final iteration

The final iteration in these designs –  $6 \times 6$  arrays of 4.2 mm square antennas with 32 slotlines – was given the name of Device 8. While this is not the ultimate design, it is the last design of the primary test arrays to be considered for telescope operation.

### 6.6.1 Changes in design

In Device 8, gold pads were added to some parts of the ground plane, allowing for the use of gold wire bonds. These allow for greatly improved tile heat sinking to the bath. This, combined with the crystalline quartz AR coat used to replace the fused silica, should effectively eliminate the problem of tile heating due to light absorption and poor thermal coupling to the stage. This also will keep the device cool enough so that tile heating does not significantly degrade the dissipation

response.

## 6.6.2 Device 8b testing

### 6.6.2.1 Tile heating reduction

The evidence is strong that the effect of tile heating was either solved or greatly reduced by the two changes – the addition of quartz (crystal SiO<sub>2</sub>) anti-reflection coat to replace the fused silica (fused SiO<sub>2</sub>) coat, and the use of gold wire bonds for tile heat sinking. Let us consider the ratio of frequency to dissipation response from hot/cold measurements. If the tile is hotter than expected, the result will be a high ratio as quasiparticles are heated and the superconductor becomes less resistive. If the device is physically cold, the quasiparticles will be more resistive, and increase the  $Q$  sensitivity. Figure 6.23 compares this ratio for several configurations. One can clearly see an improvement in Device 7c when using crystal quartz AR coat and a 420 GHz low-pass optical filter. The Device 8 data does not include a metal mesh low-pass filter, so the effect of the reduced ratio is due to the gold wire bonds and crystal quartz. This indicates that the tile must not be heated nearly as much by optical load, and this amount will only decrease with additional optical filtering. Note that, in Figure 6.23, the ratios (solid curves) are given for single temperature values, while the response indicates that the temperature changes significantly under load from 77 K to 300 K. The response measured by the detectors should be close to representing the average tile temperature between the two optical powers.

The question remains, is this all the dark response? Assuming the same dark parameters for this device as for Device 7c, the mean temperature for the dark resonators would be  $275 \pm 21$  mK, given the scatter from resonator to resonator. For the dark resonators in Device 7c, the temperature found is  $317 \pm 11$  mK with both metal mesh filter and the quartz AR tile. This is a reduction of the average quasiparticle density by a factor of roughly 3.5; one should expect a proportional drop in response due to dark load if the only cause is the thermal response of the tile to optical load.

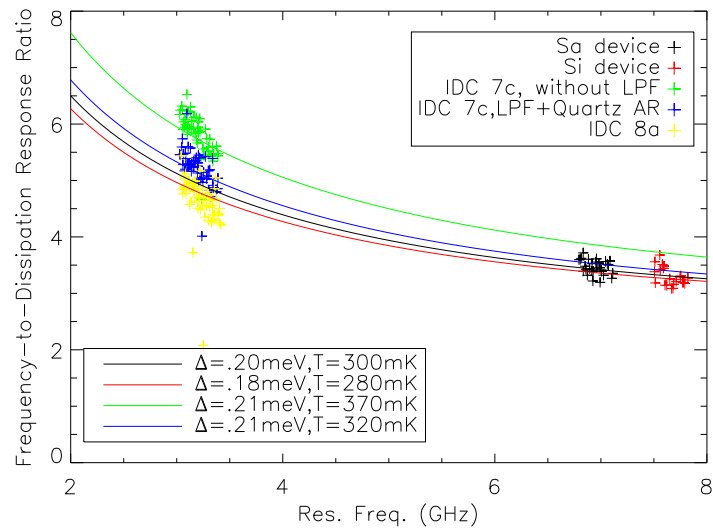


Figure 6.23: Ratio of frequency to dissipation response for several devices at different frequencies. Overplotted are lines corresponding to Mattis-Bardeen predictions of the ratio for different gap and base temperature values. Note that no formal fitting has been applied, and the lines are simply placed as a guide. Also note that all three were taken in different optics conditions; the Sa device had wider windows than the Si device data, though they both shared the same tile mounting.

### 6.6.2.2 Optical response and antenna efficiency

Much like Device 7c, there was significant scatter and relatively low response among detectors. In Figure 6.24, we plot the comparison between Device 7c in several configurations along with Device 8b. It is very significant that upon removing the 420 GHz (14 icm)<sup>3</sup> low-pass filter from the filter stack but including gold wirebonds, the dark response decreases. However, it does not decrease much, a factor less than 1.4. This is significantly smaller than the factor of  $\sim 3.5$  that one might expect. Combined with evidence of much lower tile temperature, this may indicate an additional source of loading outside of antenna pickup and tile heating.

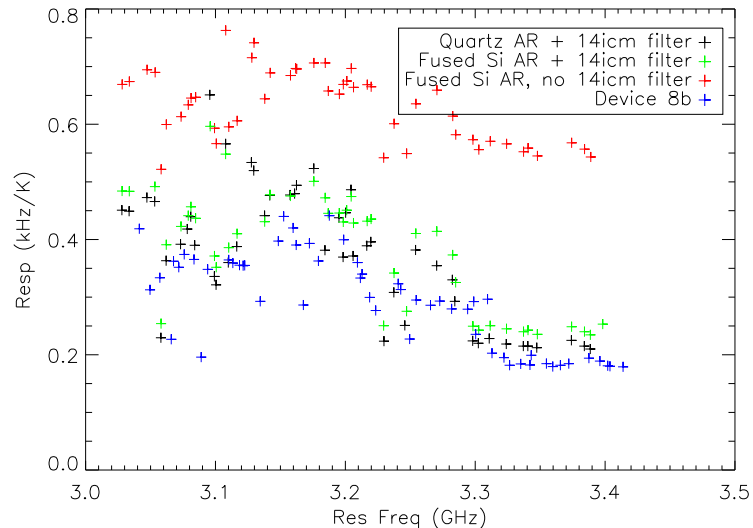


Figure 6.24: Response of Device 8b compared to 7c in different configurations. The dark resonators (typically 3.3–3.4 GHz) decrease in response with the switch to crystal quartz  $\text{SiO}_2$  AR tile and with a metal mesh LPF. Device 8b has a quartz AR tile but no metal mesh filter.

### 6.6.2.3 Optimization for telescope usage

Device 8b was the device taken to the telescope after lab testing in May 2010 (see Chapter 8). As a prototype for the design of future arrays, it is instructive to look at its parameters to see how close to optimal it is, and to find how the array design should change in the final design.

<sup>3</sup> For a reason not readily comprehensible to the author, many filter frequency values are given in inverse centimeters. This is proportional to frequency, with 10 icm equal to 300 GHz.

Above is discussed the antenna response and dark pickup which must be rectified; here we see if the resonator frequency scatter and coupling  $Q_s$  are at levels which would meet our expectations.

Given the typical  $Q_i$  is around 60,000 under 77 K load, a fair proxy for atmospheric conditions in the longer wavelengths, we must see if the  $Q_s$  are well-matched for optimal response. As Device 8b is considered to be the telescope device, we must ensure that all other variables are optimized well enough to give reasonable response. Figure 6.25 shows the histogram of these values. In general, these are fairly well-matched to the load. In addition, the  $Q_i$  is increased at the telescope with the use of a metal-mesh low-pass filter.

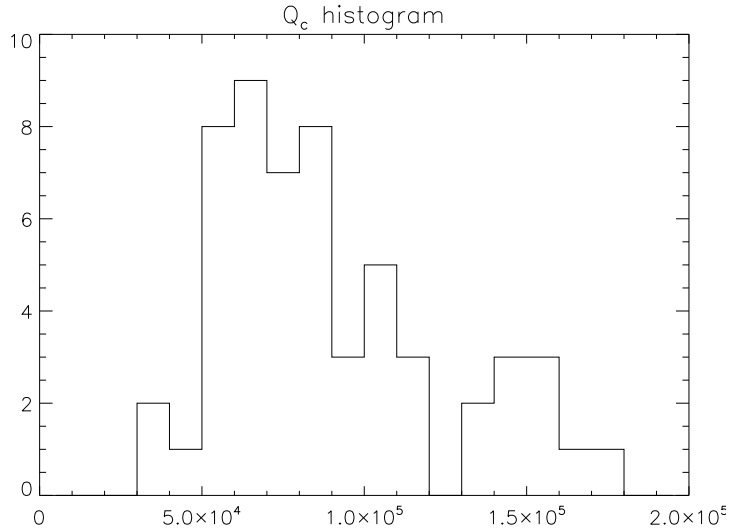


Figure 6.25: Histogram of  $Q_c$  for device 8b.

Figure 6.26 shows the scatter in resonance frequencies. Designed to be evenly spaced at 5 MHz apart, the scatter has a standard deviation of 5.3 MHz from even spacing. This is a significant improvement over the sapphire device, Device 2, but is still large enough to create significant difficulties with closely spaced resonators. For the current device, this led to only one pair of closely spaced resonators – 220 kHz apart, a separation with low enough crosstalk to warrant possible inclusion in future devices.

Assuming a 5.3 MHz RMS Gaussian scatter, we can calculate our expected losses to collisions,

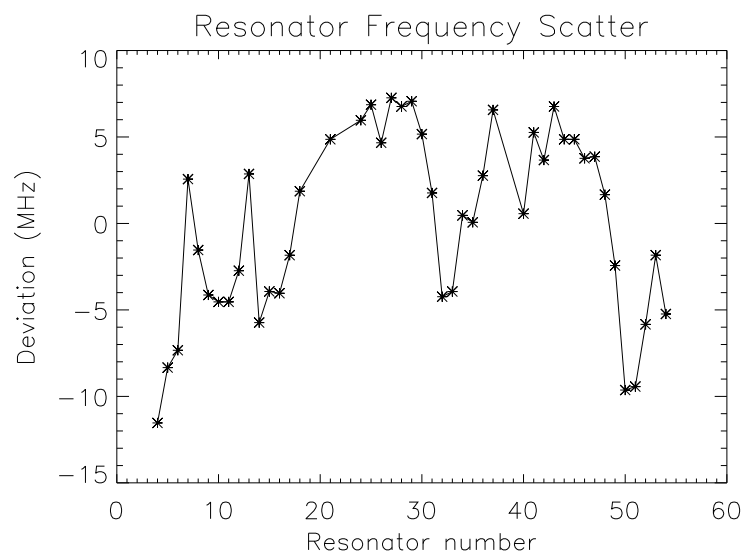


Figure 6.26: Deviation of the frequencies from the designed spacing for Device 8b. The resonator locations are found from observations of bright point sources, and the bands are found through FTS measurements. Dark resonators are excluded due to insufficient data.

Table 6.5: Number of usable resonators in each band given various frequency spacings (in MHz, columns 2-4) and 5.3 MHz scatter. Here we assume a cutoff threshold of 5 FWHM spacing for resonators to have acceptable crosstalk.

$Q$	2.1 MHz	2.8 MHz	3.5 MHz
10,000	12	18	22
15,000	20	24	27
20,000	24	27	29
30,000	28	30	31
40,000	30	32	33

as is done in Chapter 3. Several particular values are included in the Table 6.5. In the current design, the  $Q$ s are typically over 30,000. Given the low level of losses at 5 MHz spacing, and the low levels expected from the same scatter at closer spacings, it would make sense to design future devices for lower  $Q$ s and the associated higher frequency signal-to-noise ratio, if the frequency response gives the best sensitivity. However, one can clearly see the necessity of going to larger spacings given if one plans to increase frequency response.

## 6.7 IDC devices - a final analysis

In general, the IDC devices have improved to the point of working well enough to consider for astronomical use. Dark pickup was mitigated by a factor of 4 over the initial testing, and is still unlikely to couple well to astronomical sources. Inter-resonator coupling has been effectively eliminated. In addition, dark measurement of detectors yields consistent results which allow the straightforward calculation of efficiency.

Not all problems were thoroughly resolved with this mask, and it was determined that there would be additional changes in the next design. First, the stepped-impedance filter may be redesigned to reduce possible leaks in the current design which could contribute to excess loading. Systematic testing will also determine if direct pickup in the aluminum section is a problem, and geometrical changes may mitigate this problem. Second, nothing was done to address problems with the antenna efficiency; this will be addressed first by cleaning out the dielectric sputtering

system to ensure good antenna efficiency. If that does not solve the efficiency and uniformity issues, additional solutions will be considered, or thinner aluminum will be used to ensure higher responsivity to compensate for the low efficiency. Finally, this device differs from the final tiles in that all potential Band 0 detectors (detectors slated in the future to be coupled to the antenna through 150 GHz bandpasses) are still dark, not antenna coupled. This allows a full systematic diagnosis of problems, and will let us know how necessary the dark pixels are. This is explored further in Chapter 8.

## Chapter 7

### Optimal Operation of MKIDs

In this chapter, we discuss how to optimally operate MKID detectors in an astronomical camera. Here we show how to maximize signal, remove noise to low levels, and evaluate the NEP of detectors through the entirety of the optics.

#### 7.1 Noise and multi-channel noise removal

##### 7.1.1 Amplifier noise

In MKIDs, there are correlated and uncorrelated noise sources arising because of the cryogenic HEMT amplifier used in the system. Correlated noise generally takes the form of amplitude and phase variations in an amplifier which amplifies many probe signals at different frequencies. In the ideal case, this is expected to be common-mode noise. This noise tends to be greatest at low audio frequencies, and is generally lumped together as  $1/f$  noise. Uncorrelated amplifier noise is generally white Johnson noise as seen in a resistor at a given temperature. This noise is added to the signal, whereas correlated phase and amplitude fluctuations in the amplifier result in multiplication of the probe signal. Astronomical signals in the submillimeter are typically at low audio frequencies due to the slow scan speeds of many telescopes; we are concerned with the noise which, after homodyne mixing, is left at those frequencies.

Let us consider the noise as arising due to different wavenumbers  $\mathbf{k}$ , corresponding to frequencies which vary from very low frequencies (fractions of a Hz) to frequencies in the GHz. We consider  $\mathbf{k}$  to be a discrete variable, as corresponding to a frequency in a discrete Fourier transform

of time-series data. Then the signal of the probe signal sent past the HEMT<sup>1</sup> will be

$$V_{RF}(t) \propto \operatorname{Re} \left[ \sum_j B_j e^{i\omega_j t} \left( 1 + \sum_k \delta b_k \right) \exp \left( i \sum_k a_k \omega_k t \right) + \sum_k \delta V_k e^{i\omega_k t} \right]. \quad (7.1)$$

Here  $j$  is the index a single probe signal, where we have assumed that the probe signal corresponds to an infinitely narrow frequency bin.  $B_j$  represents the probe signal amplitude, and  $\omega_j$  the signal frequency for any probe signal. The terms multiplying the probe signal correspond to HEMT gain and phase fluctuations, while the added  $\delta V_k$  term corresponds to voltage fluctuations due to Johnson noise. With all this noise added in over many GHz of bandwidth, we must find what is important in contributing to our signal-to-noise ratio.

The actual resonator signal – the phase and amplitude change corresponding to a change in loading – is a multiplicative effect, similar to the phase and gain fluctuations from the HEMT. Therefore we are only concerned about audio frequencies for those noise terms multiplying the signal, which are the same as the signal frequencies. The  $\mathbf{k}$  modes causing noise are all the same low frequency modes across many detectors, and will be correlated. However, the  $\delta V$  term is added to this signal, meaning that only frequencies  $\omega_k$  near  $\omega_j$  will be demodulated down to audio frequencies. In other words, the Johnson noise frequencies that matter are those for which  $\omega_k - \omega_j$  is at low audio frequencies, near the signal band. Because  $\omega_j$  is different for each resonator, different frequency modes will be added in for each. Thus, the white noise level is uncorrelated among detectors.

To see this more explicitly, it is best to consider what happens in the IQ mixer. Let us simplify Equation 7.1 by considering only a single probe signal. As the explicit frequency bins in the gain and phase are not important here, we further simplify by rewriting the gain fluctuations  $B_j(1 + \sum_k \delta b_k)$  as  $(B + \delta B(t))$  and the phase as  $\phi(t) = a_k \omega_k t$ . This leads to the total I and Q voltage being

$$V_I = C(B + \delta B(t)) \cos(\omega_{LOT}) \cos(\omega_{RF} t + \phi(t)) + C \cos(\omega_{LOT}) \sum_k \delta V_k \cos(\omega_k t) \quad (7.2)$$

---

<sup>1</sup> This is the signal *before* mixing. In Figure 2.10, it is the voltage of the signal between the amplifier and the IQ mixer.

and

$$V_Q = C(B + \delta B(t)) \sin(\omega_{LO} t) \cos(\omega_{RF} t + \phi(t)) + C \sin(\omega_{LO} t) \sum_k \delta V_k \cos(\omega_k t) \quad (7.3)$$

respectively. Here  $C$  is an arbitrary constant relating the gains of the mixing steps. The  $\omega_{LO} = \omega_{RF}$ , so the residual upon multiplication is just the phase difference. In the additive term, the only frequencies that matter are those around  $\omega_{LO}$ , as all others are demodulated to frequencies far from the audio frequencies of interest. Simplifying the I term, we find

$$V_I = \frac{C}{2} (B + \delta B(t)) (\cos(\phi(t)) + \cos(2\omega t + \phi(t))) + \frac{C}{2} \sum_k \delta V_k (\cos(\omega_k + \omega)t + \cos(\omega_k - \omega)t) \quad (7.4)$$

or, throwing away terms far away in frequency from our actual signal,

$$V_I = \frac{C}{2} \left( (B + \delta B(t)) \cos(\phi(t)) + \sum_k \delta V_k \cos(\omega_k - \omega)t \right). \quad (7.5)$$

We are left with high frequency Johnson noise demodulated to low frequency, combined with gain and phase noise. The gain and phase noise is common to all frequencies, but the demodulated Johnson noise is not. To decrease the relative effect of Johnson noise, one must increase  $B$  – that is, increase the amplitude of the probe signal sent into the HEMT. This is what is considered in the optimization in Section 3.2.2.

### 7.1.2 Noise removal

The end result is that, in theory, it is possible to remove correlated noise down to the level at which the total noise is dominated by white Johnson noise corresponding to the noise temperature of the amplifier. We are primarily interested in low frequencies used in the sub/millimeter, usually 0.1-10 Hz,<sup>2</sup> which are typically dominated by  $1/f$  noise. The only sources of  $1/f$  (outside of sky noise) are gain and phase fluctuations in the amplifier, which are common-mode multiplicative signals. Thus we can lower noise to the level of white noise just by subtracting out the effect of a probe signal off-resonance, with frequency near to the resonance frequency.

---

<sup>2</sup> The exact signal band depends on the size of the telescope and the speed at which it can scan. These are the frequencies generally considered for a 0.5 arcmin FWHM beam and a telescope scanning at several arcmin/s.

It is possible to subtract out gain fluctuations by either sending in two probe signals on resonance, and subtracting out the common mode, or by using an off-resonance tone. In general, it is preferable to probe off-resonance, as this signal will contain HEMT noise but no TLS noise. By this method, one can subtract the proper combination of gain and phase noise, and not be constrained by the complexities of subtracting gain and phase noise from another detector, as discussed below in Section 7.1.2.2.

### 7.1.2.1 Off-resonance noise removal

First, let us consider the case of two signals off-resonance. This eliminates the complication of resonator noise and the difference in the signal transmission, and provides a simple proof-of-concept experiment. The first task is to find the gain and phase directions. If the overall transmission level is constant and the cable delay term is finite, the transmission in the IQ plane should sweep out a circle around the zero-transmission point as the frequency varies. Gain fluctuations will always be a radial effect and phase fluctuations a tangential effect.

If we know the gain and phase directions, we should be able to arbitrarily rid ourselves of the noise by projecting into the correct noise bases and subtracting a common-mode signal. If we have two signals with the gain or phase as the only noise source, and know the directions, the simplest method of noise removal is to use a Power Spectral Density (PSD)-weighted common mode subtraction. Weighting the signals by their PSD is a common method for normalizing out any gain differences between the two signals. The resulting noise spectrum is given by

$$V_{1-2}(f) = \text{FT} \left( \frac{V_1(t)/\text{PSD}_1 - V_2(t)/\text{PSD}_2}{1/\text{PSD}_1 + 1/\text{PSD}_2} \right). \quad (7.6)$$

Thus, we effectively subtract out the common mode, leaving the final timestream in volts. The  $1/f$  noise in the PSD can be compared to the PSD of the original timestream, as the units have not changed – only the weighting. This was tested using a two-resonator analog readout setup developed by Ben Mazin [76]. The PSDs of two signals sent in independently as off-resonance tones are seen in Figures 7.1 and 7.2. In both cases, the  $1/f$  noise is drastically reduced by this simple

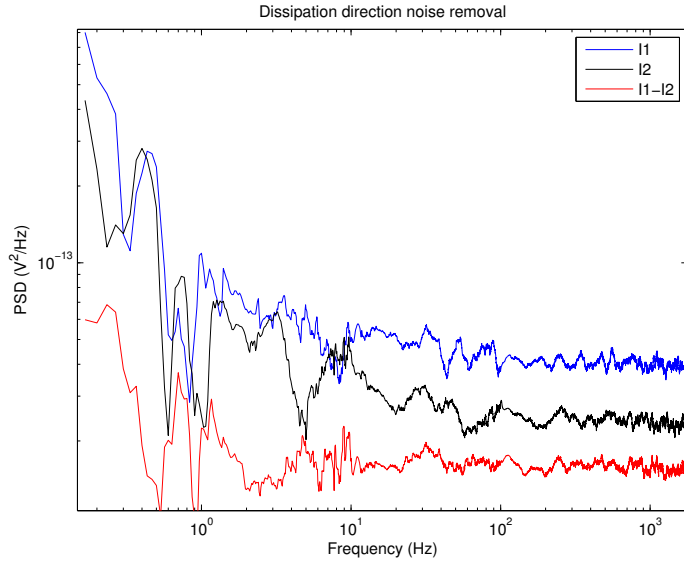


Figure 7.1: PSD weighted amplifier gain noise removal from off-resonance tones. The subtracted signal is of the form given in Equation 7.6. At high frequencies, the spectrum begins to look white and is dominated by Johnson noise. The low frequency noise (described generally as  $1/f$  noise in  $\text{V Hz}^{-1/2}$ ) corresponds to common-mode gain fluctuations, which can be mitigated by multiple tone subtraction.

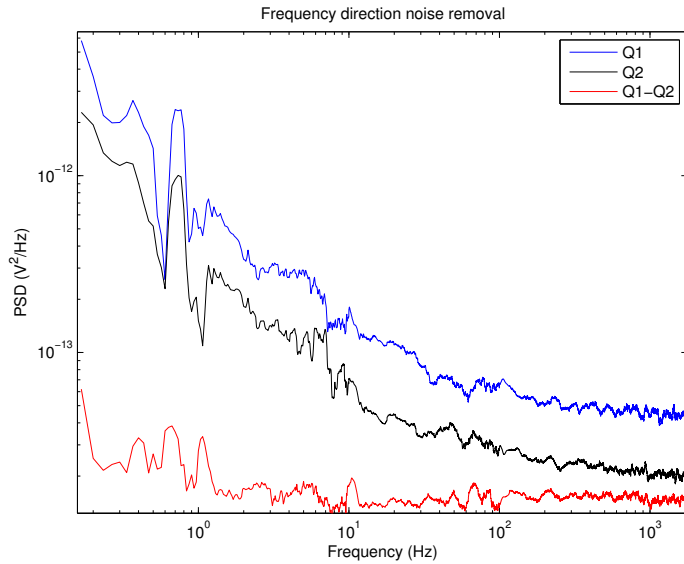


Figure 7.2: PSD weighted amplifier phase noise removal from off-resonance tones. The subtracted signal is of the form given in Equation 7.6.

subtraction. However, it is readily apparent in these figures that the low frequency noise is not completely eliminated – there is a residual upturn at low frequency. Eliminating  $1/f$  noise entirely may require a more sophisticated approach, and it may not be possible to remove HEMT  $1/f$  noise entirely on-resonance.

### 7.1.2.2 On-resonance noise removal

An additional challenge is to show that this technique can work for probe signals on resonance. One complication involves the fact that resonance frequency point is not necessarily closest to the point in IQ space indicating zero transmission.<sup>3</sup> Due to impedance mismatches in the system, it generally points in a direction not corresponding to the amplifier gain direction, as seen in Figure 7.3. This has the effect of making fluctuations in the resonator's dissipation direction not purely the same as amplifier gain fluctuations; they involve the projection of the phase and gain fluctuations of the amplifier. Thus, while subtracting noise from an off-resonance probe frequency, we must take into account this linear combination of phase and gain noise. Each resonator will have an independent angle between the frequency/dissipation direction of the resonator, and the gain/phase noise direction of the amplifier. The noise for a resonator in the correctly projected I (dissipation) and Q (frequency) directions can be written, respectively, as

$$\delta V_I^2 = [\delta V_{gain} \cos(\theta)]^2 + [\delta V_{phase} \sin(\theta)]^2 \quad (7.7)$$

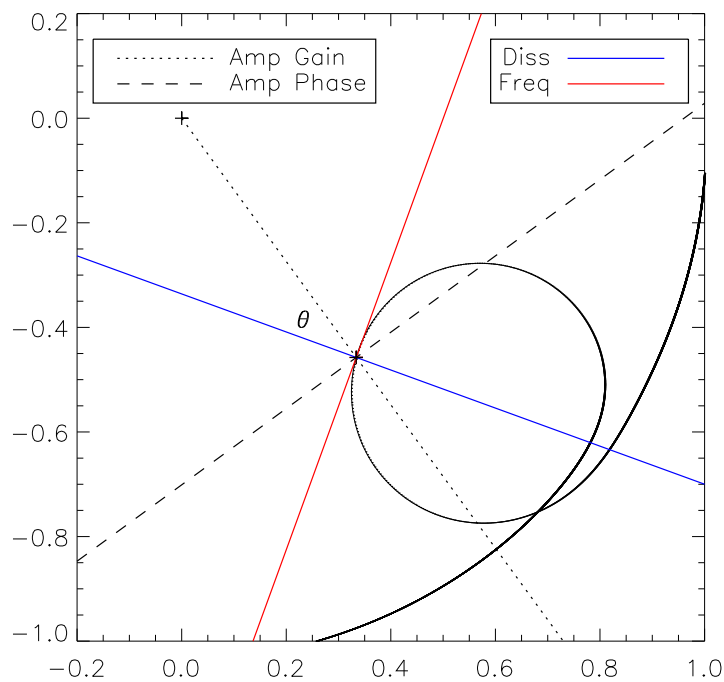
and

$$\delta V_Q^2 = [\delta V_{gain} \sin(\theta)]^2 + [\delta V_{phase} \cos(\theta)]^2 + \delta V_{TLS}^2. \quad (7.8)$$

In Figure 7.3 one can see the projections graphically. The projections, and proper removal techniques, become much more complicated. In telescope operation, this is exacerbated by the addition of  $1/f$  noise due to readout electronics noise, and is a main limiter in the sensitivity of MKIDs. The uncorrelated noise source of TLS noise in the resonator frequency direction is added, making

---

<sup>3</sup> In general, IQ mixers have an offset point  $[I_0, Q_0]$  which corresponds to zero power transmission. This can be found by greatly attenuating the signal incoming to the RF port. This offset point can be easily subtracted out once measured, but does not generally correspond to the origin for analog data. Using digital readout, the IQ mixer is not used in the same manner, so there is no offset.



↙

Figure 7.3: A simulated resonance loop as it would appear in I/Q space. The angle  $\theta$  defines the rotation of the resonator's coordinate system from the readout's radial/tangential coordinate system defining amplifier gain and phase noise.

true subtraction difficult. Techniques for the absolute removal of  $1/f$  noise from resonators are beyond the scope of this thesis, but a significant approach may be to try to limit the noise from the amplifier. It is possible that a significant portion of the noise could be mitigated by much cleaner power sources feeding the HEMT's drain current, but future testing will be required to determine what effect this will have. Also, the use of different cryogenic amplifiers, such as SiGe transistors [115], may yield better  $1/f$  performance with similar noise temperatures for the frequencies of interest. Removal, or extreme mitigation, of these multiplicative gain sources is necessary for MKIDs to reach their full potential as detectors at low frequencies.

## 7.2 Signal-to-noise ratio optimization in detectors exposed to background loads

When considering noise removal, we concentrate on the multiplicative  $1/f$  noise. Here we turn to the optimization considering the ultimate limit of Johnson noise. Given the large  $1/f$  noise, we consider the white noise level at high frequencies during open-window cooldowns. During runs in which the detectors are exposed to external loading, we can find the optimal operating conditions for both signal and noise. Under both 300 K and 77 K blackbody optical loads, we can test the relative response to a chopped source, and take noise data. The primary variable is the optimal use of readout power.

When exposed to external light, the detector's internal  $Q$  will decrease with the effective temperature of the load.<sup>4</sup> The frequency noise due to TLSs remains the same, because this noise is independent of  $Q$ . As the  $Q$  decreases under load, the voltage associated with the TLS noise, or the V/Hz calibration in the I/Q plane, will decrease. In order to compare the noise under different loading conditions, it is simplest to reference the noise data to the shift in resonance frequency it corresponds to. In this method, the PSD is converted from  $\text{V}^2/\text{Hz}$  into units of fractional frequency change squared per Hz. This is the noise in  $\text{Hz}^2/\text{Hz}$  divided by the square of the resonance frequency.

---

<sup>4</sup> As noted in the introductory chapter,  $Q$  corresponds to quality factor and  $Q$  to the quadrature output of an IQ mixer.

It is easy to find the conversion from volts to frequency from an IQ sweep with small, finite steps in frequency. For a fine enough grid of frequency points, the conversion is simply given by  $\Delta V/\Delta f$  at  $f_0$ .

### 7.2.1 Responsivity to sky loading

As is discussed in Chapter 8, skydips were performed using Device 8b to ensure functionality of the detectors and optics while mounted on the telescope. These data provide us with a small-signal optical response over which we can find how the detector response behaves with power. Unlike the preliminary analysis in Chapter 4, this does not rely on thermal response and two associated complications: the change in the frequency-to-dissipation ratio (which is temperature dependent) and the change in response with temperature (due to the exponential dependence of quasiparticle density on temperature). The latter problem in particular makes projection of a resonator's response into frequency and dissipation directions difficult. Here there is a significant steady-state quasiparticle density, but it is largely non-thermal (i.e., optical). We consider the small-signal response from the telescope pointed to two zenith angles,  $ZA = 60$  and  $ZA = 20$  degrees. Under good atmospheric conditions ( $\tau_{225} = .055$ ), a skydip gives a small signal response. We perform power sweeps at each zenith angle. This is, in essence, a small-signal equivalent of a hot/cold response measurement, where the response is small enough as to be effectively linear. Although it is simple to find the absolute response to the sky load (as is done in Chapter 4), the purpose of this exercise is to find the relative response as a function of readout power.

To find how to maximize response in terms of probe signal power, we must know how the response to a fixed optical source changes with power. Network analyzer sweeps can tell us the shift of each point in  $S_{21}$  simply by finding the distance in the  $S_{21}$  complex plane between one point and the next. This is the most important measure, as it tells us if the probe signal response increases or decreases. For an undistorted resonator, this response is given in Equation 2.4, as it depends on both the  $Q$  and the frequency shift.

In addition, from these sweeps we can find the change in frequency corresponding to each

Table 7.1: The ratio of the projected responses between an estimated -75 dBm and -95 dBm at the device ( $Resp_{-75}/Resp_{-95}$ ). Here the projected responses are calibrated out to fractional frequency and dissipation units, while the  $S_{21}$  simply takes the magnitude of the response from Network Analyzer IQ sweeps.

Band	Dissipation	Frequency	$S_{21}$
1	$0.609 \pm .096$	$0.785 \pm .061$	$1.742 \pm .198$
2	$0.510 \pm .122$	$0.717 \pm .120$	$1.712 \pm .302$
3	$0.701 \pm .137$	$0.717 \pm .127$	$1.704 \pm .554$

change in  $S_{21}$  by finding the relative distance between adjacent frequency points (i.e. finding  $dS_{21}/df$  at  $f_0$ ). In this way, we can calibrate the response to frequency shifts, and from there to the related change in  $1/Q_i$ . Figure 7.4 shows the change in response between the two skydip positions as a function of power over many resonators. Figure 7.5 takes the ratio of the skydip response at a given power to the lowest power point (i.e. the ratio at the lowest power is by definition 1) and averages over all resonators. Effectively, this figure shows the average change in response with power. Table 7.1 shows the ratio of the highest to lowest readout power response. In the regime of telescope loading, the  $S_{21}$  response increases significantly with power. Although the frequency response has declined, the resonance loop grows in size and the  $Q$  increases, which more than offsets the decline. However, the actual response in the frequency decreases, as one would expect. The improvement in  $S_{21}$  response shows that this is a net gain in signal. In addition, the relative noise from TLS and from HEMT Johnson noise are expected to decrease with increasing power. The expected decrease in NEP for frequency readout as a function of readout power is shown in Figure 7.6. This implies that using high power readout is a significant gain for MKID sensitivity, despite the fact that the frequency responsivity decreases.

While the data suggest that high power operation will improve sensitivity, the projections for dissipation response should be taken with a grain of salt. The response in the dissipation direction, being much smaller than the frequency response, can very easily be corrupted by the mixing of signals due to the large response compared to the width of the resonance. Conversely, the frequency response dominates the total signal, so a projection error due to large response (i.e. out of the linear

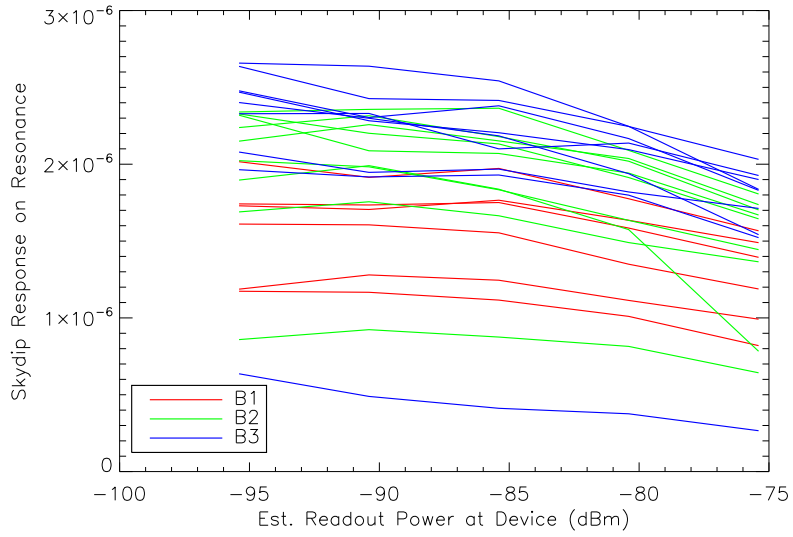


Figure 7.4: Total frequency response as a function of readout power for several resonators between two skydip points, ZA=60 and ZA=20 degrees. The response shown is calibrated to units of fractional frequency response. The resonators selected are those that did not “saturate”, or bifurcate, under the high driving power.

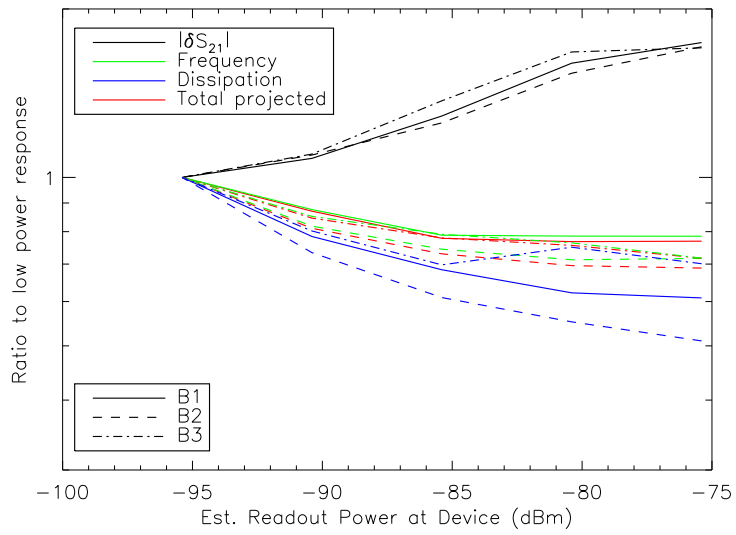


Figure 7.5: The average ratio of response at a given readout power to that of the lowest power data point. This takes the average of the response as seen in Figure 7.4, normalized to the low-power response. Here we include the  $S_{21}$  response (seen increasing), as well as the calibrated frequency and dissipation response, and the combined magnitude of frequency and dissipation (seen decreasing).

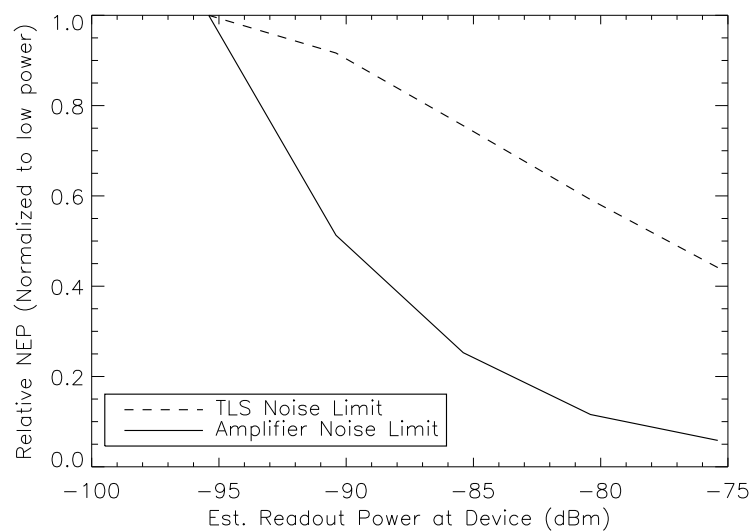


Figure 7.6: The expected decrease in NEP as a function of readout power, using the Band 2 responsivity from Figure 7.5. Here we assume TLS noise ( $\sqrt{S}$ ) decreases as  $P^{1/4}$  and amplifier-limited NEP decreases as  $P^{1/2}$ , as discussed in Chapter 3.

regime; see Appendix C) would minimally affect the frequency response. Thus, it is difficult to conclusively establish under these circumstances precisely how dissipation response changes with power. To do this, one would require very high signal-to-noise data of very small responses, with frequency shifts very small compared to the resonance width.

While it is difficult to truly pin down the effect of high readout power on the dissipation readout, it is clearly a major decrease in the NEP in the frequency readout. Very high readout powers significantly increase the probe signal response. At the same time, the high readout power both diminishes the effects of TLS noise and HEMT noise. Thus, for frequency readout, it is very clear that the mode of operation should be at high readout power.

### 7.2.2 Noise in open-window observations

Above is shown how the responsivity changes with power. We are interested in how the combination of signal and noise changes with power, and what NEP this yields. From Device 8b, we were able to find an approximate NEP given the hot/cold response and the noise measured under 300 K and 77 K load. Here we include the approximate effect of how the responsivity changes with readout power, from Figure 7.5. This was difficult, as these data only consider information up to -32 dBm at the Dewar input,<sup>5</sup> 4 dB less than the lab tests. For the slightly higher powers, we assumed an effectively static response.

Figures 7.7 and 7.8 show the NEP for the frequency and dissipation directions, respectively, when exposed to a beam-filling 77 K load. The noise projections between frequency and dissipation are selected as those projections that maximize and minimize the noise, respectively. The projection with large noise generally corresponds to two-level systems in the frequency direction, while the low-noise projection shows only HEMT noise in the dissipation direction. The response is inferred from detector skydips, explained in Section 8.1.1, rather than from the hot/cold load, as this is a better estimate of the coupling to astronomical sources. The response is then scaled to the response, in

---

<sup>5</sup> Given approximately 43 dB of attenuation inside the Dewar, calculated from figures for cryogenic loss in coaxes found by Weinreb [114], this corresponds to  $\sim 75$  dBm at the device.

Hz/W, with a 77 K load. The dissipation response is found by assuming a frequency-to-dissipation response ratio of 4.5, and scaling the response appropriately. As a result, we are able to construct how the NEP evolves with power, taking into account the changing response level as well.

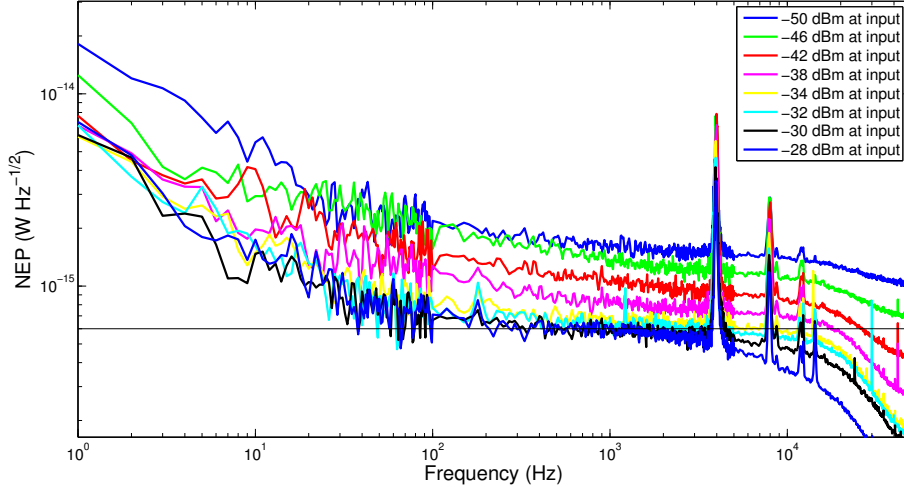


Figure 7.7: NEP for frequency readout as a function of power, under 77 K load, for a Band 2 resonator at 3.121 GHz. Powers in dBm are referenced to top of Dewar, approximately 43 dB greater than at the device. Noise data taken by Nicole Czakon.

The figures show that it is indeed beneficial to operate at high power to minimize the NEP. A horizontal line is drawn at  $6 \times 10^{-16}$  W Hz<sup>-1/2</sup> for a scale relationship between the two. Note that for the dissipation readout, we have assumed a declining response with readout power by an extrapolation from Figure 7.5. This may in fact be a lower limit to the NEP, because of the difficulty in correctly projecting out the small dissipation response. Any error in projection would lead to an overestimate of dissipation response, and therefore a low estimate of NEP. Therefore, it is best to treat the NEP here as a lower limit; Figure 7.8 is included here primarily for comparison purposes.

One important question here is why the NEPs are so high, approximately four times the photon limit assumed for good optical efficiency in Chapter 3 (approximately  $1.5 \times 10^{-16}$  W Hz<sup>-1/2</sup> for a 77 K load) in the white part of the spectrum. What is plotted in Figure 3.1 and in Figures 7.8 and 7.7 is the detector NEP, projected back out through the Dewar window. In other words,

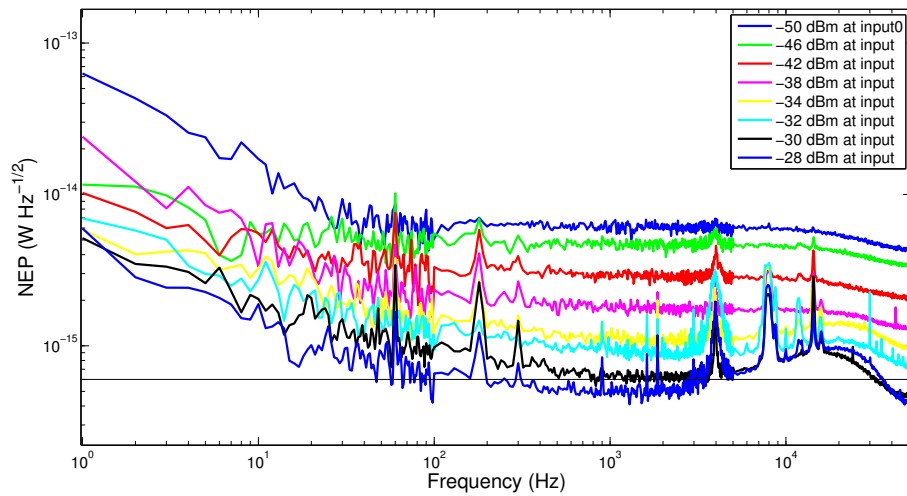


Figure 7.8: NEP for dissipation readout as a function of power, under 77 K load, for a Band 2 resonator at 3.121 GHz. Powers in dBm are referenced to top of Dewar, approximately 43 dB greater than at the device. Noise data taken by Nicole Czakon.

it is  $\text{NEP}/\eta_{Dewar}$ . The high NEP, possibly photon noise-limited, is most likely a reflection of the poor optical efficiency, discussed in Section 6.5.2.3. For a single-polarization optical efficiency of 4%, for example, the photon-limited NEP under 77 K load would be  $6 \times 10^{-16} \text{ W Hz}^{-1/2}$ , but the NEP at the detector would be  $2.5 \times 10^{-17} \text{ W Hz}^{-1/2}$

For the frequency direction, the values are somewhat sensible. The low optical efficiency of the antenna decreased the response of the MKID, causing the signal-to-noise ratio to decrease with power in the presence significant TLS noise. In Section 6.5.2.3, it is shown that the antenna response for a similar device is possibly 4-5 times lower than expected. An increase in optical efficiency by a factor of 4, to be in line with previous devices, would decrease the NEP to the levels shown in Figure 3.1. In Figure 7.7, the white levels seem to converge, and not decrease past a certain point. It is possible this is indicative of photon noise. In the dissipation direction, this leveling-off is not seen, or at least is not as apparent. However, the dissipation response is at similar white noise levels. This could indicate that we have not properly accounted for the decrease in dissipation response with power, and that the NEP is actually higher than shown here. The faster decrease in dissipation NEP with power is a reflection of the more precipitous decline in Johnson noise with power. Figure 7.8 shows the NEP dropping essentially proportionally with power, as we would expect given that we are HEMT-noise-limited, not photon-noise-limited. Given the likely low optical efficiencies, it is probable that we are near the photon limit in frequency readout at high power, but it would be premature to reach the same conclusion for dissipation.

### 7.3 Conclusions

In this chapter we have discussed the MKID in optimal operation, focusing particularly on the role of noise reduction. While  $1/f$  noise sources are generally correlated, and therefore removable in principle, other noise sources require more fundamental techniques to improve NEP. Here we have seen the effect of high readout power on both noise reduction and responsivity. In terms of both signal and noise, it is clearly beneficial to operate at high readout power when optimizing the frequency readout. Although it is not conclusive, the noise spectra from high readout powers

suggest that we are near background limited performance for very low optical efficiency antennas. Improvements in antenna efficiency will make MKIDs competitive toward reaching the background limit.

## Chapter 8

### Astronomical Observations the MKID DemoCam

This chapter describes the DemoCam’s second observing run in May 2010. The run had four main purposes:

- To display the sensitivities achievable with MKIDs in open observing conditions, or sensitivities close to the background limit.
- To display the possibility of large scale detector readout.
- To test calibration techniques using on-the-sky data.
- To fully integrate the readout system and the Dewar hardware to discover any flaws in design.

To accomplish these goals, we observed for five nights at the CSO on Mauna Kea. We performed testing on the devices via network analyzer sweeps, and took timestreams using a developed software defined readout (SDR), a digital readout system [30]. For these data, a 420 GHz low-pass filter (LPF) was installed into the DemoCam to further reduce direct pickup. Outside of these changes, the hardware remained identical to the lab testing.

#### 8.1      Miscellaneous testing

Before using the full readout system, basic tests of the functionality and systematic effects at the telescope were performed using a vector network analyzer. In particular, these involved finding the effect of the optics box in coupling to the sky, and how that changes the *effective* excess load, as discussed in Section 4.2.3.4. In addition, sweeps in azimuth were necessary to quantify the effect of magnetic fields on the MKIDs, to see if there was any residual measurable sensitivity. Many of the

tests were done with and without a polarizing grid in front of the Dewar window. The purpose of this grid is to allow the single-polarization antenna beams through, but block a significant portion of the direct, non-antenna pickup by the resonators.

### 8.1.1 Skydips

Skydips were used to ensure proper functionality of the device. A vector network analyzer was used to take frequency sweeps over the resonators at several zenith angles (ZA). The loading varies as approximately 260 K ( $1 - e^{-\tau_{atm}/\cos(ZA)}$ ), so one can see if the responsivity matches with what is found in other cases if the atmospheric opacity is known. This also gives us an indication of effective excess load from the optics box compared to the case in which hot and cold loads are placed next to the Dewar window. In the case of hot/cold tests, the window is completely filled, so that even high angle response counts as “responsivity.” In the skydip configuration, identical to the configuration for regular observing, this high-angle beam couples to warm, black surfaces. The combination of higher loading and decreased responsivity give a higher measured excess load.

Figure 8.1 shows the hot/cold lab tests, taken at the telescope with a 420 GHz LPF installed, compared to the response inferred from skydips. The skydip response is scaled to the kHz/K value expected if it were taken in the laboratory. The response is greatly reduced in these measurements. It is likely that this is due to much of the direct pickup not coupling to the sky; Figure 8.2 shows the same data, but with the mean dark resonator response, as measured in the laboratory, subtracted out.<sup>1</sup> The purpose of this is to show that the response is near what would be expected from antenna-only coupling to the sky.

In these cases, it is impossible to know the dark kHz/K response because the bandpass is unknown. Hot and cold loads are black throughout the range over which the dark detectors are sensitive, but the sky’s opacity is highly frequency dependent. Thus, it is impossible to do

---

<sup>1</sup> Subtracting out the mean dark resonator response from frequency shifts is not strictly correct, as the true antenna response in the absence of dark response would be higher than this value. However, there is the competing factor of increased excess load which would diminish the response. Knowing how these two factors interact depends on the sky opacity and the dark spectral bandpass, so here we make the blunt assumption that the two effects cancel. This is done solely for illustrative purposes.

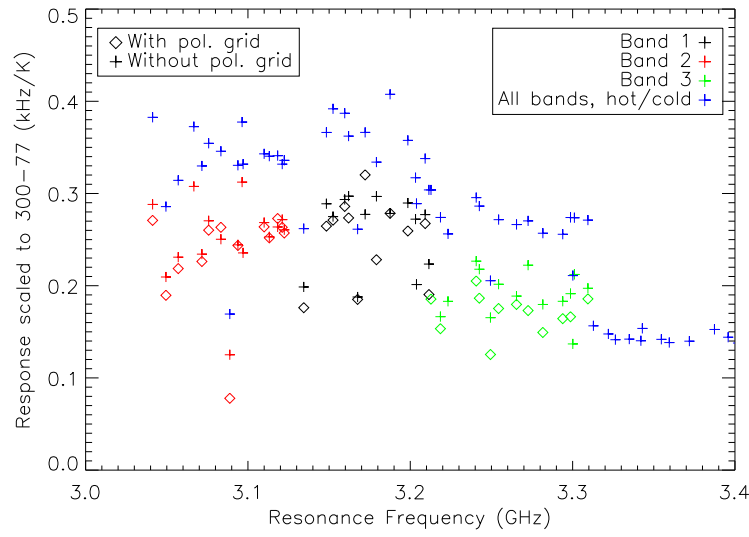


Figure 8.1: Skydip response from ZA=20 to ZA=60 degrees, scaled to 300-77 K values. Note the reduced dark response compared to Figure 6.24, due to the metal mesh filter installed for all tests.

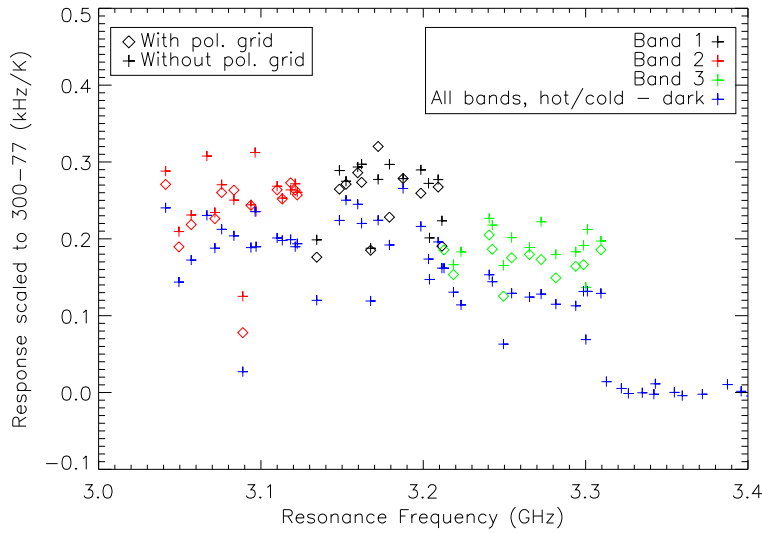


Figure 8.2: Skydip response from ZA=20 to ZA=60 degrees, scaled to 300-77 K values, but with the mean laboratory dark response subtracted off.

a direct comparison. However, one can compare the raw frequency response between dark and light resonators. This is plotted in Figure 8.3. It is clear that the relative response goes down when the polarizing grid is in place. The skydips with the grid were performed higher atmospheric opacity, and would therefore give a higher response between skydip positions. Yet they show similar response to the data without the grid, implying reduced sensitivity. Quantifying exactly how much is difficult because the dark pickup response as a function of frequency is unknown, and the atmospheric emission is highly frequency dependent. One can make the assumption that  $\tau_{225}$  represents the loading, and weight the relative response appropriately. Doing so shows a reduction in frequency response by a factor of 1.86, corresponding to a decrease in efficiency by a factor of 3.45. The dark response is therefore much less here relative to the in-band response than was the case in the laboratory.

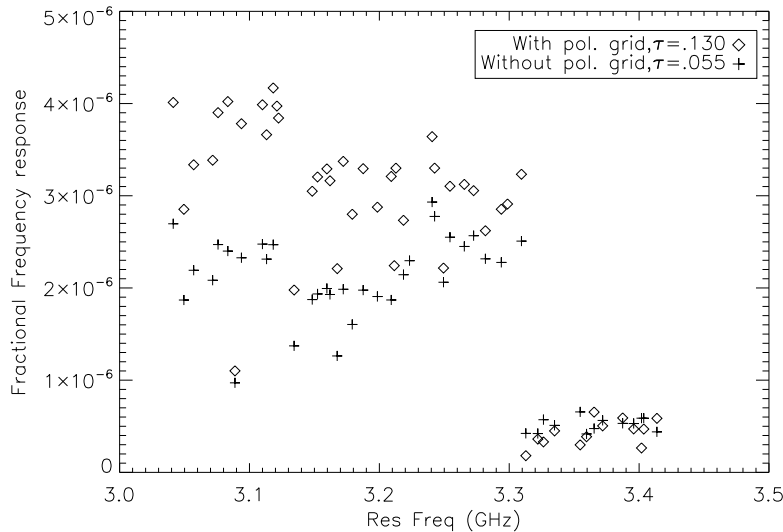


Figure 8.3: Skydip response between ZA=60 and ZA=20 degrees in fractional frequency, with and without a polarizing grid. The polarizing grid is taken with higher atmospheric opacity, giving a larger response. This shows that the dark responsivity has decreased significantly.

Finally, we must consider the effect of the observing configuration on excess load, seen in Figure 8.4. Here we see a great increase in effective excess load due to the presence of the optics box. This is due to the fact that, unlike beam-filling hot/cold measurements, the response causing

non-antenna pickup is largely landing on surfaces inside the optics box. In the optics box diagram shown in Figure 5.1, one sees a two-dimensional rendering of the mirrors in the box. Outside of these mirrors, the inside of the box is covered with Eccosorb<sup>TM</sup>, which is black in the millimeter and is at ambient telescope temperatures. Dark pickup would couple largely to light at large angles emitted from these black surfaces, adding to the excess load. The polarizing grid further increases the effective excess load by reducing the residual non-antenna (dark) response to the changes in sky loading. Less dark response to sky loading would give us a larger calculated excess load. In the final analysis, the excess load is simply unacceptably high, and must be reduced by eliminating non-antenna detector response. The median excess load is roughly 120 K for Band 1, 120 K for

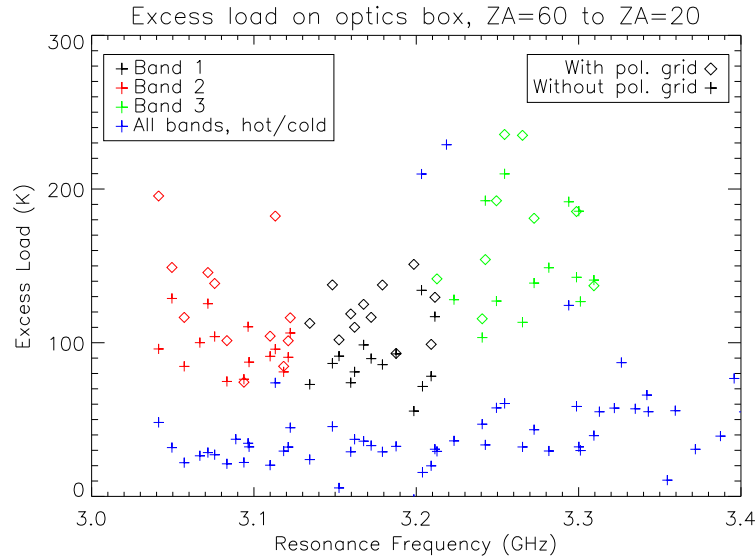


Figure 8.4: Skydip calculated excess load. Diamonds represent excess load measurements with the polarizing grid, and pluses without. The blue points represent the excess load found from hot/cold responsivity measurements, for comparison. The seeming increase with the grid in place is likely due to decreased dark responsivity to changing sky load.

Band 2, and 190 K for Band 3, but as seen in Figure 8.4 the scatter is very large. This excess must be decreased to obtain sensitivities near the background limit. This particularly harms devices limited by electronics or HEMT noise: as seen in Equation 3.19, the NEP is proportional to the submillimeter power.

Table 8.1: The shift in resonance frequency due to change in azimuth. Here the baseline is given by AZ = 295 degrees (i.e. WNW). Shifts are given in Hz.

Res. Freq.	AZ=205	AZ = 115	AZ=25
3.1343 GHz	-77 ± 510	-352 ± 547	-482 ± 531
3.1791 GHz	-82 ± 438	603 ± 483	112 ± 531
3.3547 GHz	22 ± 293	222 ± 284	-262 ± 279

### 8.1.2 Magnetic response

The magnetic response was tested by analyzing network analyzer sweeps at various azimuth directions, and finding the total shift in frequency. An example of one resonator's shift can be seen in Figure 8.5. It is greatly reduced from the levels discussed in Chapter 5. Table 8.1 shows the shifts for a random selection of resonators from the starting azimuth location.

We cannot measure any shift due to magnetic fields, to within the error of our measurements. For the purposes of illustration of this effect, let us assume an average shift of 2 Hz per degree, at the level which would be undetectable here. This gives a rough fractional frequency shift of  $6 \times 10^{-10}$ . Assuming a  $50 \text{ m}^2$  collecting area on the CSO and typical values for responsivity (Band 1, 47 GHz bandwidth, and 0.3 kHz/K response, 50 K loading), we have a conversion factor of 56 mJy/Hz. This gives us a shift of over 100 mJy per degree. This is over four orders of magnitude improvement over 2007, consistent with an improved shielding factor in the hundreds. This level of magnetic susceptibility is below the level of noise expected while observing. In the future, it will be mitigated further by two effects – improved antenna efficiency, which will increase the responsivity by an expected factor of 2 (and proportionally reduce the magnetic response in mJy), and a better design of the magnetic shield, discussed in Chapter 9. In the 2010 observing run, the main focus involved the observation of point sources, for which the acceptable threshold for magnetic pickup is much higher. Magnetic effects were not detected in any observations, indicating that they were much smaller than the level of noise, and are largely removed with simple sky subtraction techniques. Most importantly, magnetic fields had no measurable effect on the proper projection of frequency and dissipation response.

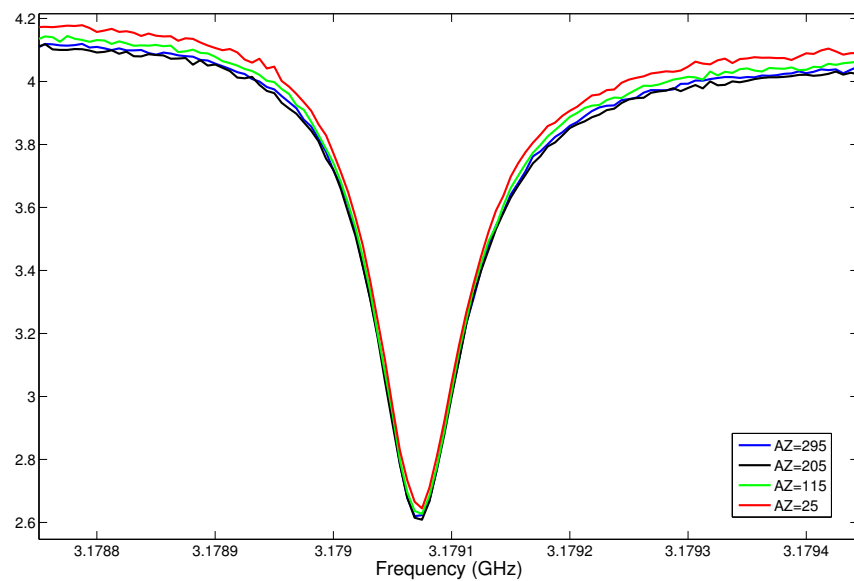


Figure 8.5: A typical resonator's response to change in azimuth. Plotted is arbitrarily-normalized  $|S_{21}(f)|$  around the resonance. The change in frequency is not measurable.

## 8.2 Readout system

The readout system used involves an open-source readout approach, as shown in Figure 2.11, and shown in more detail in Figure 8.6 [30]. This diagram is very complex, so here we focus only on the major components. In this system, a buffer comprising the sum of a total of 126 probe signals is generated by the DAQ computer. These are limited to a 300 MHz bandwidth: a clock (synthesizer) rate of 340 MHz set the maximum total frequency, while electronic filtering limits the bandwidth an additional 40 MHz. The generated signal is converted to analog, and mixed up to the band of interest ( $> 3$  GHz). The probe signals, in the cryostat, experience phase and amplitude changes associated with the loading on the resonators. After the cryostat, the signals are mixed back to low frequencies, and are converted from analog to digital. In digital form, the probe signals are effectively mixed, the equivalent of analog homodyne mixing, to find the complex transmission of each probe signal. These data, in the form of a complex timestream for each detector, are sent to the DAQ computer.

The probe signals are sent in with independent powers found, before the run, not to saturate each resonator. However, the exact power level could not be controlled precisely, leaving a 1-2 dB scatter between the actual generated power and the nominal power. This varies from buffer to buffer, leaving the actual calibration of the resonators somewhat more difficult than in the case where the powers are known precisely. In practice, this variation is small enough to not make a large difference.

At the beginning of the run, a buffer was created corresponding to the approximate frequency of each resonator within reach, a total of 55 resonators (45 antenna-coupled), as well as 71 off-resonance tones calculated to not interfere with the resonances. Before each observation, the synthesizer used as a local oscillator sweeps over a span of frequencies. The buffer played is the same, giving the effect of each probe frequency sweeping in power - an IQ sweep over each resonator and off-resonance point. From these sweeps, the optimal resonance frequencies are found quickly – the method of finding the resonance frequency on-the-fly before each scan is discussed in Appendix

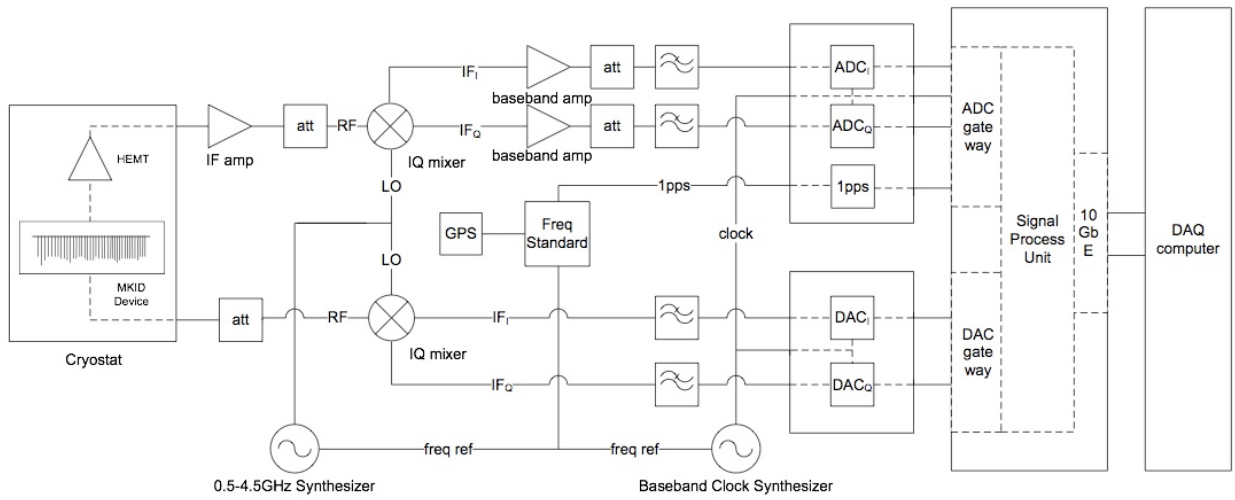


Figure 8.6: A schematic of the software defined MKID readout, from Ref. [30] (courtesy of Ran Duan). Buffers determining the probe frequencies and powers are generated by the DAQ computer (right). These are converted to analog, mixed up to MKID frequencies, and sent into the cryostat (left). The probe signals, after the cryostat, are mixed back to baseband, and converted to digital. The finally processed signals are sent back to the DAQ computer over a 10 Gb ethernet connection.

D. These sweeps, in principle, can be used to determine the calibration, as the resonator width and frequency vary with sky loading. After the resonance frequencies are found, the local oscillator is returned to its median frequency and a new buffer is created with sine waves corresponding to the newly found resonance frequencies under those sky conditions.

One significant problem involving the readout comes from the  $1/f$  noise related to the generation of signals. It is likely that temperature fluctuations in the voltage regulator of the DAC can cause excess  $1/f$  noise. This would be easily removable, as it is a common mode signal seen in unprojected I and Q directions. However, combined with HEMT noise and low-frequency sky noise, an additional  $1/f$  source greatly complicates the noise removal, and may cause it to be much more difficult to remove the total  $1/f$  noise. The timestreams have show significant  $1/f$  noise in addition to HEMT noise, which we believe to be attributable to this readout hardware. Electronics noise removal algorithms, developed by Sunil Golwala, Jack Sayers and Tom Downes, are necessary to remove significant portions of this noise.

### **8.3 Calibration**

In submillimeter and millimeter astronomy, calibration – the mapping between detector signal (typically in Volts) and source signal (typically in Janskys) – varies with atmospheric opacity. As the opacity becomes larger, the loading on detectors becomes greater, rendering the detectors less sensitive. Typically, this is accounted-for by mapping calibration sources: sources of known flux density, such as planets or other well-characterized objects. The peak response to such a source as a function of atmospheric opacity, or sky loading, is necessary to find the flux density of objects in science fields, such as submillimeter galaxies. For a true calibration curve, we must establish first a proxy for sky loading. This can be established by the observatory measurements of  $\tau_{225}$ , but this can be somewhat unreliable. A reliable instrument measurement of opacity is preferred.

### 8.3.1 A proxy for atmospheric opacity

Given the IQ sweeps before each observation, one could determine how to calibrate the data under changing sky conditions. Let us first consider the theory, and how and why calibration is applied. In general, a proxy is needed to ensure that data is coadded correctly in units of optical power (or, more typically, flux density units such as Jy). Some calibration observations are taken of planets or sources of known flux density, but most science images will not have a calibrator source as a guide. Therefore, it is necessary to find some proxy in the data which serves to determine the overall load seen by the detector, and therefore what the background loading is. This allows us to convert between the units of the map, or timestream, and the units of flux density for any arbitrary observation, with the minimum scatter.

The timestream is recorded, effectively, as the complex voltage of the transmitted signal. Given an IQ sweep in the same units, it is easy to calibrate into units of fractional frequency shift. For a given transmission,  $z(f) = S_{21}(f)V_{carrier}(f)$ , one can find the distance between adjacent frequency points in voltage. In an IQ sweep, steps are taken in probing  $z$  as a function of frequency at finite frequency steps. The goal is to measure  $dz(f)/df$  to convert into frequency shift. Simply by finding the distance between adjacent points  $z(f_1)$  and  $z(f_2)$ , near the resonance frequency, and knowing the frequency difference  $f_1 - f_2$ , one can find the conversion between voltage change and effective frequency shift. This can only be done if  $f_1 - f_2$  is very small compared to the width of the resonance; if this is not true, then the distance will significantly underestimate the response.

Putting the maps into these calibrated units is only the first part, because the frequency shift per unit power is still a function of the atmospheric loading. This causes the response,  $df/dP$ , to fall off as  $1/\sqrt{T_{load}}$  in the Rayleigh-Jeans limit. As mentioned above, the atmospheric load is proportional to  $1 - \exp(-\tau/\cos(ZA))$ , where  $\tau$  is dependent upon the frequency of the light. The question is, what is the best proxy for this atmospheric loading?

The first proxy one would think of is the resonance frequency. This clearly shifts with load, as it is the primary response to how we detect changes in power. However, we only measure resonance

frequency to the precision of the IQ sweep, which in this run was 2.6 kHz. This can yield too much scatter for the precise determination of the calibration. The average shift in resonance frequency (from an arbitrary point) is seen scaled with the smoothed  $\tau_{225}$  measured at the telescope in Figure 8.7. The frequency shifts shown here are determined by subtracting out the resonance frequency found from an arbitrary observation. Much of the scatter may be attributable to the significant variation among antennas, so it is possible this will be useful in the future to calibrate. By fitting  $df/d\tau$ , we can effectively determine  $\tau$  for any observation.

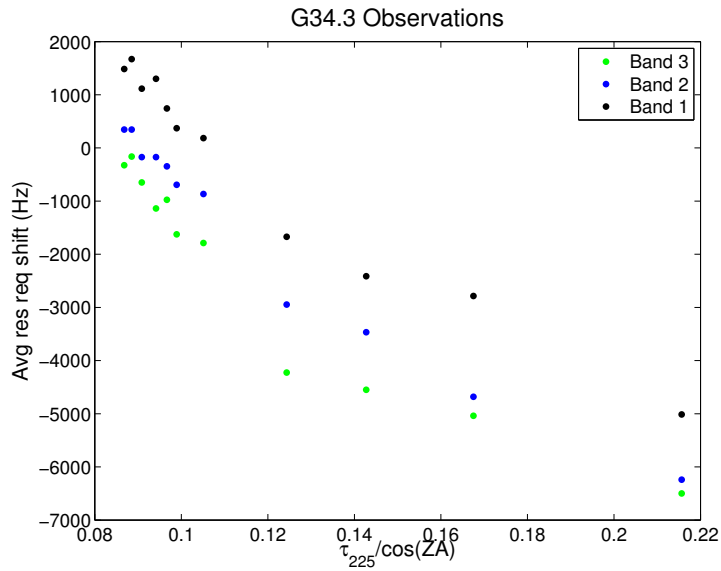


Figure 8.7: Average frequency shift from an arbitrary observation's value as a function of  $\tau_{225}$  for observations of G34.3, including a polarizing grid. Each band is averaged separately. Resonance frequencies are determined as the most responsive point in  $S_{21}$ . Shifts are not corrected for relative responsivity. The  $\tau$  plotted is smoothed with time.

Another possibility one may think is to use  $dz/df$  discussed above, or the maximum  $\Delta z/\Delta f$  in the map. In general, this should be proportional to  $Q^2/Q_c$ , or  $\frac{1}{1/Q_c+Q_c/Q_i^2}$ .  $1/Q_i^2$  should be proportional to the square root of the power of the load received. This would make it a viable calibrator, except for the large variation in  $Q_c$  among detectors, and variation in the amount of power in each. While this is very useful for calibrating individual detectors, it is not a good proxy for  $\tau_{atm}$ , except on a detector-by-detector basis.

It is difficult to determine true calibration based on peak heights for the telescope observations given. The main reason is that, given the large excess load due to dark pickup in the optics box, the peak heights do not change strongly as a function of sky conditions. This is illustrated in Figure 8.8.

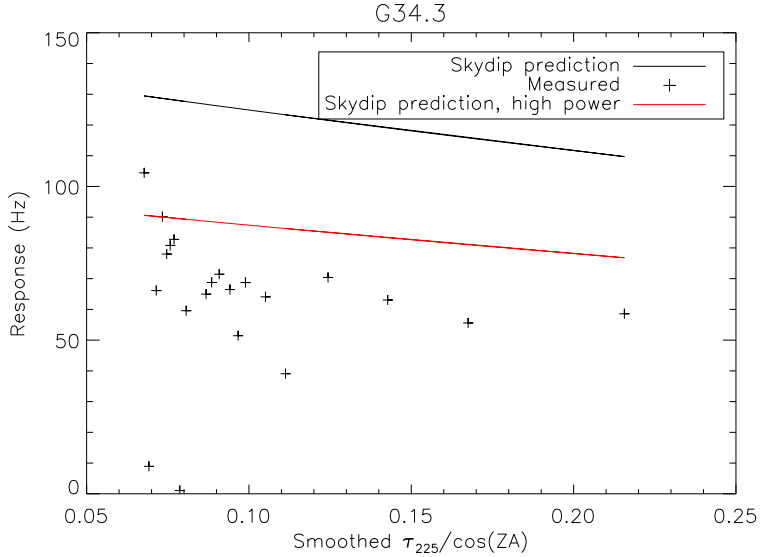


Figure 8.8: The response to the calibration source G34.3 for a typical Band 1 resonator [105]. The black line shows the predicted frequency response to the source from hot/cold measurements. The red includes a factor of 0.7, a reduction to approximately account for the high readout power used. The predictions come from the skydip response and measured effective excess load. The pluses show the measured peak response of the resonator to the source.

### 8.3.2 Dark pickup and calibration systematic effects

In these calibration data, we must additionally check one systematic effect: to see if the dark pickup (i.e. non-antenna response) biases the light (antenna-coupled) response. This would occur if the dark response added significant wide-band response to the measured peak heights of calibration sources. This effect is most easily seen by finding the dark response to a point source. Figure 8.9 shows the response to Mars in 4 colors. It is easy to see that, to the limit of noise in the maps, there is no dark response to Mars. Mars, at this time, is an exceptionally bright source, over 500 Jy in Band 3.

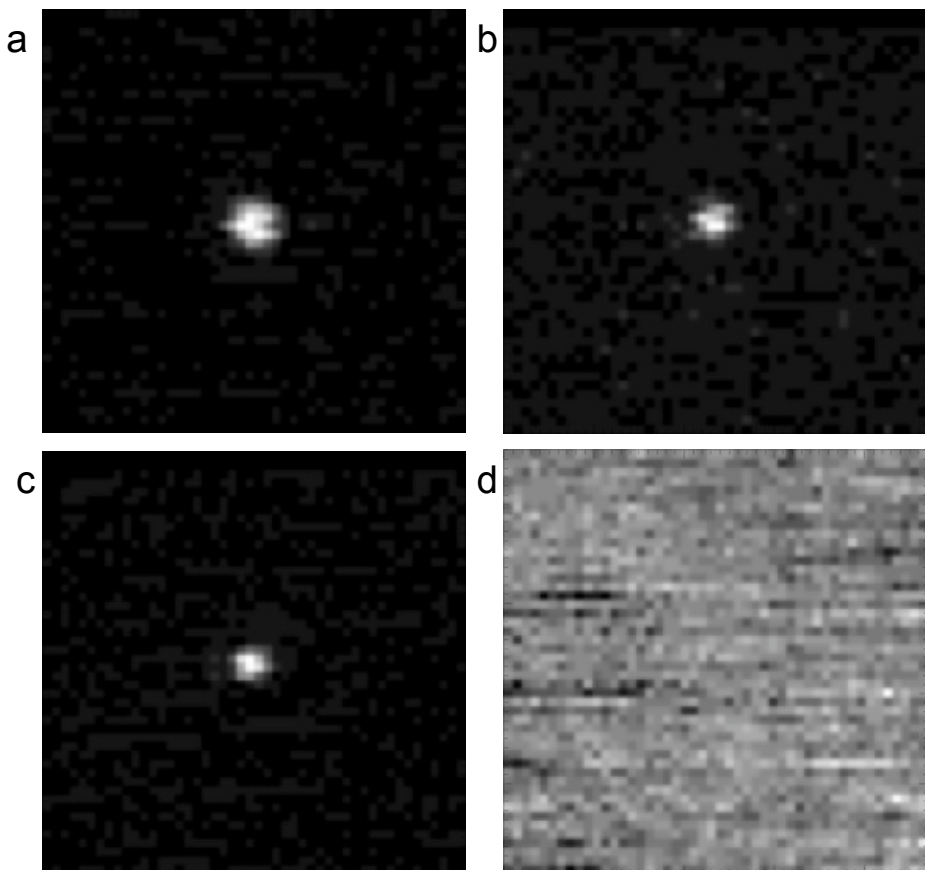


Figure 8.9: Mars viewed in a single resonator of three colors and dark [105]. Plotted are maps from a single a) 230 GHz, b) 290 GHz, c) 350 GHz, and d) dark resonator. The figures are peak-normalized, but all images have similar noise values.

This lack of dark response is somewhat intuitive: whatever the cause, it is unlikely to couple well to far-field point sources. If caused by residual pickup through the interdigitated capacitor, the beam will be very wide and not couple well to point sources. If caused by temperature changes of the array substrate, stray light from high angles would cause more pickup than high-directivity radiation.

### 8.3.3 Coaddition of multiple detectors

To correctly coadd the timestreams from multiple detectors and create an astronomical map from the entire array, the first step is to find the relative responsivity among the detectors. In general, this can be done by finding the relative response to a point source, and weighting the detectors by the peak height of their observations. A more precise method involves using the sky noise as a “source” by which the detectors can be weighted [102]. Using sky noise provides much more data, as instead of a single peak height for an observation, all the signal from a blank field can be used toward finding the relative responses. In determining a sky noise template during cleaning, each resonator is weighted relative to the mean to optimally remove fluctuations in sky loading. This is also the weighting of the response of each detector relative to the mean. In general, this relative response is a function of  $\tau_{225}$ . However, due to large excess load, the relative responsivity is effectively constant with  $\tau_{225}$ . This is seen for a typical detector’s frequency response in Figure 8.10. The dissipation direction did not yield relative responsivities that were nearly as consistent, so this method was not used for the dissipation data.

With the coaddition of all detectors, it is possible to make calibration curves – plots of source peak heights versus the sky opacity. The calibration curve for both Neptune and G34.3 is seen in Figure 8.11. All three bands are plotted for comparison, exclusively in the frequency direction. The responsivities do not change greatly with variable  $\tau$ ; this is again likely due to the high effective excess load from the dark pickup.

It is clear from Figure 8.11 that the responsivity is a factor of 2-4.5 lower than the other two bands, depending on  $\tau_{225}$ . It is expected to be less responsive simply because the bandwidth is

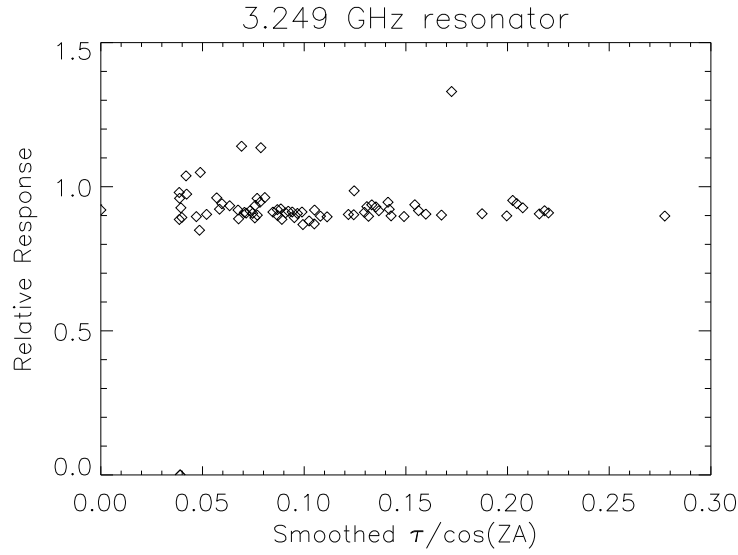


Figure 8.10: A typical resonator's relative response vs.  $\tau_{225}$ . Apart from a few outliers, the response relative to other detectors is surprisingly consistent from observation-to-observation.

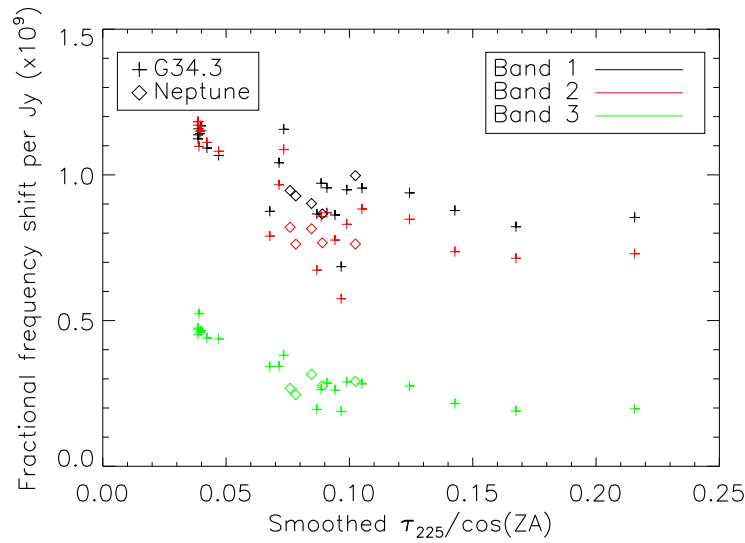


Figure 8.11: Calibration curves for all three bands, in the frequency readout direction. Here we plot the effective fractional frequency change corresponding to one Jansky of source flux as a function of sky loading.

Table 8.2: The predicted relative responsivity among bands to point sources. This includes the effect of hot/cold response and the excess load from the optics box, as well as the atmospheric attenuation, but no effects pertaining to readout power. The median responsivities are compared.

$\tau_{225}$	Resp(B1)/Resp(B2)	Resp(B1)/Resp(B3)	Resp(B2)/Resp(B3)
0.05	1.11	2.03	1.83
0.10	1.17	2.34	2.00
0.15	1.22	2.66	2.18
0.20	1.27	3.01	2.36

smaller: Janskys are units of flux density, meaning that the actual power incident is proportional to the effective bandwidth. It is also established above that the excess load is generally larger. Using the median values for excess load and responsivity, we compare the response in the bands at various sky loads in Table 8.2. Note that this does not take into account the effect of readout power, and its high variability from detector to detector. This is simply an exercise to see if, all else being equal, the relative responsivity among the bands makes sense. In fact, the Band 3 response is slightly lower than what would be predicted, as at high  $\tau_{225}$ , it is a factor of 3 lower than the Band 1 response. However, this discrepancy is relatively small in the light of so many uncertainties, and may be attributed to poorer telescope efficiency at 350 GHz or small differences in the illumination pattern of the primary mirror. The 350 GHz response here shows significant improvement over the Band 3 response in the first telescope run, discussed in Chapter 5.

The coaddition of detectors seems to work nearly as well as anticipated. The peak heights still show significant scatter, even with the proper weighting of detectors. However, the general trend towards higher responsivity at low  $\tau_{225}$  is easily seen, despite the large effective excess load.

## 8.4 Sensitivity and future prospects

The sensitivity for a camera on a given telescope is generally quoted in Noise Equivalent Flux Density (NEFD), defined in Equation 5.3. From individual resonator maps, it is straightforward to calculate the RMS noise of the map (excluding any sources) and the observing time per map pixel. The response to a point source is typically found by fitting a Gaussian profile to the point

spread function in the map. The peak value of this fit gives the signal with respect to the RMS noise. With known source flux, the NEFD is automatically known.

As seen in Figure 8.12, we reached  $\sim 400 \text{ mJy s}^{1/2}$  in Bands 1 and 2 using only sky subtraction algorithms, as calculated by Dr. Phil Maloney [68]. This was calculated from a typical observation of the source G34.3. The best sensitivities are close to  $200 \text{ mJy s}^{1/2}$  in the low frequency bands. The median sensitivity is almost an order of magnitude above the photon noise limit. In the 350 GHz band, the sensitivities are over  $1 \text{ Jy s}^{1/2}$ . This is consistent with the smaller relative response in this band, discussed in Section 8.3.3 above. The dissipation direction signal-to-noise ratio is significantly worse than that of the frequency direction. This also suggests that we are simply not removing the gain and phase fluctuations very well, and that we are still limited by the amplifier-like noise sources. It could also suggest that the large effective excess load is reducing the effective responsivity, so that the amplifier-like noise is significantly larger than the level of photon noise. Work is ongoing to improve in this regard.

The major limitations to sensitivity are the residual HEMT and electronics  $1/f$  noise and the large excess load from the direct pickup. It is also likely that there is some residual sky noise left in the maps. As shown in Equation 3.19, the NEP in the external limit of amplifier or electronics noise is proportional to the sub/millimeter load power. Thus, if the effective excess load is the same as the sky load, the NEP would be a factor of two lower as a result. In this case, the excess load is typically much larger than the skyload, reducing the NEP by a factor of several. In the amplifier or electronics noise limit, a 120 K excess load with 30 K atmospheric load, for example, will decrease the sensitivity by a factor of 5 compared to the case of no excess load, putting the detector well above BLIP.

Future work will revolve around eliminating, or reducing to a manageable level, the  $1/f$  noise and the direct pickup. Another improvement will be to increase the antenna efficiency by a factor of 4 to reach the expected level. This will have the same effect as proportionally reducing the excess load, even if the direct pickup remains unchanged.<sup>2</sup> We can ensure that we will reach BLIP in

---

<sup>2</sup> As discussed in Chapter 4, the excess load figure assumes the mechanism has the same efficiency as the response.

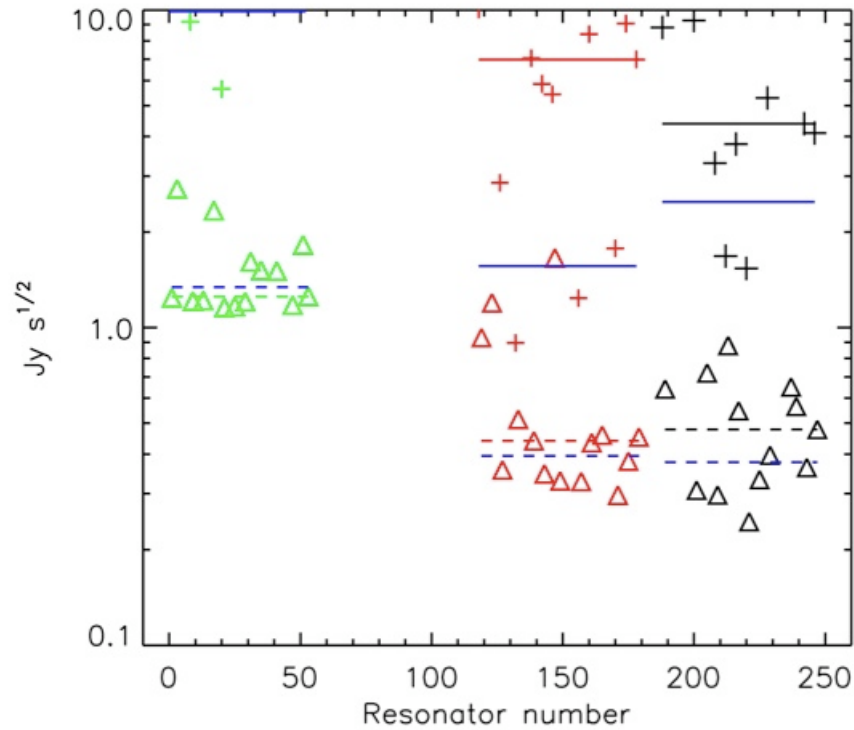


Figure 8.12: Sensitivity reached for the observed resonances during a typical observation, from Ref. [68] (courtesy of Phil Maloney). Dissipation sensitivity is denoted by plus symbols, and frequency sensitivity by triangles. The blue solid and dashed lines are inverse-variance-weighted mean values, and the other colors represent median values. This particular observation was taken on June 24, 2010.

the frequency response by either increasing optical efficiency or reducing the detector volume. If the fundamental frequency NEP is still above the background limit, these modifications can bring the frequency NEP down arbitrarily. This will likely involve a tradeoff of lower detector yield due to collisions caused by lower resonator  $Q_i$ , but may be necessary to reach background-limited sensitivity using frequency response. Finally, work will be required to eliminate the excess loading from the non-antenna resonator pickup. If antenna efficiency is greatly increased, this will be less of an issue, but will still cause excess load. Though the sensitivities found during this observing run were not good enough for a facility instrument, there is cause for optimism for reaching sensitivity goals with the final MKID camera, given reasonable changes based on the experience here.

## **8.5 Conclusions reached on MKID design from the entirety of lab and telescope testing**

From 2007 to 2010, antenna-coupled submillimeter MKIDs have been systematically tested to optimize performance on ground-based imaging cameras. Here we consider what has been accomplished in the testing of MKIDs in the course of the DemoCam's tenure, what has been learned, and what must be investigated in the future.

### **8.5.1 Accomplishments**

To see what has been accomplished in terms of understanding and optimizing MKIDs, it is useful to revisit the parameters introduced in Section 2.3.

#### **8.5.1.1 Optical efficiency**

The optical efficiency is impossible to know precisely unless the real film thickness of the aluminum absorber is known. The other vital parameters for determining MKID efficiency –  $R$ ,  $\Delta_0$ ,  $\alpha$  – have been reliably measured, or extracted from measured data, in Sections 4.2.2.1 and 4.2.2.2. Figure 4.33 shows the extracted optical efficiency as a function of assumed thickness.

---

By increasing the antenna efficiency, we effectively decrease its contribution relative to the response.

This would be a single point if the true resonator thickness was known. Although lower than the calculated values, these efficiencies appear to make sense due to several systematic effects discussed in Section 4.2.3.5. In Figure 6.22, the efficiencies are shown for assuming a certain thickness for a later IDC device, as these have much larger scatter in efficiency. We have shown that the original efficiencies are near what should be expected, but the later efficiencies seem to be too low by a factor of several.

### **8.5.1.2 Excess load**

The excess load has been found in all optical configurations. In the original DemoCam setup, discussed in Section 4.2.3.4, excess loads were manageable, and were reduced by widening the optical windows. In the later redesigned configuration, excess load increased with only Teflon filtering, but decreased to manageable levels with Fluorogold or metal-mesh filters (see Figure 6.14). In Figure 8.4 we see the excess load in the laboratory and at the telescope with the final device (8b). The telescope excess is significantly higher, largely due to wide-angle stray light directly coupling to the resonator. This load is unacceptably high (100-200 K), but the primary source – wide-angle non-antenna pickup – is understood.

### **8.5.1.3 Spectral bandpasses, beam maps and point source responsivity**

Spectral bandpasses have been measured using Fourier Transform Spectroscopy, as seen in Figure 4.28. This has been used in this thesis to confirm bandwidths for use in efficiency calculations, both in the laboratory and at the telescope (where the atmosphere's emissivity is highly frequency dependent). Beam maps have been used to show that we expect good coupling to point sources. These predictions have largely been tested by finding the response to astronomical sources of known flux density. The responsivity to these sources appears to be reasonable given the high readout power used, as seen in Section 8.3.1.

#### 8.5.1.4 Internal and external noise

Measurement of noise is not the primary thrust of this thesis, but its measurement is essential in optimizing the detector NEP. Noise measurements have been converted into NEP in Figure 7.7, and are discussed in Section 7.2.2. While not definitive, the data is suggestive that we have reached photon-limited noise performance at low optical efficiency, at least in the white noise part of the spectrum ( $\sim 1$  kHz).

#### 8.5.1.5 Systematic effects

Many different effects have been identified, and a large number have been solved. Evidence for non-uniform power absorption has been found in the lower-than-expected measured efficiency (see Section 4.2.3.5 for discussion) and in the base temperature dependence of the “naive” excess load, as well as through theoretical expectations. The source of the largest portion dark response, or direct (non-antenna) resonator pickup, has been identified to be due to the substrate heating from variable optical loads. The ratio  $\delta\sigma_2/\delta\sigma_1$ , as a measure of the array temperature, was a fundamental quantity in discovering the cause of this effect, as shown in Figure 6.21. Though greatly reduced, dark response is still an issue, but much of the response is likely non-thermal in origin (see discussion in Section 6.6.2.2). The systematic effect of crosstalk, discussed in Section 6.4.2.2, has been effectively solved by physically separating resonators nearby in resonant frequency. Finally, the effect of magnetic fields has been reduced to the point where it is difficult to measure, even with only a factor of a few hundred in magnetic field reduction.

#### 8.5.1.6 Readout power

One of the most important issues for MKIDs involves the optimal readout power for the best sensitivity. Figures 7.6 and 7.7 show that increasing power in excess of the optical load (for low efficiency, between -80 and -90 dBm, dominated by the excess load) improves the sensitivity. However, this conclusion appears to be highly dependent on quasiparticle density, as resonators at low quasiparticle densities see a decrease in signal response with power (see Section 4.2.2.4). At

low frequencies and high steady-state quasiparticle densities, heating of quasiparticles seems to be a bigger effect than the breaking of Cooper pairs, as evidenced by the fact that the resonance gets deeper with power. For MKIDs in use with sub/millimeter ground-based applications, with high steady-state quasiparticle densities, the conclusion is that high readout power improves sensitivity, until the point of saturation, or bifurcation, of the resonance loop.

#### **8.5.1.7 Other accomplishments**

The understanding of MKIDs, while a large part of the project, is not our only goal. A successful system for calibration of responsivity under varying load conditions has been explored in Section 8.3. Sensitivities, while not yet optimal, have improved significantly, highlighted by the telescope sensitivities achieved in Section 8.4. Array design issues, such as optimal resonator spacing and responsivity, have been carefully considered for the final design. Multiple frequency tones have been shown to be effective in reducing amplifier  $1/f$  noise. In telescope usage, the detectors have matured significantly, and have seen a factor of several improvement in sensitivity, despite a reduction in optical efficiency associated with the smaller detector platescale. In short, operation of MKIDs in submillimeter operation have been effectively characterized, with lessons learned which are applicable to future designs and operation.

#### **8.5.2 Lessons for the future of MKIDs**

The lessons gathered from several years of MKID testing are described in detail in the laboratory testing chapters. Here is a concise summary of some of the most important lessons in the operation of antenna-coupled MKIDs.

1. It is essential to eliminate any dark response or  $Q$  degradation as thoroughly as possible. To first order, this requires stringently filtering all light from wavelengths outside of the detector bands to ensure optimal operation. Letting in too much light can lead to tile heating or direct pickup onto the array. This can severely reduce sensitivity or, in the worst case, impose a systematic effect on the signal. Any heating, as with excess loading, can sharply degrade dissipation response. In

the amplifier noise limit, the response is proportional to  $Q^2/Q_c$ , so a degraded  $Q$  can very quickly increase NEP.

2. Optimization of readout power is the ultimate goal to improve sensitivity. As discussed in Section 8.5.1.6, the signal-to-noise ratio will increase up to the point of resonator saturation. The power level at which saturation occurs must be found for each resonator to ensure optimal sensitivity.

3. Off-resonance probes are useful for removal of low-noise amplifier (LNA) noise. The amplifier gain and phase noise generally point in different directions from the resonator frequency and dissipation noise, so it can be more difficult to perform useful subtraction from pixel-to-pixel. The addition of external photon and sky noise makes the HEMT LNA and correlated photon noise removal more complicated. Simply put, off-resonance tones are easier to work with.

4. Correct resonance frequency prediction is a key long-term goal. It is straightforward to reach BLIP in the frequency direction by making an extremely sensitive detector (i.e. low volume, high  $\alpha$ ) with low  $Q$  under load. However, this would lead to large overlap between detectors, and unacceptable crosstalk. Reducing the scatter between predicted and actual resonance frequencies is essential for the long-term usage of MKIDs for ground-based astronomy.

### **8.5.3 Future work on the understanding of MKID behavior**

The most fundamental, outstanding questions about MKID behavior – not limited to ground-based sub/millimeter MKIDs – pertain to the optimal use of readout power. The first question relates to the efficiency of readout power at creating quasiparticles. We know that the  $Q$  of a heavily loaded resonator will increase with readout power, and that the effective heating of quasiparticles must be dominant, but we must know the limits of high power. This is particularly important for applications involving low photon backgrounds, such as space-based or spectroscopic applications.

The second question involves the saturation, or bifurcation, or resonances. The exact point at which a loop becomes saturated must be well understood by uniform, systematic testing. In particular, this includes the precise effect of quasiparticle density on the saturation power, and

the dependence of the saturation power on material properties (e.g. film thickness). The power of saturation has proved highly variable from detector-to-detector, and finding the reason for this variability is an important step.

These questions will determine the ultimate sensitivity of MKIDs in all the regimes in which they will be used in the future.

## Chapter 9

### MKID Camera and future work

The primary purpose of the development, testing and demonstration of DemoCam has been to pave the way for the smooth operation of a much larger sub/millimeter MKID camera. Here are detailed the design parameters for this full MKID camera, dubbed the Multicolor Sub/millimeter (kinetic) Inductance Camera (MuSIC or MUSIC). Included is a discussion of the optics, the hardware design, the array design and integration, and the readout system. This camera is scheduled to be deployed in 2011. Individual tiles will be pre-screened in the DemoCam Dewar, and integrated into the large camera cryostat.

#### 9.1 Cryostat design

The cryostat was built by High Precision Devices in Boulder, CO. It includes a PT-415 Cryomech pulse tube cooler, capable of cooling the coldest stage well below 4 Kelvin. The cryostat is specifically designed to accept a Simon Chase He-10 fridge (3 stages of  $^4\text{He}$ ,  $^3\text{He}$  intercooler and  $^3\text{He}$  ultracold, respectively), designed for use in dry cryogenic systems, capable of reaching 220 mK under no optical load. The cryostat features a 50 K stage, analogous to the LN<sub>2</sub> stage in wet cryostats, where Teflon optical filters are included as infrared blockers. The 4 K space includes a 17-inch diameter coldplate, to which all the cold hardware is mounted. Stainless steel coaxial cables are sent in from the top of the Dewar, and are heat sunk at both 50 K and 4 K. The 4 K radiation shield is 22 inches tall; however, this length is not enough to incorporate the optical system and the magnetic shielding while limited in lateral space by the fridge. Therefore, a snout

was added around at the top of the radiation shield to give extra length. The cryogenic designs, and modifications to the cryostat, are discussed more fully in Ref. [50].

Due to the size of the windows, extensive testing was done to limit the external radiative load both on the fridge and on the individual stages. At 50 K, a split Teflon filter was introduced, such that the load from the cooler interior filter would be less of a factor on the 4 K stage. At the vacuum level, one or multiple metal mesh IR shader will be incorporated to reduce the load on the 50 K stage [99]. Further optical filtering is discussed in the optics section below.

## **9.2 Array mounting**

### **9.2.1 Tiles**

The array tiles used in the final camera will be similar in design to those in the DemoCam run. However, there are some significant differences. The antenna structure will be re-designed to operate most efficiently in the 150-350 GHz range. The frequency spacing of resonators will be reduced to  $\sim 3.5$  MHz, such that 144 resonators can fit into 500 MHz of bandwidth. Each tile will consist of 72 antennas, in a  $6 \times 12$  configuration, with a single feedline for each tile. These are to be subdivided into separate frequency bandwidths, discussed in Section 9.4 below. The tiles will be completely uniform resonators, all with the same type of fabricated MKID resonators and phased-array antennas. In DemoCam, only three observing colors were used, but in the final camera a fourth band, Band 0, is added with a center frequency of 150 GHz. The calculated bandpasses are shown in Figure 9.1. Dark pixels may still be useful for this type of camera, so a scheme will be introduced to include dark resonators in addition to the antenna-coupled resonators.

### **9.2.2 Magnetic shield and coaxes**

In order to ensure that magnetic effects on the detectors are below the noise level of the deepest integrations (and thus do not limit the mapping of extended structure with scan-synchronous signals), a multi-layer magnetic shield is used around the detectors. This consists of a two-walled

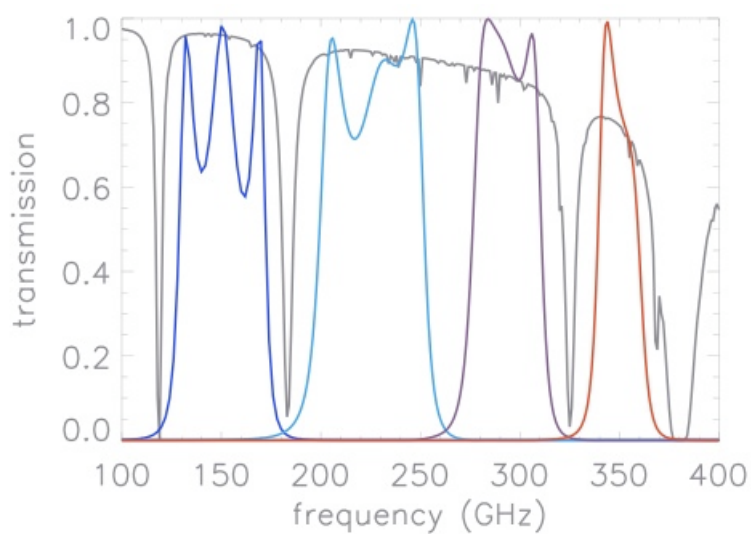


Figure 9.1: The four designed bands of the final MKID camera, plotted in frequency along with a reasonable atmospheric transmission at the CSO assuming 1.5 mm of precipitable water vapor. The bands are, from left to right, Band 0 through 3. Figure courtesy of Ran Duan.

high-permeability shield surrounding a niobium superconducting shell. This setup is shown in Figures 9.2 and 9.3. The coaxes used for readout, superconducting NbTi coaxes assembled by Coax-Co. of Japan, enter from the bottom of the shield and plug into the UC stage.

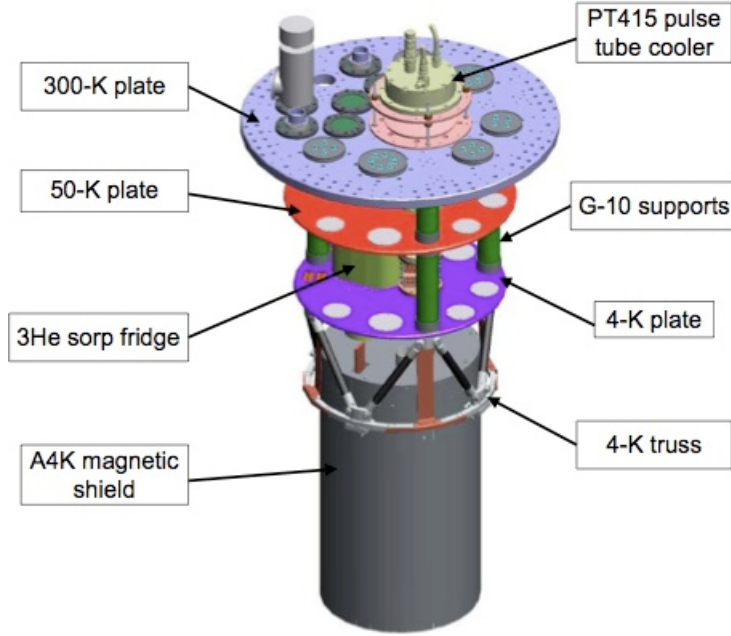


Figure 9.2: The camera interior with radiation shields removed, including magnetic shielding and support mounts, courtesy of Matt Hollister.

For simplicity, this array design consists of only 8 pairs of coaxes, each with one HEMT amplifier. To accommodate one pair per every 72 antennas, as opposed to the previous design of one every 36 pixels, the resonators are grouped into frequency batches. On one “effective” tile of 36 antennas,<sup>1</sup> all resonators are grouped into a 500 MHz bandwidth, while the other set of 36 on the same physical tile are grouped into another nearby (but not immediately adjacent) 500 MHz bandwidth. Two sets of frequency combs are generated, one for each frequency range, and combined onto the same line. The two are split after leaving the cryostat, and the appropriate bands are mixed together for readout. Thus, while the electronics requirements are the same as for 16 individual tiles of 36 antennas, the coaxial cable and HEMT amplifier requirements are

<sup>1</sup> Actual tiles have 72 antennas; an “effective” tile is half of one, analogous to a DemoCam array

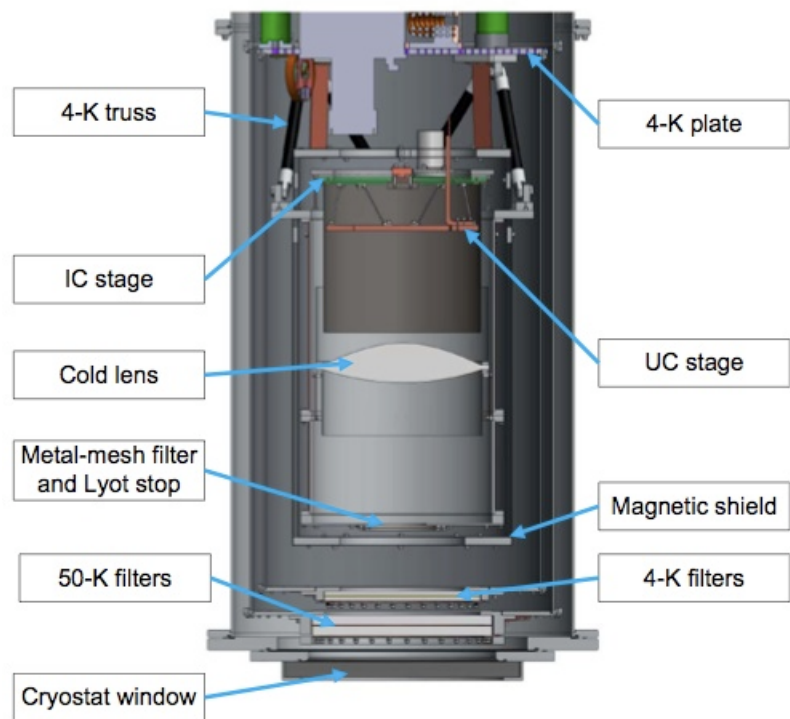


Figure 9.3: A cross-section of the camera's 4-Kelvin enclosed volume, courtesy of Matt Hollister [50].

significantly reduced.

### 9.3 Optics

The optics for MUSIC are designed to provide a wide field of view (14 arcminutes) with a Bolocam-like platescale of  $7''/\text{mm}$  [99]. This is identical to the DemoCam platescale, but with a much larger field of view and with many more detectors. While the focal plane is not fully Nyquist sampled in this regime, this does not significantly degrade mapping speed given the scan strategy of the camera. Nyquist sampling entails significant pixel-to-pixel correlations, so the mapping speed no longer rises proportionally to  $N_{det}$ . As the spacing of detectors becomes smaller than  $(f/\#)\lambda$ , then the signal is correlated among detectors: they are no longer truly independent. The mapping speed is proportional to the number of independent detectors, rather than  $N_{det}$ . With a limited number of detectors, mapping speed can instead be optimized by enlarging the field of view.<sup>2</sup> This also allows for greater per-pixel sensitivity, as a larger fraction of the beam is transmitted through the Lyot stop, coupling to astronomical sources. At  $850\ \mu\text{m}$ , the detectors are approximately  $1.75(f/\#)\lambda$  on a side, while at  $2\ \text{mm}$  they are  $0.75(f/\#)\lambda$ .

The optical train, from the focal plane to the Lyot stop, is incorporated inside the magnetic shield. At the Lyot stop is a 360 GHz low pass metal mesh filter, to block unwanted out-of-band radiation. This reduces significantly the load on the array, preventing significant tile heating and reducing the thermal load on the fridge's ultracold stage. In addition, it allows for a more optimal design of the IDC resonators' stepped impedance filter, as only frequencies up to this cutoff must be filtered.

### 9.4 Readout electronics

The readout electronics are very similar to those discussed in Chapter 8. The main difference is a scaling of the system up to 16 independent modules, and a more complex IF system to

---

<sup>2</sup> This applies only to large fields. For point sources, it is still beneficial to use smaller field of view with  $0.5(f/\#)\lambda$  sampling.

correspond to this scale-up. A single synthesizer can be used to upconvert the signals in a single tile, for a total of 8 synthesizers in the system.

The primary additional complication involves the division of tiles into two separate frequency groups, both read out with the same coaxial cable. The signals for the separate frequencies are combined using a 3 dB splitter in reverse, and sent into the cryostat. As an example, a group of probe signals mixed up to the range 3-3.5 GHz may be combined with another band from 3.6 to 4.1 GHz. At the output of the cryostat, the feed from a single HEMT cryogenic amplifier is divided into two signals, and one copy is fed into each board. Thus, while the signal sent to one board will contain the signals of two frequency groups, these are ignored on demodulation as they are far from the generated frequency tones.

Each “effective” tile will require its own DAC and ADC board, for a total of 16 units. The space required for these units, as well as the heat sinking to prevent thermal  $1/f$  noise, presents a significant engineering challenge. However, this is not insurmountable. In addition, the very high data rates coming off the boards will require significant computing power to properly process the data in real time. Thus, while multiplying the DemoCam readout system by 16 is fairly straightforward and manageable, it presents challenges of scale from the relatively simpler early systems. Indeed, one purpose of the DemoCam was to confront all the problems relating to a single unit, so that a full camera would only encounter challenges of scale.

## **9.5 Deployment and observation**

Since the completion and demonstration of basic MKID operation, the DemoCam will switch to the new tile format to test subarrays for the final camera. Rather than testing basic design, as has been the subject of this thesis, the testing will focus on yield, uniformity, proper bandpasses and the meeting of general sensitivity requirements.

While a significant number of tiles are being screened for acceptable operation, the camera will be assembled, integrated and tested to ensure relatively smooth operation at the telescope. At that point, a first engineering run will be scheduled at the CSO to test the operation in normal

conditions. This may yield preliminary science results, but the main purpose will be to solve any problems which may occur in regular operation. Unless significant problems are found with the camera, it will then be left at the CSO for regular observation runs. Improved or additional tiles will be shipped to the CSO and installed on-site.

During these observing runs, the camera will be focused on the objectives laid out in Chapter 1.1. In particular, there will be deep, multicolor surveys of large blank fields (e.g. COSMOS) and multicolor mapping of submillimeter galaxies in cluster environments. These observations, combined with *Herschel* SPIRE observations, will provide a significant step forward in the full mapping of submillimeter galaxy SEDs. In addition the multiple colors will improve understanding of systematic effects of submillimeter galaxies to SZ galaxy cluster surveys and scaling relations. Thus, the observations will be focused on two separate goals - pointed cluster observations, and wide area blank field surveys. The most interesting or rarest candidates, in turn, can be listed for follow-up spectroscopy with either wide-band spectrometers (e.g. Z-spec) or to high resolution imaging (e.g. with SMA or ALMA).

This camera, pending successful operation, will serve as the prototype for future MKID cameras at millimeter wavelengths as well as wavelengths in the far-infrared. Many of the hurdles toward ground-based observation have been successfully achieved, as well as many of the hurdles toward multicolor observation. Deployment of such cameras on large aperture telescopes, such as the proposed 25-meter Cornell/Caltech Atacama Telescope (CCAT), will allow high-resolution imaging and effective SED measurement of a wide range of sources.

## Bibliography

- [1] Randol Aikin. Design and implementation of a Fourier Transform Spectrometer for characterization of submillimeter and millimeter-wave instrumentation. Undergraduate Honors Thesis, University of Colorado, 2006.
- [2] J.E. Austermann, I. Artxaga, D. H. Hughes, Y. Kang, S. Kim, J. D. Lowenthal, T. A. Perera, D. B. Sanders, K. S. Scott, N. Scoville, G. W. Wilson, and M. S. Yun. AzTEC Millimetre Survey of the COSMOS field - II. Source count overdensity and correlations with large-scale structure. *Mon. Not. R. Astron. Soc.*, 393:1573–1583, 2009.
- [3] R. Barends, J. J. A. Baselmans, S. J. C. Yates, J. R. Gao, J. N. Hovenier, and T. M. Klapwijk. Quasiparticle Relaxation in Optically Excited High-Q Superconducting Resonators. *Physical Review Letters*, 100:257002–1–257002–4, 2008.
- [4] Rami Barends. Photon-detecting superconducting resonators. PhD thesis, Technische Universiteit Delft, 2009.
- [5] A. J. Barger, L. L. Cowie, D. B. Sanders, E. Fulton, Y. Taniguchi, Y. Sato, K. Kawara, and H. Okuda. Submillimetre-wavelength detection of dusty star-forming galaxies at high redshift. *Nature*, 394:248, 1998.
- [6] J. J. A. Baselmans and S. J. C. Yates. Long quasiparticle lifetime in Aluminum Microwave Kinetic Inductance Detectors using coaxial stray light filters. *Proc. LTD*, 13:160–163, 2009.
- [7] C.M. Baugh, C.G. Lacey, C.S. Frenk, G.L. Granato, Bressan Silva, L., A.J. A., Benson, and S. Cole. Can the faint submillimeter galaxies be explained in the  $\Lambda$  cold dark matter model? *Mon. Not. R. Astron. Soc.*, 356:1191, 2005.
- [8] D. J. Benford, J. W. Kooi, and E. Serabyn. Spectroscopic measurements of optical components around 1 terahertz. *Proc. Ninth Intl. Symp. Space Terahertz Tech*, 1998.
- [9] Dominic J. Benford, Michael C. Giadis, and Jacob W. Kooi. Optical properties of Zitex in the infrared to the submillimeter. *Applied Optics*, 42:5118–5122, 2003.
- [10] F. Bertoldi, C. Carilli, M. Aravena, E. Schinnerer, H. Voss, V. Smolcic, K. Jahnke, N. Scoville, A. Blain, K. M. Menten, D. Lutz, M. Brusa, Y. Taniguchi, P. Capak, B. Mobasher, S. Lilly, D. Thompson, H. Aussel, E. Kreysa, G. Hasinger, J. Aguirre, J. Schlaerth, and A. Koekemoer. COSBO: The MAMBO 1.2 Millimeter Imaging Survey of the COSMOS Field. *Astrophysical Journal Supplement Series*, 172:132, 2007.

- [11] R. S. Bhatia, S. T. Chase, S. F. Edgington, J. Glenn, W. C. Jones, A. E. Lange, B. Maei, A. K. Mainzer, P. D. Mauskopf, B. J. Philhour, and B. K. Rownd. A three-stage helium sorption refrigerator for cooling of infrared detectors to 280 mK. *Cryogenics*, 40:685–691, 2000.
- [12] A.W. Blain, I. Smail, R. J. Ivison, J.-P. Kneib, and D. T. Frayer. Submillimeter Galaxies. *Phys. Rept.*, 369:111, 2002.
- [13] M. Bonamente, M. Joy, S. J. LaRoque, J. E. Carlstrom, D. Nagai, and D. P. Marrone. Scaling Relations from Sunyaev-Zel'dovich Effect and Chandra X-Ray Measurements of High-Redshift Galaxy Clusters. *Astrophysical Journal*, 675:106–114, March 2008.
- [14] C. Borys, S. Chapman, M. Halpern, and D. Scott. The Hubble Deep Field North SCUBA Super-map I. Submillimetre maps, sources and number counts. *Mon. Not. R. Astron. Soc.*, 344:385, 2003.
- [15] John E. Carlstrom, Gilbert P. Holder, and Erik D. Reese. Cosmology with the sunyaev-zel'dovich effect. *Annual Review of Astronomy and Astrophysics*, 40:643–680, 2002.
- [16] Joint Astronomy Centre. Planetary Fluxes. <http://www.jach.hawaii.edu/jac-bin/planetflux.pl>, 2004.
- [17] S.C. Chapman, A.W. Blain, R.J. Ivison, and I.R. Smail. A median redshift of 2.4 for galaxies bright at submillimetre wavelengths. *Nature*, 422:695, 2003.
- [18] S. Cherednichenko and V. Drakinskiy. Low Noise Hot-Electron Bolometer Mixers for Terahertz Frequencies. *Journal of Low Temperature Physics*, 151:575–579, April 2008.
- [19] Leon N. Cooper. Bound electron pairs in a degenerate fermi gas. *Phys. Rev.*, 104(4):1189–1190, Nov 1956.
- [20] K. Coppin, E.L Chapin, A.M.J. Mortier, S.E. Scott, C. Borys, J.S. Dunlop, M. Halpern, D.H. Hughes, A. Pope, D. Scott, S. Serjeant, J. Wagg, D.M. Alexander, O. Almaini, I. Arétxaga, T. Babbedge, P.N. Best, A. Blain, S. Chapman, D.L. Clements, M. Crawford, L. Dunne, S.A. Eales, D. Edge, A.C. andFarrah, E. Gaztaaga, W.K. Gear, G.L. Granato, T.R. Greve, M. Fox, R.J. Ivison, T. Jarvis, M.J. andJenness, C. Lacey, K. Lepage, R.G. Mann, G. Marsden, A. Martinez-Sansigre, S. Oliver, M.J. Page, J.A. Peacock, C.P. Pearson, W.J. Percival, R.S. Priddey, S. Rawlings, M. Rowan-Robinson, R.S. Savage, M. Seigar, K. Sekiguchi, L. Silva, C. Simpson, I. Smail, J.A. Stevens, T. Takagi, M. Vaccari, E. van Kampen, and C.J. Willott. The SCUBA Half-Degree Extragalactic Survey II. Submillimetre maps, catalogue and number counts. *Mon. Not. R. Astron. Soc.*, 372:1621, 2006.
- [21] R. Davé, K. Finlator, B. D. Oppenheimer, M. Fardal, N. Katz, D. Kereš, and D. H. Weinberg. The nature of submillimetre galaxies in cosmological hydrodynamic simulations. *Mon. Not. R. Astron. Soc.*, 404:1355–1368, May 2010.
- [22] Peter K. Day. Resonance curve for the quarter wave resonator. *MKID collaboration internal report*, 2002.
- [23] P.K. Day, LeDuc, Mazin B.A. H.G., A. Vayonakis, and J. Zmuidzinas. A broadband superconducting detector suitable for use in large arrays. *Nature*, 425:817–821, 2003.

- [24] Piet A. J. de Korte, Joern Beyer, Steve Deiker, Gene C. Hilton, Kent D. Irwin, Mike MacIntosh, Sae Woo Nam, Carl D. Reintsema, and Leila R. Vale. Time-division superconducting quantum interference device multiplexer for transition-edge sensors. *Review of Scientific Instruments*, 74:3807–3815, 2003.
- [25] M. J. Devlin, P. A. R. Ade, I. Arétxaga, J. J. Bock, E. L. Chapin, M. Griffin, J. O. Gundersen, M. Halpern, P. C. Hargrave, D. H. Hughes, J. Klein, G. Marsden, P. G. Martin, P. Mauskopf, L. Moncelsi, C. B. Netterfield, H. Ngo, L. Olmi, E. Pascale, G. Patanchon, M. Rex, D. Scott, C. Semisch, N. Thomas, M. D. P. Truch, C. Tucker, G. S. Tucker, M. P. Viero, and D. V. Wiebe. Over half of the far-infrared background light comes from galaxies at  $z \geq 1.2$ . *Nature*, 458:737–739, April 2009.
- [26] M. Dobbs, N.W. Halverson, P.A.R. Ade, K. Basu, A. Beelen, F. Bertoldi, C. Cohalan, H.M. Cho, R. Gusten, W.L. Holzapfel, Z. Kermish, R. Kneissl, A. Kovacs?, E. Kreysa, T.M. Lanting, A.T. Lee, M. Lueker, J. Mehl, K.M. Menten, D. Muders, M. Nord, T. Plagge, P.L. Richards, P. Schilke, D. Schwan, H. Spieler, A. Weiss, and M. White. APEX-SZ first light and instrument status. *New Astronomy Reviews*, 50:960–968, 2006.
- [27] H. Dole, G. Lagache, J.-L. Puget, K. I. Caputi, N. Fernández-Conde, E. Le Floc'h, C. Papovich, P. G. Pérez-González, G. H. Rieke, and M. Blaylock. The cosmic infrared background resolved by Spitzer. Contributions of mid-infrared galaxies to the far-infrared background. *Astronomy and Astrophysics*, 451:417–429, May 2006.
- [28] C. Darren Dowell, Christine A. Allen, Sachidananda Babu, Minoru M. Freund, Matthew B. Gardner, Jeffrey Groseth, Murzy Jhabvala, Attila Kovacs, Dariusz C. Lisa, S. Harvey Moseley Jr., Thomas G. Phillips, Robert Silverberg, George Voellmer, and Hiroshige Yoshida. SHARC II- A Caltech submillimeter observatory facility camera with 384 pixels. *Proceedings of the SPIE*, 4855:73, 2002.
- [29] Simon Doyle, Philip Mauskopf, Jin Zhang, Stafford Withington, David Goldie, Dorota Glowacka, Alessandro Monfardini, Loren Swenson, and Markus Roesch. Optimisation of Lumped Element Kinetic Inductance Detectors for use in ground based mm and sub-mm arrays. *Proc. LTD*, 13:156–159, 2009.
- [30] Ran Duan, Sean McHugh, Bruno Serfass, Benjamin A. Mazin, Andrew Merrill, Sunil R. Golwala, Thomas P. Downes, Nicole G. Czakon, Peter K. Day, Jiansong Gao, Jason Glenn, Matthew I. Hollister, Henry G. Leduc, Philip R. Maloney, Omid Noroozian, Hien T. Nguyen, Jack Sayers, James A. Schlaerth, Seth Siegel, John E. Vaillancourt, Anastasios Vayonakis, Philip R. Wilson, and Jonas Zmuidzinas. An open-source software-defined radio readout for MKIDs. *Proceedings of the SPIE*, 7741:67, 2010.
- [31] Theodore Van Duzer and Charles W. Turner. *Principles of Superconductive Devices and Circuits*. Prentice Hall, 2nd edition, 1999.
- [32] Freeman Dyson. A meeting with Enrico Fermi. *Nature*, 427:297, 2004.
- [33] M.L. Enoch, K.E. Young, J. Glenn, N.J. II Evans, S.R. Golwala, A.I. Sargent, P. J. Harvey, J.E. Aguirre, A. Goldin, D. Haig, A. Lange, G.T. Laurent, P. Maloney, P.D. Mauskopf, P. Rossinot, and J. Sayers. Bolocam Survey for 1.1 mm Dust Continuum Emission in the c2d Legacy Clouds : I. Perseus. *Astrophysical Journal*, 623:293–313, 2006.

- [34] D. J. Fixsen, E. Dwek, J. C. Mather, C. L. Bennett, and R. A. Shafer. The Spectrum of the Extragalactic Far-Infrared Background from the COBE FIRAS Observations. *Astrophysical Journal*, 508:123, 1998.
- [35] Michael Gaidis. *Superconducting Tunnel Junctions as Single-Photon X-Ray Detectors*. PhD thesis, Yale University, 1994.
- [36] Jiansong Gao. *The Physics of Superconducting Microwave Resonators*. PhD thesis, California Institute of Technology, 2008.
- [37] Jiansong Gao, Miguel Daal, Anastasios Vayonakis, Shwetank Kumar, Jonas Zmuidzinas, Bernard Sadoulet, Benjamin A. Mazin, Peter K. Day, and Henry G Leduc. Experimental evidence for a surface distribution of two-level systems in superconducting lithographed microwave resonators. *Applied Physics Letters*, 92:15–17, 2008.
- [38] Jiansong Gao, Jonas Zmudzinas, Benjamin A. Mazin, Henry G. LeDuc, and Peter K. Day. Noise properties of superconducting coplanar waveguide microwave resonators. *Applied Physics Letters*, 90:817–819, 2007.
- [39] J. Glenn, J. Bock, G. Chattopadhyay, S. F. Edgington, A. E. Lange, J. Zmuidzinas, P. D. Mauskopf, B. Rownd, and L. Yuen. BOLOCAM: a millimeterwave bolometric camera. *Proceedings of the SPIE*, 3357:326, 1998.
- [40] A. Goldin, J.J. Bock, C.L. Hunt, A.E. Lange, H.G. LeDuc, A. Vayonakis, and J. Zmuidzinas. SAMBA: Superconducting antenna-coupled multi-frequency bolometric array. *AIP Conference Proceedings*, 605:251–254, 2002.
- [41] A. Goldin, J.J. Bock, C.L. Hunt, A.E. Lange, H.G. LeDuc, A. Vayonakis, and J. Zmuidzinas. Design of broadband filters and antennas for SAMBA. *Proceedings of the SPIE*, 4855:163–171, 2003.
- [42] Sunil Golwala. Future Developments in Low Temperature Detectors for CMB and Submm Astronomy. *Proc. LTD*, 13:773–782, 2009.
- [43] T. R. Greve, A. Pope, D. Scott, R. J. Ivison, C. Borys, C. J. Conselice, and F. Bertoldi. A 1200- $\mu\text{m}$  MAMBO survey of the GOODS-N field: a significant population of submillimetre dropout galaxies. *Mon. Not. R. Astron. Soc.*, 389:1489–1506, October 2008.
- [44] T.R. Greve, R.J. Ivison, F. Bertoldi, J.A. Stevens, J.S. Dunlop, D. Lutz, and C.L. Carilli. A 1200 micron mambo survey of elaisn2 and the lockman hole - i. maps, sources and number counts. *Mon. Not. R. Astron. Soc.*, 354:779, 2004.
- [45] Christopher Groppi, Christopher Walker, Craig Kulesa, Dathon Golish, Jenna Kloosterman, Sander Weinreb, Glenn Jones, Joseph Barden, Hamdi Mani, Tom Kuiper, Jacob Kooi, Art Lichtenberger, Thomas Cecil, Gopal Narayanan, Patrick Ptz, and Abby Hedden. SuperCam: A 64 pixel heterodyne array receiver for the 350 GHz Atmospheric Window. *Proc. ISSTT*, 20:90, 2009.
- [46] Christopher Emil Groppi. *Submillimeter Heterodyne Spectroscopy of Star Forming Regions*. PhD thesis, University of Arizona, 2003.

- [47] L. J. Hainline, A. W. Blain, I. Smail, D. T. Frayer, S. C. Chapman, R. J. Ivison, and D. M. Alexander. A Mid-Infrared Imaging Survey of Submillimeter-Selected Galaxies with the Spitzer Space Telescope. *Astrophysical Journal*, 699:1610–1632, July 2009.
- [48] J. E. Healey, T. Lindstrom, M. S. Colclough, C. M. Muirhead, and A. Ya. Tzalenchuk. Magnetic field tuning of coplanar waveguide resonators. *Applied Physics Letters*, 93:043513–1–043513–3, 2008.
- [49] W. S. Holland, W. D. Duncan, B. D. Kelly, K. D. Irwin, A. J. Walton, P. A. R. Ade, and E. I. Robson. SCUBA-2: A large format submillimetre camera on the James Clerk Maxwell Telescope. *Proceedings of the SPIE*, 4855:1, 2003.
- [50] M. I. Hollister, N. A. Czakon, P. K. Day, T. P. Downes, R. Duan, J. Gao, J. Glenn, S. R. Golwala, H. G. LeDuc, B. A. Mazin, P. R. Maloney, O. Noroozian, H. T. Nguyen, J. Sayers, J. A. Schlaerth, S. Siegel, J. Vaillancourt, A. Vayonakis, P. R. Wilson, and J. Zmuidzinas. The cryomechanical design of MUSIC: a novel imaging instrument for millimeter-wave astrophysics at the Caltech Submillimeter Observatory. In *Society of Photo-Optical Instrumentation Engineers (SPIE) Conference Series*, volume 7741 of *Presented at the Society of Photo-Optical Instrumentation Engineers (SPIE) Conference*, August 2010.
- [51] D.H. Hughes, S. Serjeant, J. Dunlop, M. Rowan-Robinson, A. Blain, R.G. Mann, R. Ivison, J. Peacock, A. Efstatthiou, W. Gear, S. Oliver, A. Lawrence, M. Longair, P. Goldschmidt, and T. Jenness. High-redshift star formation in the Hubble Deep Field revealed by a submillimetre-wavelength survey. *Nature*, 394:241–247, 1998.
- [52] R.E. Glover III and M. Tinkham. Kinetic-equation approach to nonequilibrium superconductivity. *Phys. Rev.*, 108:243, 1957.
- [53] K. D. Irwin. An application of electrothermal feedback for high resolution cryogenic particle detection. *Applied Physics Letters*, 66:1998–2000, April 1995.
- [54] K. D. Irwin and K. W. Lehnert. Microwave SQUID multiplexer. *Applied Physics Letters*, 85:2107–2109, 2004.
- [55] K. D. Irwin, M. D. Niemack, J. Beyer, H. M. Cho, W. B. Doriese, G. C. Hilton, C. D. Reintsema, D. R. Schmidt, J. N. Ullom, and L. R. Vale. Code-division multiplexing of superconducting transition-edge sensor arrays. *Supercond. Sci. Technol.*, 23:034004–1–034004–7, 2010.
- [56] S. B. Kaplan, C. C. Chi, D. N. Langenberg, J. J. Chang, S. Jafarey, and D. J. Scalapino. Quasiparticle and phonon lifetimes in superconductors. *Physical Review B*, 14(11):4854–4873, Dec 1976.
- [57] A. Kovács, S. C. Chapman, C. D. Dowell, A. W. Blain, R. J. Ivison, I. Smail, and T. G. Phillips. SHARC-2 350  $\mu\text{m}$  Observations of Distant Submillimeter-selected Galaxies. *Astrophysical Journal*, 650:592–603, October 2006.
- [58] S. Kumar, J. Gao, J. Zmuidzinas, B.A. Mazin, H.G. LeDuc, and P.K. Day. Temperature dependence of the frequency and noise of superconducting coplanar waveguide resonators. *Applied Physics Letters*, 92:12–14, 2008.

- [59] Shwetank Kumar. Antenna Coupled Microwave Kinetic Inductance Detectors. PhD thesis, California Institute of Technology, 2007.
- [60] Guilaine Lagache, Jean-Loup Puget, and Herv ?e Dole. Dusty Infrared Galaxies: Sources of the Cosmic Infrared Background. Annu. Rev. Astron. Astrophys., 43:72768, 2005.
- [61] Lakeshore. Germanium RTDs. <http://www.lakeshore.com/temp/sen/gtrdts.html>, 2007.
- [62] T. M. Lanting, Hsiao-Mei Cho, John Clarke, W. L. Holzapfel, M. Lueker Adrian T. Lee, P. L. Richards, Matt A. Dobbs, Helmuth Spieler, and A. Smith. Frequency-domain multiplexed readout of transition-edge sensor arrays with a superconducting quantum interference device. Applied Physics Letters, 86:112511–1–112511–3, 2005.
- [63] Glenn Laurent. The Bolocam Lockman Hole Millimeter-Wave Galaxy Survey. PhD thesis, University of Colorado, 2005.
- [64] G.T. Laurent, J.E. Aguirre, J. Glenn, P.A.R. Ade, J.J. Bock, S.F. Edgington, A. Goldin, S.R. Golwala, D. Haig, A.E. Lange, P.R. Maloney, P.D. Mauskopf, H. Nguyen, P. Rossinot, J. Sayers, and P. Stover. The Bolocam Lockman Hole Submillimeter Galaxy Survey: Galaxy Candidates and Number Counts. Astrophysical Journal, 623:742, 2005.
- [65] G.T. Laurent, J. Glenn, E. Egami, A. Kovacs, G.H. Rieke, R.J. Ivison, M.S. Yun, J.E. Aguirre, and P.R. Maloney. The Bolocam 1.1 mm Lockman Hole Galaxy Survey: SHARC II 350  $\mu$ m Photometry and Implications for Spectral Models, Dust Temperatures, and Redshift Estimation. Astrophysical Journal, 643:38, 2006.
- [66] M. Lueker, C. L. Reichardt, K. K. Schaffer, O. Zahn, P. A. R. Ade, K. A. Aird, B. A. Benson, L. E. Bleem, J. E. Carlstrom, C. L. Chang, H.-M. Cho, T. M. Crawford, A. T. Crites, T. de Haan, M. A. Dobbs, E. M. George, N. R. Hall, N. W. Halverson, G. P. Holder, W. L. Holzapfel, J. D. Hrubes, M. Joy, R. Keisler, L. Knox, A. T. Lee, E. M. Leitch, J. J. McMahon, J. Mehl, S. S. Meyer, J. J. Mohr, T. E. Montroy, S. Padin, T. Plagge, C. Pryke, J. E. Ruhl, L. Shaw, E. Shirokoff, H. G. Spieler, Z. Staniszewski, A. A. Stark, K. Vanderlinde, J. D. Vieira, , and R. Williamson. Measurements of secondary Cosmic Microwave Background anisotropies with the South Pole Telescope. ArXiv e-prints, 2009.
- [67] P. R. Maloney. The impact of star formation and active nuclei on the interstellar medium in ultraluminous infrared galaxies. Astrophys. Space Sci., 266:207–230, 1999.
- [68] Philip R. Maloney, Nicole G. Czakon, Peter K. Day, Thomas P. Downes, Ran Duan, Jiansong Gao, Jason Glenn, Sunil R. Golwala, Matthew I. Hollister, Henry G. Leduc, Benjamin A. Mazin, Omid Noroozian, Hien T. Nguyen, Jack Sayers, James A. Schlaerth, Seth Siegel, John E. Vaillancourt, Anastasios Vayonakis, Philip R. Wilson, and Jonas Zmuidzinas. MUSIC for sub/millimeter astrophysics. Proceedings of the SPIE, 7741:15, 2010.
- [69] P.R. Maloney, N.G. Czakon, P.K. Day, R. Duan, J. Gao, J. Glenn, S. Golwala, M. Hollister, H.G. LeDuc, B. Mazin, O. Noroozian, H.T. Nguyen, J. Sayers, J. Schlaerth, J.E. Vaillancourt, A. Vayonakis, P. Wilson, and J. Zmuidzinas. The MKID Camera. Proc. LTD, 13:176–179, 2009.
- [70] P.R. Maloney, J. Glenn, J.E. Aguirre, S.R. Golwala, G.T. Laurent, P.A.R. Ade, J.J. Bock, S.F. Edgington, A. Goldin, D. Haig, A.E. Lange, P.D. Mauskopf, H. Nguyen, P. Rossinot,

- J. Sayers, and P. Stover. A Fluctuation Analysis of the Bolocam 1.1mm Lockman Hole Survey. *Astrophysical Journal*, 635:1044, 2005.
- [71] J. A. B. Mates, G. C. Hilton, K. D. Irwin, L. R. Vale, and K. W. Lehnert. Demonstration of a multiplexer of dissipationless superconducting quantum interference devices. *Applied Physics Letters*, 92(2):023514–023516, January 2008.
- [72] Hiroshi Matsuo, Yasunori Hibi, Toyoaki Suzuki, Masato Naruse, Takashi Noguchi, Yutaro Sekimoto, Yoshinori Uzawa, Hirohisa Nagata, Hirokazu Ikeda, Seiichiro Ariyoshi, Chiko Otani, Tom Nitta, Yao Qi-jun, and Mikio Fujiwara. Superconducting THz Camera with GaAs-JFET Cryogenic Readout Electronics. *Proc. LTD*, 13:292–396, 2007.
- [73] D.C. Mattis and J. Bardeen. Theory of the anomalous skin effect in normal and superconducting metals. *Physical Review*, 111:412–417, 1958.
- [74] B. A. Mazin, P. K. Day, K. D. Irwin, C. D. Reintsema, and J. Zmuidzinas. Digital readouts for large microwave low temperature detector arrays. *Nuclear Instruments and Methods*, 559:799, 2006.
- [75] Benjamin Mazin. Microwave Kinetic Inductance Detectors: The First Decade. *Proc. LTD*, 13:135–143, 2009.
- [76] Benjamin A. Mazin. *Microwave Kinetic Inductance Detectors*. PhD thesis, California Institute of Technology, 2004.
- [77] W. McMillan. Transition temperature of strong-coupled superconductors. *Physical Review*, 167:331–344, 1968.
- [78] Bret J. Naylor, Peter A. R. Ade, James J. Bock, C. Matt Bradford, Mark Dragovan, Lionel Duband, Lieko Earle, Jason Glenn, Hideo Matsuhara, Hien Nguyen, Minhee Yun, and Jonas Zmuidzinas. Z-spec: a broadband, direct-detection, millimeter-wave spectrometer. *Proceedings of the SPIE*, 4855:239, 2003.
- [79] Omid Noroozian, Peter K. Day, Byeong-Ho Eom, Henry G. LeDuc, Jiansong Gao, Juan M. Bueno, and Jonas Zmuidzinas. Advanced resonator designs for far-infrared astrophysics with MKIDs. *Proceedings of the SPIE*, 7741:24, 2010.
- [80] Omid Noroozian, Jiansong Gao, Jonas Zmuidzinas, Henry G. LeDuc, and Benjamin A. Mazin. Two-level system noise reduction for Microwave Kinetic Inductance Detectors. *Proc. LTD*, 13:148–151, 2009.
- [81] C. S. Owen and D. J. Scalapino. Superconducting state under the influence of external dynamic pair breaking. *Phys. Rev. Lett.*, 28:1559–1561, 1972.
- [82] E. Pascale, P. A. R. Ade, J. J. Bock, E. L. Chapin, J. Chung, M. J. Devlin, S. Dicker, M. Griffin, J. O. Gundersen, M. Halpern, P. C. Hargrave, D. H. Hughes, J. Klein, C. J. MacTavish, G. Marsden, P. G. Martin, T. G. Martin, P. Mauskopf, C. B. Netterfield, L. Olmi, G. Patanchon, M. Rex, D. Scott, C. Semisch, N. Thomas, M. D. P. Truch, C. Tucker, G. S. Tucker, M. P. Viero, and D. V. Wiebe. The balloon-borne large aperture submillimeter telescope: Blast. *Astrophysical Journal*, 681(1):400, 2008.

- [83] G. Patanchon, P. A. R. Ade, J. J. Bock, E. L. Chapin, M. J. Devlin, S. R. Dicker, M. Griffin, J. O. Gundersen, M. Halpern, P. C. Hargrave, D. H. Hughes, J. Klein, G. Marsden, P. Mauskopf, L. Moncelsi, C. B. Netterfield, L. Olmi, E. Pascale, M. Rex, D. Scott, C. Semisch, N. Thomas, M. D. P. Truch, C. Tucker, G. S. Tucker, M. P. Viero, and D. V. Wiebe. Submillimeter Number Counts from Statistical Analysis of BLAST Maps. *Astrophysical Journal*, 707:1750–1765, December 2009.
- [84] A. A. Penzias and R. W. Wilson. A Measurement of Excess Antenna Temperature at 4080 Mc/s. *Astrophysical Journal*, 142:419421, 1965.
- [85] T. A. Perera, E. L. Chapin, J.E. Austermann, K.S. Scott, G.W. Wilson, M. Halpern, A. Pope, D. Scott, M.S. Yun, J. D. Lowenthal, G. Morrison, I. Arétxaga, J.J. Bock, K. Coppin, M. Crowe, L. Frey, D.H. Hughes, Y. Kang, S. Kim, and P.D. Mauskopf. An AzTEC 1.1mm Survey of the GOODS-N Field I: Maps, Catalogue, and Source Statistics. *Mon. Not. R. Astron. Soc.*, 391:1227–1238, 2008.
- [86] Paul J. Petersan and Steven M. Anlage. Measurement of resonant frequency and quality factor of microwave resonators: Comparison of methods. *Journal of Applied Physics*, 84:3392–3402, 1998.
- [87] A. Pope, C. Borys, D. Scott, C. Conselice, M. Dickinson, and B. Mobasher. The Hubble Deep Field North SCUBA Super-map - III. Optical and near-infrared properties of submillimetre galaxies. *Mon. Not. R. Astron. Soc.*, 358:149–167, March 2005.
- [88] David M Pozar. *Microwave Engineering*. Wiley, 3rd edition, 2005.
- [89] J.-L. Puget, A. Abergel, J.-P. Bernard, F. Boulanger, W.B. Burton, F.-X. Desert, and D. Hartmann. Tentative detection of a cosmic far-infrared background with COBE. *Astronomy and Astrophysics*, 308:L5–L8, 1996.
- [90] Partridge R.B. and Peebles P. J. E. Are Young Galaxies Visible? II. The Integrated Background. *Astrophysical Journal*, 148:377, 1967.
- [91] C. L. Reichardt, O. Zahn, P. A. R. Ade, K. Basu, A. N. Bender, F. Bertoldi, H.-M. Cho, G. Chon, M. Dobbs, D. Ferrusca, N. W. Halverson, W. L. Holzapfel, C. Horellou, D. Johansson, B. R. Johnson, J. Kennedy, R. Kneissl, T. Lanting, A. T. Lee, M. Lueker, J. Mehl, K. M. Menten, M. Nord, F. Pacaud, P. L. Richards, R. Schaaf, D. Schwan, H. Spieler, A. Weiss, and B. Westbrook. Constraints on the High-ell Power Spectrum of Millimeter-Wave Anisotropies from APEX-SZ. *Astrophysical Journal*, 701:1958–1964, August 2009.
- [92] P. L. Richards. Bolometers for infrared and millimeter waves. *Journal of Applied Physics*, 76:1–24, 1994.
- [93] P. L. Richards, T. M. Shen, R. E. Harris, and F. L. Lloyd. Quasiparticle heterodyne mixing in SIS tunnel junctions. *Applied Physics Letters*, 34:345–347, March 1979.
- [94] George Rieke. *Detection of Light*. Cambridge, 2nd edition, 2003.
- [95] Markus Roesch, Loren J. Swenson, Simon M. Doyle, and Alessandro Monfardini. Characterization of lumped element kinetic inductance detectors for mm-wave detection. *Proceedings of the SPIE*, 7741:23, 2010.

- [96] M. C. Runyan, P. A. R. Ade, R. S. Bhatia, J. J. Bock, M. D. Daub, J. H. Goldstein, C. V. Haynes, W. L. Holzapfel, C. L. Kuo, A. E. Lange, J. Leong, M. Lueker, M. Newcomb, J. B. Peterson, C. Reichardt, J. Ruhl, G. Sirbi, E. Torbet, C. Tucker, A. D. Turner, and D. Woolsey. Acbar: The arcminute cosmology bolometer array receiver. *The Astrophysical Journal Supplement Series*, 149(2):265, 2003.
- [97] S. Sabah and R. Lorenz. Design and calibration of IQ-mixers. *Proc. EPAC*, 1998:1589–1591, 1998.
- [98] G. Sandell. Secondary calibrators at submillimetre wavelengths. *Mon. Not. R. Astron. Soc.*, 271:75–80, November 1994.
- [99] J. Sayers, N. A. Czakon, P. K. Day, T. P. Downes, R. Duan, J. Gao, J. Glenn, S. R. Golwala, M. I. Hollister, H. G. LeDuc, B. A. Mazin, P. R. Maloney, O. Noroozian, H. T. Nguyen, J. A. Schlaerth, S. Siegel, J. Vaillancourt, A. Vayonakis, P. R. Wilson, and J. Zmuidzinas. Optics for MUSIC: a new (sub)millimeter camera for the Caltech Submillimeter Observatory. In *Society of Photo-Optical Instrumentation Engineers (SPIE) Conference Series*, volume 7741 of *Presented at the Society of Photo-Optical Instrumentation Engineers (SPIE) Conference*, August 2010.
- [100] J. Sayers, S. R. Golwala, P. Rossinot, P. A. R. Ade, J. E. Aguirre, J. J. Bock, S. F. Edgington, J. Glenn, A. Goldin, D. Haig, A. E. Lange, G. T. Laurent, P. D. Mauskopf, and H. T. Nguyen. A Search for Cosmic Microwave Background Anisotropies on Arcminute Scales with Bolocam. *Astrophysical Journal*, 690:1597–1620, January 2009.
- [101] Jack Sayers. Private communication.
- [102] Jack Sayers. *A Search for Cosmic Microwave Background Anisotropies on Arcminute Scales*. PhD thesis, California Institute of Technology, 2008.
- [103] J. Schlaerth, S. Golwala, J. Zmuidzinas, A. Vayonakis, J. Gao, N. Czakon, P. Day, J. Glenn, M. Hollister, H. LeDuc, P. Maloney, B. Mazin, H. Nguyen, J. Sayers, and J. Vaillancourt. Sensitivity Optimization of Millimeter/Submillimeter MKID Camera Pixel Device Design. *Proc. LTD*, 13:46–49, 2009.
- [104] J. Schlaerth, A. Vayonakis, P. Day, J. Glenn, J. Gao, S. Golwala, S. Kumar, H. LeDuc, B. Mazin, J. Vaillancourt, and J. Zmuidzinas. A Millimeter and Submillimeter Kinetic Inductance Detector Camera. *Journal of Low Temperature Physics*, 151:684, 2008.
- [105] James A. Schlaerth, Nicole G. Czakon, Peter K. Day, Thomas P. Downes, Ran P. Duan, Jiansong Gao, Jason Glenn, Sunil R. Golwala, Matthew I. Hollister, Henry G. LeDuc, Benjamin A. Mazin, Philip R. Maloney, Omid Noroozian, Hien T. Nguyen, Jack Sayers, Seth Siegel, John E. Vaillancourt, Anastasios Vayonakis, Philip R. Wilson, and Jonas Zmuidzinas. MKID multicolor array status and results from DemoCam. *Proceedings of the SPIE*, 7741:8, 2010.
- [106] K. S. Scott, J. E. Austermann, T. A. Perera, G. W. Wilson, I. Arretxaga, J. J. Bock, D. H. Hughes, Y. Kang, S. Kim, P. D. Mauskopf, D. B. Sanders, N. Scoville, and M. S. Yun. AzTEC millimetre survey of the COSMOS field - I. Data reduction and source catalogue. *Mon. Not. R. Astron. Soc.*, 385:2225–2238, April 2008.

- [107] I. Smail, R. J. Ivison, and A. W. Blain. A Deep Sub-millimeter Survey of Lensing Clusters: A New Window on Galaxy Formation and Evolution. *Astrophysical Journal Letters*, 490:L5+, November 1997.
- [108] Johannes G. Staguhn, Dominic J., Christine A. Allen, S. Harvey Moseley, Elmer H. Sharp, Troy J. Ames, Walter Brunswig, David T. Chuss, Eli Dwek, Stephen F. Maher, Catherine T. Marx, Timothy M. Miller, Santiago Navarro, and Edward J. Wollack. GISMO: a 2-millimeter bolometer camera for the IRAM 30 m telescope. *Proceedings of the SPIE*, 6275:62751D–1, 2006.
- [109] A. M. Swinbank, C. G. Lacey, I. Smail, C. M. Baugh, C. S. Frenk, A. W. Blain, S. C. Chapman, K. E. K. Coppin, R. J. Ivison, J. E. Gonzalez, and L. J. Hainline. The properties of submm galaxies in hierarchical models. *Mon. Not. R. Astron. Soc.*, 391:420–434, November 2008.
- [110] Erik A. Tholen, Adem Ergul, Evelyn M. Doherty, Frank M. Weber, Fabien Gregis, and David B. Haviland. Nonlinearities and parametric amplification in superconducting coplanar waveguide resonators. *Applied Physics Letters*, 90:253509–1 – 253509–3, 2007.
- [111] Anastasios Vayonakis. Private communication.
- [112] J. D. Vieira, T. M. Crawford, E. R. Switzer, P. A. R. Ade, K. A. Aird, M. L. N. Ashby, B. A. Benson, L. E. Bleem, M. Brodwin, J. E. Carlstrom, C. L. Chang, H.-M. Cho, A. T. Crites, T. deHaan, M. A. Dobbs, W. Everett, E. M. George, M. Gladders, N. R. Hall, N. W. Halverson, F. W. High, G. P. Holder, W. L. Holzapfel, J. D. Hrubes, M. Joy, R. Keisler, L. Knox, A. T. Lee, E. M. Leitch, M. Lueker, D. P. Marrone, V. McIntyre, J. J. McMahon, J. Mehl, S. S. Meyer, J. J. Mohr, T. E. Montroy, S. Padin, T. Plagge, C. Pryke, C. L. Reichardt, J. E. Ruhl, K. K. Schaffer, L. Shaw, E. Shirokoff, H. G. Spieler, B. Stalder, Z. Staniszewski, A. A. Stark, K. Vanderlinde, W. Walsh, R. Williamson, Y. Yang, O. Zahn, and A. Zenteno. Extragalactic millimeter-wave sources in the south pole telescope survey data: source counts, catalog, and statistics for an 87 square-degree field. *ArXiv e-prints*, December 2009.
- [113] R. Vijay, M. H. Devoret, and I. Siddiqi. Invited Review Article: The Josephson bifurcation amplifier. *Review of Scientific Instruments*, 80:111101–1–111101–17, 2009.
- [114] S. Weinreb. Cryogenic performance of microwave terminators, attenuators, absorbers and coaxial cable. *NRAO Electronics Division Internal Report*, 223, 1982.
- [115] S. Weinreb, J. Bardin, H. Mani, and G. Jones. Matched wideband low-noise amplifiers for radio astronomy . *Review of Scientific Instruments*, 80:044702, 2009.
- [116] Kurt Wiesenfeld and Bruce McNamara. Small signal amplification in bifurcating dynamical systems. *Physical Review A*, 33:629–642, 1986.
- [117] C. M. Wilson and D. E. Prober. Quasiparticle number fluctuations in superconductors. *Physical Review B*, 69:094524–1–094524–11, 2004.
- [118] G. W. Wilson, J. E. Austermann, T. A. Perera, K. S. Scott, P. A. R. Ade, J. J. Bock, J. Glenn, S. R. Golwala, S. Kim, Y. Kang, D. Lydon, P. D. Mauskopf, C. R. Predmore, C. M. Roberts, K. Souccar, and M. S. Yun. The AzTEC mm-wavelength camera. *Mon. Not. R. Astron. Soc.*, 386:807–818, 2008.

- [119] J. D. Younger, G. G. Fazio, J.-S. Huang, M. S. Yun, G. W. Wilson, M. L. N. Ashby, M. A. Gurwell, A. B. Peck, G. R. Petitpas, D. J. Wilner, D. H. Hughes, I. Arétxaga, S. Kim, K. S. Scott, J. Austermann, T. Perera, and J. D. Lowenthal. The AzTEC/SMA Interferometric Imaging Survey of Submillimeter-selected High-redshift Galaxies. *Astrophysical Journal*, 704:803–812, October 2009.
- [120] Joshua D. Younger, Giovanni G. Fazio, Jia-Sheng Huang, Min S. Yun, Grant W. Wilson, Matthew L. N. Ashby, Mark A. Gurwell, Kamson Lai, Alison B. Peck, Glen R. Petitpas, David J. Wilner, Daisuke Iono, Kotaro Kohno, Ryohei Kawabe, David H. Hughes, Itziar Arétxaga, Tracy Webb, Alejo Martínez-Sansigre, Sungeun Kim, Kimberly S. Scott, Jason Austermann, Thushara Perera, James D. Lowenthal, Eva Schinnerer, and Vernes Smolcic. Evidence for a population of high-redshift submillimeter galaxies from interferometric imaging. *Astrophysical Journal*, 671:1531–1537, 2007.
- [121] J. Zmuidzinas. Parameter fluctuations in resonant circuits. *MKID collaboration internal report*, 2003.
- [122] Jonas Zmuidzinas. Thermal noise and correlations in photon detection. *Applied Optics*, 42:4989–5008, 2003.
- [123] Jonas Zmuidzinas and Paul L. Richards. Superconducting Detectors and Mixers for Millimeter and Submillimeter Astrophysics. *Proceedings of the IEEE*, 92:1597–1616, October 2004.

## Appendix A

### Cooper pair effect on kinetic inductance

This appendix attempts to answer, at least qualitatively, the question of why the frequency of a resonator decreases under load and at high effective temperatures. This is a non-intuitive effect. The kinetic inductance which arises due to superconductivity pushes the resonance frequency down as  $\omega \sim L^{-1/2}$ . That is, one would expect lower inductance, and with it higher resonance frequencies, without taking superconductivity into account. However, breaking Cooper pairs, which pushes the detectors closer to normal metal characteristics, actually amplifies this effect. Here we explore this effect, and why increasing temperatures yields increasing inductance. For reference, the author recommends the discussion in Chapter 3 of Ref. [31].

#### A.1 What is kinetic inductance?

First, let us remind ourselves of what inductance means in an RL circuit. For a harmonic current,  $I = I_0 e^{i\omega t}$ , we have

$$V = V_0 e^{i\omega t} = (R + i\omega L)I_0 e^{i\omega t}. \quad (\text{A.1})$$

Microscopically, the inductance can be simply thought of as any condition in which the motion of the particles (i.e. the current) is out-of-phase with the force ( $e\vec{E} = e\nabla V$ ). Anything which accelerates charge carriers out-of-phase with the force is part of the inductance, while anything in-phase can be seen as resistance. The impedance for an *RL* circuit is simply  $R + i\omega L$ . We can rewrite Equation A.1 in vector notation as

$$\vec{J}_0 e^{i\omega t} = (\sigma_1 - i\sigma_2) \vec{E}_0 e^{i\omega t} \quad (\text{A.2})$$

to explicitly write this in terms of current and a term proportional to force. The complex conductivity, introduced by Glover and Tinkham [52], is very useful here. One can think of this as  $\sigma_1$  representing the free electron conductivity, while  $\sigma_2$  represents the conductivity of Cooper pairs. This is a fair approximation because the imaginary conductivity of normal metals at room temperature is many orders of magnitude below the real conductivity [36].

Now, let us consider the case of a bulk superconductor at very low temperature, with all electrons paired together in bosonic Cooper pairs. In this case, the DC resistance is zero. In fact, it is the supercurrent that has no DC resistance; there are no fermionic charge carriers, so the conductivity of free electrons is also zero. But if one applies a sinusoidal electric field across the superconductor at effectively zero temperature, the current would be totally out-of-phase with the electric field. This can be understood by the fact that resistance is zero but the inductance is finite, or that  $\sigma_1$  is zero but  $\sigma_2$  is finite.

This effective inductance is what we call kinetic inductance. Qualitatively, it arises because of the Cooper pairs themselves. As an electric field is applied, the energy can be stored in each pair's motion, because the electrons do not scatter. When the field is reversed, the energy stored must be released in motion, which is necessarily out of phase with the electric field. In other words, the inertia of the Cooper pair keeps the current out of phase with the applied electric field. This effect is indistinguishable from a geometrical inductance with a normal metal, which causes the same out of phase relationship between current and applied field, or voltage. This would be true of free electrons as well, but the short scattering timescale compared to the frequency of the field makes it impossible to store energy in the free electron's motion.

## A.2 Change in inductance with quasiparticles

We must now look at what happens in the event of a temperature change, or a change in the density of Cooper pairs compared to the density of free electrons. An increase in inductance will lead to a decrease in frequency in an *RLC* circuit, as is seen by the response of MKIDs. We know that the kinetic inductance arises solely due to the formation of Cooper pairs. The fact that the

frequency *decreases* when the Cooper pairs are broken implies an increase in surface inductance,  $L_s$ . We also know that there is no effective inductance associated with free electrons in a metal. How does this all fit together?

According to Mattis-Bardeen theory, at zero temperature  $\sigma_1 = 0$  and  $\sigma_2$  is a positive number. This means  $R_s = 0$  and  $L_s$  is some finite quantity. As Cooper pairs are broken,  $\sigma_1$  increases monotonically up to  $T_c$  due to the creation of more quasiparticles, then settles toward  $\sigma_n$  at high temperature. Meanwhile,  $\sigma_2$  monotonically decreases to the point where it is very small, and is typically ignored in normal metal applications. These effects near the transition temperature are seen in Figure A.1.<sup>1</sup> The changing conductivities suggest a view of what is happening in

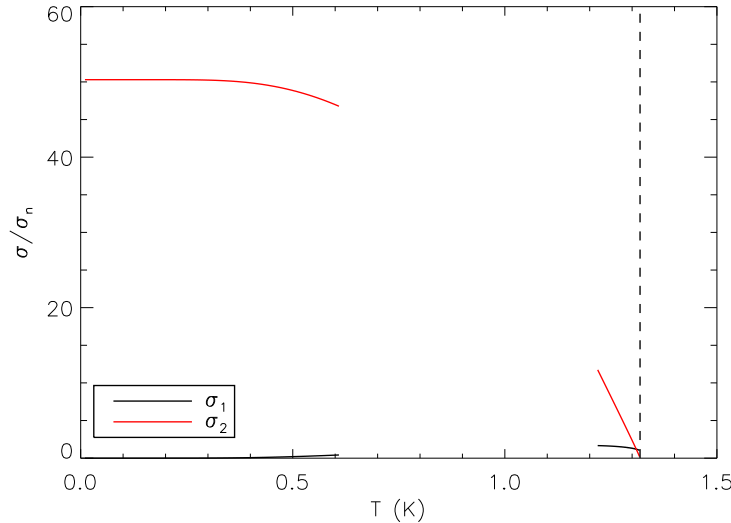


Figure A.1: Complex conductivities vs. temperature. The dotted line represents the assumed  $T_c$ . Values taken assuming a frequency of 3 GHz. The imaginary conductivity dominates until a crossover point just below  $T_c$ .

the conductor. As Cooper pairs are broken, the number of charge carriers for the supercurrent decreases. This leads to a higher impedance for the supercurrent<sup>2</sup>. Simultaneously, charge carriers are added to the normal current. If the voltage is constant across the conductor (as in the case

<sup>1</sup> In this figure, low and high temperature approximations for  $\Delta(T)$  are made, leaving the curves discontinuous in the intermediate temperatures. Those temperatures are not critical to the physical understanding.

<sup>2</sup> An analogy would be in a semiconductor: As a charge carrier is removed from the conduction band, the impedance to current flowing increases. In this analogy, the impedance is the lossy resistive portion, which increases with fewer electrons.

of a resonator coupled to a transmission line), then the separate effects – changing current and supercurrent, as well as changing inductance and resistance – must add up to a constant value. In other words,  $I_nR + \omega I_sL$  is constant, but  $I_n$  increases as  $I_s$  decreases. In the limiting case where  $R$  is small, the inductive term dominates and  $L$  increases with less current. But as the normal current comes to dominate, and the resistance grows larger than the inductance, then the inductance must decrease under constant voltage. This is effectively seen in looking at the formalism of the dependence of impedance on conductivity changes in several limiting cases, and how the quantities of inductance and resistance change in these cases.

It helps to revisit the assumptions we made in Chapter 2.1, namely that we are looking for changes in resistance and reactance from the zero temperature condition. This assumes that  $\sigma_1 \ll \sigma_2$ , which is clearly not always the case. In general, the quantities are given by

$$Z_s = R_s + i\omega L_s = \frac{\sigma_1 + i\sigma_2}{(\sigma_1^2 + \sigma_2^2)t} \quad (\text{A.3})$$

where we again assume the thin film, local limit. One can immediately see that the inductance and resistance both depend on the real and imaginary parts of the conductance; they cannot be considered independently. Let us consider then the general form of an infinitesimal change in reactance, due to an effect such as a change in temperature, given by

$$\delta(\omega L_s) = \frac{1}{(\sigma_1^2 + \sigma_2^2)t} \left[ \delta\sigma_2 \left( 1 - \frac{2\sigma_2^2}{\sigma_1^2 + \sigma_2^2} \right) + \delta\sigma_1 \left( \frac{-2\sigma_1\sigma_2}{\sigma_1^2 + \sigma_2^2} \right) \right]. \quad (\text{A.4})$$

Let us examine this in several limits. First, the low temperature case of  $\sigma_1 \ll \sigma_2$  yields

$$\delta(\omega L_s) = -\frac{\delta\sigma_2}{\sigma_2^2 t} \quad (\text{A.5})$$

as seen in Section 2.1. Here, a decrease in  $\sigma_2$  yields an increase in  $\omega L_s$ , as is observed. From Ohm's Law, Equation A.2, we see that the same electric field would then produce less current - as is expected, since we are effectively just removing a Cooper pair from the superconductor in this limit - or the same current would require a greater electric field. Another way of thinking about this is that we are effectively voltage biasing the detectors with the probe signal. If the voltage coupled to the detector is constant while the current decreases, the inductance must necessarily

increase. This is only true in the case in which inductance dominates, or when the resistance term in Equation A.1 is negligible. This effect is seen in Figure A.2, as the inductance steadily increases with temperature up to near the transition temperature.

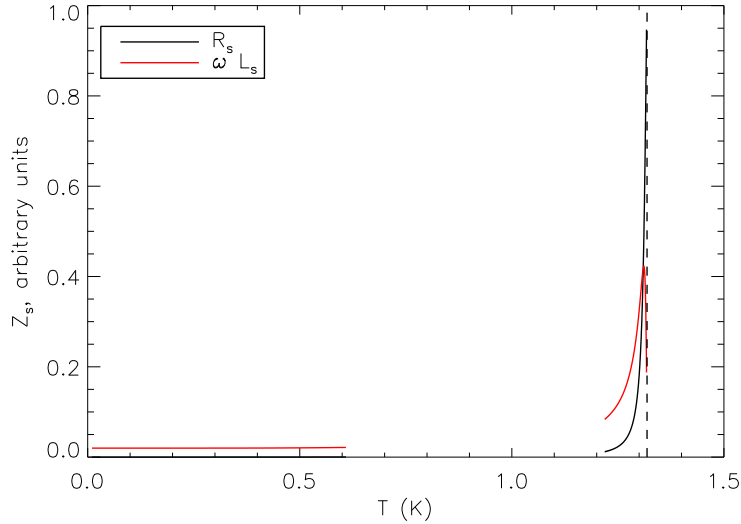


Figure A.2: Real and imaginary parts of the impedance,  $R_s + i\omega L_s$ , vs. temperature. The dotted line represents the assumed  $T_c$ .

Then, let us consider an intermediate case, occurring just below the transition temperature, in which  $\sigma_1 = \sigma_2$ . This works out as

$$\delta(\omega L_s) = -\frac{\delta\sigma_1}{2\sigma_2^2 t}. \quad (\text{A.6})$$

Here the change in  $\sigma_2$  exactly cancels out, and the only contributing factor to the change in reactance is the change in real conductance. But the change is now the opposite direction of the real conductance, which in the superconducting state means it decreases in inductance. This case is no longer analogous to simply removing a Cooper pair, because the effect of the created quasiparticles is no longer small. A closer view near the transition temperature, where this crossover occurs, is seen in Figure A.3, as the inductance peaks just below  $T_c$  and turns downward.

Now, let us consider the case corresponding to general normal metals at room temperature,

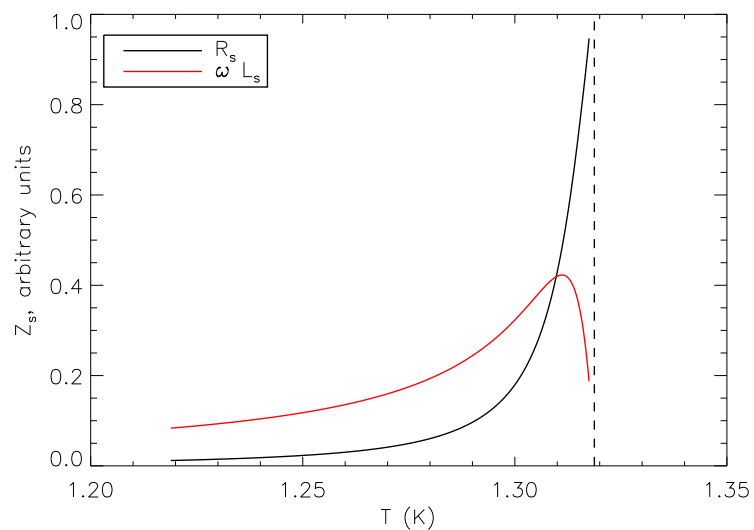


Figure A.3: Real and imaginary parts of the impedance,  $R_s + i\omega L_s$ , vs. temperature near the transition temperature. The dotted line represents  $T_c$ .

$\sigma_2 \ll \sigma_1$ . Here,

$$\delta(\omega L_s) = \frac{1}{2\sigma_2^2 t} (\delta\sigma_2 - 2\delta\sigma_1 \frac{\sigma_2}{\sigma_1}). \quad (\text{A.7})$$

Here the change in  $\sigma_2$  once again dominates, but this is misleading because any change is very small. In fact, the reactance here approaches zero, while the resistance becomes  $1/\sigma_1 t$ , as one would expect in this limit. At cold temperatures, the change in  $\sigma_2$  goes to larger inductance, but with the increase in  $\sigma_1$  it eventually returns to zero. This would correspond to the high temperature metal case.

Because  $Z_s = 1/\sigma t$  in conductors, the complex impedance is a mix of the conductivities, leaving the functional form seen in Figure A.2. Around  $T_c$  there is an inversion point, when the two  $\sigma$ 's are equal, above which the intrinsic inductance decreases. The qualitative view in Figure A.2 still holds: there is necessarily an inversion point where the inductance decreases monotonically up to high temperature, where it is negligible.

The above examples illustrate that both the resistance and the inductance play a significant role in determining how the conductance changes with these quantities. At negligible real conductance (where the effect of unpaired quasiparticles is negligible), we see an increase in inductance as Cooper pairs are removed from the conductor. In this case, it will take an infinite electric field to create current as the inductance goes to zero, leading to ever increasing inductance. But if the real conductance is finite, then current will still flow when  $\sigma_2$  goes to zero, leading to a very small inductive contribution to the current. This is the same effect that allows resistance to be zero with zero real conductance.

## Appendix B

### Resonance conditions for quarter-wave detectors

Although the resonance condition is derived elsewhere (e.g. [36]), it is useful for the understanding of submillimeter MKID detectors to go through exactly what we see in the transmitted signal around the resonance. Although derived independently, this appendix relies heavily on the derivations by Peter Day and those of Jiansong Gao referenced above, as well as Pozar [88] and internal MKID reports [22, 121]. The results can be generalized to a lumped element resonator with an inductive section shorted to ground, though a quarter-wave resonator is assumed here for simplicity.

#### B.1 Derivation of the resonance condition

There are two ways of looking at a quarter-wave detector coupled to a transmission line. The first is to view the system as a two-port network with an impedance that changes near the resonance frequency, including both reflection and loss terms. This is more straightforward to visualize, as the change in transmission can be seen as simply a change in the complex impedance value as a function of frequency. However, this approach runs into difficulty in describing intuitively the resonance condition in terms of easily measurable parameters, such as  $Q_c$ . The circuit of a resonator coupled to a feedline in this case is seen Figure B.1.

The second approach, derived by Gao, relies on looking at the system as a 3-port network, with input and output ports as before, but with the resonator as the third port. This is shown in Figure B.2. While more complex, it is more intuitive to find the resonance condition as a function

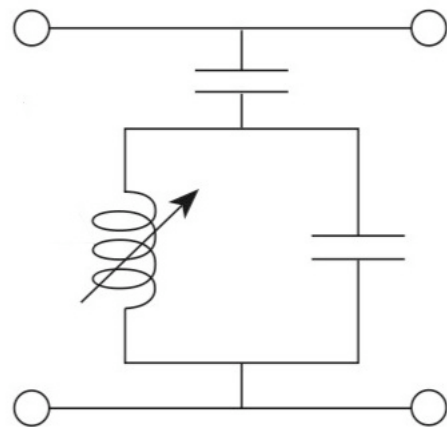


Figure B.1: Diagram of a feedline-coupled resonant circuit, adapted from Ref. [23]. The actual resonant circuit would also include resistance, which determines the internal loss described by  $Q_i$ . This is the diagram for the limiting case of zero resistance.

of  $f_0$  and  $Q_c$ . The two cases yield equivalent results, and elements of both are used here.

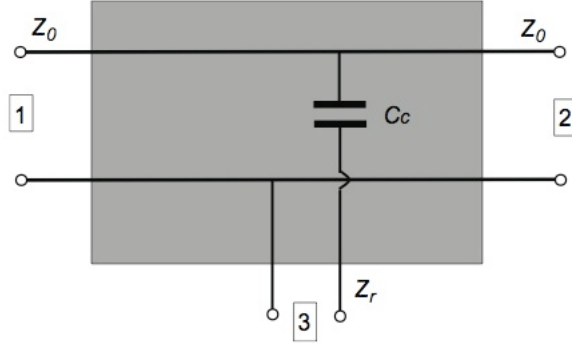


Figure B.2: Diagram of a three-port representation of a feedline-coupled resonator, adapted from Ref. [36].

First, we must find the impedance of a quarter-wave resonator uncoupled to a feedline. We consider the resonator to be a simple CPW line, with characteristic impedance  $Z_0$ . The resonator, length  $l$ , is shorted on one end and open on the other. Thus, the input impedance on the open end is given by

$$Z_l = Z_0 \tanh(i\beta l + \alpha l) \quad (\text{B.1})$$

where  $\alpha + i\beta$  is the complex propagation constant. Because this is a resonant circuit, we can find the internal  $Q$  based on this propagation constant. This internal  $Q$  can be expressed as  $Q_i = \beta/2\alpha$  (see Ref. [88], Ch. 6). With this definition, we can express the impedance in Equation B.1 as

$$Z_l = Z_0 \frac{1 - i \tanh(\alpha l) \cot(\beta l)}{\tanh(\alpha l) - i \cot(\beta l)} \quad (\text{B.2})$$

$$= Z_0 \frac{1 - i \tanh\left(\frac{\beta l}{2Q_i}\right) \cot(\beta l)}{\tanh\left(\frac{\beta l}{2Q_i}\right) - i \cot(\beta l)}, \quad (\text{B.3})$$

which is shown in Ref. [88]. If  $l$  is near  $\lambda/4$  we can express  $\beta l$  as  $\frac{\pi}{2}(1 + \frac{\omega - \omega_{1/4}}{\omega_{1/4}})$ , where  $\omega_{1/4}$  is the frequency meeting the quarter-wave condition. If we assume  $\frac{\omega - \omega_{1/4}}{\omega_{1/4}}$  is small (i.e. we are near the resonance) and  $Q_i \gg 1$ , we can simplify B.3 to be

$$Z_l = \frac{\frac{1}{\pi} 4 Z_0 Q_i}{1 - 2i Q_i \frac{\omega - \omega_{1/4}}{\omega_{1/4}}} \quad (\text{B.4})$$

Up to this point, we have been considering the impedance of the resonator in isolation. In reality, the resonators are coupled to a transmission feedline, so that MKIDs can be read out with probe signals on-resonance. Let us consider a capacitor with capacitance,  $C$ , connecting this resonator to a transmission line, also with impedance  $Z_0$ . We want to find, ultimately, the transmitted wave,  $S_{21}$ , of a signal sent through this transmission line near the resonance frequency. This is expressed as

$$S_{21} = \frac{2}{2 + \frac{Z_0}{Z}} \quad (\text{B.5})$$

where  $Z$  is the impedance of the series coupling capacitor and resonant circuit combined (see Ref. [88], Section 4.4). This new impedance is simply a capacitive term in series with the resonator impedance, and is given by

$$Z = \frac{-i}{\omega C} + \frac{\frac{1}{\pi} 4 Z_0 Q_i}{1 - 2iQ_i \frac{\omega - \omega_{1/4}}{\omega_{1/4}}} \quad (\text{B.6})$$

$$= \frac{-i}{\omega C} + \frac{\frac{1}{\pi} 4 Z_0 Q_i - i \frac{8 Z_0 Q_i^2}{\pi} \frac{\omega - \omega_{1/4}}{\omega_{1/4}}}{1 - 4Q_i^2 \left( \frac{\omega - \omega_{1/4}}{\omega_{1/4}} \right)^2}. \quad (\text{B.7})$$

Now, we want to simplify this, and find a new resonance frequency with the added capacitor. Given the additional capacitance, it must be different from the resonance of the quarter-wave resonator alone. The resonance occurs at  $\text{Im}[Z] = 0$ , which has two solutions. The solution at lower frequency is the solution with a reasonable real impedance, and thus corresponds to the resonance frequency. Solving the quadratic condition, we have

$$\omega_0 = \frac{\omega_{1/4}}{1 + 2Z_0\omega_{1/4}C/\pi}. \quad (\text{B.8})$$

Note that the factor differentiating the two should be small for a reasonable capacitance ( $< 1\text{pF}$ ), so the resonance frequency should be close to the quarter-wave condition.

Our goal is to express  $S_{21}$  in terms of quality factors and fractional frequency off resonance. To do this we must introduce the coupling quality factor, which we define as

$$Q_c = \frac{\pi}{2Z_0^2\omega_{1/4}^2 C^2}. \quad (\text{B.9})$$

To see why we are able to make this definition, we must consider the three-port network model, in which the quality factor for leaking power from the third port (here, the resonator) to the other ports is given by

$$Q_c = \frac{\pi}{2|S_{31}|^2}. \quad (\text{B.10})$$

We have defined the resonator as port 3, and consider the feedline input and output ports equivalent (i.e. the line is symmetric). Thus, this only states that  $Q_c$  is a measure of energy lost from the resonator to the feedline per cycle. Now, the strength of this coupling is determined by the capacitance, which also determines  $S_{11}$ , as a high capacitance leads to a greater impedance mismatch at the resonance frequency. As shown by Gao, it is straightforward to determine the transmission between these ports, given by  $S_{31} = i\omega C Z_0$  if the feedline impedance is the same as the resonator's. Using this definition, the coupling  $Q$  becomes the quantity given in Equation at frequencies where the quarter-wave condition is met.

This value is also the  $Q$  arising when the resonator is unloaded. If we introduce this factor back into the fractional frequency change of B.7, and define a new shift as

$$x = \frac{\omega - \omega_0}{\omega_0} \approx \frac{\omega - \omega_{1/4}}{\omega_{1/4}} + \frac{2Z_0\omega_0 C}{\pi} \quad (\text{B.11})$$

with the use of Equation B.8. With this variable, we are now referencing frequency shifts to the true resonance including the effect of the coupling capacitance, not just of the resonator alone. The impedance on the transmission line then becomes, as we throw away small terms,

$$\frac{Z}{Z_0} = \frac{\pi}{4Z_0^2(\omega_0 C)^2 Q_i} + i \frac{\pi x}{2Z_0^2(\omega_0 C)^2} = \frac{1}{2} \left( \frac{Q_c}{Q_i} + 2iQ_c x \right) \quad (\text{B.12})$$

Through some approximation we can show that

$$S_{21} = \frac{1}{1 + \frac{1}{Q_c/Q_i + 2iQ_c x}} \quad (\text{B.13})$$

$$= \frac{\frac{Q_c}{Q_i} + 2iQ_c x}{\left(1 + \frac{Q_c}{Q_i}\right) + 2iQ_c x} \quad (\text{B.14})$$

$$= \frac{\frac{Q}{Q_i} + 2iQ x}{1 + 2iQ x}. \quad (\text{B.15})$$

This is the final form of  $S_{21}$  that we are interested in, for frequencies near the resonance condition. This can easily be shown to be equivalent to Equation 2.3. In the limit of large  $x$ , or at frequencies far from the resonance, the transmission goes to 1. Near resonance, the transmission is a Lorentzian, with the depth defined by the internal MKID loss ( $Q_i^{-1}$ ) and the coupling ( $Q_c^{-1}$ ). If those two quantities are equal, the dip in transmission is a factor of 2 below the off-resonance transmission.

## B.2 Expected signal in amplitude and phase

Now let us consider the purely real and purely imaginary components, and see how these scale with change in dissipation and frequency, respectively. We here denote the fractional frequency off-resonance as  $x$  because we assume a probe signal on or near resonance, and wish to see the effect of a change in both  $x$  and  $Q_i$ , which are proportional.<sup>1</sup>

### B.2.1 Phase response

From Equation B.15, the phase of a transmitted wave near resonance is given by

$$\text{Im}[S_{21}] = \frac{2Qx \left( \frac{Q}{Q_c} \right)}{1 + 4Q^2x^2}. \quad (\text{B.16})$$

Let us consider a small perturbation in resonance frequency and in  $Q_i$ , such that the denominator is effectively 1. Then the response in the Q direction becomes

$$\delta \text{Im}[S_{21}] = -4x \frac{Q^3}{Q_c} \delta \left( \frac{1}{Q_i} \right) + 2 \frac{Q^2}{Q_c} \delta x. \quad (\text{B.17})$$

As long as  $xQ$  is small, in other words when we are nearby the resonant frequency compared to the resonance width (which should always be the case) the second term dominates, and we can ignore the first. Thus, the response goes as  $2 \frac{Q^2}{Q_c}$  times the fractional frequency shift.

---

<sup>1</sup> In other sources,  $\delta x$  defines the distance from the resonance. Here we use only  $x$  to differentiate that from a small change in the resonance frequency.

### B.2.2 Amplitude response

The amplitude of the transmitted signal is given by

$$\text{Re}[S_{21}] = \frac{\frac{Q}{Q_i} + 4Q^2x^2}{1 + 4Q^2x^2}. \quad (\text{B.18})$$

Let us consider a small perturbation, such that the denominator is effectively unity.

$$\delta\text{Re}[S_{21}] = \frac{Q^2}{Q_c}\delta\left(\frac{1}{Q_i}\right) + 8Q^2x\delta x + 8Qx^2\delta Q \quad (\text{B.19})$$

Again, these terms with the parameter  $x$  should be very small, and thus do not contribute. The final perturbation response in  $S_{21}$  is then

$$\delta S_{21} = \frac{Q^2}{Q_c}\left(\delta\frac{1}{Q_i} + 2i\frac{\delta f}{f}\right). \quad (\text{B.20})$$

If we probe on-resonance, then, the shift in transmission can be decomposed directly into changes of the loss tangent and the frequency shift. The ratio of the responses is the equivalent of  $\delta\sigma_1/\delta\sigma_2$ , given the extra factor of 2 in the frequency direction found here (see Section 2.1).

### B.3 Complexity in $S_{21}$ profiles

In general, the raw  $S_{21}$ , measured from a network analyzer, does not closely resemble B.15 due to several correctable factors. The first is the term for the cable delay. In general, the length of cable on the input and output ends are not equal, and we must correct for this by implementing a time delay phase shift to the data,

$$S_{21,\text{corr}} = S_{21}e^{2\pi i f \tau} \quad (\text{B.21})$$

where  $\tau$  is the cable delay term, on the order of 10s of microseconds. This makes the resonance loop a circle, but does not correct for the direction or offset. In general, the resonance loop is not pointed at the origin, and is in need of rotation, and the entire loop must be rotated about the center of the I/Q plane (see e.g. Figure 7.3).

We must also consider the frequency dependence of the background transmission, the transmission of a signal if there were no resonance. The transmission can vary due to several factors,

such as loss or reflections along the transmission line, or due to nonuniform amplification by amplifiers. The background transmission can either be found from high temperature data (i.e. at a high enough temperature that the resonance disappears entirely, leaving only the underlying transmission) or included in the fit to the resonance loop. The method primarily used in this thesis is to fit to the background over a small frequency section; this is discussed in Chapter 4.

## Appendix C

### Telescope Calibration

Here we consider the calibration of telescope data, simply to understand what responsivity numbers mean in each context. Our goal is to understand the response of MKIDs from laboratory tests, using hot and cold optical loads, through the response to astronomical point sources. The first section briefly reviews what is meant by lab responsivity, in particular numbers quoted in units of kHz of frequency shift per Kelvin of temperature change. The second section discusses how this converts to useful data in an astronomical context. The third section looks at the theoretical performance of MKIDs, and observes over what range of fluxes the response should be linear.

#### C.1 Laboratory responsivity

Finding the responsivity of a detector is essential for determining the NEP. Here we go through the steps of going from responsivity measurement to quantifying the detector sensitivity. In the laboratory, our goal is to measure responsivity, and find its value under an arbitrary load.

To determine responsivity, we typically use simple hot/cold blackbody loads, as discussed in Chapter 4. The resulting number, in kHz/K, is intrinsically misleading due to the fact that the frequency response per Kelvin of load change depends on the load; it is a nonlinear response with loading. In addition, it hides the fact that what matters is fractional frequency shift, not absolute change in frequency, thus misleading those comparing numbers between resonators at vastly different frequencies. Thus, to back out useful numbers, we must convert this into more useful form. We do this by considering the response in terms of quasiparticle density.

As is discussed in Chapter 3, the quasiparticle density under load is defined by a generation-recombination equation, and the response of frequency or loss per quasiparticle is constant for a given frequency and base temperature. If we assume that  $\tau_0$  is large compared to  $1/Rn_{qp}$ , as is typically justified (leading to only a few percent error in the calculated response), this greatly simplifies the responsivity calculations. Assuming that we are in the Rayleigh-Jeans limit, then the frequency shift between two load temperatures is given by

$$\frac{\delta f}{\delta T} = \frac{df}{dn_{qp}} \frac{\delta n_{qp}}{\delta T} = \frac{df}{dn_{qp}} \left( \sqrt{\frac{\eta k_B T_1(\Delta\nu)}{RV\Delta}} - \sqrt{\frac{\eta k_B T_2(\Delta\nu)}{RV\Delta}} \right) \frac{1}{T_1 - T_2}. \quad (\text{C.1})$$

This gives the often-quoted responsivity value in kHz/K. Typically,  $T_1 = 77$  K and  $T_2 = 297$  K, while the highest frequency observing band is 350 GHz, which is clearly in the Rayleigh-Jeans limit. In Equation C.3, we do not necessarily know many of the variables involved – efficiency, bandwidth, recombination constant, volume, gap parameter, or  $df/dn_{qp}$  (which depends upon kinetic inductance fraction). These individual parameters are generally knowable, and can be used to find the optical efficiency. However, we are typically interested in NEP or NEFD, and thus only need the full response. In such a case, we can combine everything into a single constant,

$$C_T = \frac{df}{dn_{qp}} \sqrt{\frac{\eta k_B(\Delta\nu)}{RV\Delta}} \quad (\text{C.2})$$

yielding

$$\frac{\delta f}{\delta T} = C_T \frac{\sqrt{T_1} - \sqrt{T_2}}{T_1 - T_2}, \quad (\text{C.3})$$

or, conversely,

$$C_T = \frac{\delta f}{\delta T} (\sqrt{T_1} + \sqrt{T_2}). \quad (\text{C.4})$$

The constant has units of Hz/K<sup>1/2</sup> (with Kelvin in RJ units, linear with power). If one knows the detector bandwidth, an alternative constant equal to  $C_P = C_T / \sqrt{k_B(\Delta\nu)}$  can be used having units of Hz/W<sup>1/2</sup>. While these constants are indeed useful, they are somewhat less intuitive than, and also degenerate with, the hot/cold response in kHz/K. They are given here as they can predict the MKID responsivity under an arbitrary load.

The latter constant is more useful for finding NEP, in which we consider the differential response under a given detector load. This leaves us with a simple method for finding the responsivity given an external loading power,

$$\frac{df}{dP} = \frac{C_T}{k_B(\Delta\nu)} \frac{1}{2\sqrt{T_{load}}} = \frac{C_P}{2\sqrt{P_{load}}}. \quad (\text{C.5})$$

If we have a noise source  $S$  in units of  $\text{Hz}^2/\text{Hz}$  (see Chapter 3), the NEP is given by

$$NEP = \left( \frac{4SP_{load}}{C_P^2} \right)^{1/2} \frac{\text{W}}{\sqrt{\text{Hz}}} \quad (\text{C.6})$$

or, in terms of the hot/cold response,

$$NEP = \left( \frac{4SP_{load}(\sqrt{T_1} + \sqrt{T_2})^2}{\frac{\delta f^2}{\delta T} k_B(\Delta\nu)} \right)^{1/2} \frac{\text{W}}{\sqrt{\text{Hz}}}. \quad (\text{C.7})$$

The good thing about this calculation is that it takes into account the optical efficiencies of the Dewar and the array; it is an NEP at the cryostat window given an arbitrary beam-filling load outside the cryostat. While several quantities must be understood in order to find a device-only NEP, the sensitivity we care about is through the entire instrument. Therefore, this is the most useful value. It should not, however, be directly compared to detector sensitivities which typically give far lower values.

## C.2 Lab-to-telescope calibration

Responsivity measurements in the lab with beam-filling blackbodies must be converted into astronomical units to understand telescope efficiency and to predict the sensitivity to astronomical sources. We typically calibrate astronomical response to a point source in units of  $\text{Jy beam}^{-1}$ . For this measurement, one must know the effective area of telescope illumination,  $A$  as well as the responsivity values. If we assume point sources, the telescope response is given by

$$Resp \left[ \frac{\text{Hz}}{\text{mJy}} \right] = \frac{df}{dP} \frac{\text{W}}{\text{mJy}} = \frac{10^{29}}{A_{tel}(\Delta\nu)\eta_{tel}} \frac{\frac{\delta f}{\delta T}}{k_B(\Delta\nu)} \frac{\sqrt{300 \text{ K}} + \sqrt{77 \text{ K}}}{2\sqrt{T_{load}}} \quad (\text{C.8})$$

where we have related it back to lab responsivity measurements. Then the mapping speed for each independent pixel is given by

$$MS = \left( \frac{10^{29}}{A_{tel}(\Delta\nu)\eta_{tel}} \frac{\Omega_{beam}}{NEP} \right)^2 \quad (\text{C.9})$$

in units of rad<sup>2</sup> Hz/mJy<sup>2</sup>. This is easy to convert into more useful units, such as arcmin<sup>2</sup>/mJy<sup>2</sup>/hr.

### C.3 Linearity in response

It is discussed in this thesis that small MKID responses are linear in both real and imaginary response (i.e. amplitude and phase). Frequency and dissipation signals have an effective 1-to-1 correspondence with phase and amplitude, respectively, in this linear regime. Yet, with astronomical signals, we must consider when this breaks down. At what level of source flux can we no longer rely on linear response in calibration?

Let us assume we have a 3.5 GHz resonator and  $Q = 20,000$  under load. Knowing how the  $Q$  and  $f_0$  of the resonator shift with loading, we can see exactly when the response diverges from linearity. If one makes reasonable assumptions for the signal at the CSO (e.g. 50 m<sup>2</sup> illumination area of the primary dish, which is 10.4 m in diameter), we can find the point source flux density, in Jy, where the response becomes nonlinear. Let us first consider relatively small fluxes, over which range we typically expect pointing and secondary calibrator sources to lie. The response as a function of flux density is shown in Figure C.1, with its derivative displayed in Figure C.2.

Many valuable calibration sources, such as planets Neptune, Uranus, and Mars at its farthest point, will exceed 20 Jy, so it is important to look to higher flux densities. This is done in Figure C.3, with the derivative given in Figure C.4. At this point, one simply has to ask what level of nonlinearity is acceptable. Typically, the calibration of planets is known at the 5% level. The systematic overestimate of amplitude response (the limiting factor) does not reach 5% until nearly 100 Jy of load.

One can see the very large effects of nonlinearity at very high flux densities. These flux densities are generally only achieved by observing very bright planets, such as Jupiter or Saturn, or Mars at its closest approach. This is seen in Figure C.5. One can see the phase response decreasing significantly, while the amplitude response actually increases. This effect is due to the fact that the probe signal is moving further and further off-resonance, leading to a large change in amplitude simply by moving away in frequency. Note that, in the figure, the amplitude response is scaled

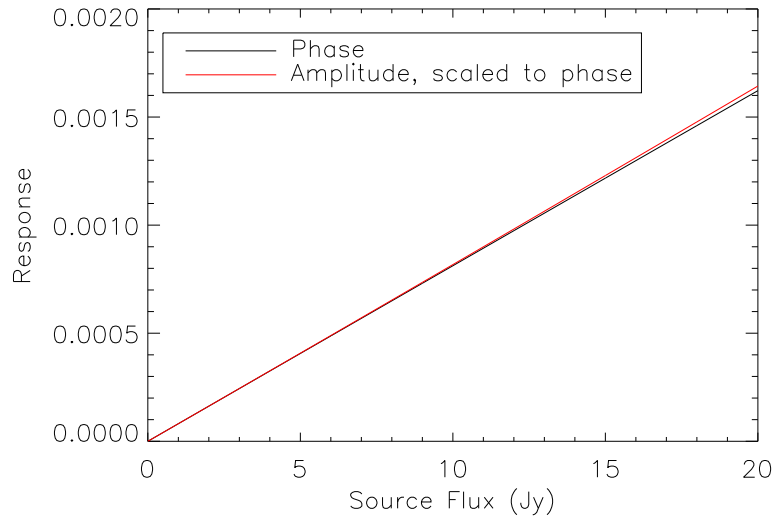


Figure C.1: The response to a point source with a given flux density out to 20 Jy. The response is given in units of fractional shift. The amplitude, which is effectively entirely dissipation response over this range, is scaled to match the larger phase response.

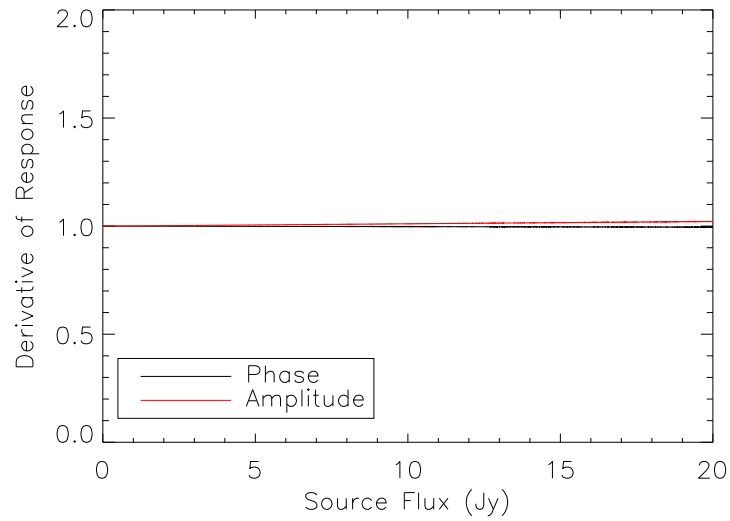


Figure C.2: The derivative of a resonator's response curve out to 20 Jy, in both phase and amplitude, scaled to unity for purely linear response. A purely linear system will have a constant value of unity at all flux densities. The deviations on the percent level shown here would be effectively immeasurable in calibration.

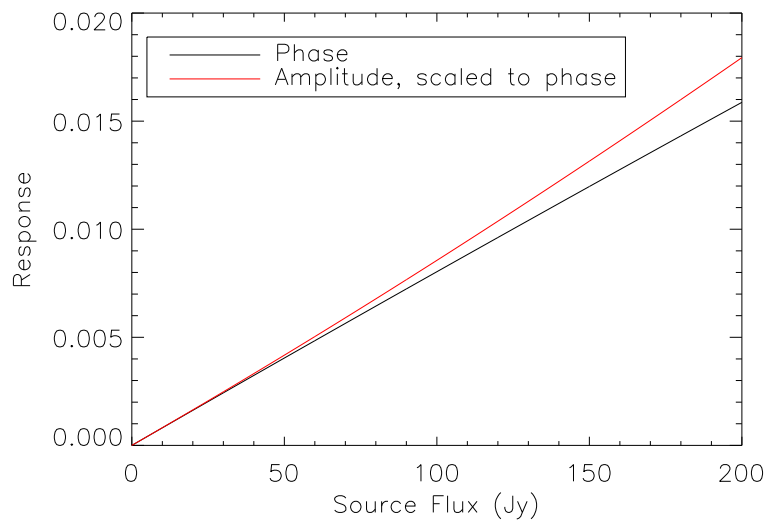


Figure C.3: The response to a point source with a flux density up to 200 Jy.

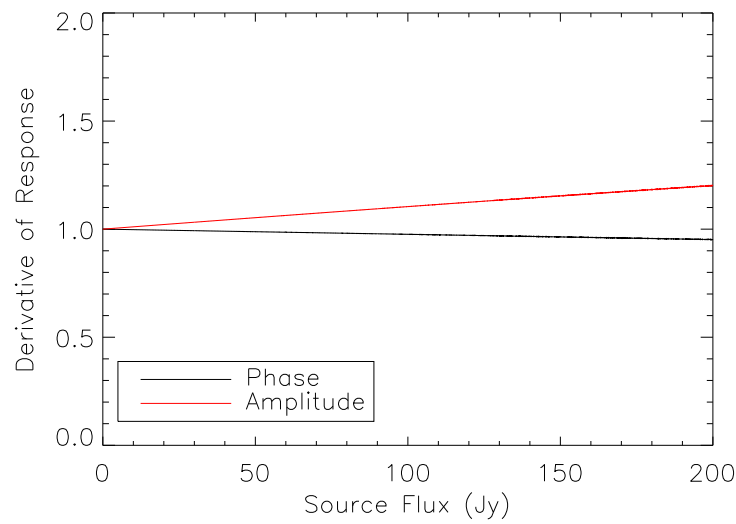


Figure C.4: The derivative of a resonator's response out to 200 Jy. A purely linear system will have a constant value of unity at all flux densities. The deviations on the percent level shown here start to become measurable in calibration.

to equal the phase response, when it should be several times smaller (depending on the resonance frequency and temperature). Taking this into account, the total signal per unit power decreases with source brightness, exactly as one would expect.

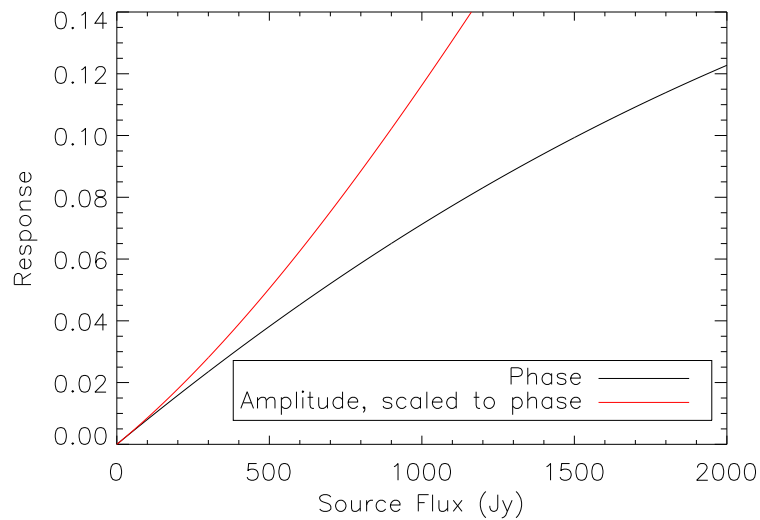


Figure C.5: The response to a point source with a flux density up to 2000 Jy. The response is clearly nonlinear, and sources at these high flux densities should not be used for calibration.

## Appendix D

### Resonance finding, I/Q projection and telescope data

In order to achieve the greatest sensitivity and properly calibrate MKID detectors, one needs to accomplish two tasks: to find the true resonance frequency, which depends on readout power and sky opacity, quickly, and to later be able to project out the correct frequency shift and dissipation directions of I and Q at that point. Both these process rely upon frequency sweeps taken around the resonance frequencies before each observation. This appendix describes both tasks. In addition, here is included the basic description of how the telescope data are collected.

#### D.1 Resonance frequencies “on-the-fly”

In order to waste the least amount of time possible between observations, the quickest possible way of finding the resonance frequency is required. Given the computing time required for doing formal resonance fits, this option is effectively useless for this application. The primary requirement is to find a close enough frequency such that there is no significant loss in responsivity. The fractional reduced responsivity due to the incorrect frequency goes as

$$err = \frac{1}{1 + i(2Q\frac{f-f_0}{f_0})}, \quad (D.1)$$

found from Equation B.15. At  $Q = 20,000$  and  $f_0 = 3.5$  GHz, a 10 kHz error results in a 0.6% flux reduction, while a 50 kHz error results in a 14.2% flux reduction. It is generally best to keep the error at the 10 kHz level to avoid having to correct for these flux discrepancies.

This can be achieved from the I/Q sweeps by looking at the magnitude of the distance in the  $S_{21}$  plane of nearby frequency points.

## D.2 Proper projection of I and Q

There are three methods for the projection of I and Q which are possible to use at the telescope. The first method is to use noise projection - that is, the fact that the frequency direction has by definition the most noise due to two-level systems. This method cannot be done with only the 100 Hz timestreams, because there are not enough frequency bins to find the optimal direction, and because sky noise may corrupt the signal. However, this can be achieved if data is taken in a “burst mode”, with high sampling rates for a brief period, before the scan. This technique is still being perfected, as sending in all frequencies simultaneously is likely to saturate the resonators.

This method is generally not preferred for optimal projection. It requires the extra data which many systems may not have the capability of offering. In addition, calibration is generally difficult with this method, as it provides no information on  $Q$  or  $Q_c$ . The direction can also be biased by optical noise, which will be purely in the response direction as opposed to the Q direction. However, the values returned by this method should be self-consistent, so one can still easily make a calibration curve of detector sensitivity versus sky opacity.

The second method involves a true fit to the resonance loop, from which it is simple to find the tangent to the circle at the frequency where the data was taken. This method is always preferred, as it also allows the fit to  $Q$  and  $Q_c$  and thus makes the results comparable to lab measurements, and able to find the efficiency of coupling to point-like sources. However, this method can be difficult when the resonators are driven into distortion or saturation, as the resonance is no longer Lorentzian. It is also recommended that high temperature data ( $T_{base} > 1.2$  K) be taken sometime during the course of the run to ensure proper fitting, given the potential for frequency-dependent transmission variability.

The third method is generally useful at high readout power, at which point noise on the resonance loop is not an issue, and the loop is too distorted to be fit by usual methods. This involves finding the tangent line to the resonance loop at the frequency of observation. This can be done in several ways, but is most easily done by averaging the lines between nearby points in

frequency. The average of the slopes around this point, given low noise, is a good approximation for the tangent at the resonance point. One can find a somewhat more accurate answer by interpolating the shape of the curve around those points. Calibration into radians, or fractional frequency shift, is difficult with this method because it is generally used at high powers, where it is difficult to measure  $Q$  and  $Q_c$  because of the distortion.

Modules for each method were written and included in the Bolocam/MKID pipeline. In practice, the third method worked the best, due to the distortion of resonators from high readout powers.

### D.3 Telescope data acquisition

The techniques described in the preceding sections need to be incorporated into a larger pipeline of data acquisition. Here we describe the basics of the organization of data from the electronics and from the telescope, as incorporated in the 2010 DemoCam engineering run. A basic schematic of how the data was planned to be taken as of 2009 is seen in Figure D.1. The basic approach was eventually used, although this does not describe many of the specific details, particularly of the software-defined readout [30].

At the beginning of the run, a list of resonance frequencies close to the actual values is generated, as well as the optimal power at which to probe the detector. In the case of the DemoCam, this was typically done by eye, but could be automated without significant degradation in performance. The information was stored in a “look-up table” called by the readout to find the optimal frequency and power to drive at. From these known powers and frequencies, a general purpose buffer of probe signals is generated. This buffer, when converted to analogue, contains one probe signal for each specified resonator. At the beginning of any observation, the telescope is pointed near, but not exactly at, a source, for an IQ sweep to be performed under the given atmospheric conditions. The IQ sweep is performed by sweeping the IF local oscillator’s frequency. This has the effect of sweeping all the probe signals simultaneously, while using the same generated buffer. Using the methods described above, new optimal probe frequencies are found for each detector,

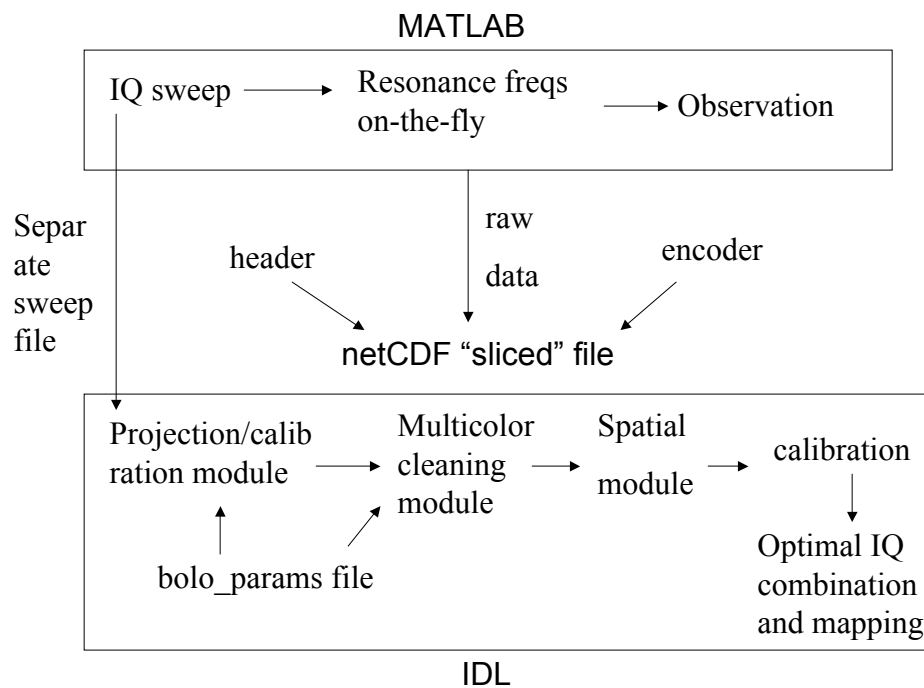


Figure D.1: Flow chart of the planned telescope data acquisition pipeline. The header and encoder store telescope data necessary for reconstructing the pointing, scanning and timing information of the telescope. Modules are programs used to calibrate and properly remove correlated noise from data timestreams. For more detail, see Ref. [63].

and a new buffer is generated corresponding to the new frequencies. This buffer is used in the observation.

The data from the observation is not merged in real time, as is done with Bolocam or in the 2007 engineering run (see Chapter 5). Instead, the data is collected from the ADC board into a single raw data file using a combination of Python and Matlab routines. This data is in sync with the GPS clock which controls the telescope signals, and is thus coordinated with the telescope pointing information. The data are merged together independently into a netCDF raw data file, including information from the IQ sweeps, and are then ready for processing and cleaning in the IDL Bolocam pipeline.

The I and Q timestreams for each detector are stored separately, and treated as separate detectors. A file in the Bolocam pipeline, called the “`bolo_params`” file, stores the information of the detector’s name<sup>1</sup> and a specific index describing what type it is, for example 9 for Band 1-I, and 10 for Band 1-Q. In this way, detectors can be separated for individual cleaning – the process of removing correlated noise among detectors – however is necessary. I and Q are treated like different types of detectors, but can be optimally combined later in the processing.

---

<sup>1</sup> For our purposes, a string containing the resonance frequency, such as “3301050000I” for a 3.30105 GHz resonator’s I projection.

## Appendix E

### Optical testbed setup

One major challenge in sub/millimeter MKID development has been the decoupling of the effects of the optical train from the resonator and antenna. Toward this purpose, we set up an independent measurement of the optical system using a feedhorn-coupled NTD bolometer. The system was set up for two main purposes: to test if the optical train creates any significant fringing in the spectral bandpasses, and to find any irregularities in beam maps which result from the optics. Assembly and testing of an optical testbed was done in collaboration with Dr. Phil Maloney of the University of Colorado, Prof. Mike Skrutskie of the University of Virginia, and Colorado undergraduate Clint Bockstiegel.

#### E.1 Description of testbed

The optical testbed was adapted from an Infrared Labs Dewar with an 8-inch diameter 4-Kelvin coldplate. In this cryostat was installed a Simon Chase two-stage 7-He refrigerator ( $^4\text{He}$  and  $^3\text{He}$  stages) capable of reaching below 380 mK under no load. The coldhead of the fridge cooled the bolometer, which was placed one half inch off-axis to mimic the effect of an MKID edge pixel. The Dewar was modified to allow for the full length of the MKID optical system, along with extra space for future testing of Polocam, the Bolocam/MUSIC polarimeter project. As in the DemoCam, the Lyot stop was formed by Eccosorb LS-30. The 4 K filter stack was a single stack, with 0.8 inches of Teflon. For several runs, in the middle of the Teflon was placed either 0.125 inches of Fluorogold or of Nylon 6/6. The filter stack at 77 K consisted of a dual-layer Teflon filter, an outer filter

0.8 inches thick, and an inner layer 0.2 inches thick, to reduce the effective load on 4 K from the warm-side Teflon. The window was composed of UHMWPE, but a Zotefoam backing was used to reduce the load onto the 77 K stage. To allow for the worst possible effects to be observed, none of the filters were tilted to reduce standing waves.

The bolometer used was a spare from the ACBAR experiment [96], which had sufficient properties for the relatively high-temperature testing performed. It was coupled to a feedhorn designed to closely approximate the far-field beam pattern expected from the 4.2 mm square antennas. However, the feedhorn itself was round for ease of fabrication. The feedhorn narrows to a waveguide designed as an approximately 330 GHz high pass filter. This is followed by metal mesh low pass filters, with cutoffs at 420 GHz and 360 GHz.

## E.2 FTS measurements

FTS measurements of the spectral bandpasses of antenna-coupled MKIDs have shown significant fringing in the spectral response, typically on scales of 10 GHz. The fringes can be quite deep, with the response at some frequencies less than half that at other frequencies. An example of this fringing is seen in Figure 4.28. To find the source of such fringing, whether from the optics or from the antenna, the optical testbed was tested using a similar Fourier Transform Spectrometer, developed by Randol Aikin [1].

Measurements of the bandpass spectrum were performed for several optical configurations. In Figure E.1 we plot the results from the detector given different configurations of the 4 K filter stack. Although fringing is seen in all cases, it is not as severe as seen in the MKID devices, pointing to the likelihood that it comes from reflections in or near the device rather than in the filter stack.

## E.3 Beam maps

Beam maps in the DemoCam configuration occasionally exhibited “skirts” of low-level response at higher angles than would be expected. An example is seen in Figure E.2. In this figure, one expects the beam to roll off as a sinc function, but the response is effectively constant out to

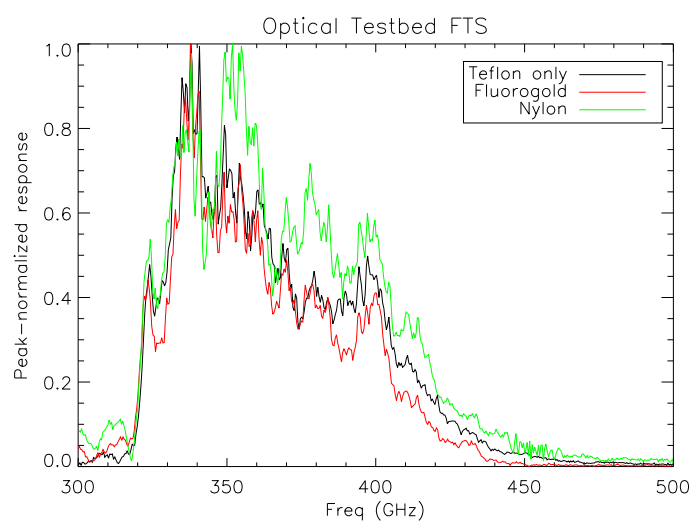


Figure E.1: FTS spectra taken from the optical testbed, in several filter stack configurations. The nylon filter stack looks anomalous compared to the other two cases, though this could be because of reduced optical transmission. All cases are peak-normalized.

wide angles. In addition, the skirts were often highly asymmetric. The mechanism for the response was not known. It could have been caused by diffraction through the optics, by wide-angle direct resonator pickup.

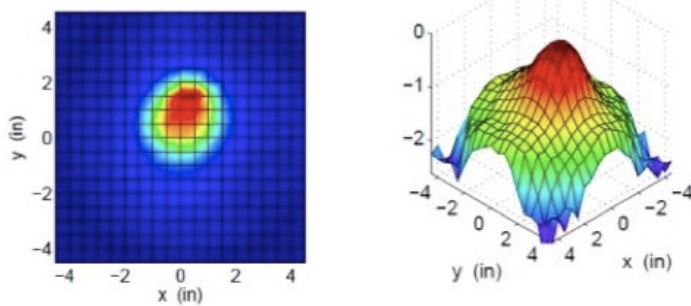


Figure E.2: Beam maps taken in the DemoCam, 4.3 inches beyond the window. Left is shown a linear map of response from a given resonator, and the logarithmic response is shown to the right (the vertical axis is shown in factors of 10). Plots courtesy of Tasos Vayonakis and Nicole Czakon.

It was impossible to truly replicate the beam map system used with the DemoCam, because that system uses a beam mapper which points upward. Thus, we had to use a 45-degree mirror to project a sideways-facing beam mapper into the downward-looking Dewar. The effective distance between the beam map blackbody source and the external Dewar window was 23 inches, placing it closer to the far field than many MKID beammaps.

Beam maps were taken on several different cooldowns, showing very little discrepancy from run to run. In Figure E.3 one can see the results. Clearly, any “skirt” does not arise from the optics. This, again, suggests a device-specific explanation for the cause of this low-level pickup.

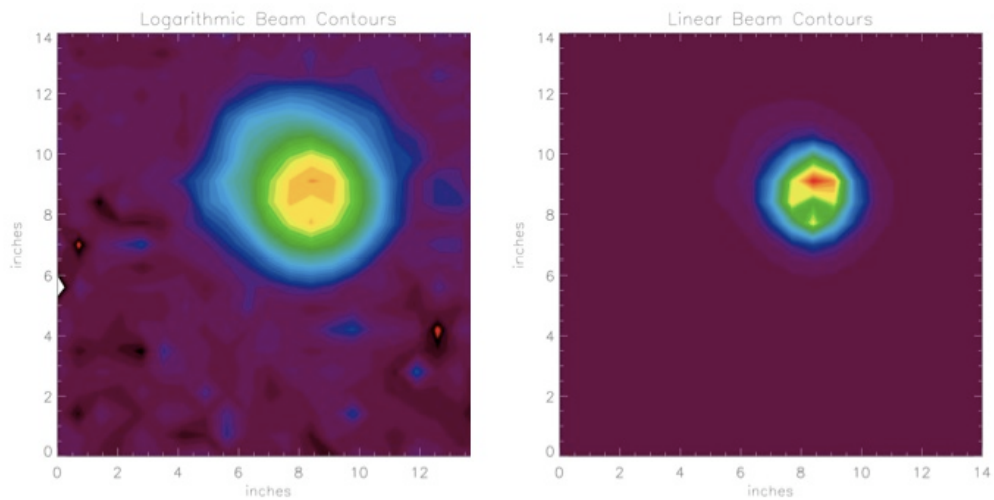


Figure E.3: Beam maps taken from the optical testbed, plotted logarithmically (left) and on a linear scale (right). Note the lack of a significant “skirt” in the logarithmic plot. Figure courtesy of Dr. Phil Maloney.

## **Appendix F**

### **Variable reference**

In this thesis, there is a large number of variables, the definitions of which can be difficult to track. For the reader's convenience, the variables used elsewhere in the thesis are given in Tables F.1 and F.2 are given.

Table F.1: Greek variables used in this thesis.

Variable	Meaning	Typical Units
$\alpha$	Kinetic inductance fraction	none
$\Delta$	Superconducting gap parameter	meV
$\Delta_0$	Superconducting gap parameter at $T = 0$	meV
$(\Delta\nu)$	Bandwidth	GHz
$\eta$	Efficiency	none
$\lambda$	Wavelength	mm
$\mu$	Effective chemical potential	eV
$\nu$	Frequency – submillimeter	GHz
$\psi$	Quasiparticle angle of response relative to frequency	rad
$\sigma_1$	real part of conductivity	$(\Omega \text{ m})^{-1}$
$\sigma_2$	imaginary part of conductivity	$(\Omega \text{ m})^{-1}$
$\sigma_n$	normal state conductivity	$(\Omega \text{ m})^{-1}$
$\tau$	Quasiparticle lifetime	$\mu\text{s}$
$\tau_0$	Quasiparticle lifetime at $T = 0$ , unloaded	$\mu\text{s}$
$\tau_{e\omega}$	Timescale for electron-phonon interactions	$\mu\text{s}$
$\tau_{225}$	Atmospheric opacity at 225 GHz	none
$\xi$	Ratio of microwave to optical QP creation efficiency	none
$\omega$	Angular frequency	rad/s

Table F.2: Latin variables used in this thesis.

$c$	Speed of light	GHz mm
$c(\Delta_0, T, \omega)$	Variable defined in Equation 3.5	$\mu\text{m}$
$C_T$	Responsivity variable determining Hz/K under load	$\text{Hz}/\text{K}^{1/2}$
$C_P$	Responsivity variable determining Hz/W undel load	$\text{Hz}/\text{W}^{1/2}$
$E$	Energy	eV
$f$	frequency – audio, microwave, or submillimeter	Hz or GHz
$f_0$	Resonance frequency	GHz
$f/\#$	Focal length / diameter of optic	none
$\hbar$	Planck's constant	eV s
$h$	$2\pi\hbar$	eV/Hz
$k$	From Equation 3.11	$\mu\text{W}^{1/2}/\text{Hz}$
$k_B$	Boltzmann's constant	eV/K
$L_k$	Kinetic Inductance	$\Omega \text{ s} / \text{rad}$
$L_m$	Geometric (or magnetic) inductance	$\Omega \text{ s} / \text{rad}$
$L_s$	Surface Inductance	$\Omega \text{ s} / \text{rad}$
$MS$	Mapping speed	$\text{arcmin}^2 \text{ mJy}^{-1} \text{ hr}^{-1}$
NEFD	Noise Equivalent Flux Density	$\text{Jy s}^{1/2}$
NEP	Noise Equivalent Power	$\text{W}/\text{Hz}^{1/2}$
$N_{fw}$	Number of FWHM	none
$N_0$	Single-spin density of states at Fermi energy	$\text{eV}^{-1}\mu\text{m}^{-3}$
$n_{qp}$	Quasiparticle density	$\mu\text{m}^{-3}$
$P$	Power – microwave or submillimeter	$\mu\text{W}$
$P_{\mu w}$	Microwave power	dBm
$P_{int}$	Internal resonator power	dBm
$Q$	Resonator quality factor	none
$Q_c$	Quality factor due to feedline coupling	none
$Q_i$	Quality factor internal to resonator	none
$R$	Quasiparticle recombination constant	$\mu\text{m}^3/\text{s}$
$R_s$	Surface resistance	$\Omega$
$T$	Temperature	K
$T_c$	Superconducting transition tempetature	K
$T_{eff}$	Effective (or quasiparticle) temperature	K
$T_n$	Noise temperature	K
$t$	conductor thickness	nm
$S$	Noise spectrum	$\text{V}^2/\text{Hz}$ or $1/\text{Hz}$
$S_{21}$	Carrier-normalized transmission	none
$S_{11}$	Carrier-normalized reflection	none
$s$	CPW center strip width	$\mu\text{m}$
$V$	Detector volume	$\mu\text{m}^3$
$V_\theta$	Signal voltage entering HEMT	V
$w$	Bandwidth (i.e. for readout)	GHz
$X_s$	Surface reactance, $\omega L_s$	$\Omega$
$Z$	Impedance	$\Omega$
$z$	Cosmological redshift	none

Table F.3: Abbreviations and Acronyms.

Acronym	Meaning
ADC	Analog-to-Digital Converter
AR	Anti-Reflection
CCAT	Cornell Caltech Atacama Telescope
CPW	Coplanar Waveguide
CSO	Caltech Submillimeter Observatory
DAC	Digital-to-Analog Converter
DAQ	Data Acquisition
DC	Direct Current
FWHM	Full Width at Half Maximum
FT	Fourier Transform
FTS	Fourier Transform Spectroscopy
GRT	Germanium Resistance Thermometer
HDPE	High Density Polyethylene
HEMT	High Electron Mobility Transistor (cryogenic amplifier)
IDC	Interdigitated Capacitor
IF	Intermediate Frequency
IQ	In-phase and Quadrature
LDPE	Low Density Polyethylene
LEKID	Lumped Element Kinetic Inductance Detector
LO	Local Oscillator
LPF	Low-Pass Filter
MKID	Microwave Kinetic Inductance Detector
MUSIC (or MuSIC)	Multiwavelength Submillimeter (kinetic) Inductance Camera
UHMWPE	Ultra-High Molecular Weight Polyethylene
PCA	Principal Component Analysis
PSD	Power Spectral Density
PTFE	Polytetrafluoroethylene (includes Teflon and Fluorogold)
RF	Radio Frequency
RJ	Rayleigh-Jeans
RMS	Root Mean Squared (also r.m.s.)
RRR	Residual Resistivity Ratio
SDR	Software Defined Readout (formerly, Radio)
SED	Spectral Energy Distribution
SIS	Superconductor-Insulator-Superconductor
SQUID	Superconducting Quantum Interference Device
SZE	Sunyaev-Zel'dovich Effect (sometimes just SZ)
TLS	Two-Level Systems
UC	Ultracold (refrigerator coldhead)
ZA	Zenith Angle (angle away from zenith)